Investigation into Ion Channel- and Nitric Oxide-Mediated Vasodilation in Resistance Arteries

UNIVERSITY OF
OXFORD

Lillian Eleanor Wallis
Magdalen College
University of Oxford

A thesis submitted for the degree of
Doctor of Philosophy
Michaelmas 2024

ABSTRACT

Effective regulation of resistance artery tone is essential in maintaining adequate tissue perfusion across the body. Artery tone is determined by various ion channels, with voltage-gated calcium channels (VGCCs) expressed by vascular smooth muscle cells (VSMCs) being key in facilitating the influx of Ca^{2+} required for vasoconstriction. The endothelium provides the main vasodilatory signals, including nitric oxide (NO) and endothelium-derived hyperpolarisation (EDH).

The first part of this study develops a protocol to detect basal and stimulated NO release in intact, *ex vivo* resistance arteries using a fluorescent dye. For the first time, this will allow real-time NO release to be monitored in physiologically relevant artery preparations, addressing an important gap in vascular research.

The second part of this study investigates the function and expression of T-type VGCCs in rat mesenteric and coronary arteries. While the role of L-type VGCCs has been long established in larger arteries, recent research has highlighted the importance of T-type VGCCs in smaller resistance arteries and their potential involvement in vasodilation. Using RNAscope and immunohistochemistry, we confirm the presence of $Ca_V3.1$, $Ca_V3.2$, and $Ca_V3.3$ channels in endothelial cells (ECs) and VSMCs. Functional studies indicate that these channels contribute to vasodilation through smooth muscle-mediated signalling, particularly by interacting with BK_{Ca} channels. For the first time in myogenically-active coronary arteries, we show that blocking $Ca_V3.2$ channels produces vasoconstriction, revealing their paradoxical role in opposing contraction and maintaining vascular tone. Furthermore, we show the expression of T-type VGCCs by VSMCs at the points where myoendothelial projections (MEPs) make contact, raising the possibility that these channels contribute to myoendothelial feedback vasodilation.

The final part of this study explores the expression of hyperpolarisation-activated cyclic nucleotide-gated (HCN) channels by ECs of resistance arteries. We provide the first evidence that HCN channels are present in the endothelium, which corresponds to unpublished functional data from the Dora/Garland group demonstrating their role in facilitating Ca^{2+} influx in hyperpolarised cells.

Overall, these findings enhance our understanding of microvascular function and provide a basis for further research which may have significant clinical implications.

ACKNOWLEDGEMENTS

I would like to thank my supervisors, Professors Kim Dora and Christopher Garland, for the opportunity to undertake this research. Their guidance and expertise have been instrumental in shaping this thesis, and I am grateful for their mentorship throughout my DPhil.

I also wish to acknowledge the members of the Dora/Garland group for their collaboration and valuable input, with special thanks to Dr JinHeng Lin, Dr Lauren Phillips, Dr William Stockdale, Dr Lucy Donovan, Dr Hanson Ng, Dr Katherine Banecki, and DPhil student Toby Brown, for their assistance and thoughtful discussions.

To my family and friends, thank you for your support, patience, and encouragement during this journey. I want to specially thank my lovely partner, Sam, for his unwavering support in every way.

Lastly, I am grateful to Magdalen College and Leon and Iris Beghian for the scholarship which has made this research possible.

PUBLICATIONS AND CONFERENCE COMMUNICATIONS

Wallis, L., Donovan, L., Johnston, A., Phillips, L., Lin, J., Garland, C.J. and Dora, K.A. 2023. Tracking endothelium-dependent NO release in pressurised arteries. *Front Physiol*, 14:1108943.

Ng, Y.Y.H., Dora. K.A., Lemmey, H.A.L., Lin, J., Alden, J., Wallis, L., Donovan, L., Shorthose, O., Leiper, F.C., Leiper, J. and Garland, C.J. 2024. Asymmetric dimethylarginine enables depolarizing spikes and vasospasm in mesenteric and coronary resistance arteries. *Hypertension*, 81(4), pp. 764-755.

Wallis, L., Donovan, L., Johnston, A., Garland, C.J. and Dora. K.A. Protocol optimisation for a fluorescent nitric oxide indicator in rat mesenteric arteries *ex vivo.* Selected for poster presentation at Europhysiology 2022, 16th-18th September 2022, Copenhagen, Denmark.

CONTENTS

FIGURES

TABLES

ABBREVIATIONS

ACh	Acetylcholine
ADMA	Asymmetric dimethylarginine
AF	Alexa Fluor™ 633 Hydrazide
ANG-II	Angiotensin II
ATP	Adenosine triphosphate
BH_4	Tetrahydrobiopterin
CaM	Calmodulin
cAMP	Cyclic adenosine monophosphate
cGMP	Cyclic guanylyl monophosphate
CNBD	Cyclic nucleotide binding domain
Cx	Connexin
DAF	Diaminofluorescein
DAR	Diaminorhodamine
ECs	Endothelial cells
EDH	Endothelium-dependent hyperpolarisation
EDHF	Endothelium-derived hyperpolarising factor
EETs	Epoxyeicosatrienoic acids
eNOS	Endothelial NOS
Hb	Haemoglobin
HbNO	Nitrosylhaemoglobin
HCN	Hyperpolarisation-activated cyclic nucleotide-gated
HIFs	Hypoxia-inducible factors
HNO	Nitroxyl
HUVECs	Human umbilical vein endothelial cells
IEL	Internal elastic lamina
IP3	Inositol 1,4,5-trisphosphate
IP_3Rs	Inositol 1,4,5-trisphosphate receptors
K_{ir} channels	Inwardly-rectifying K+ channels
L-NAME	N(ω)-nitro-L-arginine methyl ester
L-NMMA	N(ω)-monomethyl L-arginine
MEGJs	Myoendothelial gap junctions
MEPs	Myoendothelial projections
MLC	Myosin light chain
MLCK	Myosin light chain kinase

MT tension	Myogenic tone tension
nNOS	Neuronal NOS
NO	Nitric oxide
NO_2^-	Nitrite
NO_3^-	Nitrate
NOS	NO synthase
NPY	Neuropeptide Y
PBS	Phosphate buffered saline
PE	Phenylephrine
PFA	Paraformaldehyde
PGI2	Prostacyclin
PKA	Protein kinase A
PKC	Protein kinase C
PP1	Protein phosphatase 1
PP2A	Protein phosphatase 2A
RCos	Rat coronary arteries
RCres	Rat cremaster arteries
RMAs	Rat mesenteric arteries
ROI	Region of interest
RT-PCR	Reverse transcription polymerase chain reaction
RyRs	Ryanodine receptors
SAN	Sinoatrial node
sGC	Soluble guanylyl cyclase
SNAP	*S*-Nitroso-N-acetyl-DL-penicillamine
SNO-Hb	*S*-nitrosohaemoglobin
SR	Sarcoplasmic reticulum
SSC	Saline-sodium citrate
STOCs	Spontaneous transient outward currents
TRAM-34	1-[(2-chlorophenyl) diphenylmethyl]-1H-pyrazole
TRPV1	Transient receptor potential vanilloid 1
VECTors	VGCC-dependent endothelial calcium transients
VGCCs	Voltage-gated calcium channels
VSMCs	Vascular smooth muscle cells

1. Introduction

1.1 The role of resistance arteries in the cardiovascular system

The mammalian cardiovascular system, composed of the heart and blood vessels, delivers vital oxygen and nutrients to tissues of the body whilst removing waste products. As blood from the heart flows towards tissues, it is diverted through increasingly narrow arteries and arterioles, producing a drop in blood pressure as resistance to flow increases. These small resistance vessels, < 300 μm in diameter, are key in controlling blood pressure, with even minor changes to their luminal diameter influencing blood pressure. A common feature of resistance arteries is their ability to develop myogenic tone in response to increased intraluminal pressure, which is important in stabilising tissue blood flow across the body (Bayliss, 1902). The basal level of contraction of myogenically-active arteries allows them to sensitively and dynamically respond to changes in blood pressure and flow by increasing or decreasing tone, which is essential in meeting the metabolic demands of tissues including skeletal muscle and the myocardium.

Resistance artery dysfunction, which manifests as elevated arterial tone, underlies the development of hypertension and other related cardiovascular diseases including coronary artery disease (progressing to myocardial infarction) and heart failure (Schiffrin, 1992). Accounting for up to one third of deaths globally, our understanding of the mechanisms governing resistance artery contraction and relaxation is key in treating hypertension and preventing the onset of life-threatening cardiovascular diseases. Using rat resistance arteries supplying the mesentery, heart, and cremaster, this thesis investigates novel mechanisms contributing to the tone of arteries supplying smooth, cardiac, and skeletal muscle, respectively. Additionally, it aims to develop a protocol for directly detecting nitric oxide (NO), a key signalling molecule involved in vasodilation, in *ex vivo* resistance arteries.

1.2 Structure of resistance arteries

Like all blood vessels, resistance arteries consist of three distinct cell layers: the tunica intima (composed of endothelial cells; ECs), the tunica media (vascular smooth muscle cells; VSMCs) and the tunica adventitia (connective tissue and perivascular nerve endings). Forming a monolayer coating the vessel lumen, ECs respond to circulating molecules, such as hormones and other vasoactive mediators, as well as mechanical changes derived from blood pressure and flow, by transmitting signals to the underlying media (Garland *et al.*, 2011).

The tunica media is the thickest layer of the artery wall, consisting of multiple layers of VSMCs mostly oriented circumferentially around the lumen. The contractile force generated by these cells, which act in syncytium, determines the luminal diameter of blood vessels and hence blood pressure and flow. Finally, the tunica adventitia contains sympathetic nerve terminals which release a range of neurotransmitters, including adenosine triphosphate (ATP), noradrenaline, and neuropeptide Y (NPY), which influence arterial tone by binding to G-protein coupled receptors on VSMCs. The influence of innervation on artery contractility varies between vascular beds, although mesenteric, coronary and cremaster resistance arteries are all densely innervated (Aalkjær *et al.*, 2021).

Despite being separated by a sheet of connective tissue (the internal elastic lamina; IEL), ECs and VSMCs work together to regulate resistance artery tone via a complex interplay. Their communication occurs via many pathways, either involving the release of diffusible factors such as NO and endothelium-derived hyperpolarising factor (EDHF), or the intercellular, contact-mediated transfer of signalling molecules and ions (Garland *et al.*, 2011). Facilitating this intercellular communication are myoendothelial projections (MEPs; see **Figure 1.2.1**), which originate from ECs and establish contact with VSMCs through fenestrations in the IEL (Chaytor *et al.*, 1998). At these points of contact, plasmalemmal connexin (Cx) proteins from

apposing cells dock to form myoendothelial gap junctions (MEGJs), creating a cytoplasmic continuum between the cell types. Additionally, homocellular gap junctions in the endothelium and vascular smooth muscle layer contribute to coordinated contractile responses, which are especially important in coupling blood flow to local metabolic demand (Segal and Duling, 1989). Whilst the physiological role of MEPs and gap junctions in the resistance vasculature is not fully understood, extensive evidence suggests they are important in regulating arterial diameter by facilitating the movement of signalling molecules between cells.

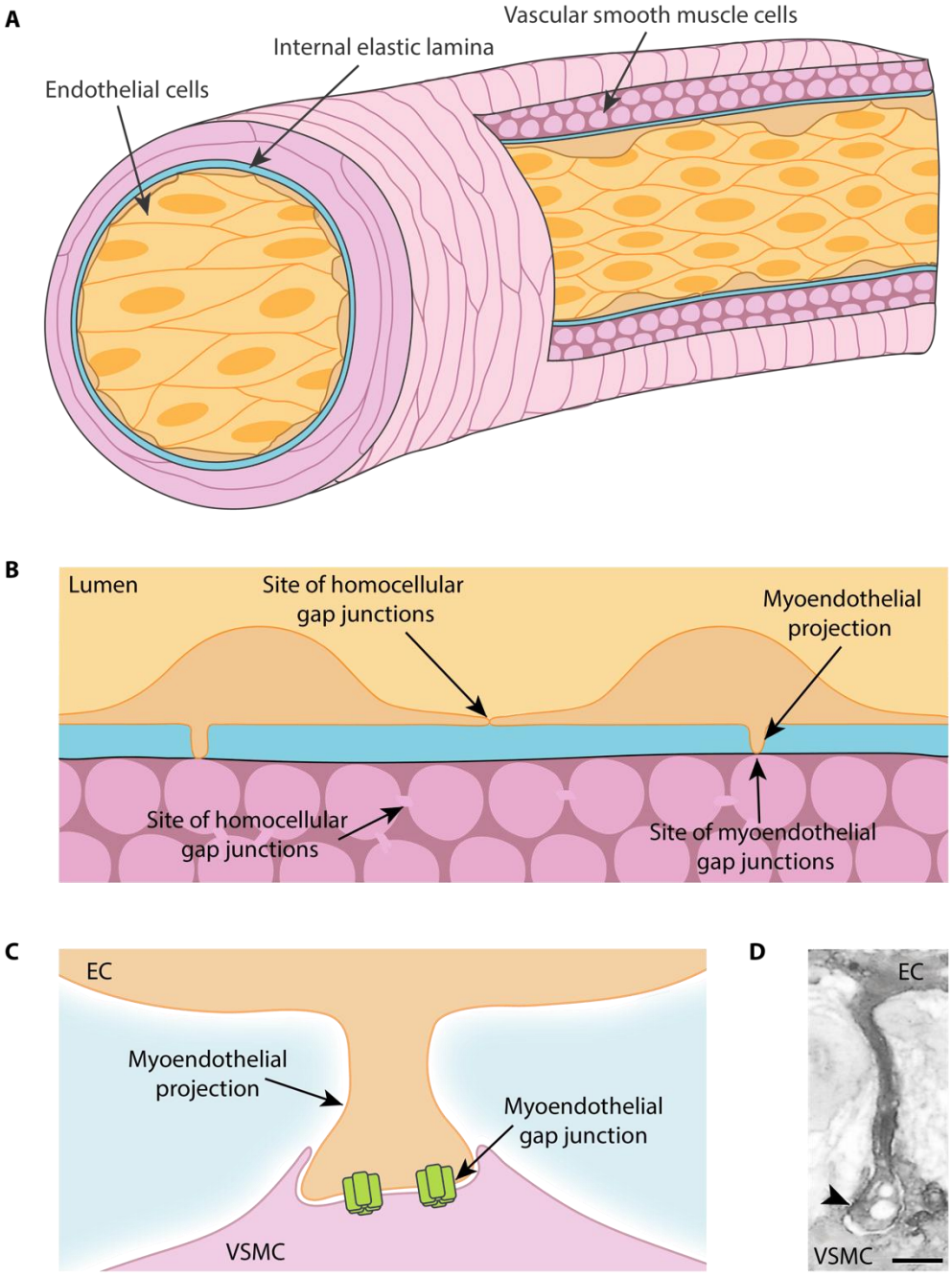

Figure 1.2.1. Structure of a resistance artery with cell-to-cell connections shown. (A, B, C) Schematic cross-section through artery wall with myoendothelial projections highlighted. These projections allow endothelial cells (ECs) to physically contact underlying vascular smooth muscle cells (VSMCs) through the internal elastic lamina, where myoendothelial gap junctions connect the cell types. (**D**) Electron micrograph showing transverse cross-section through mesenteric resistance artery (~ 115 μm diameter). The black arrowhead indicates the point where the myoendothelial projection makes contact with the VSMC. Scale bar is approximately 250 nm. Electron micrograph taken from Sandow and Hill (2000).

1.3 Voltage-gated calcium channels determine arterial tone

As previously mentioned, the degree of arterial tone generated is dependent on the synchronised contraction of individual VSMCs in the artery wall. Their contractile tension is primarily governed by cytosolic Ca^{2+} concentration ($[Ca^{2+}]$), which is determined by (1) depolarisation-driven Ca^{2+} influx via sarcolemmal ion channels and (2) voltage-insensitive Ca^{2+} release from the sarcoplasmic reticulum (SR). The relative contribution of each pathway differs between vessel type and size, with small resistance arteries relying more on Ca^{2+} influx via sarcolemmal voltage-gated calcium channels (VGCCs) compared to larger conduit arteries. This is likely due to the increased abundance of L- and T-type VGCCs expressed in resistance arteries relative to large arteries, their opening resulting in sufficiently elevated cytosolic $[Ca^{2+}]$ to drive contraction (Ball *et al.*, 2009). Ca^{2+} drives vasoconstriction by binding to calmodulin and activating myosin light chain kinase (MLCK), leading to the phosphorylation of serine residues on myosin light chain (MLC) filaments and facilitating crossbridge formation between myosin and actin. Due to their importance in regulating artery diameter, this section of the thesis will primarily focus on Ca^{2+} entry via VGCCs.

The VGCC family comprises ten molecular sub-types, although the predominant isoforms expressed in arteries are high-voltage activated L-type VGCCs ($Ca_V1.1$-1.4) and low-voltage activated T-type VGCCs ($Ca_V3.1$-3.3). All functional VGCCs have a pore-forming α_1 subunit containing 4 homologous domains, each with six transmembrane helical segments (Perez-Reyes, 2003). This subunit facilitates the selective conductance of Ca^{2+} and contains voltage-sensing machinery, either existing in isolation (in T-types; see **Figure 1.3.1**) or in association with other auxiliary subunits (in L-types). These auxiliary subunits, such as α_2 and β, provide additional regulation of ion conductance and kinetics through their impact on the channel's voltage sensitivity, and account for the differences in biophysical characteristics of T- and L-type VGCCs. All VGCCs are characterised by depolarisation-dependent activation, voltage-dependent inactivation and hyperpolarisation-induced deactivation, however, T- and L-type

channels exhibit significant differences in terms of their voltage sensitivity and activation/inactivation kinetics. Compared to L-type VGCCs, T-type VGCCs open at lower voltages and activate and inactivate faster, thus providing a transient rather than sustained current. The three T-type channel subtypes share a high degree of amino acid sequence identity in their transmembrane segments (60 – 100%), with most variation between the channels occurring within the I-II linker and C-terminus region (Perez-Reyes *et al.*, 1998). This divergence in structure is reflected in subtle differences between the channels' biophysical properties; $Ca_V3.1$ and $Ca_V3.2$ display the fastest activation kinetics (1-2 ms) compared to $Ca_V3.3$ (7 ms), and $Ca_V3.1$ displays the slowest deactivation kinetics, followed by $Ca_V3.2$ then $Ca_V3.3$ (Klöckner *et al.*, 1999).

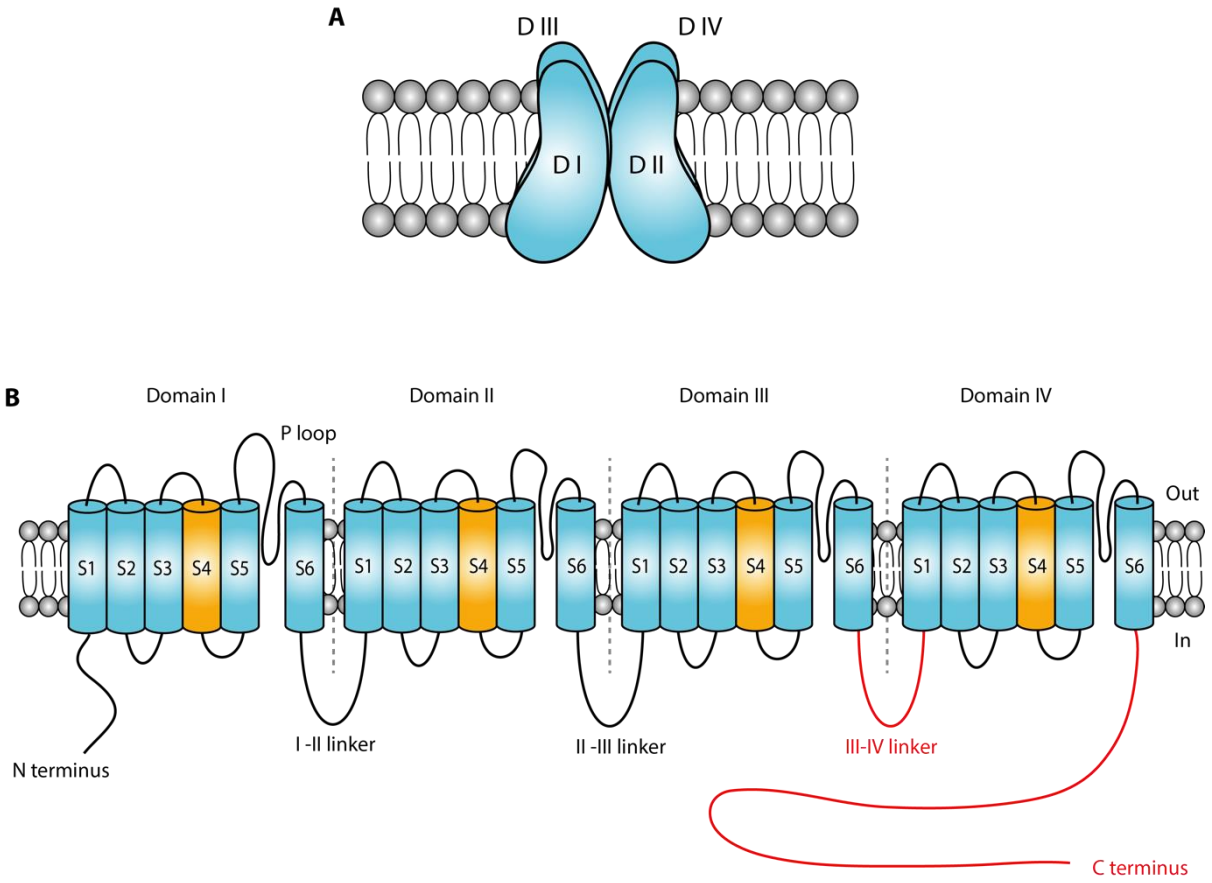

Figure 1.3.1. Membrane topology of T-type voltage-gated calcium channels. (**A**) The α_1 pore-forming subunit is formed of a single protein with 4 homologous domains (DI – IV) connected by cytosolic linkers (I-II, II-III, and III-IV) shown in **B**. (**B**) The arginine/lysine-rich S4 segments (coloured orange) form the voltage sensor, whereas the re-entrant P-loops form the pore of the channel and provide Ca^{2+} selectivity. The three T-type channel subtypes share a high degree of amino acid sequence similarity within the transmembrane segments, with the major sites of divergence occurring in the I-II linker and the C-terminus regions. Alternative splicing occurs in the III-IV linker and C-terminus regions (coloured red), which produces various splice variants with right-shifted current-voltage curves and prolonged activation kinetics. L-type VGCCs, such as $Ca_V1.2$, comprise a similar α_1 pore-forming subunit but have additional auxiliary subunits such as α_2 and β. Figure adapted from Weiss and Zamponi (2019).

1.4 The roles of voltage-gated calcium channels in the vasculature

Investigations into the expression and function of L- and T-type VGCCs in the systemic circulation have often yielded contradictory results which differ depending on species and vascular bed (see **Table 1.4.1** for summary). Of the two families, evidence suggests that L-type VGCCs are major contributors to the elevated VSMC [Ca^{2+}] associated with sustained vasoconstriction. Their importance was demonstrated by Langton and Standen (1993), who recorded Ca^{2+} currents (I_{Ca}) in isolated rat basilar artery SMCs. Despite incrementally increasing cells' holding potential from -88 to -48 mV, they did not identify transient and rapidly inactivating T-type currents, concluding that only L-type VGCCs contributed to the steady-state Ca^{2+} influx they observed. Subsequent investigations using intact, pressurised rat cerebral arteries, showed that selectively blocking L-type VGCCs with dihydropyridine drug nisoldipine (10 nM) almost completely abolished myogenic tone development and K^+-induced vasoconstriction (Knot and Nelson, 1998). Taken together, these studies reveal that L-type VGCCs are essential in facilitating the depolarisation-driven Ca^{2+} influx required for rat cerebral artery constriction. Another study however, also using rat cerebral arteries, showed that ~20% of myogenic tone remained after the application of L-type VGCC inhibitors diltiazem or nifedipine to pressurised arteries, implicating a larger role for non-L-type VGCCs than first thought (Mufti *et al.*, 2010). More thorough analysis of Knot and Nelson's work reveals that the Ca^{2+} chelator EGTA was not added to the zero Ca^{2+} buffer used to estimate arteries' passive diameter. Consequently, the maximum diameters were likely underestimated, whilst the contribution of L-type channels to vasoconstriction was overestimated; Mufti *et al.* compared the diameters of pressurised arteries in zero Ca^{2+} buffer with those of arteries in zero Ca^{2+} buffer plus EGTA and found that the addition of EGTA caused further dilation.

Select studies have shown that resistance arteries do not always express functional L-type VGCCs. Employing reverse transcription polymerase chain reaction (RT-PCR) and gel

electrophoresis to probe mRNA expression in rat mesenteric arterioles, Gustafsson *et al.* (2001) found that L-type VGCCs are not expressed in arterioles < 40 μm diameter. The effects of various VGCC blockers on the diameter of small arterioles *in vivo* was measured. Dihydropyridines (nifedipine or nimodipine, both 10 μM) had no significant effect on vasoconstriction in response to local stimulation with current or noradrenaline, whereas T-type VGCC blockers Ni^{2+} (1 mM) and mibefradil[1] (10 μM) abolished vasoconstriction. An absence of L-type VGCCs in the smallest resistance vessels was also observed by Morita *et al.* (1999), who found that the fraction of nifedipine insensitive I_{Ca} increased as guinea pig mesenteric arteries became more distal, amounting to almost 100% of global I_{Ca} in the most peripheral vessels. Taken together, these studies indicate that T-type VGCCs contribute more to depolarisation-induced vasoconstriction as artery diameter decreases, whereas L-types contribute less. As the smallest resistance arteries contribute most to blood pressure control, T-type VGCCs may provide a promising target to reduce blood pressure in hypertension without inducing the negative side effects associated L-type VGCC blockers.

The significant role for T-type VGCCs in small arterioles does not mean that these channels are not functionally relevant in larger arteries. Studying isolated dog basilar artery VSMCs, Nikitina *et al.* (2007) identified both T- and L-type Ca^{2+} currents, as well as mRNA and protein corresponding to $Ca_V1.2$, $Ca_V3.1$ and $Ca_V3.3$ VGCCs ($Ca_V3.2$ expression was not probed). Interestingly, they found that cells were heterogenous in the Ca^{2+} currents they exhibited, with some displaying mostly T-type currents and others mainly L-type currents. This highlights the

[1] It should be noted that the use of mibefradil to block T-type VGCCs is controversial, as it has been shown to antagonise L-type VGCCs and other ion channels, particularly at concentrations greater than 1 μM. Despite this, it is still the most widely used T-type VGCC antagonist, but the potential for non-specific effects should be taken into account when interpreting its effects.

importance of exercising caution when interpreting current measurements from a small sample of VSMCs and may be one reason why studies have produced conflicting data.

The potential for T-type VGCCs to contribute significantly to vasoconstriction in resistance arteries is surprising as their associated Ca^{2+} currents are tiny and transient. These characteristics make them unlikely candidates for eliciting substantial increases in VSMC $[Ca^{2+}]$. Despite this, evidence indicates that T-type VGCCs can modulate arterial tone in a variety of vascular beds, both directly and indirectly (summarised in **Figure 1.4.1**). Understanding the complex roles of T-type VGCCs in arteries is especially important in the context of drug development, as the use of T-type channel blockers to treat a range of diseases is gaining interest.

Citation	Species / vascular bed	Experimental method	L-type	T-type
Hirst *et al.* (1986)	Rat cerebral arterioles	Sharp microelectrode recording of pinned brain tissue	✓	✓
Smirnov and Aaronson (1992)	Human mesenteric arteries	Whole-cell patch clamp on isolated cells	✓	✓
Langton and Standen (1993)	Rat cerebral arteries	Whole-cell patch clamp on isolated cells	✓	✗
Quignard *et al.* (1997)	Human coronary myocytes	Whole-cell patch clamp on freshly isolated cells	✓	✗
		Whole-cell patch clamp on cultured cells	✓	✓
Knot and Nelson (1998)	Rat cerebral arteries	Pressure myography and sharp microelectrode recording	✓	
Morita *et al.* (1999)	Guinea pig mesenteric arteries	Whole-cell patch clamp on isolated cells	✓	✓
Hayashi *et al.* (2003)	Rat renal arterioles	Isolated perfused kidney	✗	✓
Nikitina *et al.* (2007)	Dog cerebral arteries	Whole-cell patch clamp on isolated cells	✓	✓
Mufti *et al.* (2010)	Rat cerebral arteries	Pressure myography and sharp microelectrode recording	✓	✓
Smirnov *et al.* (2013)	Rat afferent renal arterioles	Whole-cell patch clamp on isolated cells	✓	✗
	Rat efferent renal arterioles	Whole-cell patch clamp on isolated cells	✗	✗
Harraz *et al.* (2014b)	Rat cerebral arteries	Pressure myography		✓
Harraz *et al.* (2015)	Mouse mesenteric arteries	Pressure myography		✓
El-Lakany *et al.* (2023)	Mouse mesenteric arteries	Pressure myography and VSMC calcium imaging		✓

Table 1.4.1. Summary of selected studies investigating L- and T-type calcium currents in vascular smooth muscle cells (VMSCs) of arteries. A tick (✓) indicates studies that reported the presence of L- or T-type Ca^{2+} currents, while a cross (✗) denotes studies that did not find such evidence. Blank cells represent studies that either did not investigate these currents or did not reach a definitive conclusion.

1.4.1 Direct role for T-type voltage-gated calcium channels in the vasculature

A direct role for T-type VGCCs in sustained vasoconstriction may result from continuous and accumulating Ca^{2+} influx occurring within the voltage window between the channels' overlapping steady-state activation and inactivation curves (between -65 and -45 mV measured in cardiac Purkinje cells using a 1 second pulse protocol; Hirano *et al.*, 1989). The ability of T-type VGCCs to mediate sustained Ca^{2+} entry in VSMCs over their window current has been demonstrated in guinea pig mesenteric arteries, where most of the I_{Ca} in VSMCs from small arteries was attributed to nifedipine-insensitive, Ni^{2+}-sensitive VGCCs (Morita *et al.*, 1999). Although it has not yet been demonstrated, it is plausible that the increased intracellular [Ca^{2+}] attributed to T-type window currents could directly affect vasoconstriction. This is supported by findings from a study on human myoblast cells, where T-type currents were shown to elevate intracellular [Ca^{2+}] by approximately 40 nM (Bijlenga *et al.*, 2000). The purported ability of T-type VGCCs to directly influence VSMC [Ca^{2+}] is challenged by fact that the window current of the channels falls outside of the range of membrane potentials recorded in VSMCs of pressurised arteries (between -45 and -30 mV; Knot and Nelson, 1998). Despite this discrepancy, emerging evidence suggests that splice variants of T-type VGCCs may be expressed in the vasculature with more favourable electrophysiological properties for significantly elevating intracellular [Ca^{2+}].

All three T-type VGCC subtypes are subject to extensive splicing, with the majority of changes occurring in the III-IV linker and C-terminal regions, where channel function would likely change as a result (Mittman *et al.*, 1999; Zhong *et al.*, 2006). Evidence suggests that alternative splicing in the III-IV linker region of human $Ca_V3.1$ and $Ca_V3.2$ channels shifts both activation voltages and window currents to more depolarised potentials (Chemin *et al.*, 2001; Zhong *et al.*, 2006), and splicing of human $Ca_V3.3$ channels produces variants which display slower activation/inactivation kinetics and faster recovery times following inactivation (Murbartián *et al.*, 2002). It should be noted that short pulse protocols used in these studies

(all less than 500 ms) may not accurately reflect the kinetics of channels expressed by VSMCs. Unlike rapidly firing cardiac myocytes or neurones, electrically quiescent VSMCs normally display graded depolarisations, which would be better replicated using longer pre-pulse stimulations. In any case, the shifted window currents towards the physiological range of membrane potentials found in pressurised arteries makes it likely that select T-type channel splice variants underly part of the nifedipine-insensitive I_{Ca}. Furthermore, if $Ca_V3.3$ channel splice variants are expressed by VSMCs, they may underpin sustained Ca^{2+} influx due to their prolonged activation.

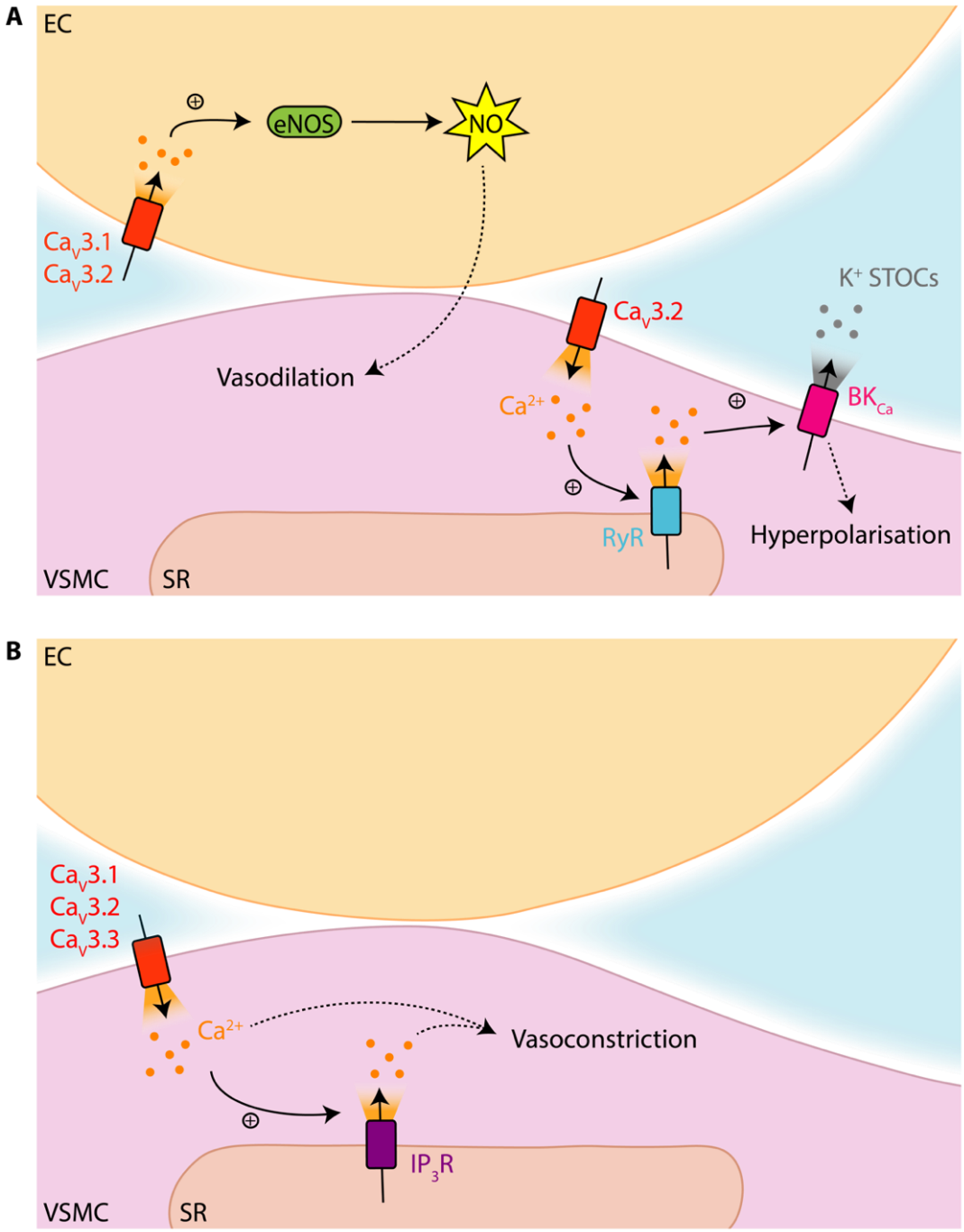

Figure 1.4.1. Indirect and direct effects of T-type voltage-gated calcium channels (VGCCs) on arterial tone. (**A**) Ca^{2+} influx through T-type VGCCs may cause vasodilation by activating endothelial nitric oxide synthase (eNOS) to produce nitric oxide (NO), or by forming signalling microdomains with VSMC ryanodine receptors (RyRs) and BK_{Ca} channels to trigger spontaneous transient outward currents (STOCs). (**B**) Ca^{2+} influx through T-type VGCCs expressed by VSMCs may cause vasoconstriction directly by raising intracellular [Ca^{2+}], or indirectly by contributing to the activation of IP_3 receptors (IP_3Rs).

1.4.2 Indirect role for T-type voltage-gated calcium channels in the vasculature

The indirect influence of T-type I_{Ca} on vasoconstriction is believed to involve amplification of the Ca^{2+} signal via activation of nearby Ca^{2+} channels located on the SR. This link was first observed in Fluo-3 loaded cultured dysgenic mouse skeletal muscle cells, which lack L-type VGCCs but express T-type channels. Using changes in fluorescence to estimate intracellular [Ca^{2+}], the increase in cell Ca^{2+} triggered by test pulses (~ -20 mV) to activate T-type VGCCs was significantly higher than predicted (~200 nM compared to ~12 nM). The authors concluded that this unexpected increase was a result of Ca^{2+} influx through T-type VGCCs activating Ca^{2+} release from intracellular stores, providing a positive feedback mechanism for increasing intracellular [Ca^{2+}] (Garcia and Beam, 1994).

The same mechanism was identified in rat renal arteriole VSMCs where vessel diameters were measured in isolated perfused kidneys. First, it was established that angiotensin II (ANG-II) caused constriction of arterioles due to Ca^{2+} release from intracellular stores, which was inhibited by mibefradil (1 μM; Hayashi *et al.*, 2003). The blocking effect of mibefradil on ANG-II-induced vasoconstriction persisted even in the presence of staurosporine, a protein kinase C (PKC) pathway inhibitor, indicating that T-type VGCCs cause vasoconstriction through their activation of SR Ca^{2+} channels. Further work by El-Lakany *et al.* (2023) in mouse mesenteric arteries confirms that T-type VGCCs, specifically the $Ca_V3.1$ subtype, interact with SR inositol 1,4,5-trisphosphate (IP_3) receptors (IP_3Rs) to contribute to Ca^{2+} wave generation and myogenic tone development. Combining pressure myography with Ca^{2+} imaging, the authors found that VSMCs from $Ca_V3.1^{-/-}$ mice displayed 65% fewer Ca^{2+} waves compared to arteries from control mice, which were further reduced in the presence of IP_3R blocker xestospongin C.

A link between T-type VGCCs and other SR Ca^{2+} channels has also been proposed. Intriguingly, Harraz *et al.* (2014a) found that instead of contributing to vasoconstriction, $Ca_V3.2$

channels can oppose it by interacting with functionally coupled ryanodine receptors (RyRs) and Ca^{2+}-activated K^+ channels. In pressurised rat cerebral arteries, the selective T-type VGCC blocker Ni^{2+} (50 μM) evoked vasoconstriction while reducing VSMC Ca^{2+} spark frequency. This indicates that in slightly depolarised VSMCs, $Ca_V3.2$ channels underpin Ca^{2+} influx and RyR-associated Ca^{2+} spark generation. Structural analysis including a proximity ligation assay revealed the close association between $Ca_V3.2$ channels and RyRs (<40 nm apart), which were confined to discrete microdomains in or close to caveolae. Finally, the group found that BK_{Ca} channel blocker paxilline elicited arterial constriction equivalent, but not additive, to Ni^{2+}, suggesting that $Ca_V3.2$ channels oppose excess vasoconstriction by triggering Ca^{2+} sparks which activate hyperpolarising spontaneous transient outward currents (STOCs) via BK_{Ca} channels.

Although the VSMC $Ca_V3.2$/RyR/BK_{Ca} channel axis has been identified in rat and human cerebral arteries, and mouse mesenteric arteries (Harraz *et al.*, 2014a; Harraz *et al.*, 2015), it is not a ubiquitous feature of all resistance arteries. The application of Ni^{2+} (30 μM) to pressurised murine superior epigastric arteries produced vasoconstriction which was not attenuated by paxilline, suggesting that $Ca_V3.2$ channels regulate arterial tone independently of BK_{Ca} channels in these arteries (Mullan *et al.*, 2017). The same group also repeated this protocol in mouse mesenteric arteries, where Ni^{2+} produced constriction even in the presence of paxilline, a finding at odds with the results published by Harraz *et al*. A possible explanation for these conflicting results is the difference in arterial diameters. Mullan *et al.* studied larger second and third order mesenteric arteries, whilst Harraz *et al.* focused on smaller third and fourth order arteries. As a link between T-type VGCCs and artery size has already been established, the interaction between $Ca_V3.2$ channels, RyRs, and BK_{Ca} channels may be more pronounced in smaller arteries.

Together, these studies demonstrate that T-type VGCCs expressed by VSMCs can both directly and indirectly modulate arterial tone. T-type channels, specifically splice variants with

right-shifted activation curves, facilitate sustained I_{Ca} across their window current, leading to MLC phosphorylation and vasoconstriction at low intravascular pressures. Evidence also suggests that T-type VGCCs exert their effects indirectly by functionally coupling with other proteins such as IP_3Rs, RyRs and BK_{Ca} channels. Signalling through the $Ca_V3.2$/RyR/BK_{Ca} channel microdomain appears to be heterogeneous both between and within vascular beds, and further studies are required to establish the reproducibility of results. Notably, there have been no studies on T-type VGCC microdomain signalling in coronary resistance arteries, despite the critical role of the coronary microcirculation in meeting the myocardium's oxygen demands.

1.4.3 Endothelial T-type voltage-gated calcium channels

While ECs are generally considered to be non-excitable, the presence and functional significance of VGCCs in these cells remains a topic of debate due to the emergence of contradictory evidence over the past 30 years. Early experiments using patch-clamp electrophysiology to measure whole-cell currents in cultured ECs from conduit arteries found no evidence for voltage-gated Ca^{2+} channels (Takeda *et al.*, 1987; Daut *et al.*, 1988). Around the same time, however, two distinct VGCC populations were identified in cultured ECs from bovine adrenal gland capillaries (Bossu *et al.*, 1989). Transient T-type currents and sustained L-type currents were detected as cells were depolarised from -80 mV to -30 mV, perhaps suggesting that these channels underpin endothelial Ca^{2+} influx in only the smallest vessels. This idea is supported by functional evidence of T-type VGCCs in cultured ECs from rat pulmonary arterioles, but not in larger rat pulmonary arteries (Wu *et al.*, 2003). Further molecular characterisation of total RNA isolated from arteriolar ECs revealed that $Ca_V3.1$ VGCCs were responsible for the T-type I_{Ca} recorded. The findings reported by these studies should be interpreted with care, however, as the ECs used to investigate Ca^{2+} currents had been maintained in culture for extended periods of time, some over successive passages. Indeed, differences in the presence of T-type I_{Ca} have been reported in freshly isolated vs

cultured human coronary VSMCs (Quignard *et al.*, 1997). ECs are known to undergo significant changes in protein expression when cultured *in vitro* compared to their native environment (Afshar *et al.*, 2023). To address this potential issue, recent studies investigating endothelial T-type VGCCs have moved away from using cultured ECs, instead using advanced imaging techniques in whole arteries or observing functional differences in T-type channel knockouts.

The first direct demonstration of T-type VGCCs in native ECs came from Braunstein *et al.* (2009), who claimed that $Ca_V3.2$ channels are expressed in ECs of rat mesenteric arteries and arterioles. However, the only evidence presented are longitudinal confocal micrographs of immunolabelled arteries, which were not flushed or pressurised prior to fixing. This makes it difficult to verify that the ECs were accurately characterised and were not mistaken for immune cells which are known to express T-type VGCCs, such as T lymphocytes (Picard *et al.*, 2023). Nevertheless, other studies using immunohistochemistry in intact vessels have identified both $Ca_V3.2$ and $Ca_V3.1$ channels in ECs from rat cerebral arteries (Kuo *et al.*, 2010) and mouse aortas and mesenteric arteries (Svenningsen *et al.*, 2014), offering further confirmation of their expression.

Although there is support for $Ca_V3.1$ and $Ca_V3.2$ channels being expressed in the endothelium, there is little evidence demonstrating their impact on artery function. One study found that secondary vasodilation was severely compromised in pressurised mesenteric arteries from $Ca_V3.1^{-/-}$ mice compared to arteries from wild-types, leading the authors to conclude that endothelial $Ca_V3.1$ channels are important in NO-mediated vasodilation (Svenningsen *et al.*, 2014). However, the same paper reports that $Ca_V3.1^{-/-}$ arteries displayed similar vasodilation to acetylcholine (ACh) as wild-type arteries, a finding which casts doubt on the paper's conclusions as ACh produces vasodilation by stimulating NO synthesis (Ignarro *et al.*, 1987). Using $Ca_V3.1^{-/-}$ mice from the same colony used by Svenningsen *et al.* (2014), Gilbert *et al.* (2017) reported that ACh-mediated dilation of wire myograph-mounted pulmonary arteries

was significantly impaired in the absence of $Ca_V3.1$ channels. Although this supports a role for $Ca_V3.1$ channels in NO-mediated vasodilation, the inconsistencies between the functional responses observed in the two studies may indicate that compensatory mechanisms were at play in some vascular beds, potentially invalidating data obtained from these mice. Another study using pressurised coronary arteries from $Ca_V3.2$ knockout mice also found that ACh-mediated vasodilation was impaired, although the authors speculated that this was a result of a loss of $Ca_V3.2$ channels in VSMCs, not ECs (Chen *et al.*, 2003).

Overall, more research is required to determine whether native ECs express functional VGCCs. If endothelial T-type VGCCs do indeed contribute to NO production and vasodilation, the therapeutic benefits of T-type VGCC blockers may be limited by their reduction of NO availability.

1.4.4 Regulation of T-type voltage-gated calcium channels

T-type VGCCs can be regulated indirectly by NO or directly by its more reactive oxidation products. NO indirectly regulates T-type VGCCs via activation of downstream effectors, namely PKG; activation of PKG suppressed T-type currents in VSMCs isolated from rat cerebral arteries (Harraz *et al.*, 2014b). Studies using rat brain slices have also shown that endogenous NO-generating compounds such as *S*-nitrosoglutathione and *S*-nitrosocysteine can rapidly and reversibly inhibit T-type currents (Joksovic *et al.*, 2007). The mechanism of this regulation is via *S*-nitrosylation of cysteine residues on T-type VGCCs, located in extracellular regions of domains I and II of the α_1 subunit (Lee *et al.*, 2013). In accordance with this, it is also believed that oxidative stress, a consequence of reduced NO bioavailability, increases VSMC T-type channel expression and their contribution to peripheral vascular tone (Howitt *et al.*, 2013). The inhibition of T-type VGCCs by NO may explain the increased electrical activity of rabbit coronary artery VSMCs observed following endothelial denudation

(Garland, 1985). This ‘electrical remodelling’ has been linked to the development of various cardiovascular diseases, including hypertension (Joseph *et al.*, 2013).

1.4.5 T-type voltage-gated calcium channels as a therapeutic target

The evidence discussed above indicates that T-type VGCCs may be a promising target for treating hypertension, particularly in cases associated with endothelial dysfunction and decreased NO production. Chronic loss of NO results in upregulated $Ca_V3.1$ and $Ca_V3.2$ channels in VSMCs and increased vascular tone, indicating that T-type VGCCs expressed in the smooth muscle play a greater role in vascular responses in diseased rather than healthy arteries (Howitt *et al.*, 2013).

One of the first-line treatments for hypertension are L-type VGCC blockers such as nifedipine and amlodipine, although a considerable proportion of patients do not experience blood pressure reduction when taking these drugs, perhaps due to resistant hypertension (Epstein, 2007). Along with the evidence that T-type VGCCs contribute to vascular tone, it is possible that blocking T-type channels instead of, or as well as, L-type channels, may prove effective in treating hypertension. Indeed, clinical studies indicate that T-type VGCCs blockers are more effective at reducing blood pressure than L-type channel blockers. For example, the combined T- and L-type VGCC blocker benidipine was found to lower blood pressure more effectively in hypertensive patients compared to the L-type VGCC blocker amlodipine (Ohishi *et al.*, 2007). However, since no selective T-type channel blockers have approved for therapeutic use, the isolated effects of blocking these channels on blood pressure has not yet been assessed *in vivo.*

The study by Ohishi *et al.* (2007), and others, which found that blocking T-type VGCCs reduces arterial tone, suggests that the vasoconstrictive effects of T-type channels outweigh their vasodilatory effects. Therefore, despite the emerging role of endothelial T-type VGCCs

in NO production, and the purported VSMC $Ca_V3.2$/RyR/BK_{Ca} microdomain, it appears that the predominant effect of T-type blockade *in vivo* is vasodilation. More research into the vasodilatory effects of T-type VGCCs across vascular beds is required, however, to better understand the specific effects of channel blockade in different artery types. Furthermore, the heterogeneous expression and function of the different T-type channel subtypes across ECs and VSMCs means that drugs which preferentially target one subtype over the others may be useful in treating disease. For example, inhibiting VSMC $Ca_V3.3$ channels could reduce direct Ca^{2+} influx and attenuate vasoconstriction, whilst activating EC $Ca_V3.1$ channels could enhance NO production and vasodilation.

Since the market withdrawal of mibefradil, the first and only FDA-approved T-type VGCC blocker, due to its reactions with other drugs, extensive efforts have been made to develop alternative therapies. This is exemplified by the publication of over 40 patents between 2012 and 2018 describing new small molecule T-type channel inhibitors (Nam, 2018). There are currently three promising pan-T-type VGCC blockers which have advanced to clinical trials: apinocaltamide (also known as ACT-709478), ulixacaltamide (also known as Z944), and suvecaltamide (also known as CX 8998). Apinocaltamide was well-tolerated in healthy patients in a phase 1 trial (Richard *et al.*, 2019), and both ulixacaltamide and suvecaltamide showed improvements in pain and essential tremor symptoms, in phase 2 and phase 1b trials, respectively (Papapetropoulos *et al.*, 2021; Lee, 2014). As these T-type VGCC inhibitors progress through clinical trials, it will become increasingly important to understand their effects on the vasculature to avoid unwanted side effects.

1.5 The Endothelium Coordinates Vasodilation

Artery relaxation occurs when intracellular [Ca^{2+}] decreases, either through its re-uptake into the SR or expulsion out of the cell. Hyperpolarisation is a prerequisite for vasodilation, as

VGCCs must remain closed to prevent Ca^{2+} from entering cells. The generation of negative membrane potentials in VSMCs occurs when K^+ channels open, facilitating the outward flow of positive charge. The K^+ channels expressed by VSMCs are numerous, and they can be activated by high voltages (K_v channels), elevated intracellular [Ca^{2+}] (BK_{Ca} channels), elevated extracellular [K^+] (inwardly-rectifying K^+ channels; K_{ir} channels), and elevated ATP levels (K_{ATP} channels) (Nelson *et al.*, 1990). In addition to being gated by various stimuli, K^+ channel opening is independently regulated by the endothelium through its release of diffusible factors such as NO, EDHF, prostacyclin (PGI_2) and epoxyeicosatrienoic acids (EETs), each causing hyperpolarisation of VSMCs by opening K^+ channels (Jackson, 2017).

The first evidence that the endothelium mediates vasodilation came from experiments by Furchgott and Zawadzki (1980), who found that removing the endothelium from rabbit aortic strips abolished ACh-induced vasodilation. At the time of publication, it was understood that ACh caused robust vasodilation when administered *in vivo*, but the same response was not consistently observed in *ex vivo* artery preparations. The authors' explanation for this discrepancy was that the endothelium was unintentionally damaged in previous *ex vivo* experiments, and that activation of endothelial muscarinic receptors by ACh is responsible for vasodilation. This finding led to an explosion of interest into the role of the endothelium and laid the foundations for subsequent important discoveries. These include the findings that ECs produce diffusible vasodilators PGI_2 (Ingerman-Wojenski *et al.*, 1981) and NO (Ignarro *et al.*, 1987), as well as a non-PGI_2, non-NO vasodilator at the time termed EDHF (Chen *et al.*, 1988), but nowadays more accurately described as endothelium-dependent hyperpolarisation (EDH). As the NO and EDH pathways are most relevant to this thesis, they are discussed in more detail below.

1.5.1 Nitric Oxide

1.5.1.1 Mechanism of Action

After Ignarro and colleagues' discovery that the unidentified EDRF released from ECs was NO, efforts focused on elucidating how it caused vasodilation. It was already understood that EDRF was a humoral agent with a short half-life (3-5 seconds), which stimulated VSMC soluble guanylyl cyclase (sGC) to increase levels of cyclic guanylyl monophosphate (cGMP) and induce vasodilation (Förstermann *et al.*, 1986; Holzmann, 1982). The link between cGMP and vasodilation is complex, with evidence indicating that cGMP modulates multiple independent signalling pathways. It was first reported that cGMP affected protein phosphorylation when levels of radioactive phosphorus in myosin MLC were measured in rat aortas. After adding ACh or NO donor sodium nitroprusside to intact tissue, the ^{32}P content of MLC was reduced, providing an explanation as to why increased cGMP levels resulted in vasodilation (Rapoport *et al.*, 1983). The protein kinase intermediary between cGMP and MLC was identified as PKG, and its presence was confirmed in vascular tissue (Hofmann and Sold, 1972; Wolfe *et al.*, 1987). As well as phosphorylating MLC, PKG is thought to phosphorylate other targets, including IK_{Ca} channels, L-type VGCCs, sarcoendoplasmic Ca^{2+}-ATPases, and phospholamban, all of which contribute to reduced intracellular [Ca^{2+}] and vasodilation (Robertson *et al.*, 1993; Tewari and Simard, 1997; Yoshida *et al.*, 1991). In parallel to causing vasodilation via the sCG/cGMP/PKG/MLC pathway, NO hyperpolarises smooth muscle by directly stimulating BK_{Ca} and K_{ATP} channels (Bolotina *et al.*, 1994; Mistry and Garland, 1998; Garland and McPherson, 1992).

1.5.1.2 Synthesis and Storage

NO is synthesised when the enzyme NO synthase (NOS) converts L-arginine and molecular oxygen to NO and L-citrulline. Of the three isoforms of this enzyme, which include neuronal

NOS (nNOS) and inducible NOS (iNOS), endothelial NOS (eNOS) is the main source of NO in the vasculature, the activity of which is regulated by numerous factors (Leo *et al.*, 2021). These include local substrate and cofactor availability, regulatory protein binding partners and post-translational modifications of specific serine, tyrosine and threonine residues.

The enzyme is composed to two identical monomer subunits, each containing an oxygenase domain at the N-terminus and a reductase domain at the C-terminus (Fleming and Busse, 1999). Separated by a linker region, the enzyme's activity depends on the transfer of electrons from the reductase domain of one subunit to the oxygenase domain of the other. This transfer relies on a number of essential cofactors including tetrahydrobiopterin (BH_4), which binds to the oxygenase domain to facilitate subunit dimerization, and calmodulin (CaM), which binds to the linker region to initiate the conformational changes required for subunit interaction.

EC [Ca^{2+}] has long been thought to regulate eNOS activity through its activation of calmodulin, resulting in its initial classification as a Ca^{2+}-dependent enzyme (Luckhoff and Busse, 1990). Regulation of eNOS by calmodulin requires an elevation in EC Ca^{2+}, which primarily occurs through the release of Ca^{2+} from intracellular stores following stimulation of $G_{q/11}$ protein-coupled receptors by endogenous agonists (Busse *et al.*, 1991). Additionally, the endothelium can be activated during vasoconstriction by VSMC-derived signalling molecules which negatively regulate vasoconstriction to prevent vasospasm from occurring. This mechanism, termed myoendothelial feedback, was first observed in isolated, pressurised hamster cheek pouch arterioles. In vessels with myogenic tone, basal EC [Ca^{2+}] increased in response to PE and high [K^+], and vasoconstriction was enhanced by blocking eNOS (Dora *et al.*, 1997). This suggests that the endothelium can be indirectly stimulated by agents which act on VSMCs, and that the signal from these cells increases NO production which opposes vasoconstriction. The precise identity of the VSMC signal involved in myoendothelial feedback is contested, although most agree that it is a combination of both Ca^{2+} and IP_3 (Isakson *et al.*, 2007; Kansui *et al.*, 2008; Garland *et al.*, 2017).

At rest, ECs [Ca^{2+}] sits between 30-100 nM, and increases up to 10-fold during agonist stimulation (Dalal *et al.*, 2020). Evidence indicates that CaM is unable to bind to the eNOS-CaM binding domain at resting intracellular Ca^{2+} concentrations (< 100 nM), whereas it can bind at elevated free [Ca^{2+}] of 225 nM (Piazza *et al.*, 2015). Combined with earlier data from Greif *et al.* (2004), which showed that CaM has ~10% of its maximum activity at 100 nM Ca^{2+}, this suggests there is very little Ca^{2+}-dependent eNOS activation in 'resting' ECs.

In addition to the binding of regulatory cofactors, sustained activation of eNOS requires post-translational modifications of multiple serine, tyrosine and threonine residues. Of these, the most extensively characterised is Ser1177 in the C-terminal reductase domain, which when phosphorylated, enhances eNOS activity by increasing electron flux between the enzyme's subunits. The mediators responsible for eNOS phosphorylation following external stimulation are well characterised, and include protein kinases such as AKT, protein kinase A (PKA), and PKC (Lu and Kassab, 2011). Ser114 and Thr495 are two amino acid residues whose phosphorylation downregulates enzyme activity. Specifically, Thr495, situated in the linker region, acts as the key inhibitory site for eNOS and is constitutively phosphorylated at rest, blocking the binding of CaM. A study using cultured porcine aortic ECs showed that application of bradykinin results in the Ca^{2+}-dependent phosphorylation of Ser1177 residues and dephosphorylation of Thr495 residues, both of which contribute to increased enzymatic activity and NO production (Fleming *et al.*, 2001). Relatively little is understood about the dephosphorylating phosphatase enzymes involved in eNOS regulation, although roles for Ca^{2+}-independent protein phosphatase 1 (PP1) and protein phosphatase 2A (PP2A) have been proposed, whilst Ca^{2+}/CaM-dependent calcineurin has been ruled out (Fleming *et al.*, 2001).

As well as being activated by Ca^{2+}-elevating agonists like bradykinin, eNOS activity can be enhanced independently of a rise in intracellular Ca^{2+}. This was first observed by Presta *et al.*

(1997) who found that purified bovine eNOS still produced NO in the absence of Ca^{2+}. Combined with observations that isolated arteries released NO in response to flow, even in the absence of extracellular Ca^{2+}, this indicated an alternative mechanism of eNOS activation, mediated by flow and independent of EC [Ca^{2+}]. This mechanism involves the activation of kinases such as AKT and PKA, which form mechanosensing complexes with proteins expressed on the luminal surface of ECs, including PECAM-1, VE-cadherin, and integrins. Changes in shear stress e.g., due to increased blood flow to exercising muscles, are detected by these complexes, leading to phosphorylation of key eNOS residues and NO-mediated vasodilation. This mechanism of NO release contributes to flow-induced vasodilation, an important physiological response which ensures the metabolic needs of muscles are met. Sustained increases in NO release induced by shear stress appear to be largely independent of increased EC Ca^{2+}. In experiments using cultured human umbilical vein ECs, flow-mediated NO production was not abrogated by either CaM blocker calmidazolium and Ca^{2+} chelator quin-2 AM, whereas bradykinin-mediated NO production was (Kuchan and Frangos, 1994). Combining this with evidence discussed previously, it appears that eNOS activity can be enhanced by two independent, yet synergistic pathways: 1) via CaM and various kinases activated by elevated intracellular [Ca^{2+}], and 2) via Ca^{2+}-independent kinases activated by shear stress.

There is also evidence of a NOS-independent NO source in arteries, demonstrated by the fact that ACh-induced NO release was not fully inhibited by eNOS inhibitor N(ω)-nitro-L-arginine methyl ester (L-NAME), even at high concentrations (Cohen *et al.*, 1997). Due to its highly labile nature, it is unlikely that ‘free’ NO is stored in cells as it rapidly decomposes into nitrites and nitrates (Lancaster, 1994). Instead, it has been suggested that NO reacts with haemoglobin (Hb) to form stable adducts which release NO under specific conditions where additional vasodilation is required. NO can directly bind to iron in Hb, forming nitrosylhaemoglobin (HbNO), or it can interact with cysteine residues on the β-chain of Hb to form S-nitrosohaemoglobin (SNO-Hb; Jia *et al.*, 1996). The release of NO from HbNO and

SNO-Hb is dependent on the oxygenation state of Hb; when Hb is deoxygenated, NO is released, promoting vasodilation and improved blood flow. Although the extent to which this NOS-independent NO release mechanism contributes to vasodilation is unknown, it may be important in hypoxic conditions where eNOS expression and activity are often diminished (Murata *et al.*, 2002).

1.5.2 Basal and Stimulated Nitric Oxide Release in Disease

While the relationship between impaired NO release and the subsequent development of cardiovascular diseases is widely recognised (reviewed by Lundberg *et al.*, 2015), relatively little is known about how changes in NO signalling within the coronary circulation affect disease progression. Studies have indicated that coronary endothelial dysfunction can predict the development and progression of coronary artery disease, as well as future cardiovascular events, implicating a role for coronary endothelial health in cardiac-specific pathologies (Schachinger *et al.*, 2000; Halcox *et al.*, 2002; Lerman and Zeiher, 2005). However, these studies fail to recognise the importance of basal NO release, and instead only measure coronary vascular resistance in response to agonist stimulation. Understanding the difference between basal and stimulated NO release is crucial, especially in coronary resistance vessels, as it reflects different aspects of vascular health; basal release indicates ongoing endothelial function, whereas stimulated release demonstrates the adaptive capacity of arteries to respond to stimuli. These two NO release pathways may also be regulated by different mechanisms and affected differently in disease states. Furthermore, the distinction is important because basal and stimulated NO release could respond differently to therapeutic interventions, making it important to develop a more comprehensive understanding of both mechanisms in the coronary circulation.

From the limited studies that have distinguished between the two NO release pathways in the coronary circulation, it has emerged that basal NO production in these arteries is variable.

Comparing healthy individuals to those with cardiovascular disease risk factors, Quyyumi *et al*. (1995) measured the diameter of large and small epicardial arteries following intracoronary infusion of eNOS inhibitor N^{ω}-monomethyl L-arginine (L-NMMA). They found that L-NMMA-evoked vasoconstriction was more pronounced in healthy subjects at rest compared to in subjects exhibiting risk factors, suggesting that basal NO has a tonic dilator effect in coronary arteries which is reduced in diseased arteries. However, another paper published around the same time conflicts with this, reporting no difference in basal NO release in coronary resistance arteries between healthy subjects and those with coronary artery disease (Nishikawa and Ogawa, 1997). Evidence presented in these papers for the role of stimulated NO release in coronary arteries is more harmonious. Quyyumi *et al.* (1995) found that peak ACh-induced vasodilation was higher in healthy individuals than those with risk factors, and pre-infusion of L-NMMA inhibited this dilation to a greater extent in healthy patients. This indicates that agonist-stimulated, Ca^{2+}-dependent NO release is impaired in diseased coronary arteries. Nishikawa and Ogawa (1997) expanded on this, finding that Ca^{2+}-independent NO release stimulated by increased blood flow was also impaired in atherosclerotic coronary arteries.

Given the incongruent findings concerning basal NO release presented by these papers, it is clear that a more extensive investigation into NO release in healthy and diseased coronary arteries is warranted. If further research confirms that basal NO release is dysregulated in diseased arteries, it will be important to determine the underlying cause, which may be eNOS uncoupling, increased superoxide production, or something else unknown. Understanding why changes in NO production occur during coronary artery disease progression will help in the development of new treatments, potentially reducing the risk of catastrophic cardiac events occurring. Moreover, additional research may lead to the development of therapies which target either basal or stimulated NO release, allowing treatments to be tailored to patients' needs.

1.5.3 Studying Nitric Oxide Release in Isolated Arteries

The vasoconstrictive effects of eNOS inhibition have been extensively replicated in isolated artery preparations, where researchers can carefully manipulate experimental conditions such as the presence of agonists and the rate of luminal flow. This is particularly useful when studying basal NO release, as stimuli which are known to enhance eNOS activity can be removed to reflect the amount of NO released in completely unstimulated arteries. Indeed, studies using isolated resistance arteries from a range of vascular beds and species have informed our understanding of basal NO release; they indicate that eNOS inhibition causes vasoconstriction even in the absence of agonists and flow (Tschudi *et al.*, 1991; Garcia and Bund, 1998; McNeish *et al.*, 2005). Moreover, the application of NO scavenger oxyhaemoglobin to isometrically mounted rat mesenteric arteries reduced luminal [NO] to below baseline levels, further reinforcing the idea that NO is produced basally (Simonsen *et al.*, 1999). This means that eNOS can be activated without the need for increased EC Ca^{2+} or Ca^{2+}-independent phosphorylation, although the exact mechanism by which it is activated is unknown.

Studies using isolated arteries track changes in arterial diameter using wire or pressure myograph systems, requiring arteries to be manually stretched to replicate the effects of blood pressure *in vivo*. However, recent studies using cultured ECs show that stretch itself can activate eNOS by phosphorylating key residues (Kuebler *et al.*, 2003; Hu *et al.*, 2013), meaning that previous studies measuring so-called basal NO release in isolated arteries may not have eliminated all the factors stimulating NO production. As such, there is a need to develop new methods for investigating NO release in isolated arteries which are not mechanically stretched in a fixed position and do not rely on observing functional changes in artery diameter.

1.5.3.1 Direct and Indirect Measurements of Nitric Oxide

As our understanding of NO's role in the vasculature has improved over the past 30 years, different methods for measuring its production have emerged. Whilst some methods measure NO directly, its short half-life and high reactivity means that most methods instead detect levels of NO-derived species, including nitrite (NO_2^-), nitrate (NO_3^-), and nitroxyl (HNO). The main methods used to detect NO or its oxidation products are: 1) chemiluminescence, where the reaction of NO derivatives with ozone produces a measurable light signal, 2) spectrophotometric assays such as the Griess reaction, which measures the intensity of a highly coloured azo dye produced from the conversion of nitrites, and 3) electrochemical sensors, which measure the electric current that results from oxidation or reduction of NO on an electrode's surface.

Whilst each of these methods are useful in different situations, they are not without limitations. Measuring NO derivatives such as nitrites or nitrates using spectrophotometric assays only provides an estimation of NO levels, as each assay typically detects a single derivative. As NO can give rise to ~10 different chemical species, there is a risk that these may go undetected, resulting in an underestimation of [NO] (Möller *et al.*, 2019). Spectrophotometric techniques such as the Griess assay are usually used to measure the NO content of fluids including cell supernatant and blood plasma and are rarely used to measure NO produced by isolated arteries.

Directly measuring NO using chemiluminescence is considered the gold-standard method for quantification, although analysis of samples requires a time-consuming multi-step protocol. Again, this may lead to the inaccurate quantification of original NO levels due to its short half-life and rapid degradation over time. Chemiluminescence has been used to detect NO production in intact arteries, where the buffer perfusing the artery is collected and analysed. Evidence suggests that this method may not be robust, however, as endothelium denudation

and pharmacological blockade of eNOS do not always significantly reduce [NO] detected (Boric *et al.*, 1999; Figueroa *et al.*, 2001).

Electrochemical sensors are the most widely used method to detect NO production in arteries *in situ,* whether they are in a living system or mounted *ex vivo.* The first report using an electrochemical sensor to detect NO was published in 1990, where microelectrodes (under 50 µm diameter tip) were inserted into freshly-harvested rat cerebral slices (Shibuki, 1990). After this, NO-sensitive microelectrodes were developed for *in situ* use in isolated rabbit aorta and later in human superficial hand veins (Malinski *et al.*, 1993; Vallance *et al.*, 1995). While this technique can detect NO in diverse biological settings, its accuracy is compromised by interference from anions such as nitrite and nitrate, and its limited sensitivity means that small, but potentially physiologically important amounts of NO may go undetected.

It is therefore clear that alternative methods are needed to accurately quantify NO production in intact arteries. More recently, the use of NO-sensitive fluorescent dyes has been explored, with varying degrees of success. In all cases, the binding of NO to the dye is not reversible; therefore, changes in the rate and magnitude of fluorescence are measured, and ideally compared to time courses in the presence of a NOS inhibitor. The first fluorescent NO dyes developed were diaminobenzene-based fluorophores such as diaminofluoresceins (DAFs), which produce a fluorescent signal when bound to NO. Although simple to use and sensitive to low concentrations of NO, they have been criticised due to severe interference by Ca^{2+} which enhances conversion of the dye into its fluorescent product (Broillet *et al.*, 2001). Structurally related to DAFs, diaminorhodamine (DAR) dyes are another class of fluorescent NO dye (see **Figure 1.5.3.1** for structure). Rhodamine-based dyes are considered superior to fluorescein-based dyes as they are more photostable, and their signal is less influenced by artery autofluorescence (e.g., from elastin) due to the longer excitation wavelength. A cell-trappable DAR dye, DAR-4M AM, has been successfully used in cultured bovine aortic ECs, but has not yet been validated in intact artery preparations (Kojima *et al.*, 2001). Once inside

cells, DAR-4M AM is deacetylated by intracellular esterases to form DAR-4M, trapping it intracellularly. It is then converted to fluorescent DAR-4M triazole (DAR-4M T) by binding with NO.

Additionally, membrane-permeable NO dyes, such as copper-based fluorophores, are also available and have shown promise in their ability to detect NO (see **Figure 1.5.3.1**). Similar to DAF/DAR dyes, they detect NO directly and are non-toxic; however, previous protocols using copper-based fluorophores such as Cu_2FL2E have required the use of high concentrations of both Cu^{2+} (McQuade *et al.*, 2010) and DMSO (McQuade *et al.*, 2010; Ghosh *et al.*, 2013), which are both known to cause arterial dysfunction (Yi *et al.*, 2017). Optimisation of these dyes for use in *ex vivo* arteries would provide valuable insights into the spatial and temporal release of NO from the endothelium, both basally and following eNOS stimulation. Using a NO dye in isolated arteries where the stimulating influences of agonists, flow and stretch are removed would allow for the detection of basal NO release, addressing the key question of whether NO is produced at rest.

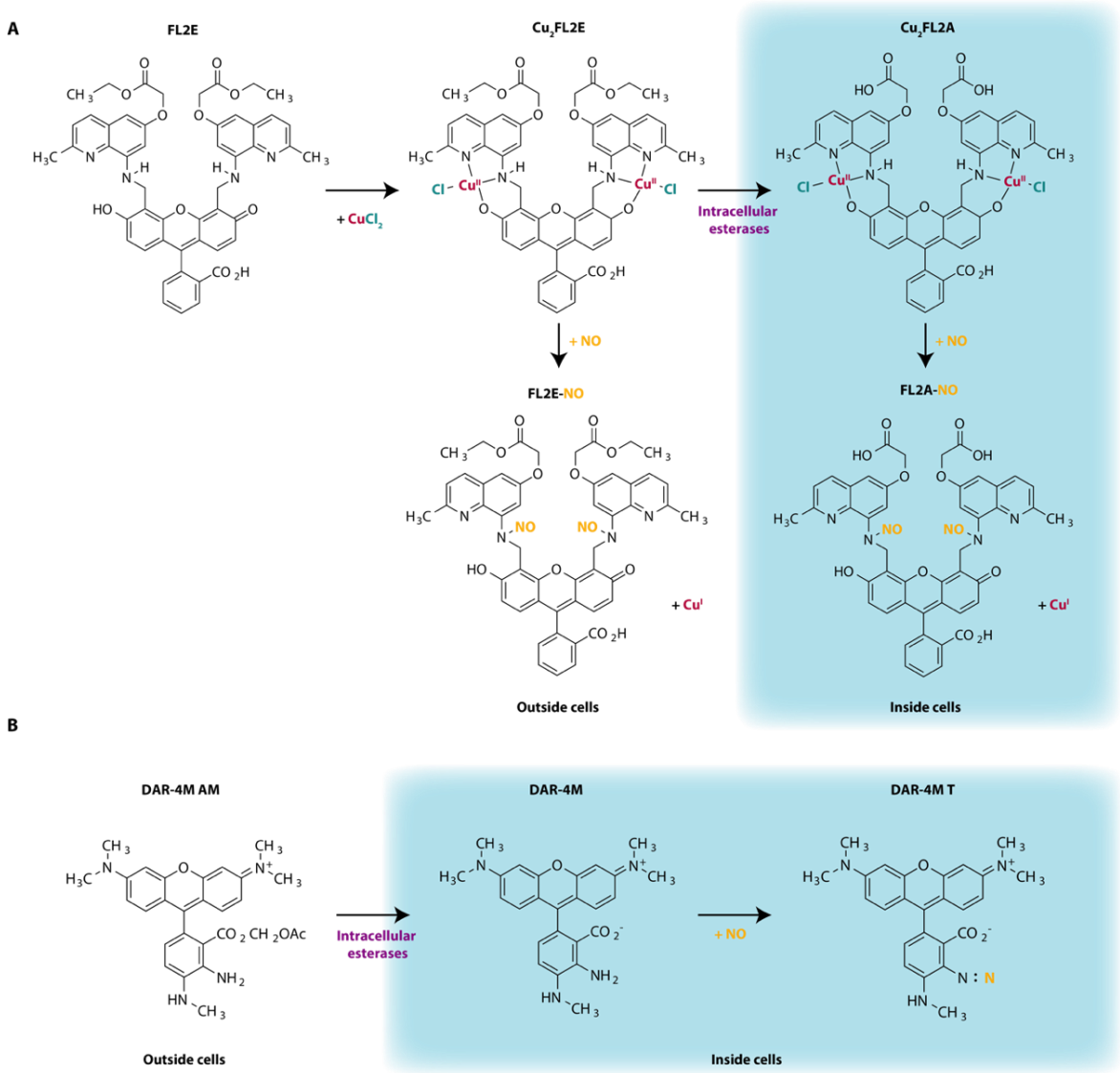

Figure 1.5.3.1. Schematic diagram of Cu_2FL2E and DAR-4M AM dye entry into cells and binding of NO to produce fluorescence. (**A**) FL2E combines with Cu^{2+} to form Cu_2FL2E (note the two Cu^{2+}-binding sites), which can be loaded into cells. The ester moiety confers the cell-trappability of the probe, as cytosolic esterases cleave the ester bonds to yield a carboxylate which is negatively charged at physiological pH (not shown in diagram), and thus unable to diffuse out of cells. Reaction of the probe with NO displaces Cu^{2+} to produce fluorescence. Intracellular and extracellular dye (FL2A) can both bind NO, emphasising the importance of washing away excess dye after artery loading. (**B**) Cell-permeable DAR-4M AM can be loaded into cells, where removal of the acetoxymethyl group (AM group) by esterases produces DAR-4M which is membrane impermeable. The reaction of NO with DAR-4M results in a triazolo-rhodamine analogue (DAR-4M T) which exhibits fluorescence.

1.5.4 Endothelium-Derived Hyperpolarisation

1.5.4.1 Mechanism of Action

Along with NO, PGI_2 and EETs, another endothelium-dependent vasodilation mechanism exists whereby hyperpolarisation 'spreads' from ECs to underlying smooth muscle cells, opposing the action of VGCCs to maintain low levels of intracellular Ca^{2+}. The contribution of the two main vasodilatory pathways, NO and EDH, varies according to blood vessel size, with the influence of NO diminishing and EDH becoming increasingly important as artery diameter decreases (Shimokawa *et al.*, 1996). This relationship reflects both the increased expression of channels involved in generating hyperpolarisation as well as the increased reliance on VGCCs to increase intracellular [Ca^{2+}] in small resistance arteries compared to larger conduit arteries.

Initially considered to be mediated by a diffusible factor, it is now accepted that EDH is caused by the action of extracellular K^+ originating from ECs, as well as the direct conduction of hyperpolarisation from ECs to VSMCs via MEGJs. The precise mechanism underpinning EDH was elucidated over many years, starting with the observation that smooth muscle hyperpolarisation evoked by muscarinic agonists required an intact endothelium (Bolton *et al.*, 1984). Following this, it became clear that endothelial Ca^{2+}-sensitive K^+ channels, namely SK_{Ca} and IK_{Ca} channels, are responsible for generating EDH (Adeagbo and Triggle, 1993; Waldron and Garland, 1994), and their activation by elevated EC [Ca^{2+}] results in the accumulation of K^+ in spatially restricted 'clouds' in the arterial wall. The mechanism by which elevated extracellular [K^+] evoked VSMC hyperpolarisation and relaxation was later determined in isolated rat resistance arteries by selectively blocking various smooth muscle targets with pharmacological inhibitors. Edwards *et al.* (1998) found that smooth muscle hyperpolarisation and vasodilation to either exogenous K^+ or EDH (activated by stimulating the endothelium with ACh) could be abolished with a combination of Ba^{2+} and ouabain, which block K_{ir} channels

and Na^+/K^+-ATPases. Taken together, these experiments revealed that K^+ is a component of EDH which lowers VSMC membrane potential by increasing K_{ir} conductance and stimulating electrogenic Na^+/K^+-ATPases.

The contribution of SK_{Ca} and IK_{Ca} channels in generating outward current in ECs changes depending on the artery type being studied, perhaps due to differences in their expression or sensitivity to Ca^{2+}. In wire myograph-mounted rat mesenteric arteries, the membrane potential of VSMCs was measured at rest and following PE-induced vasoconstriction in the absence and presence of apamin (SK_{Ca} channel blocker) or 1-[(2-chlorophenyl) diphenylmethyl]-1H-pyrazole (TRAM-34; IK_{Ca} channel blocker) (Crane *et al.*, 2003a). In non-contracted arteries, smooth muscle hyperpolarisation to ACh was abolished by apamin, but unaffected by TRAM-34, indicating that SK_{Ca} channels are solely responsible for generating 'true' EDH (i.e., EDH that is not a result of myoendothelial coupling). A role for IK_{Ca} channels in EDH was demonstrated only after adding ACh to PE-constricted arteries, where their activation was found to cause vasodilation by repolarising VSMCs back to resting levels. This difference in SK_{Ca} and IK_{Ca} channel activation may reflect differences in their Ca^{2+} sensitivity; SK_{Ca} channels appear to be activated by basal levels of EC Ca^{2+}, whereas IK_{Ca} channel activation requires the increased $[Ca^{2+}]$ associated with vasoconstriction. Alternatively, this apparent difference in the channels' Ca^{2+} sensitivity may reflect their specific subcellular location. Immunohistochemical studies indicate that IK_{Ca} channels are only expressed in MEPs of rat mesenteric arteries, whereas SK_{Ca} channels are distributed across the whole EC membrane but are particularly enriched at the points where ECs contact each other (Sandow *et al.*, 2006). As such, it may be that SK_{Ca} channels are exposed to higher concentrations of Ca^{2+} due to their localisation near IP_3 receptors, which facilitates their activation more readily than IK_{Ca} channels. Whether endothelial IK_{Ca} and SK_{Ca} channels have different Ca^{2+} sensitivities or not, their distinct subcellular expression profiles allow their functional effects to be separated, potentially providing novel therapeutic targets for modulating vascular tone.

Following the suggestion that K^+ was responsible for EDH, various research groups attempted to replicate vasodilation to K^+ in arteries from different vascular beds and species (see Garland *et al.*, 2011 for review) . Amongst others, Lacy *et al.* (2000) failed to observe hyperpolarisation and vasodilation to K^+ in rat mesenteric arteries, despite successfully inducing EDH with ACh. This can be explained by the experimental design used, which failed to consider the role of physiological antagonism between phenylephrine (PE) and K^+. Preconstriction of these arteries to high concentrations of PE (10 μM) blocked relaxation to K^+ as stimulation of α_1-adrenoreceptors increases VSMC $[Ca^{2+}]$ which activates BK_{Ca} channels, resulting in efflux of K^+ and its accumulation in the extracellular space (Dora *et al.*, 2002). This saturates Na^+/K^+-ATPases so that additional, exogenous K^+ does not have any effect on membrane potential. The masking effect of BK_{Ca} channel activation of K^+-induced hyperpolarisation was directly demonstrated by Dora *et al.* (2002) who used iberiotoxin to block BK_{Ca} channels and showed that exogenous K^+ was able to evoke hyperpolarisation and vasodilation of PE-contracted arteries.

The presence of gap junctions in the artery wall has long been recognised (Rhodin, 1967), and a their ability to conduct both depolarisation and hyperpolarisation along the vessel wall has been clearly demonstrated in resistance arterioles of the microcirculation (Segal and Duling, 1989). Gap junctions were shown to be involved in EDH responses by Yamamoto *et al.* (1999) when they measured whole-cell currents in ECs and VSMCs of guinea pig arterioles. The biphasic hyperpolarisation profile of ECs was almost identical to that of adjacent VSMCs following ACh application, and blockade of gap junctions by 18β-glycyrrhetinic acid prevented the hyperpolarisation of VSMCs but not ECs. This revealed that in small resistance vessels, MEGJs are essential in facilitating the rapid and direct transmission of hyperpolarising current which contributes to EHD along with extracellular K^+. The importance of MEGJs in EDH, especially in small arteries, was further established by a morphological study where anatomical evidence for the existence of MEGJs was obtained using reconstructed serial-section micrographs of mesenteric arteries of different sizes. These images showed that

MEGJ expression was inversely proportional to vessel diameter, with more MEGJs present in distal compared to proximal regions (Sandow and Hill, 2000). This is consistent with the important functional contribution of EDH to vasodilation in small arteries (Si *et al.*, 2006), and suggests that the direct hyperpolarising route may predominate over the action of K^+ clouds.

1.5.5 Conducted Vasodilation

In addition to hyperpolarisation from the endothelium spreading radially to VSMCs, it also spreads axially to neighbouring ECs in a process called conducted vasodilation. This allows vasodilation of distal arteries to spread upstream, affecting a more widespread drop in vascular resistance which is necessary to increase blood flow and to coordinate blood flow distribution within tissues. This coordination is particularly important in maintaining adequate tissue perfusion, for example, during exercise, where local metabolic changes in active tissues trigger a coordinated vascular response to increase blood flow in a process known as functional hyperaemia. Originally attributed to agonist-induced nerve activation (Krogh, 1920), it later became clear that conducted vasodilation was mediated by the transmission of a vasodilatory signal along the arterial wall via intercellular low-resistance pathways subsequently identified as homocellular EC-EC gap junctions.

After ruling out the input of NO, nerves, and blood flow (Hilton, 1959; Segal and Duling, 1986; Dora *et al.*, 1997), a key question was whether conduction through the artery wall occurred though the endothelium or smooth muscle layer. Emerson and Segal (2000) mounted hamster feed arteries in a pressure myograph and selectively damaged either a section of endothelium or smooth muscle. They found that hyperpolarisation of one end of the artery evoked by focal application of ACh did not spread beyond the area of damaged endothelium but did spread across the area of damaged smooth muscle. It was therefore concluded that conducted vasodilation spreads via the endothelium, an idea reinforced by 1) the high density of gap junctions between ECs with a low resistance to ion flow (Lidington *et al.*, 2002; Sandow *et al.*,

2006), and 2) the axial arrangement of ECs in the artery wall, which allows for efficient and direct hyperpolarisation of VSMCs via MEGJs.

1.5.6 Impaired Conducted Vasodilation in Disease

Impaired NO bioavailability and EDH are ubiquitous features of cardiovascular disease which not only affect local vasodilation responses at the point of endothelial damage, but also conducted vasodilation of distal sites with healthy endothelium. Impaired homo- and heterocellular coupling between cells in the artery wall disrupts the spread of hyperpolarisation and associated vasodilatory responses. This has been observed in hypertension, where changes to the structural and contractile properties of arteries are well documented. In exteriorised cremaster arterioles from spontaneously hypertensive hamsters, conducted vasodilatory responses evoked by ACh decayed faster than in vessels from normotensive controls (Kurjiaka, 2004). The increased electrical resistance of the endothelium observed in this study aligns with reports of reduced Cx expression, particularly Cx43 and Cx37, in arteries from animal models of hypertension (Haefliger *et al.*, 1999; Yeh *et al.*, 2006). These Cxs are enriched at the boundaries of neighbouring ECs, making it likely that their reduced expression is responsible for the impaired spread of hyperpolarisation across the endothelium (de Wit and Griffith, 2010). Similar patterns of reduced Cx expression and impaired conduced vasodilation responses have also been linked to diabetes (Sato *et al.*, 2002; Lemmey *et al.*, 2018), emphasising the importance of identifying therapeutic strategies to preserve or restore conducted vasodilation responses.

Indeed, peptide drug rotigaptide, which potentiates Cx43 conductance, has been effective in improving intercellular communication between cardiac cells, both *in vitro* and *in vivo* (Clarke *et al.*, 2006; Chowdhury *et al.*, 2021). Surprisingly, only one study has investigated the effects of rotigaptide on vascular function. In a phase I clinical trial, rotigaptide treatment improved endothelium-dependent vasodilation of forearm arteries following blood flow restriction,

perhaps illustrating its ability to preserve or enhance conducted vasodilation responses (Pedersen *et al.*, 2016). Despite this, there are currently no approved gap junction modulators for the treatment of cardiovascular diseases, highlighting an area requiring further research. Another avenue for improving conducted vasodilation could be to activate ion channels involved in amplifying EC hyperpolarisation. As the mechanisms underlying this amplification are not yet fully understood, further research is required to identify possible drug targets to inform the development of novel therapeutics.

1.6 Propagation of Conducted Vasodilation

As conducted vasodilation is observed over distances greater than can be explained by passive decay of hyperpolarising current (1-2 mm), it follows that there must be a positive-feedback mechanism which sustains its spread. Indeed, it appears that amplification of intracellular hyperpolarising current occurs in conducted vasodilation, as hyperpolarisation in response to ACh spreads over longer distances than hyperpolarisation stimulated by current injection (Emerson *et al.*, 2002). The specific amplification mechanism triggered by ACh has not been identified, although various candidates have emerged which may be responsible, including 1) K_{ir} channels, 2) Na^+/K^+-ATPases, and 3) hyperpolarisation-activated cyclic nucleotide-gated (HCN) channels.

Although there is evidence for the expression of K_{ir} channels in resistance artery ECs (Crane *et al.*, 2003b), their role in amplifying hyperpolarisation in conducted vasodilation is unclear. Due to the high density of SK_{Ca} channels expressed near EC-EC contact points, it follows that their opening will increase extracellular $[K^+]$ sufficiently to activate proximate K_{ir} channels of neighbouring ECs, triggering outward currents and hyperpolarisation. The unique biophysical characteristics of K_{ir} channels further supports a role for them in the positive feedback generation of hyperpolarisation, as their activity increases with cell hyperpolarisation (known

as negative slope conductance). Selectively blocking K_{ir} channels with Ba^{2+} (30 μM) impairs remote vasodilatory responses to ACh in pressurised porcine coronary arteries, rat mesenteric arteries and hamster retractor muscle arteries, although the exact location of the channels in the artery wall is unclear (Rivers *et al.*, 2001; Goto *et al.*, 2004; Jantzi *et al.*, 2006). Of these papers, only Goto *et al.* speculate that the K_{ir} responsible for conducted vasodilation are expressed by ECs, although they fail to present convincing evidence which rules out expression of these channels by VSMCs. Another paper, again using rat mesenteric arteries, found that the same concentration of Ba^{2+} did not alter conducted vasodilation in response to ACh, casting doubt around the obligatory role of K_{ir} channels in this phenomenon (Takano *et al.*, 2004).

Much like how the activation of Na^+/K^+-ATPases by K^+ induces hyperpolarisation in VSMCs, it is plausible that these pumps play a similar role in ECs which may sustain conducted vasodilation over long distances. Inhibiting Na^+/K^+-ATPases by removing extracellular K^+ depolarised rat aortic ECs from *en face*-pinned arteries by 11 mV from a resting potential of -43 mV, and the reintroduction of K^+ produced abrupt endothelial hyperpolarisation which was blocked by the specific Na^+/K^+-ATPase inhibitor ouabain (500 μM; Bondarenko and Sagach, 2006). This indicates that Na^+/K^+-ATPases are important in regulating membrane potential in resting ECs, and their activity alone can result in hyperpolarisation. The same study also found that sustained endothelial hyperpolarisation to ACh was attenuated by ouabain, implicating a role for EC Na^+/K^+-ATPases in sustaining, and possibly amplifying conducted vasodilation. Despite these results, evidence for the role of endothelial Na^+/K^+ ATPases in conducted vasodilation in pressurised resistance arteries is lacking, highlighting an unmet area of research.

1.6.1 A possible role for HCN Channels in Conducted Vasodilation

Due to the inconclusive evidence for the roles of K_{ir} channels and Na^+/K^+-ATPases in amplifying hyperpolarisation along the endothelium, HCN channels have been suggested to play a role, in part due to their unusual voltage dependence characteristics. Reflected in their name, HCN channels are activated by both hyperpolarisation (< -60 mV; DiFrancesco *et al.*, 1986) and cyclic nucleotides, resulting in the influx of cations such as Na^+, K^+ and Ca^{2+} (Yu *et al.*, 2004). Widely expressed in the heart and central nervous system (see **Table 1.5.7.1**), these channels are responsible for triggering action potentials which generate the 'funny current' (I_f) in the sinoatrial node (SAN) of the heart (Brown *et al.*, 1979) and the 'hyperpolarising current' (I_h) in neurones (Halliwell and Adams, 1982).

Citation	Tissue	mRNA/ protein	Relative expression
Calejo *et al.* (2014)	Rat whole heart	mRNA	Hcn2>Hcn4>Hcn1>>>Hcn3
Baruscotti *et al.* (2005)	Rabbit SAN	mRNA	Hcn4>Hcn1>Hcn2 (no Hcn3)
	Rabbit heart ventricle	mRNA	Hcn2 only
Huang *et al.* (2016)	Rat SAN	Protein	HCN2 and HCN4 only
Moosmang *et al.* (1999)	Rat neocortex	Protein	HCN2>HCN1>HCN3>HCN4
	Rat hippocampus	Protein	HCN1>HCN2>HCN >HCN4
	Rat cerebellum	Protein	HCN1>HCN3>HCN2=HCN4
	Mouse hippocampus	mRNA	Hcn1=Hcn2>Hcn4>Hcn3
Calejo *et al.* (2014)	Rat liver	mRNA	Hcn2>>Hcn3>Hcn1≥Hcn4
Bolivar *et al.* (2008)	Rat kidney	mRNA	Hcn1>Hcn4>Hcn2>Hcn3
Greenwood and Prestwich (2002)	Rat portal vein smooth muscle cells	mRNA	Hcn4>Hcn2>Hcn3>>>Hcn1
Xiao *et al.* (2004)	Mouse colon	mRNA	Hcn2>Hcn1>Hcn4>>Hcn3

Table 1.5.7.1. Summary of relative levels of expression of hyperpolarization-activated cyclic nucleotide-gated channel genes (italicised) and proteins in different tissues.

The HCN family consists of 4 tetrameric channels, HCN1-4, each with six transmembrane segments (S1-6; see Figure 1.5.7.1). The S4 segment contains the channel's voltage sensor, and the intracellular C-terminus carries the cyclic nucleotide binding domain (CNBD) which is connected to the S6 helix via a C-linker protein. The 4 HCN isoforms share a sequence homology of ~60%, with each member of the family displaying distinct biophysical properties primarily relating to level of hyperpolarisation required for channel activation; HCN1 channels open at more depolarised potentials compared to the others, whereas HCN4 channels open at more hyperpolarised potentials. Similarly, the kinetics of activation vary widely, with HCN1 channels showing the fastest opening kinetics, followed by HCN2 and HCN3 channels, and with HCN4 channels activating (and inactivating) the most slowly (Santoro and Shah, 2020). These features allow a significant degree of specialisation for HCN channel activity, which may be significant for the function of blood vessels. The intracellular binding of cyclic nucleotides, such as cyclic adenosine monophosphate (cAMP) or cGMP, modulates channel activation by shifting the voltage dependence to more depolarised voltages, increasing the maximum current amplitude, accelerating the activation kinetics and slowing the deactivation kinetics (Zong et al., 2012). HCN channel activation can still occur in the absence of cyclic nucleotide binding, which may allow these channels to open in ECs without elevated cyclic nucleotide levels, such as in those not being stimulated by G_s-coupled receptor agonists.

Due to their inward conduction of cations, the role of HCN channels in vasodilation appears paradoxical. However, if expressed by ECs, the influx of cations, including Ca^{2+}, through these channels may lead to the generation of NO and/or the activation of SK_{Ca} and IK_{Ca} channels, thereby producing hyperpolarisation and vasodilation. Furthermore, endothelial expression of HCN channels, particularly in close proximity to SK_{Ca} channels, could provide a means to amplify the spread of hyperpolarisation to remote ECs (see **Figure 1.5.7.2**). Interestingly, increases in EC Ca^{2+} following hyperpolarisation have previously been reported in cultured and freshly dissociated cells, although the ion channel responsible was not identified (Luckhoff and Busse, 1990; Langheinrich *et al.*, 1998). Since hyperpolarisation would increase the

electrochemical gradient for Ca^{2+} entry into ECs, the Ca^{2+} rise has historically been attributed to Ca^{2+} influx via an undefined Ca^{2+} 'leak' channel (Johns *et al.*, 1987). More recently, it has been proposed that a specific gated pathway might underlie Ca^{2+} influx in hyperpolarised ECs, namely, HCN channels (Dora and Garland, 2013).

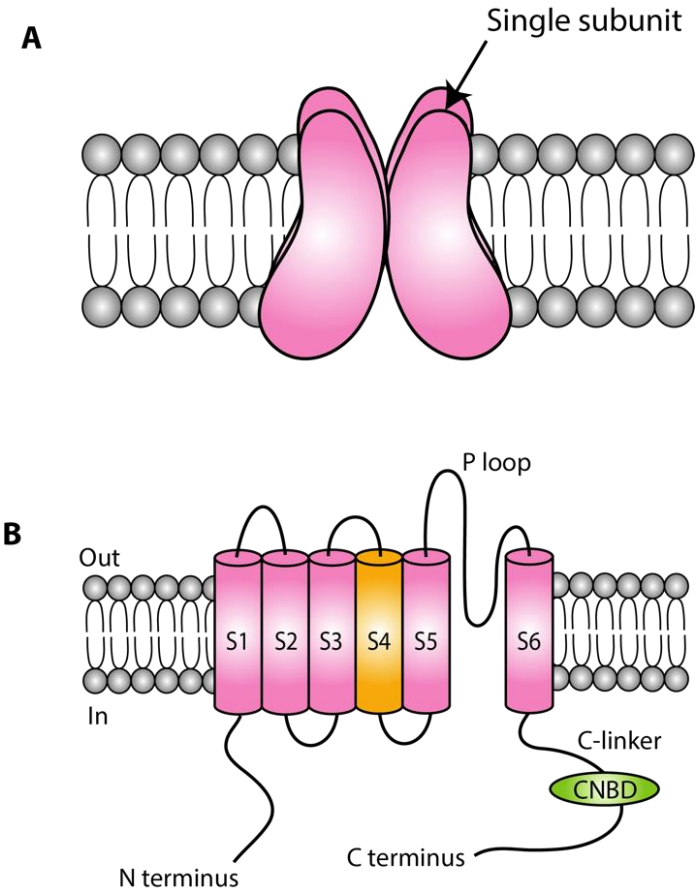

Figure 1.5.7.1. Membrane topology of hyperpolarisation-activated cyclic nucleotide-gated (HCN) channels. (**A**) These channels are formed from 4 separate subunits (HCN 1-4), each of which consist of 6 transmembrane segments (S1-6), shown in **B**. (**B**) Like in voltage-gated calcium channels, the arginine-rich S4 segment (coloured orange) forms the voltage-sensor, whereas the re-entrant P-loop forms the pore of the channel and provides cation sensitivity. The C-terminus of each subunit contains a cyclic nucleotide-binding domain (CNBD) connected to S6 via a C-linker. Together, the CNBD and C-linker regulate channel gating by cyclic nucleotides such as cyclic adenosine monophosphate (cAMP). Figure adapted from Postea and Biel (2011).

To date, there are no published studies investigating the expression or function of HCN channels in the native vasculature. HCN2 and HCN3 channels have recently been identified

in smooth muscle cells of human lymphatic vessels using RT-PCR analysis, although the relevance of this to arterial expression is likely limited (Majgaard *et al.*, 2022). Another study using human umbilical vein ECs (HUVECs) found that HCN1 and HNC2 channels were expressed at the mRNA and protein level, although they didn't investigate HCN3 or HCN4 expression (Civil Urkmez *et al.*, 2024). Whether this mirrors the HCN channel expression profile of native ECs in resistance arteries is unknown, highlighting an area for further research.

The non-selective HCN channel blocker, ivabradine, has been shown to improve endothelium-dependent vasodilation in both mice and humans (Drouin *et al.*, 2008; Hohneck *et al.*, 2019). This effect is thought to be secondary to its negative chronotropic action via inhibition of the I_f in the SAN, rather than through a direct effect on the vasculature. In support of this, a different HCN channel blocker, S 16256, did not exhibit direct effects on coronary artery diameter or coronary blood flow *in vivo* when measured with an ultrasonic transit-time micrometer and Doppler flow wire (Simon *et al.*, 1995). Despite this, preliminary data from pressurised cremaster arterioles suggests that ivabradine prevents Ca^{2+} influx evoked by hyperpolarisation in ECs (unpublished results from Dora/Garland group), although its effects on conducted vasodilation have yet to be investigated. If endothelial HCN channels are indeed important in propagating conducted vasodilation, HCN channel blockers such as ivabradine may disrupt normal blood flow regulation and distribution. This could have broad implications for cardiovascular health such as exercise intolerance, organ dysfunction, and vascular remodelling, limiting the effectiveness of such drugs.

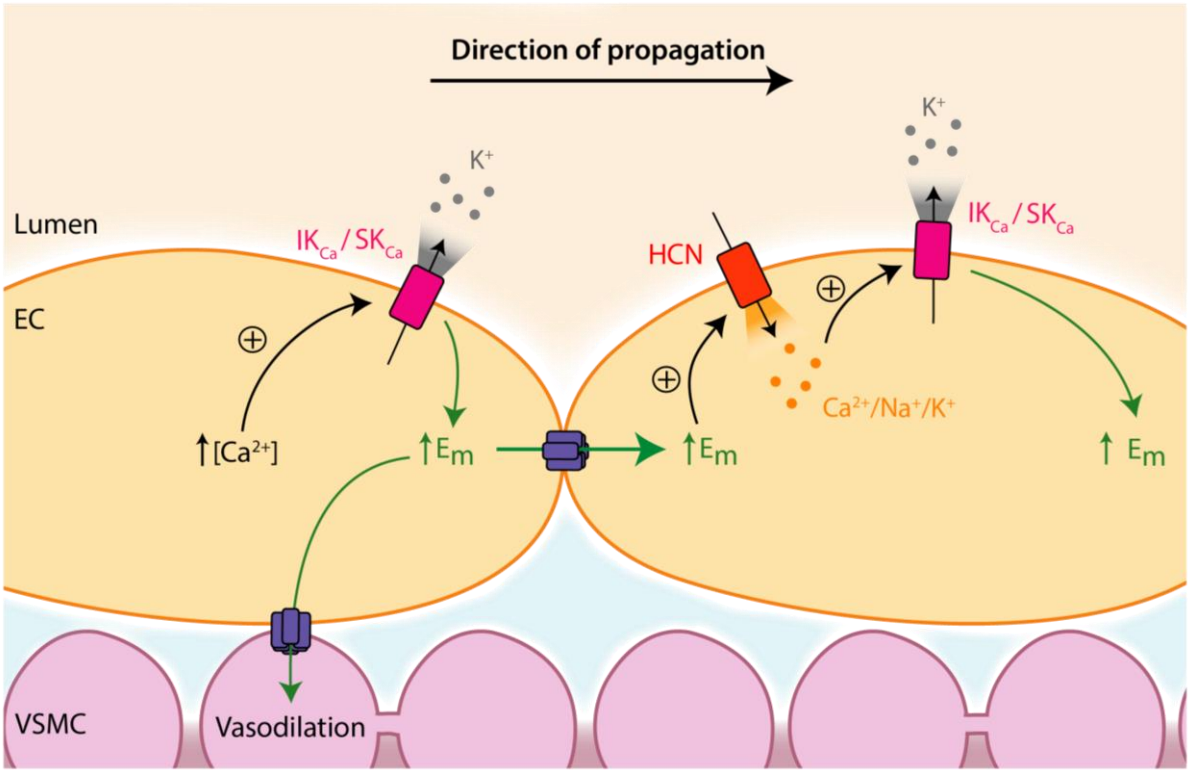

Figure 1.5.7.2. Proposed role of hyperpolarisation-activated cyclic nucleotide-gated (HCN) channels in propagating conducted vasodilation in resistance arteries. An increase in endothelial cell (EC) Ca^{2+} (eg. triggered by agonists such as acetylcholine binding to muscarinic receptors on ECs) activates IK_{Ca} and SK_{Ca} channels, resulting in K^+ efflux and membrane hyperpolarisation (↑Em). Hyperpolarisation spreads to neighbouring ECs via gap junctions, where it activates HCN channels leading to Ca^{2+} influx. The increased intracellular [Ca^{2+}] then activates IK_{Ca} and SK_{Ca} channels, generating more hyperpolarisation upstream. When hyperpolarisation passes to VSMCs, it affects vasodilation by reducing the open probability of voltage-gated calcium channels expressed by VSMCs, preventing a rise in [Ca^{2+}].

1.7 Thesis aims and objectives

Despite growing evidence demonstrating that NO signalling is disrupted in many cardiovascular diseases, our understanding of the conditions under which NO is synthesised is limited. Optimising a protocol for detecting NO production *in situ* in *ex vivo* arteries is therefore a priority as it will help elucidate mechanisms of basal and stimulated NO release. Secondly, advancing our understanding of how T-type VGCCs contribute to vascular tone is necessary as recent reports have found that activation of these channels can have vasodilatory effects in mesenteric and cerebral resistance vessels, challenging the long-held view that Ca^{2+} influx through these channels mediates vasoconstriction only. The possible vasodilatory influence of T-type VGCCs should be further probed as the use of T-type VGCCs to treat neurological disorders may result in unwanted cardiovascular side effects. Finally, elucidating the expression profile of HCN channels in the endothelium is important as preliminary studies indicate they may underly Ca^{2+} entry into hyperpolarised ECs and contribute to conducted vasodilation responses. If HCN channels are indeed important in propagating hyperpolarisation between ECs, inhibitors of these channels might produce unintended consequences, while activators (targeting the vasculature specifically) could offer therapeutic benefits for certain cardiovascular diseases.

The objectives of the following chapters are:

i. To develop a protocol for tracking NO production in *ex vivo* arteries using a fluorescent indicator.
ii. To understand the role of T-type VGCCs in regulating the tone of resistance coronary arteries.
iii. To characterise the expression of HCN channels in arteries to determine whether they may have a role in conducted vasodilation.

2. Materials and Methods

2.1 Animals and tissue preparation

All animal procedures were conducted in accordance with the University of Oxford local ethical guidelines, the ARRIVE guidelines, and the UK Home Office Animal (Scientific Procedures) Act, 1986.

Wild-type male Wistar rats (6-8 weeks, 200-300 g; Charles River, UK or Germany) were used in the present investigations. Animals were housed in individually ventilated cages under a 12:12 h light:dark cycle at 20-22°C. Standard chow and water were available *ad libitum*. Rats were killed in accordance with UK legislation as specified by Schedule 1 of the Animals (Scientific Procedures) Act by increasing concentration of CO_2 and confirmed with cervical dislocation. The heart, mesentery, and cremaster muscle were excised and placed in ice-cold Krebs-buffered solution (see Section 2.9).

2.1.1 Isolation of mesenteric arteries

The mesenteric arcade was pinned out in a Sylgard-coated dissection dish containing ice-cold Krebs-buffered solution (**Figure 2.1.1**). Third-order mesenteric arteries (diameter between 150 and 250 μm) were isolated from adhering connective tissue, perivascular fat and the parallel mesenteric vein. Mesenteric arteries were used in Sections 3, 4, and 5.

2.1.2 Isolation of coronary septal arteries

The excised heart was pinned down in a Sylgard-coated dissection dish containing ice-cold Krebs-buffered solution (**Figure 2.1.2**). The wall of the left atrium and right ventricle was partially removed to allow the interventricular septal coronary artery to be isolated from the adhering connective tissue and cardiomyocytes. Coronary arteries were used in Sections 4 and 5.

2.1.3 Isolation of cremaster arteries

The cremaster muscle was pinned down in a Sylgard-coated dissection dish containing ice-cold Krebs-buffered solution. The muscle and connective tissue surrounding the cremaster artery were removed. Cremaster arteries were used in Section 5.

2.1.4 Isolation of EC tubes from mesenteric arteries

The endothelial layer of arteries can be isolated as an intact tube of cells, providing a useful approach to studying EC function. Separating native ECs from the surrounding smooth muscle layer allows them to be studied without the influence of myoendothelial feedback, providing insights into their intrinsic intra- and intercellular signalling mechanisms.

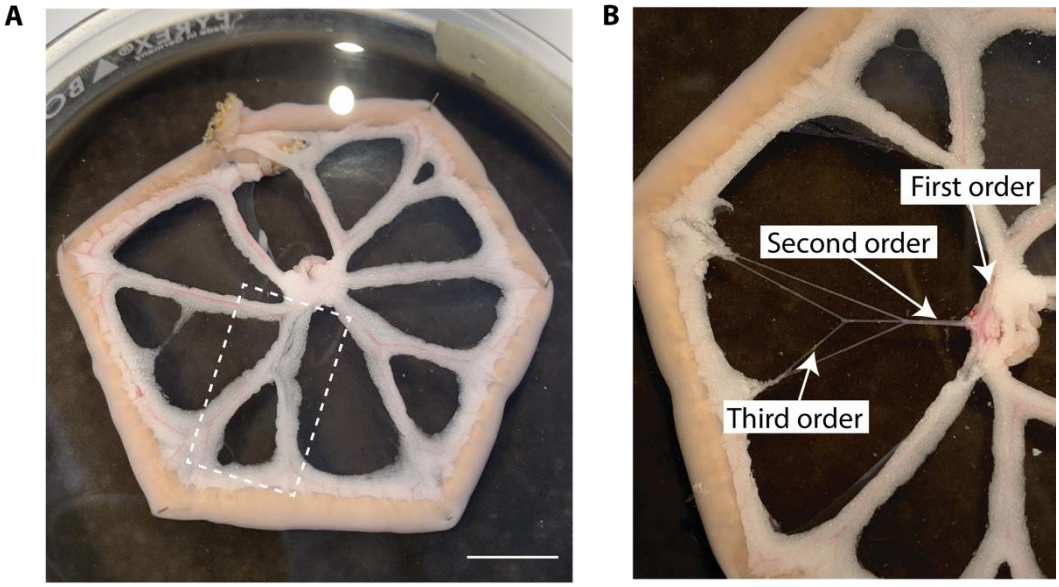

Figure 2.1.1. Rat mesenteric artery dissection. (**A**) Pinned mesenteric arcade, where the dashed box represents the region of magnification in (**B**). **B** shows first, second, and third order arteries which have been cleared of adherent tissue, alongside a parallel mesenteric vein. Third order resistance arteries were used in the present study. Scale bar = 1 cm.

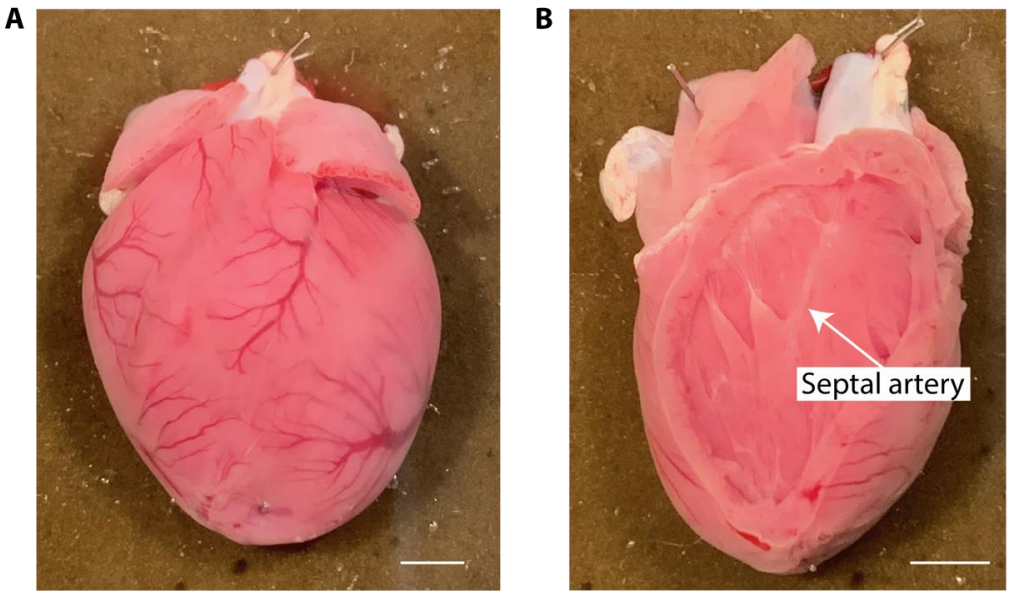

Figure 2.1.2. Rat heart dissection. Pinned heart before (**A**) and after (**B**) removal of part of the ventricular wall, revealing the intraventricular septum. The septal artery is visible running from the aorta towards the apex. Scale bars = 2 mm.

The mesenteric arcade was pinned out in a Sylgard-coated dissection dish containing ice-cold dissection buffer (see Section 2.9). Third-order mesenteric arteries were dissected free of surrounding tissue, cannulated at one end by a glass micropipette (~150 um outer diameter), and flushed with dissection buffer to remove residual blood. Arteries were then cut into 2 or 3 smaller segments ~ 1 mm in length and transferred into a 1.5 mL Eppendorf tube on ice containing 1 mL of dissection buffer.

The artery segments were then left to warm to room temperature, and the solution was aspirated and gently replaced with dissociation buffer to remove residual dissection buffer. This solution was aspirated and replaced with preheated dissociation buffer containing the following enzymes: papain (0.62 mg mL^{-1}; P4762, Sigma, USA), dithioerythritol (1.0 mg mL^{-1}; D8255, Sigma, USA), and collagenase (1.5 mg mL^{-1}; C8051, Sigma, USA). Artery segments were incubated for 25 minutes at 37°C, then the buffer was replaced with enzyme-free dissociation buffer to prevent over digestion.

Artery segments were transferred to a 35-mm × 10-mm culture dish (430165, Corning, SUA) containing enzyme-free dissociation buffer for trituration. Endothelial cell tubes were dissociated from surrounding smooth muscle cells by gentle trituration using a glass micropipette with an inner diameter of ~90 to 150 μm. An injector (Nanoliter 2010, ~300 to 500 nL minute^{-1}) coupled with a Micro4 controller (both World Precision Instruments, USA) was mounted on an upright BX51WI microscope (Olympus, Japan) to allow for real-time visualisation of the trituration procedure.

Freshly isolated endothelial cell tubes were transferred to a 2 mL confocal imaging chamber (RC-27, Warner Instruments, USA) containing room-temperature perfusion buffer. Endothelial cell tubes were pinned on the bottom of the chamber using two round-tipped pinning pipettes (~140- to 160-μm tip diameter) positioned using micromanipulators. Tubes were then stretched to their approximate physiological lengths by adjusting the horizontal tension on the tissue using the micromanipulators. EC tube experiments were conducted at room temperature as the integrity of the tubes is reduced at higher temperatures.

2.2 Wire myography

A Mulvany-Halpern myograph, described in detail by Mulvany and Halpern (1976), was used to record the tension responses of isolated arteries ~2 mm in length. Wires are carefully inserted through the lumen of an artery and secured onto two parallel jaws, one of which is attached to a force transducer and the other a micrometer. This configuration allows the artery to be stretched by known increments whilst measuring tension, generating a length-tension relationship curve. The resting tension of the vessel can then be set to reflect the *in vivo* blood pressure across that artery bed, without masking changes in active wall tension

2.2.1 Artery set up

Two 25 µm diameter gold-plated tungsten wires were threaded through the lumen of artery segments and secured to the jaws of a 5 mL chamber Mulvany-Halpern wire myograph (Danish Myo Technology Organ Bath Model 700MO or 610M, Denmark; **Figure 2.2.1**) in Krebs-buffered solution gassed with a 21% O_2, 5% CO_2, and 74% N_2 mixture. Chambers were warmed to 37°C and arteries were normalised to a resting tension equivalent to that generated at 90% of the diameter of the vessel at 70 mmHg (mesenteric arteries) or 80 mmHg (coronary and cremaster arteries).

Changes in tension (mN) were recorded at 10 Hz using a PowerLab/4SP data acquisition system (ADInstruments, New Zealand) and LabChart software (v8.1.17, AD Instruments, New Zealand).

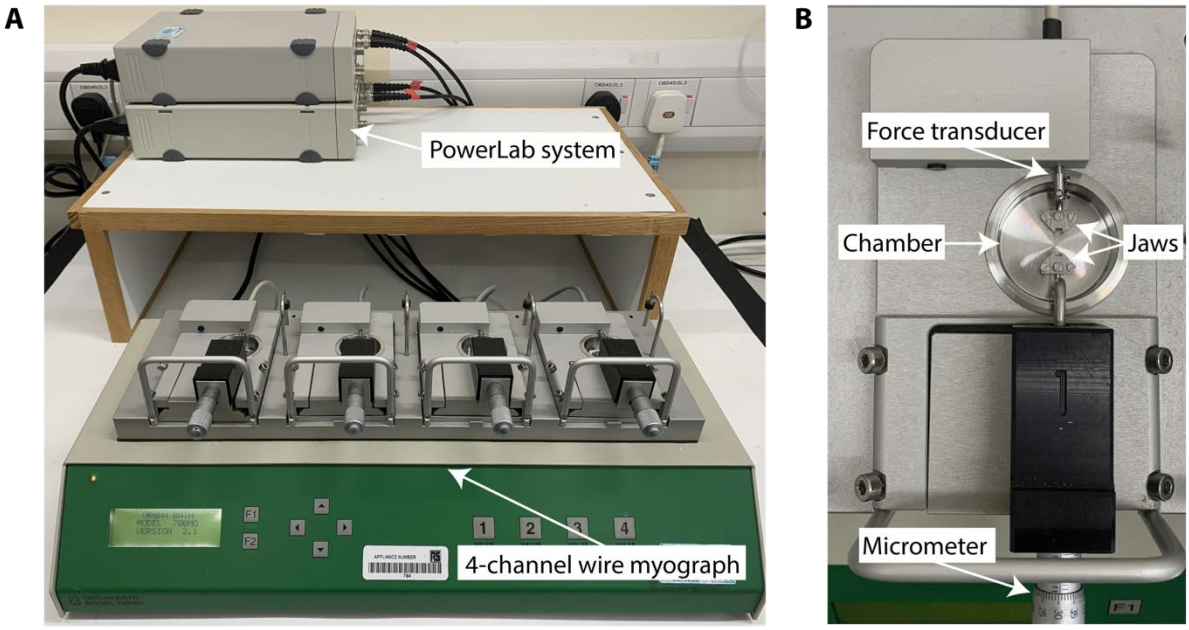

Figure 2.2.1. Wire myograph apparatus. (A) Image of equipment used to measure artery tension under isometric conditions. (**B**) A channel from the wire myograph with force transducer and micrometer indicated. Arteries are secured to the jaws with tungsten wires

2.2.2 Studying mesenteric arteries under isometric conditions

After equilibrating for 30 minutes at their normalised tension, artery function was assessed using PE, an α_1-adrenergic agonist, and ACh, a muscarinic M_3 receptor agonist. Only arteries that demonstrated robust and sustained constriction to PE (1-3 μM) and >95% relaxation to 100 nM ACh were considered functional. To study vasodilation, arteries were precontracted with a submaximal concentration of PE. Arteries were not exposed to multiple inhibitors, unless where indicated, nor washed out after their addition to eliminate the possibility of irreversible effects confounding other results.

2.2.3 Studying coronary arteries under isometric conditions

Arteries were left to equilibrate at their normalised tension for 60 minutes. Artery function was assessed by the development of spontaneous myogenic tone followed by endothelium-dependent relaxation to ACh. Arteries that developed >0.5 mN/mm spontaneous myogenic tone and relaxed >95% to 100 nM ACh were considered functional. If sufficient myogenic tone was not developed, PE (1-5 μM) was used to contract arteries, followed by ACh (10–1 μM) to stimulate endothelium-depended vasodilation. In this case, arteries that demonstrated robust and sustained contraction to PE and >95% relaxation to 100 nM ACh were considered functional.

In experiments assessing the function of vascular smooth muscle only, the endothelium was removed by passing a human hair through the lumen. Successful endothelial denudation was confirmed by <10% relaxation to 1 μM ACh.

Arteries were not exposed to multiple inhibitors, unless where indicated, nor washed out after their addition to eliminate the possibility of irreversible effects confounding other results.

2.2.4 Analysis of mesenteric artery tension recordings

Each data point used for analysis represents the mean tension over a 10-second period. For relaxation responses, the preconstriction tension was obtained by adding PE, and the baseline tension was taken as the tension immediately following normalisation (**Figure 2.2.4 A**):

$$\text{Vasodilation (\%)} = \frac{\text{tension at peak} - \text{preconstriction tension}}{\text{baseline tension} - \text{preconstriction tension}}\ x\ 100$$

Vasoconstriction was expressed as the increase in tension above baseline and was adjusted to account for the length of each artery (mN/mm).

2.2.5 Analysis of coronary artery tension recordings

Each data point used for analysis represents the mean tension over a 10-second period. For relaxation responses, the myogenic tone tension (MT tension) was taken as the level of myogenic tone prior to the addition of the test agent, or if arteries did not generate myogenic tone, the maximum contraction to L-NAME + NS 6180. The baseline tension was taken as the tension immediately following normalisation (**Figure 2.2.4 B**):

$$\text{Vasodilation (\%)} = \frac{\text{tension at peak} - \text{MT tension}}{\text{baseline tension} - \text{MT tension}}\ x\ 100$$

For constriction experiments, data were presented either as the increase in tension above MT tension (adjusted for artery length), or as a percentage of vasoconstriction evoked by 45 mM KCl, which was applied at the end of experiments (**Figure 2.2.4 C**):

$$\text{Vasoconstriction (\% of 45 mM KCl)} = \frac{\text{tension at peak} - \text{MT tension}}{\text{baseline tension} - \text{maximum tension (after KCl)}}\ x\ 100$$

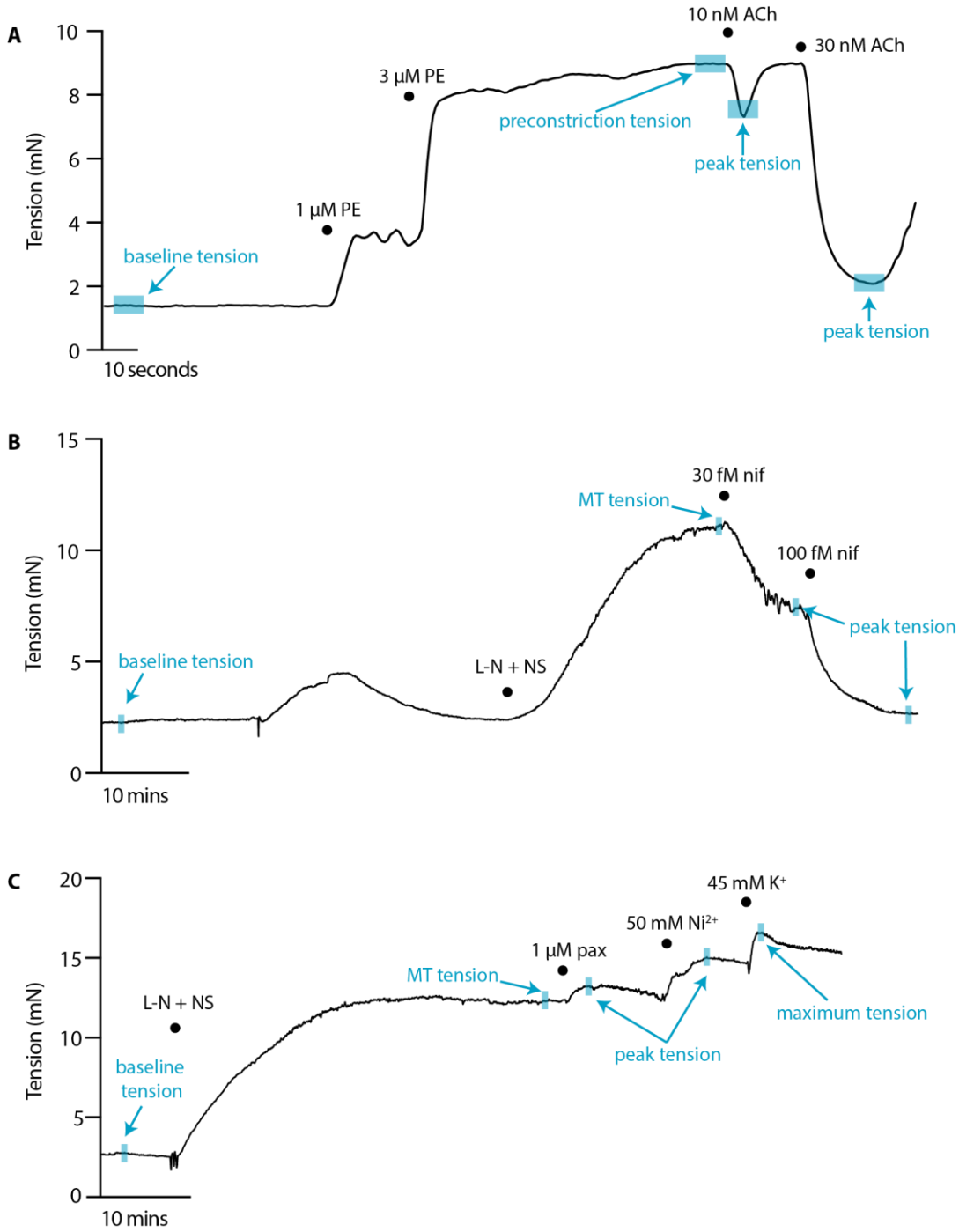

Figure 2.2.4. Sample traces demonstrating analysis method for wire myography tension experiments. (A) Sample trace from mesenteric artery indicating the values used for analysing vasodilation responses. (**B**) Sample trace from coronary artery indicating the values used for analysing vasodilation responses. As the artery did not develop stable myogenic tone (MT), MT tension is taken as the maximum tension generated after adding 10 µM L-NAME (L-N) and 1 µM NS 6180. (**C**) Sample trace from coronary artery indicating the values used for analysing vasoconstriction responses. Blue rectangles indicate the data points used to calculate mean tension. Black dots indicate when labelled drugs were added.

2.3 Pressure myography

The pressure myography set up used for these experiments was adapted from the original method published by Duling *et al.* (1981), which aimed to replicate the *in vivo* state of blood vessels more closely than previous methods had achieved. As well as facilitating the measurement of changes in artery diameter, pressurised arteries can be loaded with fluorescent indicators to measure the levels and localisation of endogenous signalling molecules such as NO and Ca^{2+}. Furthermore, the direct access to the lumen provided by this set up allows for selective loading of fluorescent indicators into either ECs or VSMCs, thus providing a valuable tool for investigating cell type-specific signalling in arteries.

2.3.1 Artery set up

Following isolation, mesenteric and coronary artery segments (1-2 mm length) were transferred to a 2 mL confocal imaging chamber (RC-27, Warner Instruments, USA; **Figure 2.3.1**). Each end of the artery was cannulated with a glass micropipette (inner diameter ~ 80 µm, outer diameter ~120 µm) and secured with 11-0 nylon sutures (Ethicon, USA). The chamber was secured to the stage of an inverted microscope (IX70; Olympus, Japan), attached to a confocal scanning unit (FV500 or FV1000; Olympus, Japan), with a heating platform (PH-6; Warner Instruments, USA) connected to a temperature controller (TC-342C; Warner Instruments, USA).

Unless otherwise stated, arteries were continually superfused at a rate of 2 mL/minute with Krebs-buffered solution warmed to 36.6–37.2°C and gassed with a 21% O_2, 5% CO_2, and 74% N_2 mixture. One pipette was attached to a pressure head which could be vertically adjusted to alter the intraluminal pressure of the artery. The intraluminal pressure was gradually increased to 70 mmHg (mesenteric) or 80 mmHg (coronary), longitudinally stretching the artery with each pressure step. Whilst pressurised, an inline 3-way tap was closed to check for artery deflation

to ensure that no side-branches were present in the artery and that the sutures had been adequately secured. Arteries were visualised using a 10x objective (NA 0.3; Olympus, Japan) and images were recorded at 1 Hz. Changes in artery diameter were recorded using FluoView software (v5.0; Olympus, Japan).

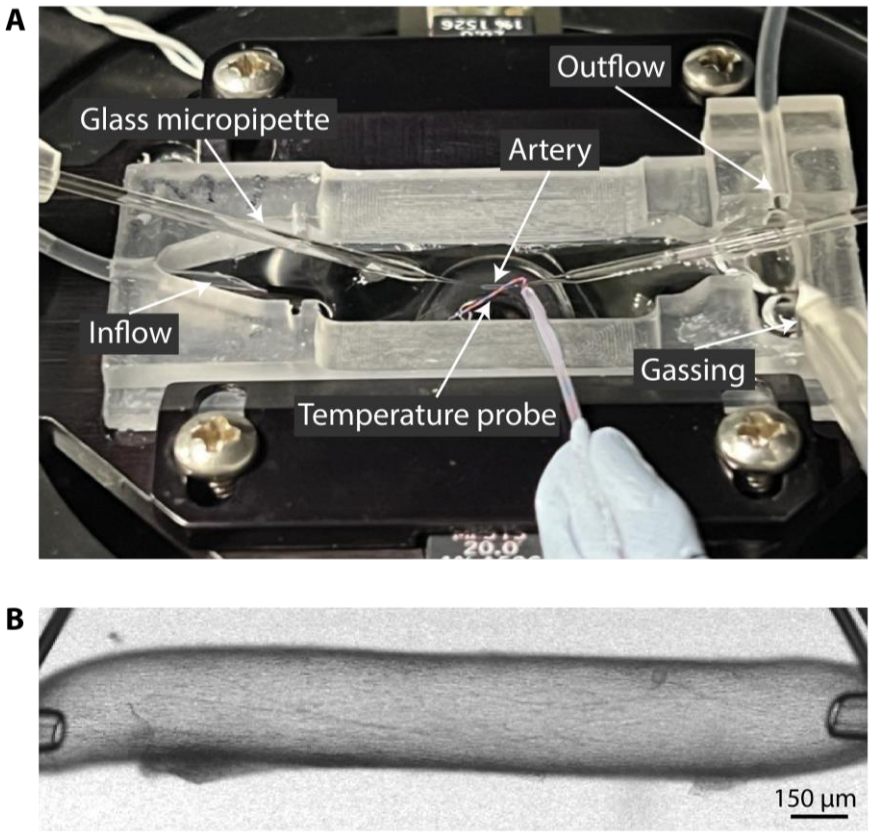

Figure 2.3.1. Pressure myography set up and pressurised artery. (**A**) Temperature-controlled imaging chamber with artery mounted on two glass micropipettes. (**B**) Cannulated and pressurised mesenteric artery.

2.3.2 Studying mesenteric arteries under isobaric conditions

If no leaks were detected, mesenteric arteries were left to equilibrate for 30 minutes followed by the same function test as detailed in Section 2.2.2. The superfusion was stopped immediately prior to adding agents to the chamber.

In NO dye experiments using mesenteric arteries, measures were required to prevent movement artefacts. This was achieved by performing experiments in the continued presence of the L-type VGCC blocker nifedipine (1 μM; Sigma, USA).

2.3.3 Studying coronary arteries under isobaric conditions

If no leaks were detected, coronary arteries were left to equilibrate for 60 minutes. Artery function was assessed by the development of spontaneous myogenic tone followed by endothelium-dependent relaxation to ACh (10 nM–1 μM). Only arteries that developed >20% myogenic tone and >95% vasodilation to 100 nM ACh were considered functional. The superfusion was stopped immediately prior to adding agents to the chamber.

2.3.4 Analysis of coronary artery diameter recordings

The inner diameter was measured using VasoTracker Offline Diameter Analyser (v1.1.0, VasoTracker, UK) (Lawton *et al.*, 2019). Each data point represents the mean diameter over 10 seconds. Myogenic tone is calculated as the percentage decrease from the passive diameter (pre-myogenic tone development):

$$\text{Myogenic tone } (\%) = \frac{\text{passive diameter} - \text{diameter with myogenic tone}}{\text{passive diameter}} \; x \; 100$$

2.4 Calcium imaging

2.4.1 Loading mesenteric EC tubes with Ca^{2+} indicator

The perfusion buffer bathing pinned EC tubes was gently removed and replaced with perfusion buffer containing the Ca^{2+} indicator, Calbryte 520 AM (50 nM, AAT Bioquest, USA) and 0.0025% pluronic F-127 (Invitrogen, USA). EC tubes were loaded for ~10 minutes until they could be clearly visualised, and excess indicator was removed from the chamber by aspiration and replaced with normal perfusion buffer. The loaded dye was left to de-esterify and equilibrate for 10 minutes before imaging.

EC tube Ca^{2+} activity was imaged at 40x (40x/1.15W, UApo N340 objective; Olympus, Japan) using an inverted microscope (IX81, Olympus, Japan) attached to a linescan confocal microscope (FV5000; Olympus, Japan). Images were acquired at a frequency of 3 Hz in a 640x128-pixel clip box at 2x zoom. Calbryte 520 AM was excited at 488 nm and emitted light detected at ≥ 505 nm.

2.4.2 Analysis of mesenteric EC tube Ca^{2+} fluorescence measurements

Whole cell Ca^{2+} activity was analysed offline using MetaMorph (v7.7.4.0; Molecular Devices, USA). Only cells that responded to ACh were included in analyses. Ca^{2+} activity is expressed as F/F_0 where F and F_0 are both taken as a 10 second average ~2 minutes after treatment and at baseline, respectively. Each data point represents the mean fluorescence intensity of at least 3 cells per tube.

2.4.3 Loading mesenteric arteries with Ca^{2+} indicator

To visualise MEPs, the ECs of pressurised mesenteric arteries were selectively loaded with calcein AM (C3100MP, Invitrogen, USA). Although no longer widely used as a Ca^{2+} indicator, calcein is used as a cytoplasmic marker due to the fluorescent signal it produces when taken up by cells. The reconstruction of serial images through the Z-axis of the artery allows the artery wall to be viewed in 3D, where bright MEPs are clearly visible. Calcein remains inside cells post-fixation, allowing MEPs to be visualised alongside immunolabelled proteins.

Krebs-buffered solution containing calcein AM (3 μM; Invitrogen, USA) and 0.05% pluronic F-127 (Invitrogen, USA) was luminally pumped into pressurised mesenteric arteries for 10 minutes. Excess dye was washed out of the vessel lumen by pumping through normal Krebs-buffered solution, and loaded dye was left to de-esterify and equilibrate for 30 minutes. Arteries were then fixed (see Section 2.6.1), ready for immunostaining.

2.4.4 Loading coronary arteries with Ca^{2+} indicator

ECs of pressurised coronary arteries were selectively loaded by intraluminally pumping filtered Krebs-buffered solution containing 50 nM Calbryte 520 AM (AAT Bioquest, USA) and 0.0025% pluronic F-127 (Invitrogen, USA). ECs were loaded for ~10 minutes until they could be clearly visualised. Excess indicator was washed out the vessel lumen by pumping through normal Krebs-buffered solution, and the loaded dye was left to de-esterify and equilibrate for 30 minutes. EC Ca^{2+} activity was imaged at 40x (40x/1.15W, UApo N340 objective; Olympus, Japan) using an IX81 inverted microscope (Olympus, Japan) attached to a linescan confocal microscope (FV1000; Olympus, Japan). Images were acquired at a frequency of 3 Hz in a 640x128-pixel clip box at 2x zoom.

2.4.5 Analysis of coronary artery Ca^{2+} fluorescence measurements

Sub-cellular Ca^{2+} activity was analysed offline using MetaMorph (v7.7.4.0; Molecular Devices, USA). Only cells that responded to ACh were included in analyses. Ca^{2+} activity is expressed as F/F_0 where F and F_0 are both taken as a 10 second average ~2 minutes after treatment and at baseline, respectively.

2.5 NO dyes

Cell-trappable NO-sensitive fluorescent dyes, including DAR-4M AM and Cu_2FL2E, directly measure NO synthesis and release. Optimisation of an NO dye for use in live, *ex vivo* arteries would provide insights into the spatial and temporal release of NO from ECs *in situ*, advancing our knowledge of the mechanisms of vasodilation.

2.5.1 Cu_2FL2E preparation

FL2E (0.5 mg; 07-0291, STREM Chemicals, Cambridge, UK) was dissolved in DMSO to make a stock solution of 1.0 mM FL2E. This was aliquoted and stored at -80 °C as per the product sheet. When thawed, the solution was kept chilled in the dark and used as quickly as technically feasible; any unused dye was discarded.

The steps in preparing Cu_2FL2E (1 μM) for use in cell-free chambers were:

1. Prepare the working solution of Cu_2FL2E (1 μM, working ratio 1:2) by adding 2 μL of stock (1 mM in DMSO) FL2E and 4 μL of stock (1 mM in H_2O) $CuCl_2$ to 2 mL buffered solution (either phosphate buffered saline (PBS) or Krebs-buffered solution), at 25 °C, mixing well.
2. In some experiments, higher concentrations of Cu_2FL2E were used (2 μM and 5 μM).

3. In some experiments, the concentration of $CuCl_2$ was increased to make working ratios of 1:5 and 1:10.

The steps in preparing Cu_2FL2E (2.5 μM) for use in arteries were:

1. Prepare the working solution of Cu_2FL2E (working ratio 1:2) by adding 5 μL of stock (1 mM in DMSO) FL2E and 10 μL of stock (1 mM in H_2O) $CuCl_2$ to 2 mL Krebs, mixing well.
2. Add 3 μL pluronic F-127 (Invitrogen, USA) to the 2 mL working solution, mixing well.
3. Remove the Krebs from the chamber bathing the artery and immediately replace with 1 mL Krebs working solution (2.5 μM Cu2FL2E; 0.03% pluronic, 0.37% DMSO).
4. Wash with Krebs for > 5 minutes to remove residual NO dye.

2.5.2 DAR-4M AM preparation

DAR-4M AM (1 mg; 251765, Calbiochem, USA) was dissolved in DMSO to make a stock solution of 5.0 mM DAR-4M AM. This was aliquoted and stored at -20 °C. When thawed, this solution was kept chilled in the dark and used as quickly as technically feasible.

The steps for preparing DAR-4M AM (5 μM) to use in cell-free chambers were:

1. Dilute the stock DAR-4M AM (5 mM) into buffered solution (PBS or Krebs).

In experiments where DAR-4M AM was loaded into cells of intact arteries, additional steps were followed. We chose 5 μM DAR-4M AM as this allowed us to maximise the ability to visualise NO dye loading as well as maintain levels of pluronic F-127 and DMSO similar to those used for Cu_2FL2E.

The steps in preparing DAR-4M AM (5 μM) for use in arteries were:

1. Prepare the working stock by adding 1 μL of stock (5 mM) DAR-4M AM to 3 μL pluronic F- 127 (Invitrogen, USA) in a 0.5 mL Eppendorf tube and triturate well.
2. Add the 4 μL of working stock to the chamber bathing the artery in Krebs (1 mL). This working solution contains 5 μM DAR-4M AM, 0.06% pluronic F-127, 0.34% DMSO.
3. Ensure gassing is on and incubate for 20 minutes to load the artery.
4. Wash with Krebs for > 5 minutes to remove residual NO dye.

2.5.3 Cell-free experiments

The first set of experiments aimed to establish the extent of NO dye fluorescence in response to the NO donor *S*-Nitroso-*N*-acetyl-DL-penicillamine (SNAP; Abcam, UK), and the effect of different experimental conditions on this response. These experiments were performed using a 2 mL chamber (RC-27; Warner Instruments, CT, USA) containing room temperature (~25°C) buffered solution, seated within the stage of an XI81 inverted microscope. The solution was routinely visualised 200 μm above the coverslip using an Olympus 20x water immersion (0.17 NA, 0.70 mm WD) and linescan confocal microscope (FV300 or FV500) with FluoView software (Olympus, Japan). Each image was 512 x 512 pixels, equating to images of X = 318 μm by Y = 318 μm. The frequency of acquiring images for each NO dye was 0.45 Hz.

Each NO dye was added to the chamber, mixed and allowed to equilibrate for at least 2 minutes. Once the signal was stable, SNAP was added, and acquisition continued for ~15 minutes. The acquisition settings remained consistent between data sets for each NO dye. Cu_2FL2E was excited at 488 nm, emitted light detected at ≥ 505 nm; DAR-4M AM was excited at 543 nm, emitted light detected at ≥ 560 nm.

2.5.4 Loading NO dyes into pressurised mesenteric arteries

First, arteries were incubated for 10 minutes with the elastin label Alexa Fluor™ 633 Hydrazide (AF, 10 nM; A30634, Invitrogen, USA). Since the internal elastic lamina separating ECs and VSMCs is very thin yet visible, and there is elastin between adjacent VSMCs, this 'template' of artery structure could be captured by acquiring Z-stacks. The same focal planes could then be selected for comparative images over time.

Each NO dye was then added to the chamber, mixed, and allowed to load from the outside of arteries. Once the signal was clear above the background autofluorescence, the time course of baseline, 1 μM ACh, and 10 μM SNAP (each 30 minutes), was recorded in a static chamber with gassing. In some experiments no agonists were added (time control), and other experiments were performed in the presence of the NOS inhibitor L-NAME (100 μM; Sigma, USA).

The artery wall was imaged using a 40x (1.15 NA, 0.25 mm WD, Olympus, Japan) water immersion objective, initially obtaining 13.5 μm Z-stacks in 1.5 μm steps. Each image plane was 780 x 340 pixels, equating to image volumes of X = 351 μm, Y = 153 μm and Z = 13.5 μm.

The acquisition settings remained consistent between data sets for each NO dye. AF was excited at 635 nm, emitted light detected ≥ 660 nm. Cu_2FL_2E was excited at 488 nm, emitted light detected at 505-550 nm; DAR-4M AM was excited at 543 nm, emitted light detected at ≥ 560 nm. Z-stacks spanning 13.5 μm were acquired every 120 s, with 83.2 s rest time between each stack, 90 minutes per run. Z-stacks of 130 μm were acquired every 330 s, with 214.4 s rest time between each stack, 90 minutes per run. In all cases, each line was the average of two scans (line Kalman) and the wavelengths were captured sequentially. The transmitted light signal was also recorded.

Signal from AF was not detected in the wavelengths used for acquiring the NO dyes (488 nm and 543 nm), and equally no NO dye signal was visible at 635 nm, even during maximal responses to SNAP.

2.5.5 En face mounting

While pinned in the dissecting dish, cleaned arteries were partially cut transversely to reveal an opening in the lumen. Curved Vannas micro scissors (World Precision Instruments, USA) were used to cut longitudinally through the wall along one side, leaving a flat, rectangular-shaped artery with ECs on one surface and adventitia on the other. The flat section of artery, around 1-2 mm in length, was cut away from the rest of the tissue and transferred to an imaging chamber (5 mL volume; Confocal Cardiac Myograph, Danish Myo Technology, Denmark) containing chilled Krebs-buffered solution. The artery was secured at each end by two micro clamps (Fine Science Tools, USA) and stretched to resemble its physiological length *in vivo.* Arteries were loaded with AF and either NO dye using the same concentrations and durations as pressurised arteries (see Section 2.4.4).

2.5.6 Analysis of NO dye experiments

2.5.6.1 Cell-free experiments

For data analysis of cell-free experiments, data were analysed offline using MetaMorph software (version 7.7.4.0, Molecular Devices, USA). The whole image field was defined as the region of interest (ROI), which was used to generate time courses of DAR-4M AM and Cu_2FL2E fluorescence. Each fluorescence intensity value (F) was divided by the 30 s average before adding SNAP (F_0), giving F/F_0.

2.5.6.2 Experiments in arteries

For data analysis of the artery wall, data were first analysed using Imaris software (v8.0.2; Bitplane, USA). The 13.5 µm Z-stacks were visually inspected for the AF and NO dye. The AF signal, indicating elastin, was an excellent indicator of artery movement. We noted that in all cases there was little movement of the artery, hence the AF signal did not vary over time. Once this was established, the Z-stack was merged into a single image plane, averaging the fluorescence for each time point and for each dye (wavelength). The files were saved as separate TIF files and opened in MetaMorph for further analysis. ROIs the size of the image field were used to generate separate time courses of fluorescence intensity for AF and each NO dye. The fluorescence ratio (FR) of NO dye/elastin over time was calculated to provide data as FR/FR_0. For these experiments, the FR increased under baseline conditions; therefore, the value for FR_0 was taken 30 minutes into each acquisition run, as the timepoint immediately prior to the addition of 1 µM ACh in other experiments. The FR/FR_0 value was also expressed as a percentage of the fluorescence response to 10 µM SNAP, which represents maximum fluorescence in each experiment.

2.6 Immunohistochemistry

2.6.1 Immunostaining of pressurised arteries

Arteries mounted for pressure myography experiments (see Section 2.3) can be fixed and stained to identify proteins of interest. Pressurised arteries were fixed *in situ* by adding 4% paraformaldehyde aqueous solution (PFA; J61899.AK; Thermo Fisher Scientific, USA) to the chamber for 60 minutes at room temperature before being washed with PBS (P3813; Sigma, USA). Arteries were then blocked for 90 minutes by luminal pumping of blocking buffer containing 1% bovine serum albumin (A3059; Sigma, USA), 0.5% Triton X-100 (T8532;

Sigma, USA), and 0.05% Tween20 (P2287; Sigma, USA) diluted in PBS. Blocking buffer was also added to the chamber. Arteries were incubated with the primary antibodies overnight at 4°C. The following day, arteries were washed in PBS and incubated with the secondary antibodies, Hoechst 33342 (10 µg/mL), and AF (10 nM; all diluted in blocking buffer) for 2 hours at room temperature, before being washed in PBS again. Arteries were imaged immediately.

2.6.2 Immunostaining of wire-mounted arteries

Following functional experiments, arteries were fixed *in situ* by adding 4% PFA solution to the chamber for 60 minutes at room temperature, before being washed with PBS. Fixed arteries were cut open laterally and removed from the wire myograph. Arteries were then blocked for 90 minutes with blocking buffer and incubated with the primary antibodies overnight at 4°C. The following day, arteries were washed in PBS and incubated with the secondary antibodies, Hoechst 33342 (10 µg/mL), and sometimes AF (10 nM) for 2 hours at room temperature, before being washed in PBS again. Antibodies, Hoechst and AF were diluted in blocking buffer. After staining, the arteries were carefully opened and placed flat on glass slides in mounting medium (VECTASHIELD, H-1000; Vector Laboratories Inc., USA), with the EC layer facing up. Coverslips were lowered on top and sealed (CoverGrip, 23005; Biotium, USA) ready for imaging.

2.6.3 Imaging of immunostaining

Arteries were excited at 405, 488, 543, and 635 nm using sequential scans. The emitted fluorescence was acquired through a 40x water immersion objective (NA 1.15; WD 0.25 mm; 1024x1024-pixel clip box; Olympus, Japan) using a laser scanning confocal microscope (FV1200; Olympus, Japan). Arteries were imaged at 1-3x digital zoom. Scans were Kalman line arranged. Sequential Z-stacks through the artery wall were acquired at 0.5 µm intervals

using FluoView Software (FV10-ASW 3.0; Olympus) and reconstructed in Imaris Software (v8.0.2; Bitplane, USA).

2.7 RNAscope

2.7.1 Artery preparation

RNAscope (Advanced Cell Diagnostics, ACD; USA) allows single mRNA molecules to be visualised *in situ* at a cellular level, where every punctate dot represents an individual RNA molecule. It uses an oligo-based double 'Z'-probe system with each 'Z' probe containing a complementary target binding sequence of 18-25 base pairs, a linker sequence, and a 14-base tail sequence which, when paired with another 'Z'-probe, acts as a binding site for the preamplification scaffold and amplifiers. Fluorescent label probes then bind to the amplifiers, allowing molecules of RNA to be visualised using fluorescence microscopy (see **Figure 2.7.1**).

Wire-mounted arteries were fixed for 60 minutes with 4% PFA (see Section 2.6.2). After this initial fixing, arteries were washed in PBS, removed from the wires, and fixed overnight in 4% PFA at 4°C. Fixed arteries were then washed twice in 0.1% PBS-T (0.1% Tween-20 in PBS) for 5 minutes each. Arteries were dehydrated in a methanol (Sigma, USA) gradient (methanol diluted in PBS-T; 25%, 50% 75% and 100% x 2 for 10 minutes each). Once in 100% methanol, arteries can be stored at -20°C for up to 6 months.

2.7.2 RNAscope protocol

To detect the hybridisation signal, RNAscope Multiplex Fluorescent Detection Reagents v2 (ACD, USA), utilising the TSA Vivid 520 and TSA Vivid 570 fluorophores respectively (Perkin Elmer, USA), were applied. Arteries were rehydrated using the same methanol gradient and

washed twice in 0.1% PBS-T. Arteries were treated with hydrogen peroxide (ACD, USA) at room temperature for 10 minutes before being washed with PBS-T. This was followed by digestion with RNAscope protease plus at 40°C for 10 minutes before arteries were washed with 0.2x saline-sodium citrate (SSC; Sigma, USA) 5 minutes x3. Following protease treatment, arteries were incubated with the RNAscope probes: Rn-*Cacna1g* (319661, ACD, USA), Rn-*Cacna1h*-C3 (319671, ACD, USA), Rn-*Cacna1i*-C2 (414231, ACD, USA), Rn-*Cacna1c* (415141, ACD, USA), Rn-*Hcn1* (590421, ACD, USA), Rn-*Hcn2* (592111, ACD, USA), Rn-*Hcn3*-C2 (1160711, ACD, USA), Rn-*Hcn4*-C2 (580491, ACD, USA), for approximately 5 hours at 40°C and overnight at room temperature. The recommended positive control probe against *Ppib* (Rn-*Ppib*-C3, 313921, ACD, USA) was used to confirm successful detection of RNA. *Ppib* encodes a cyclosporine-binding protein which is ubiquitously expressed at a low level by all cell types, thereby providing a rigorous control for sample quality. Arteries were then washed with 0.2x SSC. Probe signals were amplified by incubation with AMP1, AMP2 and AMP3 at 40 °C for 50, 50 and 20 minutes respectively, with 0.2x SSC washes after each.

Following this, RNAscope HRP-C1-3 was applied for 20 minutes at 40°C before the addition of TSA Vivid 520 (for the *Cacna* and *Hcn* probes), with 0.2x SSC washes between and after fluorophore addition. HRP blocker was then applied for 20 minutes at 40°C followed by a 0.2x SSC. This was then repeated with RNAscope HRP in the appropriate channel for the *Ppib* probe, and TSA Vivid 570, followed by HRP blocker before a final 0.2x SSC wash. Nuclei were then stained as per the IHC protocol described in Section 2.6.2, and imaged as described in Section 2.6.3.

2.7.3 RNAscope analysis and quantification

RNAScope images were analysed offline using Imaris software (v8.0.2; Bitplane, USA), where average projections through the EC and VSMC layers were obtained by selecting and merging

3 consecutive 0.5 μm Z-axis sections (**Figure 2.7.1**). First, the number of discrete mRNA molecules per cell in each cell type was quantified. mRNA staining was modelled as a 3D surface and the mean volume of 10 puncta believed to be single mRNA molecules was calculated. The total volume of the modelled mRNA surface was then divided by the mean volume of a single mRNA molecule. The number of nuclei in the field of view was counted, giving the number of individual mRNA molecules per cell.

To calculate the nuclear to cytoplasmic ratio of mRNA molecules, 3 ECs or VSMCs per Z-stack were selected and the total volume of all puncta in both cell compartments was calculated, using the stained nuclei as a guide. Again, this total was divided by the mean volume of a single mRNA molecule, giving the number of individual mRNA molecules in the nucleus and the cytoplasm. Cell borders were visualised using a polyclonal conjugated IgG antibody against mouse/rat CD31 (2 μg/mL; FAB3628G, Biotechne).

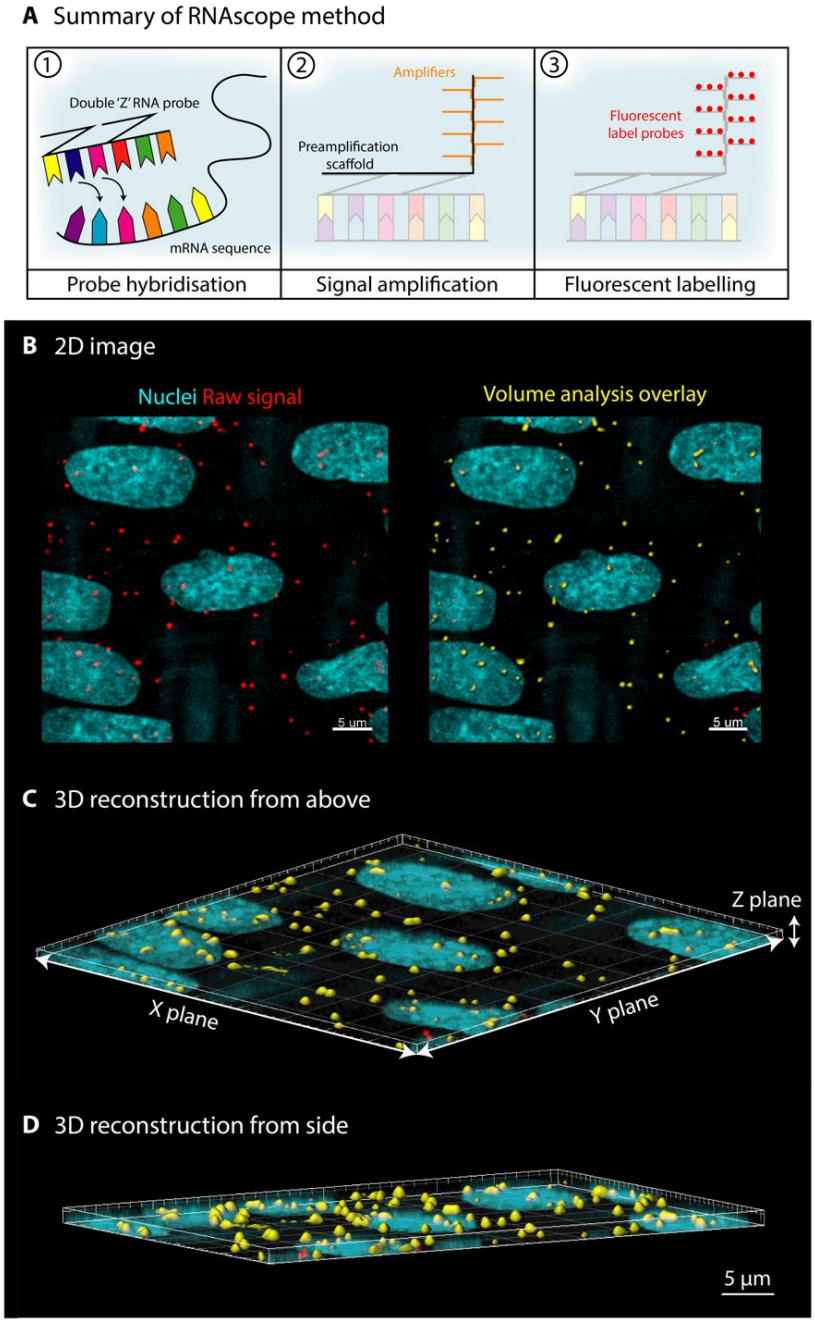

Figure 2.7.1. RNAscope in *en face*-fixed mesenteric arteries. (**A**) Schematic diagram summarising the principles of the RNAscope protocol. First, double 'Z'-RNA probes bind to the mRNA sequence of interest, providing a foundation for the preamplification scaffold and amplifiers. Fluorescent label probes then bind to the amplifiers, allowing the fluorescent signal for even single mRNA molecules to be detected. (**B**) Merged confocal micrographs (3x 0.5 µm Z-axis planes) showing EC nuclei (cyan) and the raw fluorescent signal (red) corresponding to mRNA molecules. The volume of each cluster was calculated in Imaris (yellow), allowing the number of mRNA molecules per cell to be calculated. The degree of overlap between the red and yellow signal in **C** and **D** demonstrates the accuracy of this quantification method.

2.8 Western blotting

Mesenteric arteries from rats (n = 3) were dissected and cleaned, then snap frozen in liquid N_2 and stored at -80°C. Arteries were homogenised and total protein collected and quantified. Briefly, tissue was homogenised in cell lysis buffer containing protease and phosphatase inhibitors using a MiniLys homogeniser (Bertin Technologies, France). The samples were centrifuged at 12,000 rpm for 20 minutes at 4°C and the supernatant was collected for protein content quantification.

For the western blotting, 10 µg of protein lysate from rat mesenteric arteries (RMAs) and rat brain were loaded into precast polyacrylamide gels (4-12% Bis Tris; Invitrogen, USA) for separation by electrophoresis (80 V for 10 minutes, then 115 V for 60 minutes). Following this, proteins were transferred from the gel onto a polyvinylidene difluoride membrane and Ponceau S stain was used to verify successful transfer. After blocking in milk (5%), membranes were immunoblotted for 2 hours at room temperature with primary antibodies. After washing, membranes were incubated for 1 hour at room temperature with secondary antibody, and bands were visualised with fluorescence detection using an Odyssey M imager (Li-COR, USA).

2.9 Solutions and drugs

During tissue collection, dissection, and myography experiments, Krebs-buffered solution was used containing (in mM): 118 NaCl, 25 $NaHCO_3$, 3.6 KCl, 1.2 $MgSO_4(7H_2O)$, 1.2 KH_2PO_4, 11 glucose, and 1.25 CaCl, and gassed with 21% O_2, 5% CO_2, and 74% N_2.

The dissection buffer used in the EC tube protocol contained (in mM): 137 NaCl, 5.6 KCl, 1 $MgCl_2$, 10 Hepes, 10 glucose, 0.01 sodium nitroprusside, and 0.1% BSA. The dissociation buffer used in the EC tube protocol contained (in mM): 137 NaCl, 5.6 KCl, 1.0 $MgCl_2$, 10.0

Hepes, 10.0 glucose, 2.0 $CaCl_2$, and 0.1% BSA. The perfusion buffer used in the EC tube protocol contained (in mM): 137 NaCl, 5 KCl, 1 $MgCl_2$, 10 Hepes, 10 glucose, and 2 $CaCl_2$.

Drug and compound stock solutions were diluted in Krebs-buffered solution. The total level of DMSO arteries were exposed to never exceeded 0.4%, which the laboratory has proven is the maximum amount that can be used before stimulating ECs (unpublished data from Dora/Garland group). Arteries were allowed at least 15 minutes between experiments to recover. All inhibitors were incubated with the tissue for at least 15 minutes prior to experimentation and until myogenic tone had plateaued when relevant. Details of drugs and compounds used in the current investigations are given in **Table 2.9.1**.

Drug/Compound	Product code	Supplier	[Stock] (mM)	Stock solvent
Acetylcholine	A6625	Sigma, USA	10	Milli-Q
Bay K 8644	1544	Tocris, UK	10	DMSO
CuCl	229628	Sigma, USA	10	Milli-Q
L-NAME	N5751	Sigma, USA	100	Milli-Q
NiCl	339350	Sigma, USA	10	Milli-Q
nifedipine	N7634	Sigma, USA	10	Ethanol
NNC 55-0396	2268	Tocris, UK	10	Milli-Q
NS 6180	353262-04-1	Alomone, Jerusalem	10	DMSO
Paxilline	P2928	Sigma, USA	10	DMSO
Phenylephrine	P6126	Sigma, USA	10	Milli-Q
SNAP	ab120014	Abcam, UK	100	DMSO

Table 2.9.1 Drugs and compounds used in experiments.

2.10 Statistical analysis and data presentation

Data were analysed using Microsoft Excel 2011 (v16, Microsoft Corporation, USA) and GraphPad Prism (v8.0, GraphPad Software, USA) software. Figures were made using Adobe Illustrator (v29.1, Adobe, USA) software unless otherwise indicated. All results are summarised as mean ± SEM of n replicates (unless otherwise stated), where n is the number of separate cell-free chamber experiments, or the number of individual arteries obtained from separate animals.

Concentration-response curves were fitted using variable slope nonlinear regression. Normality was assessed using the Shapiro-Wilk test. If data were normally distributed, statistical testing was applied using a student's t-test, or one- or two-way ANOVA, using multiple comparisons where appropriate. Datasets which didn't pass the normality test were analysed using a nonparametric two-tailed Mann-Whitney U or Wilcoxon test, or a Kruskal-Wallis test followed by a Bonferroni's post-test. Statistical significance is defined as $p<0.05$.

3. Optimising a Fluorescent Dye to Detect Nitric Oxide Production in Rat Resistance Arteries

3.1 Introduction

NO plays a crucial role in vascular physiology, acting as a potent vasodilator and regulator of vascular tone. Since its discovery as EDRF by Furchgott and Zawadzki in 1980, our understanding of NO's importance in cardiovascular health has grown exponentially (Furchgott and Zawadzki, 1980; Ignarro *et al.*, 1987). However, accurately measuring NO production in intact arteries remains a significant challenge due to its short half-life and high reactivity. This chapter focuses on the optimisation of fluorescent indicators for detecting NO in *ex vivo* arteries, addressing a critical need in vascular research.

NO is synthesised in ECs by the enzyme eNOS, which converts L-arginine to NO and L-citrulline. The activity of eNOS is regulated by various factors, including substrate availability, cofactors, and post-translational modifications. Once produced, NO diffuses to nearby VSMCs, where it activates sGC, leading to increased cGMP levels and subsequent vasodilation.

The release of NO in resistance arteries can be broadly categorised into two types: basal and stimulated. Basal release occurs continuously at low levels in unstimulated conditions, whereas stimulated release occurs in response to various stimuli, such as shear stress or agonists like ACh. Both types of NO release are critical for maintaining vascular health; basal NO production contributes to the regulation of resting vascular tone (see **Figure 3.1.1**) (Rees *et al.*, 1989; Stamler *et al.*, 1994), while stimulated NO release allows blood vessels to adapt to changing physiological demands (Gryglewski *et al.*, 1988). Importantly, dysregulation of either basal or stimulated NO release has been implicated in various cardiovascular diseases, including coronary artery disease (Quyyumi *et al.*, 1995; Nishikawa and Ogawa, 1997).

Despite the importance of NO in vascular function, accurately measuring its production in intact arteries remains challenging. Existing methods for NO detection each have their

limitations. Chemiluminescence, while considered the gold standard, requires time-consuming sample preparation, which may lead to inaccurate quantification due to the short half-life of NO. Spectrophotometric assays typically measure NO derivatives and may underestimate total NO production by failing to detect all relevant species. Electrochemical sensors, although widely used for *in situ* measurements, are prone to interference from anions and may lack the sensitivity to detect small, physiologically relevant changes in NO levels.

Several classes of fluorescent NO indicators have been developed, each with their own advantages and limitations. DAFs were among the first fluorescent NO dyes developed, which are sensitive to low NO concentrations, although they suffer from significant interference by calcium ions which limits their utility. DARs, structurally related to DAFs, offer improved photostability and reduced interference from tissue autofluorescence. The cell-trappable DAR-4M AM has shown promise in cultured endothelial cells (Kojima *et al.*, 2001) but has not been widely validated in intact artery preparations. Copper-based fluorophores, which are membrane-permeable, have demonstrated potential for direct NO detection (McQuade *et al.*, 2010; Ghosh *et al.*, 2013). However, previous protocols have required high concentrations of copper and DMSO, both of which can cause arterial dysfunction. The optimisation of these fluorescent indicators for use in *ex vivo* arteries would provide valuable insights into the spatial and temporal release of NO from the endothelium, both under basal conditions and following eNOS stimulation. The experiments described in this chapter address a gap in our ability to measure NO production in intact arteries. By optimising fluorescent indicators for NO detection in *ex vivo* arterial preparations, this work will further our understanding of artery function in several ways.

Existing methods for studying basal NO production in isolated arteries often rely on observing functional changes in artery diameter. However, these approaches may inadvertently stimulate NO production through mechanical stretch. The development of a fluorescence-based method that does not require arterial stretching will allow for more accurate

measurements of truly basal NO release. Fluorescent indicators offer the potential for real-time, spatially resolved measurements of NO production. This could provide new insights into the dynamics of NO release from the endothelium and its diffusion to VSMCs. Moreover, the ability to accurately measure both basal and stimulated NO release in the same preparation will allow for a more comprehensive understanding of how these two aspects of NO signalling are regulated and how they may be differentially affected in disease states.

While much of our understanding of NO signalling comes from studies of large conduit arteries, the regulation of coronary artery tone is particularly important for cardiac health. The methods developed in this study could be applied to coronary resistance arteries, providing new insights into how NO signalling in these vessels is affected in conditions like coronary artery disease. Finally, a more nuanced understanding of basal and stimulated NO release in healthy and diseased arteries could inform the development of new therapies targeting specific aspects of NO signalling. By addressing these areas, the work presented in this chapter aims to contribute to our understanding of vascular physiology and may ultimately inform new approaches to treating cardiovascular diseases.

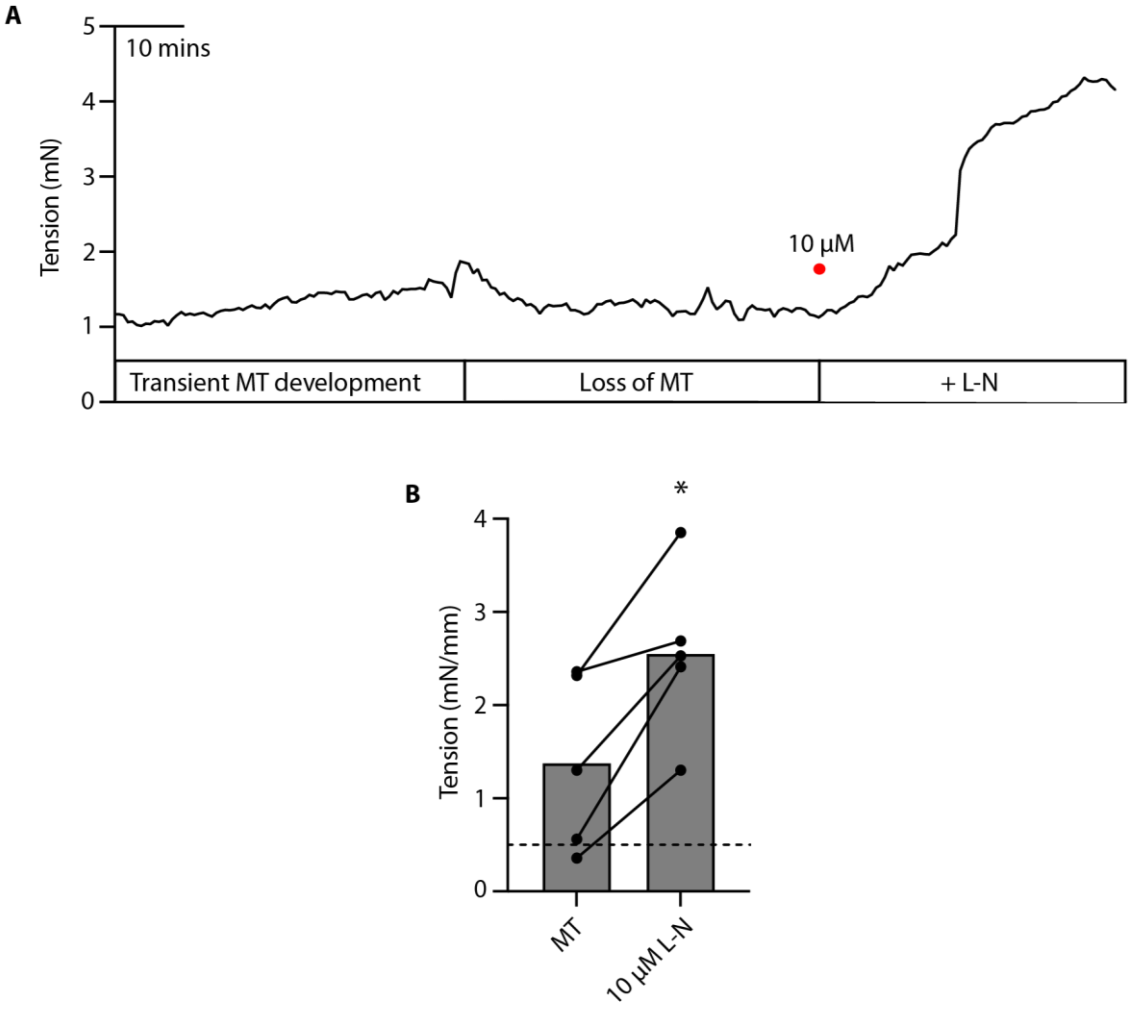

Figure 3.1.1. Effect of eNOS inhibition on tension of rat coronary arteries mounted in a wire myograph. (**A**) Representative trace of an artery showing transient spontaneous myogenic tone (MT) development followed by enhanced contraction in the presence of eNOS inhibitor L-NAME (L-N;10 µM). Red dot indicates when drug was added. (**B**) Bar graph showing the tension generated from spontaneous MT compared to after adding 10 µM L-N. Data are paired means, n = 5. *P = 0.0107 vs MT using paired student's t test.

3.1.1 Aims and objectives

The present study aimed to develop a protocol to detect NO using a fluorescent indicator in intact, pressurised arteries. This was achieved through several specific objectives:

i. To evaluate and optimise the performance of two fluorescent NO indicators, Cu_2FL2E and DAR-4M AM, in cell-free conditions and intact arterial preparations.
ii. To assess the ability of these indicators to detect both basal and stimulated NO production in pressurised mesenteric arteries, using ACh as an endothelium-dependent NO stimulator and SNAP as an exogenous NO donor.
iii. To validate the specificity of the NO detection by using the eNOS inhibitor L-NAME to confirm that the observed fluorescence changes are indeed due to NO production.

By achieving these objectives, this study sought to address an important gap in vascular research methodology, namely the accurate measurement of NO production in physiologically relevant, intact artery preparations. The development of such a protocol would provide valuable insights into the spatial and temporal aspects of both basal and stimulated NO release from the endothelium. This, in turn, could enhance our understanding of vascular physiology and potentially inform new approaches to treating cardiovascular diseases associated with endothelial dysfunction and altered NO signalling.

3.2 Materials and methods

3.2.1 NO dye preparation

NO dyes Cu_2FL2E and DAR-4M AM were prepared from stock solutions as detailed in Sections 2.5.1 and 2.5.2. In all experiments, the working solution of NO dye was freshly prepared immediately before use.

For Cu_2FL2E, note that each FL2E molecule has the potential to bind two copper ions (hence Cu_2), and each of the copper ions can be displaced by NO to form FL2E-NO (or FL2A-NO once deesterified inside cells) and increase dye fluorescence. Therefore, when NO binds, Cu^{2+} becomes free in solution. We commenced studies using a working ratio of 1:2, although effects of increasing the ratio of Cu^{2+} to FL2E were investigated.

3.2.2 Cell-free experiments

To establish the extent of NO dye fluorescence in response to SNAP, experiments were performed in 2 mL chambers containing room-temperature (~25°C) PBS or Krebs-buffered solution (see Section 2.5.3). These experiments were performed by PhD students Lucy Donovan and Aaron Johnston.

3.2.3 Wire myography

Mesenteric arteries were prepared for wire myograph chambers (see Section 2.2) where the effects of SNAP and Cu^{2+} on tension were investigated. In wire myography experiments, arteries were normalised to a resting tension equivalent to that generated at 90% of the diameter of the vessel at 70 mmHg.

3.2.4 Pressure myography

Mesenteric arteries were prepared for pressurisation (see Section 2.3) and then loaded with AF and either Cu_2FL2E or DAR-4M AM, which were added to a static bath to load from the outside (see Section 2.5.4). Excess dye was washed out when loading was complete. As this protocol was being developed, it was clear that measures were required to prevent movement artefacts. This was achieved by performing these experiments in the continued presence of L-type VGCC blocker nifedipine (1 μM). Nifedipine was used instead of other anti-contractile agents such as MLCK inhibitors due to its well-characterised mechanism of action and limited off-target effects.

3.2.5 *En face* mounting

Mesenteric arteries were cut longitudinally through one side to produce a flat, rectangular section, which was mounted in a custom-made imaging chamber and loaded with AF and either NO dye (see Section 2.5.5). These experiments were also performed in the continued presence of nifedipine (1 μM).

3.3 Results

3.3.2 Cu^{2+} enhanced SNAP-mediated vasodilation and impaired artery function

SNAP stimulated concentration-dependent relaxation of mesenteric arteries, with an EC_{50} of 0.74 μM and E_{max} of 10 μM (**Figure 3.3.1 A**). Therefore, to replicate functionally-relevant concentrations of SNAP, 10 μM was used to characterise the NO dyes. Next, since Cu^{2+} is added to the FL2E solution and is displaced from Cu_2FL2E to allow binding of NO, the influence of Cu^{2+} on arteries' response to SNAP and overall artery function was investigated. Preincubation with 1 μM Cu^{2+} left-shifted the SNAP concentration response curve (the EC_{50} became 0.24 μM; *P < 0.05 vs Cu^{2+}-free; **Figure 3.3.1 A**). Mechanistically, this is most likely attributable to the Cu^{2+}-catalysed decomposition of *S*-nitrosothiols to yield NO (Dicks and Williams, 1996; Williams, 1999). By increasing the degree of SNAP decomposition, and thus NO generation, the presence of 1 μM Cu^{2+} augmented the relaxation to SNAP. Moreover, the rate of SNAP decomposition has been suggested to be proportional to the product of [Cu^{2+}] and [*S*-nitrosothiol]; perhaps explaining the heightened rate of fluorescence accumulation in the presence of Cu^{2+}. The effect of Cu^{2+} on EC and VSMC function was then established. Since 2 μM and 5 μM Cu^{2+} were added to generate working ratios of 1:2 when using 1 μM and 2.5 μM Cu_2FL2E, respectively, arteries were preincubated with 2 μM and 5 μM Cu^{2+} and their responses to ACh and PE were compared to Cu^{2+}-free conditions. Relaxation to ACh tended to be reduced by the presence of Cu^{2+}, and Cu^{2+} significantly reduced contraction to PE (**Figure 3.3.1 B and C**). At higher concentrations (10 μM), Cu^{2+} caused a slow but substantial increase in artery tone over 20 minutes followed by aberrant relaxation to ACh (data not shown due to analytical limitations). This indicates that elevated extracellular Cu^{2+} is damaging to arteries, and as such, levels of exposure should be minimised. In light of this, [Cu^{2+}] was kept to a minimum in live-cell experiments. Furthermore, care was taken when considering responses to SNAP in the presence of Cu_2FL2E. The Cu^{2+} displaced by NO would potentially

be available to augment the release of NO from SNAP, establishing a positive feed-forward loop resulting in increased fluorescence.

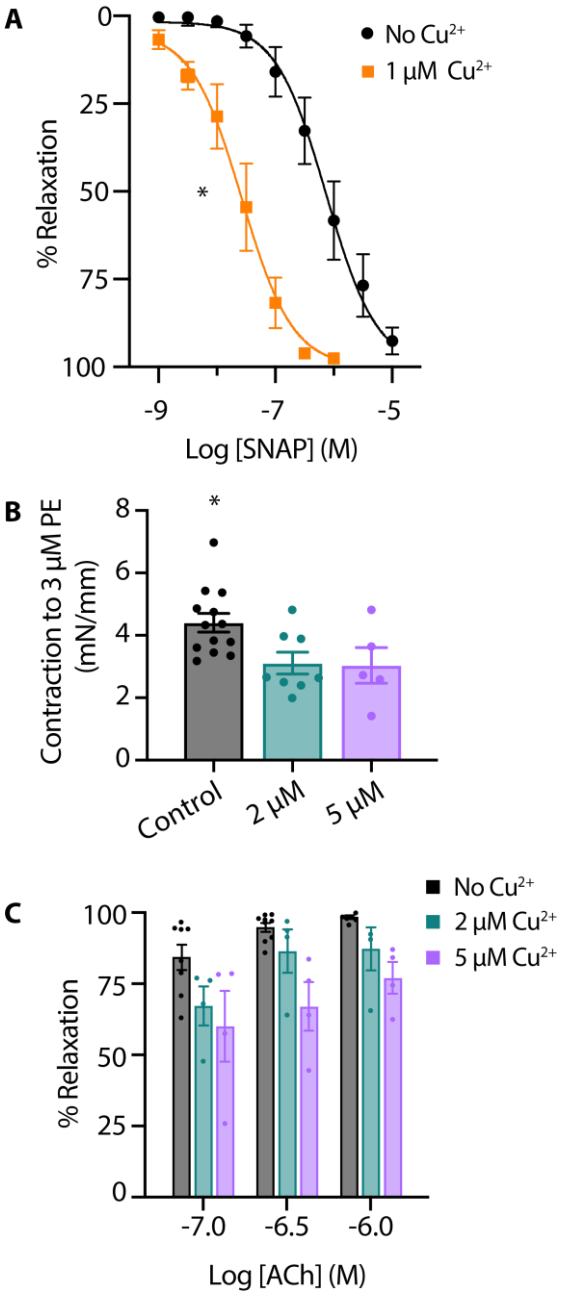

Figure 3.3.1. Cu^{2+} impairs the function of wire-mounted rat mesenteric arteries. (**A**) Effect of 1 µM Cu^{2+} on concentration-dependent relaxation to SNAP in arteries preconstricted with 3 µM phenylephrine (PE). n = 6. *P < 0.05 vs Cu^{2+} -free using paired Wilcoxon test for log EC_{50} values. (**B**) Effect of Cu^{2+} on contraction to 3 µM PE. n = 5-8. *P = 0.0479 vs 2 µM Cu^{2+} and P = 0.1062 for control vs 5 µM Cu^{2+}, using unpaired Kruskal Wallis test (**C**) Effect of Cu^{2+} on concentration-dependent relaxation to acetylcholine (ACh) in arteries preconstricted with 3 µM PE (n = 4-8). All data are means ± SEM.

3.3.2 Response of Cu_2FL2E and DAR-4M AM to SNAP in cell-free chambers

The first step in validating the use of Cu_2FL2E and DAR-4M AM was to test their response to 10 μM SNAP in cell-free chambers containing PBS.

Cu_2FL2E (1 μM) was intrinsically fluorescent and the addition of SNAP concentration-dependently increased fluorescence, both in rate of increase and magnitude (**Figure 3.3.2 A**). A 6.5 ± 1.0-fold increase in fluorescence was observed to 10 μM SNAP (**P = 0.0012 vs 1 μM SNAP; n = 3; **Figure 3.3.2 B**). To establish whether a working ratio of 1:2 was limiting for fluorescence, it was increased to 1:5 and 1:10 (**Figure 3.3.2 C**). No significant differences were observed between working ratios of 1:2. 1:5 or 1:10 (**Figure 3.3.2 D**), suggesting an optimal working ratio of 1:2 for Cu_2FL2E fluorescence. This had the advantage of limiting the levels of free and potentially damaging Cu^{2+}. Similar Cu_2FL2E responses to 10 μM SNAP were observed in gassed Krebs-buffered solution (5.0 ± 1.0-fold increase; n = 5; **Figure 3.3.2 E**). The increased response to SNAP in the presence of 10 μM Cu^{2+} can be explained by an increase in the relative amount of FL2E bound to Cu^{2+} or an increase in the amount of NO generated from SNAP.

DAR-4M AM (5 μM) was also intrinsically fluorescent, however, addition of SNAP alone had little effect on fluorescence (**Figure 3.3.3 A**). A small 1.3 ± 0.1-fold increase in fluorescence was observed to 10 μM SNAP (**Figure 3.3.3 B**). Raising [Cu^{2+}] to 2 μM and 10 μM increased the fluorescence response of DAR-4M AM to 10 μM SNAP (**Figure 3.3.3 A and B**), indicating that Cu^{2+} facilitates the release of NO from SNAP. A similar effect was also observed in gassed Krebs-buffered solution at 37°C, where 1 μM Cu^{2+} enabled the NO dye to respond to 10 μM SNAP (***P = 0.0004 vs Cu^{2+}-free; n = 3; **Figure 3.3.3 C**).

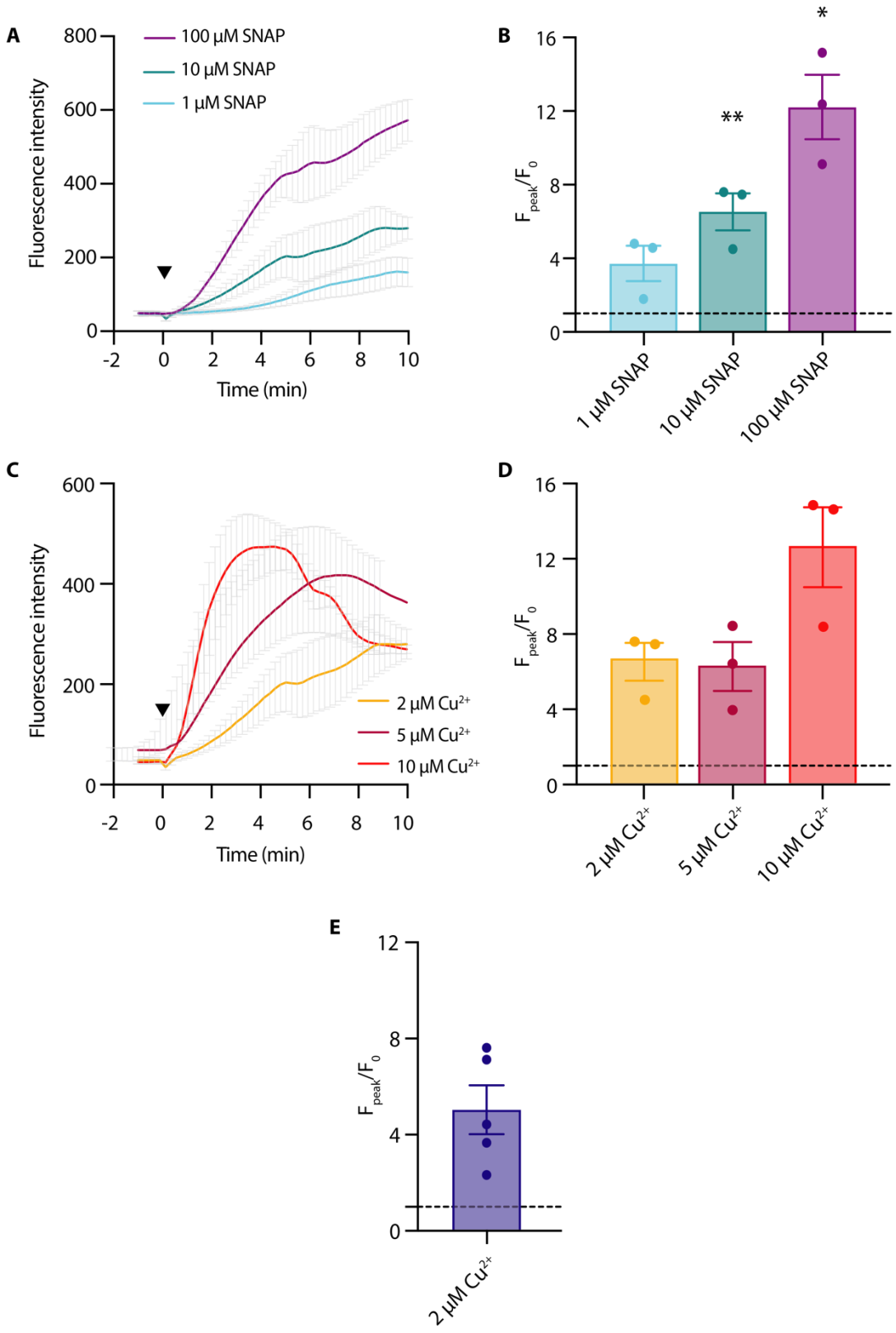
A
100 µM SNAP
10 µM SNAP
1 µM SNAP
Fluorescence intensity
Time (min)
B
F_peak/F_0
1 µM SNAP
10 µM SNAP
100 µM SNAP
C
2 µM Cu2+
5 µM Cu2+
10 µM Cu2+
Fluorescence intensity
Time (min)
D
F_peak/F_0
2 µM Cu2+
5 µM Cu2+
10 µM Cu2+
E
F_peak/F_0
2 µM Cu2+

Figure 3.3.2. Cu_2FL2E response to SNAP in a cell-free set up. Time course (**A**) and summary (**B**) of concentration-dependent increases in Cu_2FL2E fluorescence in response to SNAP. Cu_2FL2E was used at 1 μM, working ratio 1:2, in PBS at 25ºC. SNAP was added to the chamber at t = 0 mins (black arrowhead). n = 3. **P =0.0012 and *P = 0.0361 for 10 μM and 100 μM vs 1 μM SNAP, respectively, using repeated measures one-way ANOVA with Bonferroni's correction. Time course (**C**) and summary (**D**) of the effect of [Cu^{2+}] on Cu_2FL2E fluorescence in response to 10 μM SNAP. Cu_2FL2E was used at 1 μM, working ratios 1:2, 1:5 and 1:10 in PBS at 25ºC. SNAP was added to the chamber at t = 0 mins. n = 3. P = 0.0955 and P = 0.0823 for 2 μM and 5μM Cu^{2+} vs 10 μM Cu^{2+}, using ordinary one-way AVOVA with Bonferroni's correction. (**E**) Effect of 2 μM Cu^{2+} on Cu_2FL2E fluorescence in response to 10 μM SNAP in gassed (21% O_2, 5% CO_2, and 74% N_2) Krebs-buffered solution at 25ºC. n = 4-6. All data are means ± SEM. These experiments were performed by PhD students Lucy Donovan and Aaron Johnston.

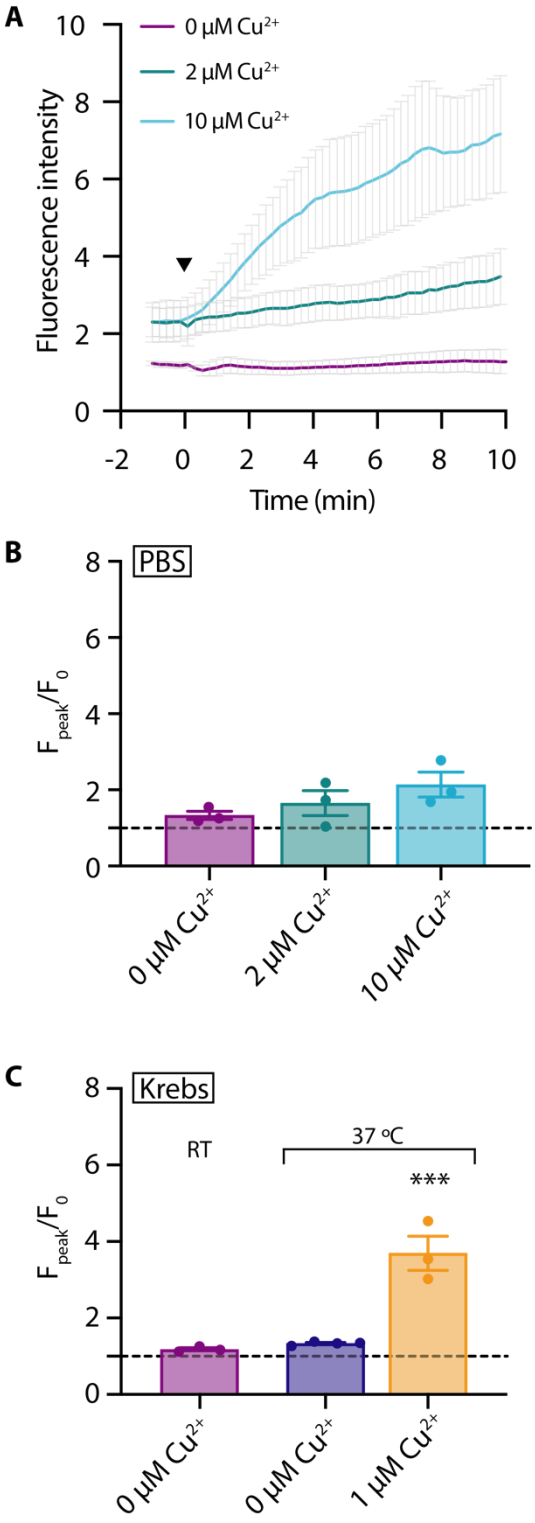
A
0 μM Cu2+
2 μM Cu2+
10 μM Cu2+
Fluorescence intensity
Time (min)
B
PBS
Fpeak/F0
0 μM Cu2+
2 μM Cu2+
10 μM Cu2+
C
Krebs
RT
37 ºC
***
Fpeak/F0
0 μM Cu2+
0 μM Cu2+
1 μM Cu2+

Figure 3.3.3. DAR-4M AM response to SNAP in a cell-free-set up. Time course (**A**) and summary (**B**) of the effect of [Cu^{2+}] on DAR-4M AM fluorescence in response to 10 μM SNAP. DAR-4M AM was used at 5 μM in PBS at 25ºC. SNAP was added to the chamber at t = 0 mins (black arrowhead). Data are means ± SEM; n = 3. P = 0.8390 and P = 0.2382 in the presence of 2 μM and 10 μM Cu^{2+} vs Cu^{2+} -free, respectively, using ordinary one-way ANOVA with Bonferroni's correction. (**C**) Effect of 10 μM SNAP and [Cu^{2+}] on DAR-4M AM fluorescence in gassed Krebs-buffered solution at either 25ºC or 37ºC. In all experiments, 5 μM SNAP was added to the chamber for 10 mins. Data are means ± SEM; n = 3-4. ***P = 0.0004 in the presence of 1 μM Cu^{2+} at 37ºC vs 0 μM Cu^{2+} at 25ºC and 37ºC, using ordinary one-way ANOVA with Bonferroni's correction. These experiments were performed by PhD students Lucy Donovan and Aaron Johnston.

3.3.3 Response of Cu_2FL2E and DAR-4M AM to ACh and SNAP in pressurised arteries

After confirming that both Cu_2FL2E and DAR-4M AM can respond to NO released from SNAP, the ability of each dye to load into pressurised mesenteric arteries was tested.

Loading mesenteric arteries with AF and Cu_2FL2E resulted in strong labelling of the arterial elastin with both dyes, as well as labelling VSMCs (**Figure 3.3.4 A**). Importantly, before loading the dyes, there was almost no autofluorescence, but during NO dye loading, the IEL in particular displayed intense labelling. This provided a good indicator that the dye had passed through all the VSMC layers, but also meant that a large percentage of the fluorescence signal came from the elastin. Furthermore, it was essential that the NO dye was washed away thoroughly following loading, as any residual dye in the chamber would respond to SNAP, as shown in cell-free conditions (**Figure 3.3.4**).

The response to activation of eNOS was then assessed by adding the EC-dependent vasodilator ACh, followed by exposure to the NO donor SNAP. The 90-minute time course for CU_2FL2E-loaded arteries showed a constant, gradual increase in NO dye fluorescence and a relatively stable level of AF fluorescence (**Figure 3.3.4 B**). The rate of increase remained unchanged over this time course and was not augmented by addition of either 1 μM ACh or 10 μM SNAP (**Figure 3.3.4 C and D**). The increase in Cu_2FL2E, but not AF, fluorescence intensity and a lack of clear response to ACh or SNAP suggests that caution must be exercised when using this dye in intact arteries and that Cu_2FL2E is not suitable for use in pressurised mesenteric artery experiments.

In contrast to Cu_2FL2E, loading of DAR-4M AM into mesenteric arteries enabled the detection of an increase in fluorescence in response to both endogenous and exogenous NO. Loading mesenteric arteries with AF and DAR-4M AM resulted in strong arterial elastin label by both dyes, and the DAR-4M AM also labelled VSMCs (**Figure 3.3.5 A**). Similar to Cu_2FL2E, there

was no detectible autofluorescence observed before dye loading, and during loading, the IEL was intensely labelled. This again was used as a strong indication that the dye had passed through all the VSMC layers, but again also means that a large percentage of the fluorescence signal came from the elastin. As previously described, the NO dye was washed away from the artery after loading, although the likelihood of signal from extra-arterial dye in the chamber was low with DAR-4M AM (**Figure 3.3.3**).

The sequence of DAR-4M responses was matched to the Cu_2FL2E dataset. As with Cu_2FL2E, there was a constant, gradual increase in NO dye fluorescence and a relatively stable level of AF fluorescence (**Figure 3.3.5 B**). Note that at the start of the protocol (~15 minutes) a slight dip in NO dye fluorescence was consistently observed, which may represent active pumping of DAR-4M out of VSMCs. The fluorescence ratio is shown as raw data in **Figure 3.3.5 C,** and compared to t = 0 minutes in **Figure 3.3.5 D**, the latter enabling better comparisons between arteries.

When directly compared, the summary time courses for each NO dye are quite different (**Figure 3.4.6**). While in Cu_2FL2E-loaded arteries there was a significant increase to both 1 μM ACh and 10 μM SNAP, these increases did not reflect any increase beyond the gradual basal increase and were of small magnitude (**Figure 3.3.6 A and B**). In contrast, the response to SNAP was clear in DAR-4M-loaded arteries (5.3 ± 0.8-fold increase in fluorescence ratio at 60 minutes compared to 0 minutes; **P < 0.0046; n = 3; **Figure 3.3.6 A and C**). The response to 1 μM ACh was also significant as reported by DAR-4M (1.8 ± 0.2-fold increase at 30 minutes compared to 0 minutes, *P = 0.0204; n = 3), but to overcome possible gradual increases in baseline FR/FR_0, time controls were performed where no ACh was added, and the effect of eNOS blockade using L-NAME on fluorescence was measured (**Figure 3.3.7**).

Although responses to ACh were not different to the control increase in FR/FR_0, this can at least partly be accounted for by the apparent basal release of NO from arteries. Addition of L-

NAME not only prevented the increase in FR/FR_0 to ACh, but importantly also reduced the baseline increase (**0-30 minutes; Figure 3.3.7 A**). Since the response to SNAP varied between arteries and data sets, data were normalised as a percentage of the SNAP response. This additional analysis step made comparisons between arteries more reliable. In so doing, it became clear that the release of NO from arteries (combined basal and ACh-stimulated), was significantly reduced by L-NAME (*P = 0.0166; n = 5-6; **Figures 3.3.7 B and C**). This same pattern emerged when reporting the rate of fluorescence ratio increase, an index of the rate of NO release (**Figures 3.3.7 D and E**). This supports the use of DAR-4M AM in pressurised arteries, although its utility may be restricted to a short timeframe of ~30 minutes.

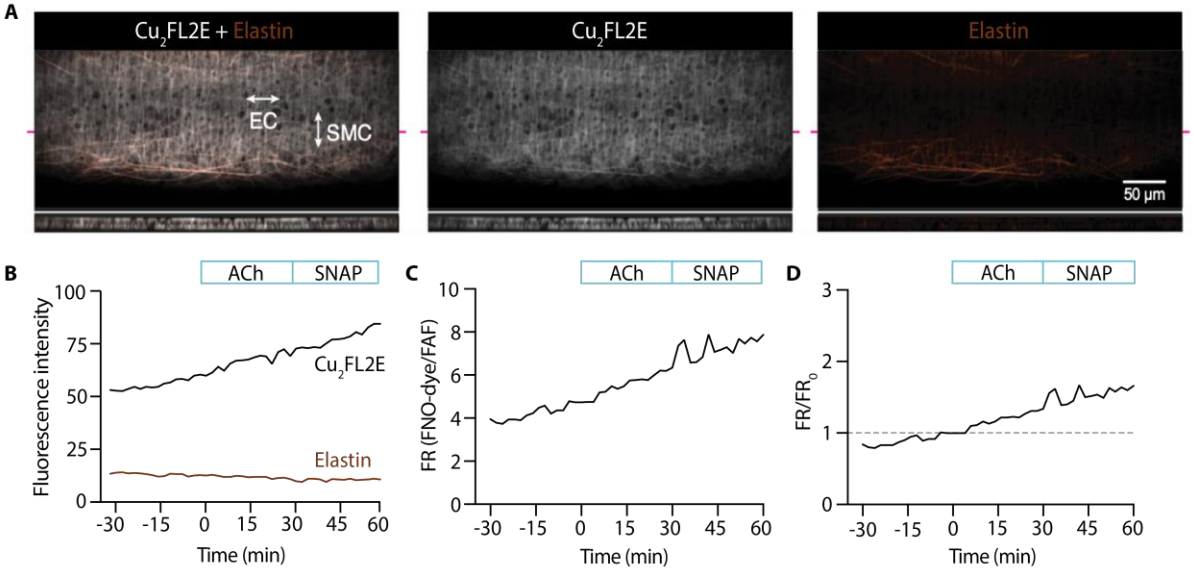

Figure 3.3.4. Cu_2FL2E response in pressurised mesenteric arteries. (**A**) Representative confocal micrographs illustrating the ability of Cu_2FL2E to load arteries. While the NO dye clearly labelled elastin (black holes visible in internal elastic lamina), smooth muscle cells (SMCs) were often visible. Cu_2FL2E was used at 2.5 µM, working ratio 1:2, in gassed Krebs-buffered solution at 37ºC. The elastin was separately labelled with Alexa Fluor 633 hydrazide (AF; 10 nM). The bottom panels are cross sections through the artery wall at points indicated by magenta lines. Multiple Z-stacks spanning 13.5 µm were merged into single XY images. (**B**) Time course of changes in Cu_2FL2E and AF fluorescence following additions of 1 µM ACh at t = 0 mins and 10 µM SNAP at 30 mins, representative of >5 experiments with slightly modified loading protocols. Time courses are also expressed as either a fluorescence ratio (FR; **C**) or FR/FR_0, where t = 0 is always 1 (dashed line; **D**). There was no clear response above the steady, gradual rise in Cu_2FL2E fluorescence observed.

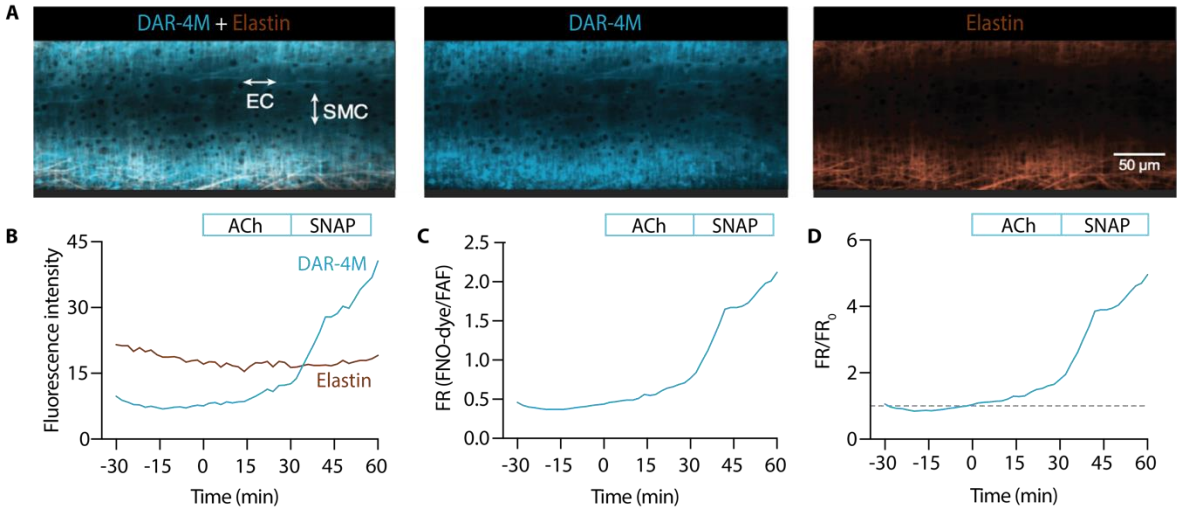

Figure 3.3.5. DAR-4M AM response in pressurised mesenteric arteries. (**A**) Representative confocal micrographs illustrating the ability of DAR-4M AM to load arteries. While the NO dye clearly labelled elastin (black holes visible in internal elastic lamina), smooth muscle cells (SMCs) were often visible. DAR-4M AM was used at 5 µM in gassed Krebs-buffered solution at 37ºC. The elastin was separately labelled with Alexa Fluor 633 hydrazide (AF; 10 nM). Multiple Z-stacks spanning 13.5 µm were merged into single XY images. (**B**) Time course of changes in DAR-4M AM and AF fluorescence following additions of 1 µM ACh at t = 0 mins and 10 µM SNAP at 30 mins, representative of >5 experiments with slightly modified loading protocols. Time courses are also expressed as either a fluorescence ratio (FR; **C**) or FR/FR_0, where t = 0 is always 1 (dashed line; **D**).

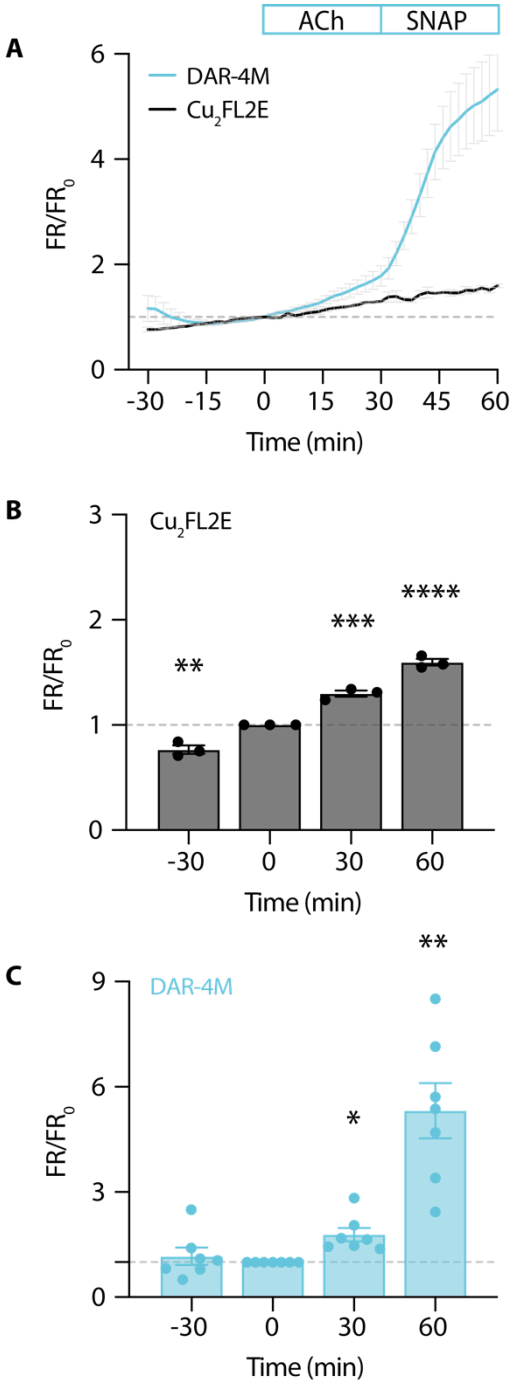

Figure 3.3.6. NO dye responses to ACh and SNAP in pressurised mesenteric arteries. Comparison of summary data for each NO dye. In all experiments 1 μM ACh was added at t = 0 mins, and 10 μM SNAP at 30 mins. (**A**) Summary data expressed as FR/FR_0 for Cu_2FL2E (n = 3) and DAR-4M (n = 7) loaded arteries. (**B**) Summary data for Cu_2FL2E. **P = 0.0015, ***P = 0.0003, and ****P < 0.0001 for t = -30 mins, 30 mins, and 60 mins vs 0 mins, respectively, using repeated measures one-way ANOVA with Bonferroni's correction. (**C**) Summary data for DAR-4M. *P = 0.0204 and **P = 0.0046 vs 0 mins, respectively, using repeated measures one-way ANOVA with Bonferroni's correction.

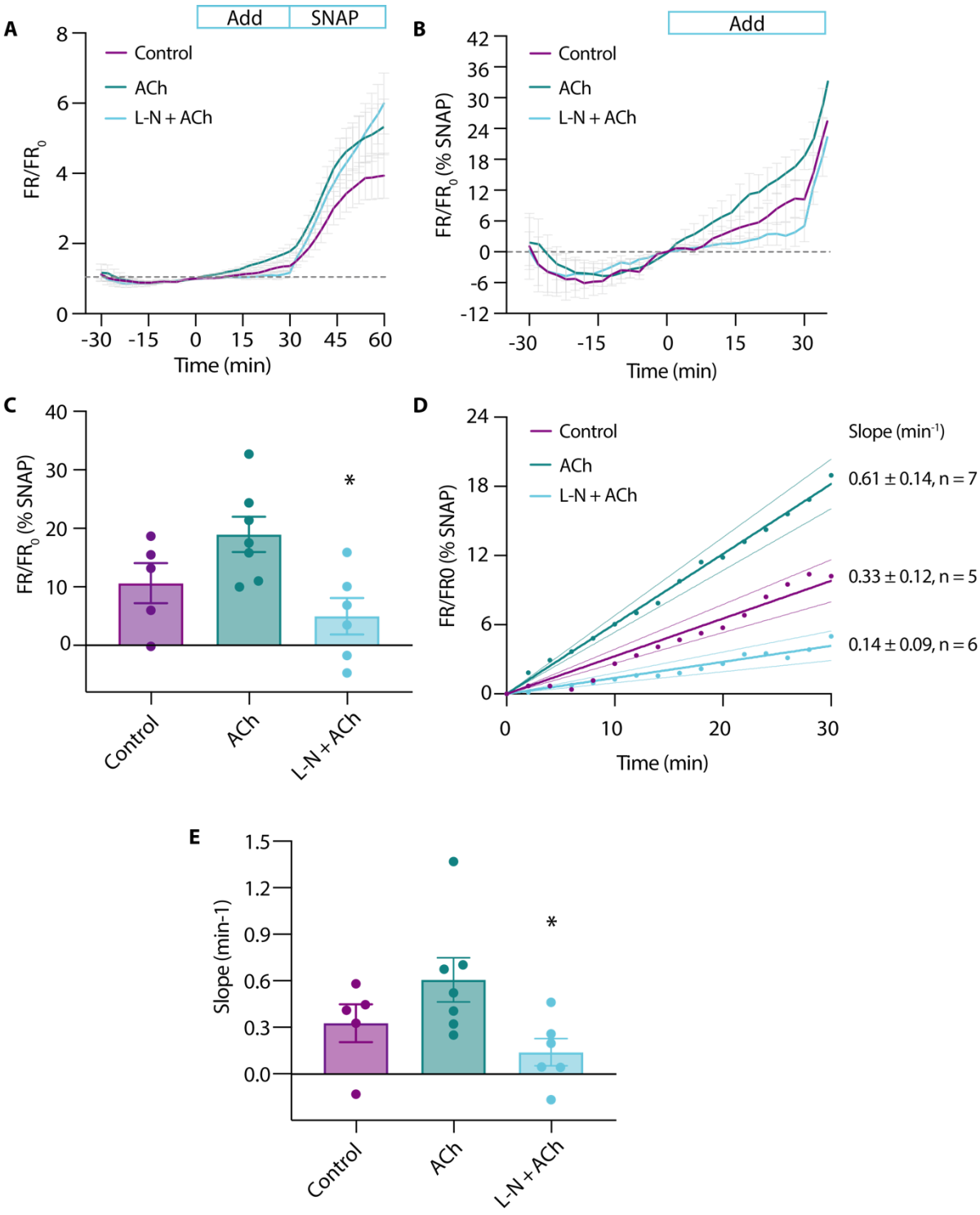
A
Add
SNAP
Control
ACh
L-N + ACh
FR/FR0
Time (min)
B
Add
Control
ACh
L-N + ACh
FR/FR0 (% SNAP)
Time (min)
C
FR/FR0 (% SNAP)
*
Control
ACh
L-N+ACh
D
Control
ACh
L-N + ACh
FR/FR0 (% SNAP)
Time (min)
Slope (min-1)
0.61 ± 0.14, n = 7
0.33 ± 0.12, n = 5
0.14 ± 0.09, n = 6
E
Slope (min-1)
*
Control
ACh
L-N+ACh

Figure 3.3.7. Summary of DAR-4M AM responses to ACh and SNAP in pressurised mesenteric arteries. In these experiments, responses to 1 μM ACh (n = 7) were compared to control (basal accumulation without ACh, n = 5), and 1 μM ACh in the presence of L-NAME (L-N; 100 μM; n = 6), each added at t = 0 mins. In all experiments, 10 μM SNAP was added at 30 mins. (**A**) Summary data expressed as FR/FR_0. (**B**) Summary data expressed as a percentage of the response to 10 μM SNAP to better normalize the responses between arteries. Add represents addition of either nothing (control), ACh, or L-N + ACh. (**C**) Summary of values at 30 mins. *P = 0.0166 vs ACh alone, P = 0.2597 for control vs ACh, and P = 0.7463 for control vs L-N + ACh, using ordinary one-way ANOVA with Bonferroni's correction. (**D**) Linear regression of individual experiments was averaged to obtain an index of the rate of NO release over the t = 0-30 min period (min^{-1}); shown with 95% confidence intervals. Values are summarized in (**E**). *P = 0.0429 vs ACh alone using ordinary one-way ANOVA with Bonferroni's correction. All data are means ± SEM.

3.3.4 Response of DAR-4M AM over an extended time course

As the ACh-evoked increase in DAR-4M fluorescence measured at 30 minutes was prevented by L-NAME, the protocol was extended to see whether this effect held over 60 minutes (**Figure 3.3.8**). This was important as future experiments using this dye would likely rely on its accuracy over longer periods. The fluorescence response of DAR-4M to stimulated NO was more pronounced 60 minutes after ACh addition (~20% increase in FR/FR_0 (% SNAP) compared to at 30 minutes after ACh addition; P = 0.5848; n = 5; **Figure 3.3.8 B**), reflecting sustained NO release over this time. Interestingly, in the presence of L-NAME, there was a significant increase in NO dye fluorescence measured 60 minutes after ACh was added, but not at 30 minutes (FR/FR_0 (% SNAP) = 42.94 for 60 minutes vs 27.65 for 30 minutes; **Figure 3.3.8 C**). This indicates that the fluorescence response of DAR-4M to ACh is only blocked by L-NAME up to 30 minutes, but by 60 minutes, fluorescence increased to similar levels to when L-NAME is not present (FR/FR_0 (% SNAP) = 42.94 for L-NAME and 57.44 for control). This may reflect incomplete inhibition of eNOS by L-NAME, where NO is still produced, albeit more slowly than under control conditions. Further experiments are required to investigate the reason for this unexpected increase in fluorescence.

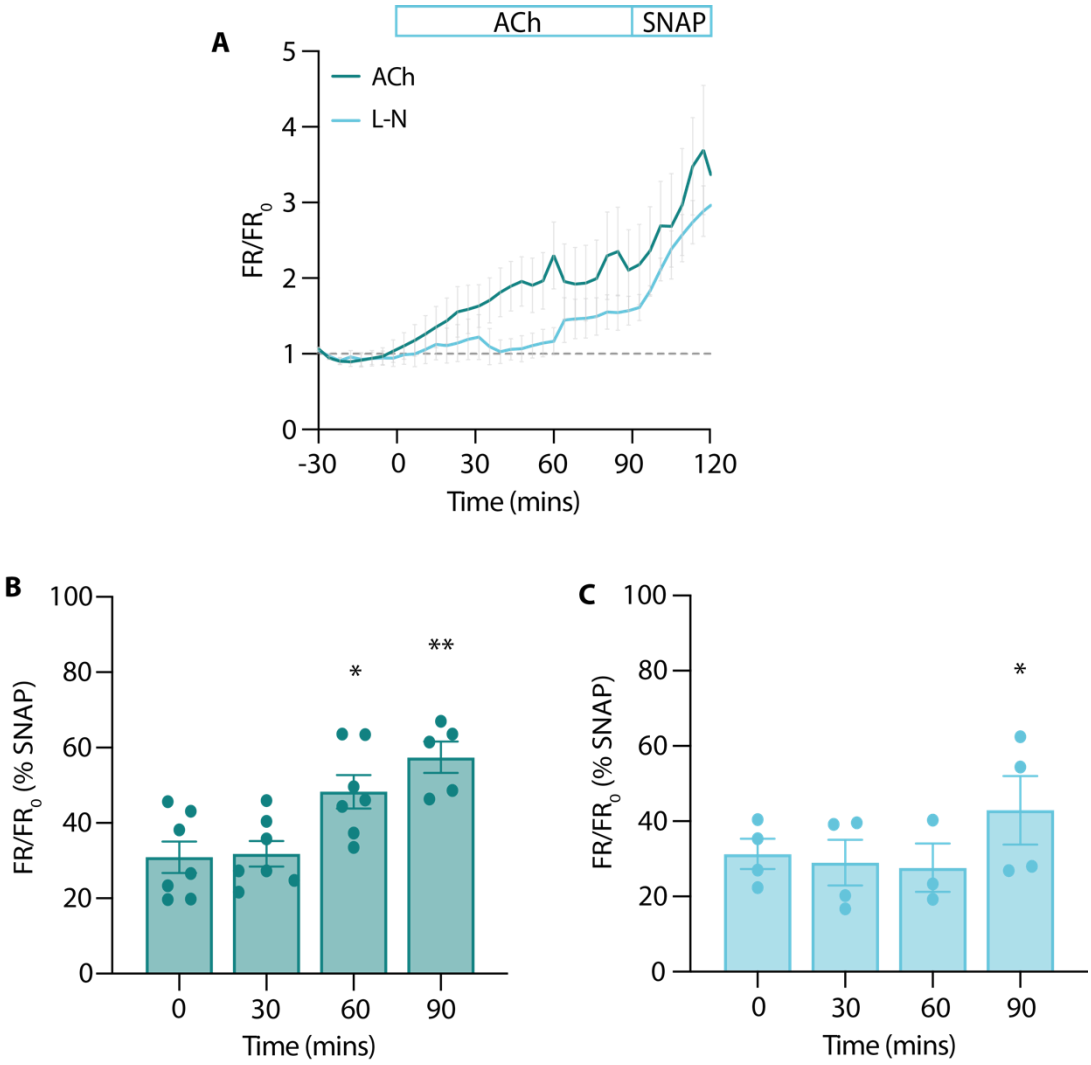

Figure 3.3.8. DAR-4M AM response to ACh and SNAP in pressurised mesenteric arteries over an extended time course. (**A**) In these experiments, responses to 1 μM ACh were compared in the presence (n = 3-4) and absence of L-N (L-NAME; 100 μM; n = 5-7) over 90 mins, where ACh was added at t = 0 mins. In all experiments, 10 μM SNAP was added at t = 90 mins. (**B**) Summary data expressed as FR/FR_0 as a percentage of the response to SNAP for DAR-4M fluorescence response to ACh at 0, 30, 60, and 90 mins. *P = 0.0291 vs 30 mins and **P = 0.0014 vs 30 mins, using repeated-measures one-way ANOVA with Bonferroni's correction. (**C**) Summary data expressed as FR/FR_0 as a percentage of the response to SNAP for DAR-4M fluorescence response to ACh in the presence of L-N, at 30, 60, and 90 mins. *P = 0.0307 vs 30 mins and P > 0.9999 for 30 vs 60 mins, using repeated-measures one-way ANOVA with Bonferroni's correction. All data are means ± SEM.

3.3.5 Response of DAR-4M AM and Cu_2FL2E to ACh and SNAP in *en face* arteries

Finally, to ensure the insensitivity of Cu_2FL2E to NO was a result of the dye rather than ineffective cell loading, an alternative method of imaging intact arteries was used. Arteries were cut longitudinally to expose the ECs and mounted in a custom-made imaging chamber, allowing ECs and VSMCs to be imaged with the ECs *en face* (**Figure 3.3.9**). Following the same sequence of NO dye responses as in pressurised arteries, it was clear than even with visible ECs, the Cu_2FL2E was unresponsive to either ACh or SNAP, yet DAR-4M was (**Figures 3.3.9 B – D**). While this confirmed that both indicators could be loaded into ECs and VSMCs, it shows that intracellular or elastin-bound Cu_2FL2E did not respond to increased [NO] and this NO dye should not be used in future experiments.

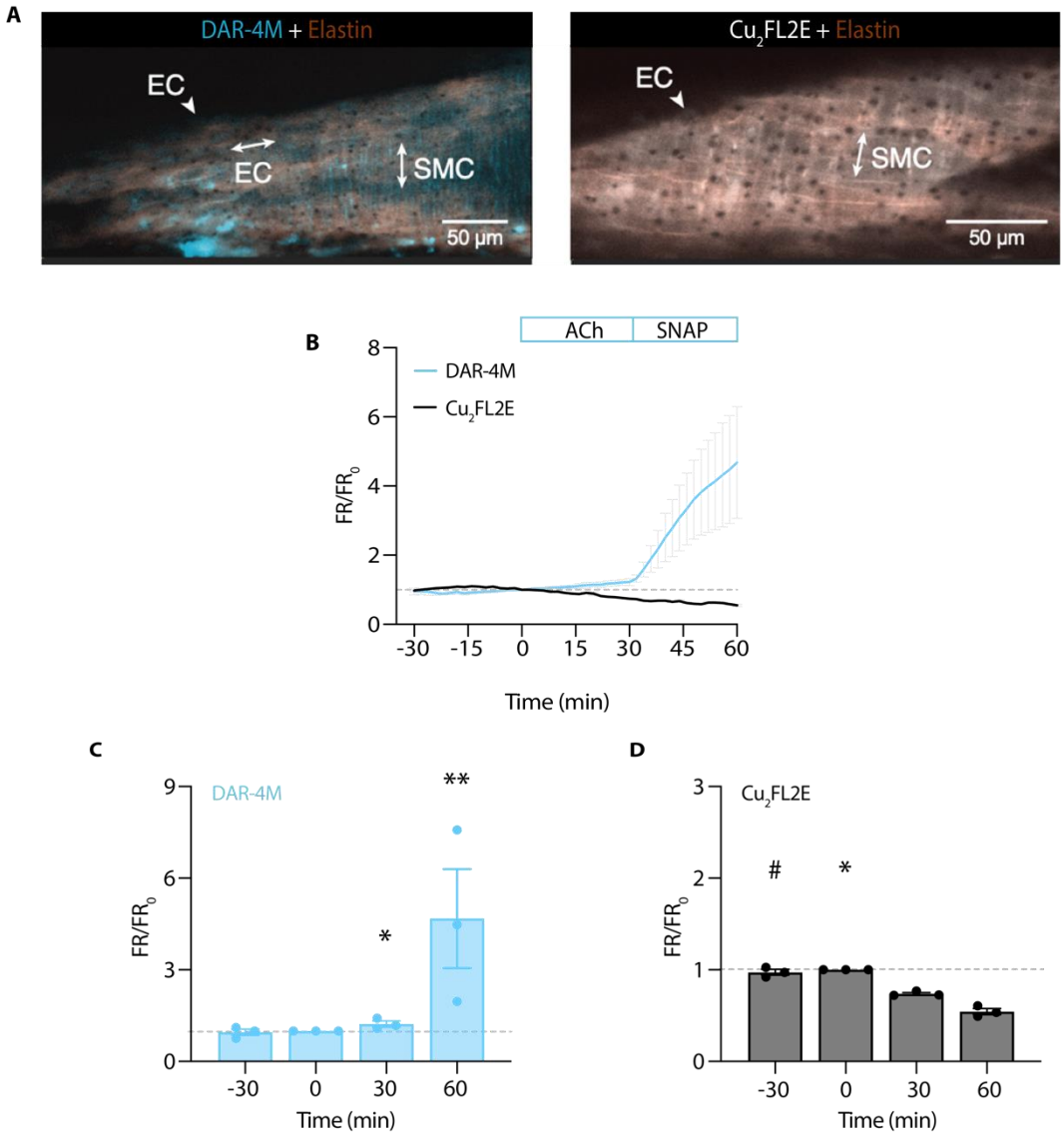

Figure 3.3.9. NO dye response to ACh and SNAP in *en face* mesenteric arteries. Representative confocal micrographs illustrating the ability of DAR-4M AM (5 µM) and Cu_2FL2E (2.5 µM, working ratio 1:2) to load arteries in gassed Krebs-buffered solution at 37ºC (**A**). The elastin was labelled with Alexa Fluor 633 hydrazide (AF; 10 nM). Multiple Z-stacks spanning 13.5 µm were merged into single XY images. (**B**) Summary data expressed as FR/FR_0 for DAR-4M AM (n = 3) and Cu_2FL2E (n = 3). (**C**) Summary data for DAR-4M AM. *P = 0.0204 and **P = 0.0046 vs 0 mins using repeated measures one-way ANOVA with Bonferroni's correction. (**D**) Summary data for Cu_2FL2E. #P = 0.0420 vs 60 mins, *P = 0.0188 and *P = 0.0313 vs 30 and 60 mins, respectively, using repeated measures one-way ANOVA with Bonferroni's correction. All data are means ± SEM.

3.4 Discussion

The present study proposes a simple and reproducible protocol for the use of a NO indicator, DAR-4M AM, in pressurised, *ex vivo* arteries. Our comparison of DAR-4M AM with Cu_2FL2E in both cell-free chambers and live mesenteric arteries illustrates the importance of validating the characteristics of the fluorescence NO dye used. We found that while both DAR-4M AM and Cu_2FL2E responded to NO released from SNAP, only DAR-4M responded to endogenous NO produced by ECs.

Although there are many experimental NO donors available, including sodium nitroprusside and SIN-1, we chose SNAP because of its widespread use in research associated with a well-characterised temporal release profile (Feelisch, 1991; Simonsen *et al.*, 1999; Ghosh *et al.*, 2013). SNAP releases NO at a controlled rate, with one estimation claiming 1.4 μM NO is released from 100 μM SNAP per minute, in PBS at 37°C and pH 7.4 (Feelisch, 1991). The relationship between [SNAP] and [NO] is complicated; NO release kinetics are highly sensitive to factors including transition metal ions (such as Cu^{2+}), free thiols, pH, and redox products (He and Frost, 2016). As such, it is difficult to accurately quantify the amount of NO released from 10 μM SNAP in our experiments. Nevertheless, we used 10 μM SNAP as a positive control as it produced maximal vasodilation in isometrically mounted mesenteric arteries and corresponds to physiological [NO] reported in arteries (Simonsen *et al.*, 1999). Using microelectrodes to record NO production in RMAs, Simonsen *et al.* found that 10 μM SNAP caused relaxation and yielded a maximum NO concentration of 19 nM.

The use of NO donors to characterise Cu_2FL2E in cell-free systems is established (McQuade *et al.*, 2010; Ghosh *et al.*, 2013) and our data support these findings. The ability of Cu^{2+} to enhance the responses to SNAP is of interest when using this dye as both the working ratio of FL2E to Cu^{2+} and the Cu^{2+} freed upon binding of NO to FL2E will affect the final magnitude

of response to SNAP. Interestingly, while the response to SNAP is clear, the nitroxyl-donor Angeli's salt did not affect Cu_2FL2E fluorescence (McQuade *et al.*, 2010), suggesting that Cu_2FL2E is selective for the free radical form of NO (NO•). Responses to DAR-4M AM in cell-free preparations have also been characterised (Kojima *et al.*, 2001; Lacza *et al.*, 2005). This dye did not respond to Angeli's salt (Lacza *et al.*, 2005), suggesting that DAR-4M AM is also selective for NO•. This is a limitation of DAR-4M AM, as it does not report EC release of other physiologically relevant nitrogen species, such as HNO, which is known to be released from mesenteric artery ECs upon stimulation by ACh (Yuill *et al.*, 2011). An ability to detect both forms of NO would therefore be an advantage in elucidating the relative functional importance of NO• and HNO in arteries. Additionally, the data presented herein suggests that the AM groups of DAR-4M may reduce responses to SNAP (**Figure 3.3.3 and 3.3.5**). Interestingly, addition of Cu^{2+} improved SNAP responses (**Figure 3.3.3 A**), which could reflect increased NO release from SNAP or perhaps a modification of the esterified dye to improve fluorescence upon binding of NO.

When used in cells previously, Cu_2FL2E was able to respond to agonists. In the original study by McQuade *et al.,* isolated cells and olfactory bulb slices responded to applied NO-producing agents, when using 1-5 μM Cu_2FL2E at a working ratio of 1:2 with Cu^{2+} (McQuade *et al.*, 2010). Moving to arterial cells, Ghosh *et al*. used 20 μM Cu_2FL2E (working ratio 1:2) to load ECs in culture and reported a ~4-fold increase in fluorescence in response to 10 μM ACh, which was effectively abolished by 100 μM L-NAME (Ghosh *et al.*, 2013). In the same study, again using 20 μM, Cu_2FL2E clearly loaded mouse carotid artery ECs and VSMCs, and 10 μM ACh dilated the arteries and increased fluorescence signal. The relaxation and fluorescence increase were both blocked by L-NAME. While these data seem convincing, the high concentrations of Cu_2FL2E (20 μM) and Cu^{2+} (40 μM) cannot be used in RMAs for multiple reasons. First, the high concentration of DMSO and pluronic used would activate EC Ca^{2+} and hence eNOS, during the loading protocol. We specifically used the lowest concentration of DMSO possible (<0.4%), as high concentrations of DMSO increase

mesenteric artery EC Ca^{2+} (unpublished data from Dora/Garland group). This is especially relevant when using NO dyes since the binding of NO to the dye is not reversible. Therefore, in our hands using 8-times more DMSO was not feasible, but we do appreciate that different vascular beds may have different sensitivities to DMSO. Second, the use of 40 μM Cu^{2+} is highly likely to cause arterial damage. Even under the assumption that all Cu^{2+} is bound to FL2E at the start of experiments (working ratio 1:2), as soon as NO displaces Cu^{2+} from FL2E the levels of Cu^{2+} could rapidly increase beyond 5 μM which we have shown is toxic to both ECs and VSMCs (**Figure 3.3.1 B** and **C**). Our observation that Cu^{2+} impairs the function of wire-mounted RMAs remains unexplained but may reflect a pro-oxidant effect, resulting in the generation of harmful free radicals. Finally, our decision not to use Cu_2FL2E in RMAs followed the observation that Cu_2FL2E generated a very clear and intense label of elastin, and while this signal increased over time, it was not enhanced further by either ACh or SNAP (**Figure 3.3.4 B**). We suggest the binding of Cu_2FL2E to elastin likely interferes with the ability of Cu_2FL2E to bind NO. This is in addition to the fundamental failure of not detecting any response to either ACh or SNAP within loaded ECs or VSMCs. These data suggest the use of Cu_2FL2E in pressurised resistance arteries is not a reliable way to assess NO generation by ECs.

The data presented herein indicate that DAR-4M AM is suitable to detect NO production by ECs in healthy mesenteric arteries. The rate of increase in fluorescence to 1 μM ACh was slow compared to 10 μM SNAP, but both the basal release and that stimulated by ACh could be detected (**Figure 3.3.5**, **3.3.6 A** and **3.3.7**). The NO detection threshold for DAR-4 AM is reported as 7 nM (Kojima *et al.*, 2001), suggesting that this dye should be sufficiently sensitive to detect physiological NO in the nanomolar rage. Moreover, our finding that L-NAME blocks the increase in DAR-4M (DAR-4M T) fluorescence following ACh addition (at 30 minutes only) suggests that the indicator is specific in detecting NO (**Figure 3.3.7**). It is important to note that DAR-4M does not directly bind to NO, and instead binds to NO^+ equivalents such as nitric anhydride (Kojima *et al.*, 2001). These equivalents are produced from the rapid auto-oxidation

of NO; therefore, this NO dye can only indirectly reflect NO levels. Nevertheless, the response to SNAP was marked, more so than in the cell-free chambers. This may reflect intracellular Cu^{2+} more effectively releasing NO from SNAP and/or a supra-additive effect of SNAP with other reactive oxygen species (Lacza *et al.*, 2005), many of which would be present within cells. The optimisation of a protocol to use an NO dye in arteries was our initial aim, and an enhanced response within cells present is an advantage. It does, however, underly the importance of checking cell viability and keeping experimental conditions as consistent as possible (e.g., laser intensity, dye loading, and pH), as cellular damage (as seen in many vascular diseases) is associated with increased levels of reactive oxygen species.

The detection of NO following 60 minutes of continuous stimulation with ACh, even in the presence of 100 μM L-NAME, highlights the incomplete inhibition of eNOS by L-NAME over extended periods (**Figure 3.3.8**). Evidence for incomplete eNOS inhibition by L-NAME is provided by Cohen *et al*., who found that L-NAME (30 μM) only partially reduced NO release in *en face* rabbit carotid arteries (Cohen *et al.*, 1997). Other studies show that L-NAME's inhibitory effect on eNOS can decrease over time (Pechanova *et al.*, 2020), and that L-NAME itself slowly releases NO *in vivo* (Liu *et al.*, 2019). Taken together, this may explain why in pressurised arteries, DAR-4M AM detected NO at 60 minutes but not at 30 minutes after ACh addition in the presence of L-NAME, as endogenous and exogenous NO gradually accumulated. Whilst the present study supports the notion that L-NAME incompletely inhibits eNOS, and may even release NO, it should be recognised that this phenomenon is highly variable and may not be common across all species and vascular beds (Kopincova *et al.*, 2012). Further experiments should be conducted to investigate this further using higher concentrations of L-NAME as well as alternative eNOS inhibitors.

Finally, there is scope to further optimise the method presented above and ultimately enable the use of DAR-4M AM in other vascular beds. First, minimising movement artefacts will allow [NO] to be compared within difference arterial cell types. Our method allows ECs to be

distinguished from VSMCs in both pressurised and *en face* preparations (**Figure 3.3.5 A and 3.3.9 A**). However, the movement of arteries during imaging makes measuring fluorescence within specific cells a challenge. Pressurised and *en face* artery experiments were conducted in the presence of nifedipine to minimise movement artefacts. Nifedipine cannot be used in experiments to establish whether basal NO release occurs normally in arteries with myogenic tone or during vasoconstriction. By blocking VSMC L-type VGCCs, nifedipine would prevent indirect activation of ECs by increased VSMC [Ca^{2+}] (Garland *et al.*, 2017), signalling that may contribute to or even explain the basal release of NO. Instead, alternative approaches such as midplane imaging using 2 photon lasers could be characterised, retaining the use of AF to indicate the elastin signal. This method could then be used to elucidate mechanisms of NO production in myogenic coronary and cerebral arteries which contract to L-NAME (Szekeres *et al.*, 2004; McNeish *et al.*, 2005). Investigating the fundamental properties of artery function, including NO production, is essential in understanding how healthy arteries work and how this is altered in disease states. As such, the technique described herein provides potential to explore different aspects of vascular functionality.

For the visualisation of ECs in this study, we used an *en face* method for continuous live-cell imaging in arteries (**Figure 3.3.9**). Although this preparation is not as physiological as pressure myography, *en face* mounting offers many benefits. It allows arteries, even those with microscopic side-branches, to be quickly and easily mounted, and allows homogenous populations of ECs or VSMCs to be visualised at high magnification. This makes the *en face* method of mounting arteries a valuable tool to use with many fluorescent indicators.

3.5 Conclusions

This study has established a robust protocol for using DAR-4M AM as a NO indicator in pressurised, *ex vivo* arteries, addressing an important gap in vascular research. Our comparative analysis of DAR-4M AM and Cu_2FL2E in both cell-free systems and live mesenteric arteries underscores the importance of rigorous validation when selecting NO dyes for experimental use. The findings demonstrate that DAR-4M AM exhibits superior performance in detecting endogenous NO produced by ECs, while Cu_2FL2E's utility is limited. DAR-4M AM was able to detect both basal and stimulated NO release in live mesenteric arteries, and further optimisation of this protocol will aid research into the significance of basal vs stimulated NO release.

4. The Role of T-type Voltage-Gated Calcium Channels in Vasodilation in Rat Resistance Arteries

4.1 Introduction

It is widely accepted that both L- and T-type VGCCs are expressed by VSMCs of resistance arteries, their opening resulting in Ca^{2+} influx and tension development in response to depolarisation. Whilst the functional role of L-type VGCCs has long been recognised, the importance of T-type VGCCs has only recently gained attention. Evidence suggests that although Ca^{2+} influx via L-type VGCCs is essential to achieve sustained vasoconstriction in larger conduit arteries, T-type channels become increasingly important as artery diameter decreases (Knot and Nelson, 1998; Gustafsson *et al.*, 2001). This is due to their increased expression in smaller arteries and the possible presence of splice variants with right-shifted current-voltage curves, making T-type VGCCs likely candidates for underpinning Ca^{2+} entry into VSMCs of resistance arteries. The ability of T-type VGCCs to meaningfully contribute to the tone of resistance arteries is surprising due to their tiny and transient Ca^{2+} currents. Despite this, it has been suggested that VSMC T-type channels cause vasoconstriction by increasing intracellular [Ca^{2+}] directly (Morita *et al.*, 1999), although their indirect action in elevating intracellular [Ca^{2+}] has also been recognised (Garcia and Beam, 1994; El-Lakany *et al.*, 2023). Recently, a role for VSMC T-type VGCCs in vasodilation has emerged, which is the focus of this chapter.

Recent studies suggest that Ca^{2+} influx through T-type VGCCs may activate signalling pathways which produce vasodilation. Of particular interest is the functional interaction between VSMC $Ca_V3.2$ channels and RyRs/BK_{Ca} channels, which has been shown to attenuate vasoconstriction in rat cerebral and mouse mesenteric resistance arteries (Harraz *et al.*, 2014a; Harraz *et al.*, 2015). Selective blockade of $Ca_V3.2$ channels with Ni^{2+} (50 μM) resulted in vasoconstriction and reduced Ca^{2+} spark frequency in pressurised arteries, and separate application of BK_{Ca} channel blocker paxilline evoked vasoconstriction equivalent, but not additive, to Ni^{2+} (Harraz *et al.*, 2014a). This suggests that $Ca_V3.2$ channels paradoxically

oppose vasoconstriction by triggering Ca^{2+} sparks which activate hyperpolarising STOCs via BK_{Ca} channels (see **Figure 1.3.2** for diagram).

This axis, however, does not appear to be a ubiquitous feature of all resistance arteries. The application of Ni^{2+} (30 μM) to pressurised murine superior epigastric arteries produced vasoconstriction which was not attenuated by pre-incubation with paxilline, indicating that $Ca_V3.2$ channels operate independently of BK_{Ca} channels in these arteries (Mullan *et al.*, 2017). Furthermore, attempts to replicate Harraz *et al.*'s findings in mouse mesenteric arteries yielded similar results: Ni^{2+} induced vasoconstriction even in the presence of paxilline, suggesting that BK_{Ca} channel activation is not obligatory in $Ca_V3.2$-mediated vasodilation. The conflicting findings may be due to the difference in arterial diameters of the mouse mesenteric arteries used by the two groups; Harraz *et al*. used third and fourth order arteries, whereas Mullan *et al.* used second and third order arteries. Whilst this implies that Harraz *et al.* used narrower arteries, it is not conclusive, as neither publication includes absolute diameter measurements nor details of how the branches of the mesenteric arcade were counted. This lack of consensus means that additional work is required to understand the importance of the $Ca_V3.2$/RyR/BK_{Ca} axis. To date, there have been no studies on T-type VGCC microdomain signalling in coronary resistance arteries, despite the critical role of the coronary microcirculation in meeting the myocardium's oxygen demands.

Given the potentially fatal consequences of excess vasoconstriction in coronary arteries, it follows that multiple parallel mechanisms may exist to prevent it from occurring, likely involving depolarisation-activated VGCCs. Indeed, the expression of VGCCs by ECs has been extensively investigated due to their potential role in stimulating NO synthesis. Early experiments using patch-clamp electrophysiology to measure Ca^{2+} currents in cultured conduit artery ECs found no evidence for VGCC expression (Takeda *et al.*, 1987; Daut *et al.*, 1988), however T-type currents were observed in cultured ECs from capillaries (Bossu *et al.*, 1989). The first evidence of T-type VGCCs in native ECs came from Braunstein *et al.* (2009), who

identified $Ca_V3.2$ channels in rat mesenteric arteries using immunohistochemistry. Expression of $Ca_V3.2$ channels in the endothelium of intact rat cerebral arteries was soon confirmed by Kuo *et al.* (2010), who also reported the presence of $Ca_V3.1$ channels. Due to the Ca^{2+}-dependence of eNOS, it is possible that the contribution of T-type VGCCs to EC [Ca^{2+}] may lead to NO production and subsequent vasodilation. Notably, this has been demonstrated in mice, where ACh-mediated vasodilation was significantly impaired in $Ca_V3.1^{-/-}$ and knockouts compared to wild-type controls (Gilbert *et al.*, 2017). The expression of VGCCs by ECs remains a contentious issue, however, requiring further investigation using native cells from wild-type animal models.

In addition to promoting vasodilation by directly facilitating Ca^{2+} influx into ECs, T-type VGCCs expressed by coronary artery VSMCs may also contribute to endothelium-dependent vasodilation via myoendothelial feedback. The role of VSMC VGCCs in feedback vasodilation has been demonstrated in rat skeletal muscle arterioles, where Ca^{2+} entering via L-type VGCCs diffused into adjacent ECs through MEGJs, leading to the generation of EDH (Garland *et al.*, 2017). A similar phenomenon has been suggested to occur in porcine coronary arteries, although the precise mechanisms, including the potential involvement of VGCCs, remain unclear (Budel *et al.*, 2001).

Should future research find that the vasodilatory influence of specific T-type channel isoforms is widespread, especially in the vasculature supplying the heart, it may have important implications for the therapeutic use of selective T-type VGCC blockers. If blocking these channels does indeed reduce BK_{Ca} channel-driven VSMC hyperpolarisation and endothelium-dependent vasodilation *in vivo,* excess vasoconstriction may occur as a side effect. Systemically, this would elevate total peripheral resistance and initiate or exacerbate hypertension. Alternatively, if the vasodilatory effect of T-type channels is vascular-bed specific, inhibitors could restrict blood flow to vital organs, resulting in, for example, chronic kidney disease, pulmonary hypertension, or stroke. In the heart, this could induce angina,

myocardial ischaemia, or myocardial infarction, possibly resulting in death. Due to this, it is important to gain a better understanding of T-type VGCCs, especially in coronary resistance vessels.

4.1.1 Aims and hypotheses

It was hypothesised that T-type VGCCs could be involved in vasodilation of rat coronary resistance arteries following on from previous reports from small arteries from a range of vascular beds.

To address this hypothesis, it was first necessary to investigate the expression profile of the 3 T-type VGCC subtypes in rat coronary arteries before probing any functional effects due to channel activation. The investigation primarily focused on coronary arteries due to their clinical relevance with mesenteric arteries included for comparison as peripheral resistance arteries.

The aims of the present study were as follows:

i. To characterise the expression of T-type VGCCs in ECs and VSMCs of rat mesenteric and coronary arteries at the mRNA and protein level.

ii. To determine whether T-type VGCCs influence arterial tension in coronary arteries using a mechanism involving myoendothelial feedback and/or endothelium-dependent vasodilation.

iii. To identify whether the VSMC $Ca_V3.2$/RyR/BK_{Ca} channel signalling microdomain exists in rat coronary resistance arteries.

4.2 Materials and methods

4.2.1 RNAscope

RNAscope was used to detect and quantify T- and L-type VGCC mRNA expression in mesenteric and coronary arteries, as described in Section 2.7. Arteries were fixed whilst isometrically stretched on a wire myograph, where they were normalised to a resting tension equivalent to that generated at 90% of the diameter of the artery at 70 mmHg (mesenteric) or 80 mmHg (coronary). Arteries were imaged as described in Section 2.7.2. The method used to determine the nuclear: cytoplasmic localisation of mRNA transcripts is detailed in Section 2.7.3.

4.2.2 Immunohistochemistry

Immunohistochemistry was used to detect protein-level expression of T-type VGCCs in mesenteric and coronary arteries (see Section 2.6). Arteries were fixed either on a wire myograph (see Section 2.2) or whilst pressurised (see Section 2.3). In pressure myography experiments, intraluminal pressure was set to 70 mmHg (mesenteric) or 80 mmHg (coronary).

The following antibodies were used to label VGCCs:

Target protein	Primary antibody	Immunogen
$Ca_V1.2$	• Alomone ACC-003 • Polyclonal • Raised in rabbit • 2 µg/mL	Amino acid residues 848-864 of rat $Ca_V1.2$, intracellular linker connecting domains II and III
$Ca_V3.1$	• Alomone ACC-021 • Polyclonal • Raised in rabbit • 2 µg/mL	Amino acid residues 1-22 of rat $Ca_V3.1$, N-terminus
$Ca_V3.2$	• Sigma C1868 • Polyclonal • Raised in rabbit	Amino acid residues 581-595 of rat $Ca_V3.2$, intracellular linker connecting domains I and II

	• Unknown concentration, diluted 1:800	
$Ca_V3.3$	• Alomone ACC-009 • Polyclonal • Raised in rabbit • 1.87 µg/mL	Amino acid residues 1053-1067 of rat $Ca_V3.3$, intracellular linker connecting domains II and III

The same secondary antibody was used for all 4 channels, which was a polyclonal anti-rabbit IgG antibody raised in goat and conjugated to Alexa Fluor 633 (2 µg/mL; A21070, Invitrogen; excitation wavelength = 633 nm, emitted light detected at ≥ 650 nm). A polyclonal IgG antibody raised in goat against mouse/rat CD31 and conjugated to Alexa Fluor 488 was used as an EC marker (2 µg/mL; FAB3628G, Biotechne; excitation wavelength = 488 nm, emitted light detected at ≥ 545 nm). AlexaFluor 633 Hydrazide was used to visualise elastin (1 µg/mL; Thermo Scientific; excitation wavelength 517 nm, emitted light detected at ≥ 490 nm). Arteries were imaged as described in Section 2.6.3.

Calcein AM (3 µM; C3100MP, Invitrogen, USA) was used to visualise MEPs in pressurised mesenteric arteries as described in Section 2.4.3. MEPs were classified as areas of intense fluorescence overlapping with a perforation in the IEL, and empty holes were classified as perforations in the IEL which did not contain an area of intense fluorescence.

4.2.3 Western blotting

The antibodies used for T-type VGCC immunolabeling were validated using western blotting (see Section 2.8). 10 µg of protein lysate from RMAs and rat brain were loaded into polyacrylamide gels (4-12%) for separation by electrophoresis. Membranes were incubated for 2 hours at room temperature with primary antibodies (detailed above, $Ca_V3.1$ antibody used at 4 µg/mL, $Ca_V3.2$ diluted 1:200 from unknown stock concentration, and $Ca_V3.3$ antibody used at 2.5 µg/mL). After washing, membranes were incubated for 1 hour at room

temperature with secondary antibody, polyclonal anti-rabbit IgG raised in donkey and conjugated to Alexa Fluor 647 (133 ng/mL; AB_2536183, Invitrogen, USA).

4.2.4 EC tube Ca^{2+} imaging

Endothelial tubes devoid of VSMCs were freshly isolated from mesenteric arteries (see Section 2.1.3) and loaded with Ca^{2+} indicator Calbryte 520 AM (see Section 2.4.1). The effects of different pharmacological tools on intracellular Ca^{2+} were investigated.

4.2.5 Pressurised artery Ca^{2+} imaging

Coronary arteries were prepared for pressurisation (see Section 2.3) then ECs were selectively loaded with Ca^{2+} indicator Calbryte 520 AM (see Section 2.4.4). The effects of different pharmacological tools on intracellular Ca^{2+} were investigated.

4.2.6 Wire myography

Mesenteric arteries were prepared for wire myograph chambers (see Section 2.2) and the effects of different pharmacological antagonists on tension were investigated. When necessary, ECs were removed with a human hair and successful removal was confirmed by <10% relaxation to 1 μM ACh.

4.2.7 Agonists and antagonists

The following drugs were used in this chapter to inhibit or activate their respective targets, at concentrations which have previously been shown to be effective: 30 nM Bay K 8644 to activate L-type VGCCs (Rae and Calixto, 1989), 50 μM Ni^{2+} to block $Ca_V3.2$ channels (Lee *et*

al., 1999), 1 μM paxilline to block BK_{Ca} channels (Sanchez and McManus, 1996), 300 nM NNC to block T-type VGCCs (Huang *et al.*, 2004) , and 1 μM nifedipine to block L-type VGCCs (Stork and Cocks, 1994).

4.3 Results

Endothelium-dependent vasodilation

4.3.1 Rat mesenteric and coronary arteries express T-type voltage-gated calcium channel mRNA

To better understand the expression profile of L- and T-type VGCCs in resistance arteries, RNAscope was used to detect mRNA transcripts in ECs and VSMCs of small mesenteric and coronary arteries following fixation in a wire myograph.

Unexpectedly, all 4 VGCC mRNA transcripts (*Cacna1c* (encoding $Ca_V1.2$), *Cacna1g* ($Ca_V3.1$), *Cacna1h* ($Ca_V3.2$) and *Cacna1i* ($Ca_V3.3$)) were detected in both ECs and VSMCs of RMAs (**Figures 4.3.1 – 4.3.4**) and rat coronary arteries (RCos; **Figures 4.3.5 – 4.3.8**). *Cacna1c* ($Ca_V1.2$) was the most highly expressed transcript in mesenteric and coronary ECs (67.46 ± 8.85 molecules per cell and 81.28 ± 5.69 molecules per cell, respectively; P = 0.0017 and 0.0001 vs negative control, respectively; n = 3 rats for each; **Figure 4.3.1 A and D** and **Figure 4.3.5 A and D**). In RMAs, this was followed by *Cacna1i* ($Ca_V3.3$; 23.26 ± 6.34 molecules per cell; n = 3; P = 0.0238 vs negative control; **Figure 4.3.4 A and C**), *Cacna1g* ($Ca_V3.1$; 7.35 ± 1.42 molecules per cell; n = 3; P = 0.0103 vs negative control; **Figure 4.3.2 A and C**), and *Cacna1h* ($Ca_V3.2$; 5.23 ± 0.59 molecules per cell; n = 3; P = 0.0023 vs negative control; **Figure 4.3.3 A and C**). In RCos, the next most highly expressed transcript in ECs was *Cacna1i* ($Ca_V3.3$; 6.64 ± 1.38 molecules per cell; n = 3; P = 0.0137 vs negative control; **Figure 4.3.8 A and C**), then *Cacna1g* ($Ca_V3.1$; 3.19 ± 0.67 molecules per cell; n = 3; P = 0.0274 vs negative control; **Figure 4.3.6 A and C**), then *Cacna1h* ($Ca_V3.2$; 2.28 ± 0.23 molecules per cell; n = 3; P = 0.0103 vs negative control; **Figure 4.3.7 A and C**).

In both RMA and RCo VSMCs, *Cacna1c* was expressed the most ($Ca_V1.2$; 41.48 ± 4.28 molecules per cell and 97.04 ± 16.22 molecules per cell, respectively; P = 0.0008 and 0.0043 vs negative control, respectively; n = 3 for both; **Figure 4.3.1 B and D** and **4.3.5 B and D**), followed by *Cacna1i* ($Ca_V3.3$; 21.20 ± 2.29 molecules per cell and 19.42 ± 2.10 molecules per cell, respectively; P = 0.0012 vs negative control for both; n = 3 for both; **Figure 4.3.4 B and C** and **4.3.8 B and C**), *Cacna1h* ($Ca_V3.2$; 16.40 ± 2.51 molecules per cell and 12.46 ± 2.05 molecules per cell, respectively; P = 0.0032 and 0.0075 vs negative control, respectively; n = 3 for both; **Figure 4.3.3 B and C** and **4.3.7 B and C**) and *Cacna1g* ($Ca_V3.1$; 7.45 ± 0.70 molecules per cell and 10.41 ± 2.11 molecules per cell, respectively; P = 0.0020 and 0.0176 vs negative control, respectively, n = 3 for both; **Figure 4.3.2 B and C** and **4.3.6 B and C**).

Due to the unexpectedly high expression of VGCC mRNA transcripts in RMA and RCo ECs, the sub-cellular location of mRNA molecules was further investigated. The sub-cellular location of mRNA may have important consequences for its fate, determining whether it is translated, degraded, or stored, directly affecting levels of protein expression. To determine the likelihood of VGCC mRNA transcripts being translated into proteins, the number of mRNA molecules in the nucleus was compared with the number in the cytoplasm of ECs. In RMA ECs, both *Cacna1c* ($Ca_V1.2$) and *Cacna1h* ($Ca_V3.2$) transcripts localised more extensively in the nucleus than the cytoplasm. For *Cacna1c* ($Ca_V1.2$), there was approximately 6 times more mRNA in the nucleus than the cytoplasm (67.83 ± 12.1 molecules compared to 11.80 ± 11.37 molecules; P = 0.02765; n = 3; **Figure 4.3.1 E**), and for *Cacna1h* ($Ca_V3.2$), there was over 2 times more mRNA in the nucleus than the cytoplasm (7.13 ± 1.76 nuclear mRNA molecules per cell compared to 3.03 ± 0.87 in the cytoplasm; P = 0.0382; n = 3; **Figure 4.3.3 D**). In RCo ECs, only *Cacna1c* ($Ca_V1.2$) was differentially localised, with 15.60 ± 2.25 nuclear mRNA molecules per cell compared to 6.39 ± 1.11 in the cytoplasm (approximately 2-fold difference; P = 0.0031; n = 3; **Figure 4.3.5 E**). All other transcripts studied, including control probe *Ppib*, were distributed evenly across both compartments of ECs.

The distribution of mRNA transcripts in VSMCs was also analysed, although the only significant difference between nuclear vs cytoplasmic localisation of VGCCs was for *Cacna1h* in RMAs (2.3-fold difference; P = 0.0173; n = 3; **Figure 4.3.3. E**). Control probe *Ppib* was localised more to the cytoplasm in VSMCs from RMAs (10.03 ± 1.14 cytoplasmic mRNA molecules compared to 3.450 ± 1.05 in the nucleus, P = 0.0060; n =3; **Figure 4.3.1 F**) and RCos (26.08 ± 1.93 cytoplasmic mRNA molecules compared to 9.76 ± 2.31 in the nucleus, P = 0.0056; n = 3; **Figure 4.3.5 F**). A summary of this RNAscope data is provided in **Figure 4.3.9.**

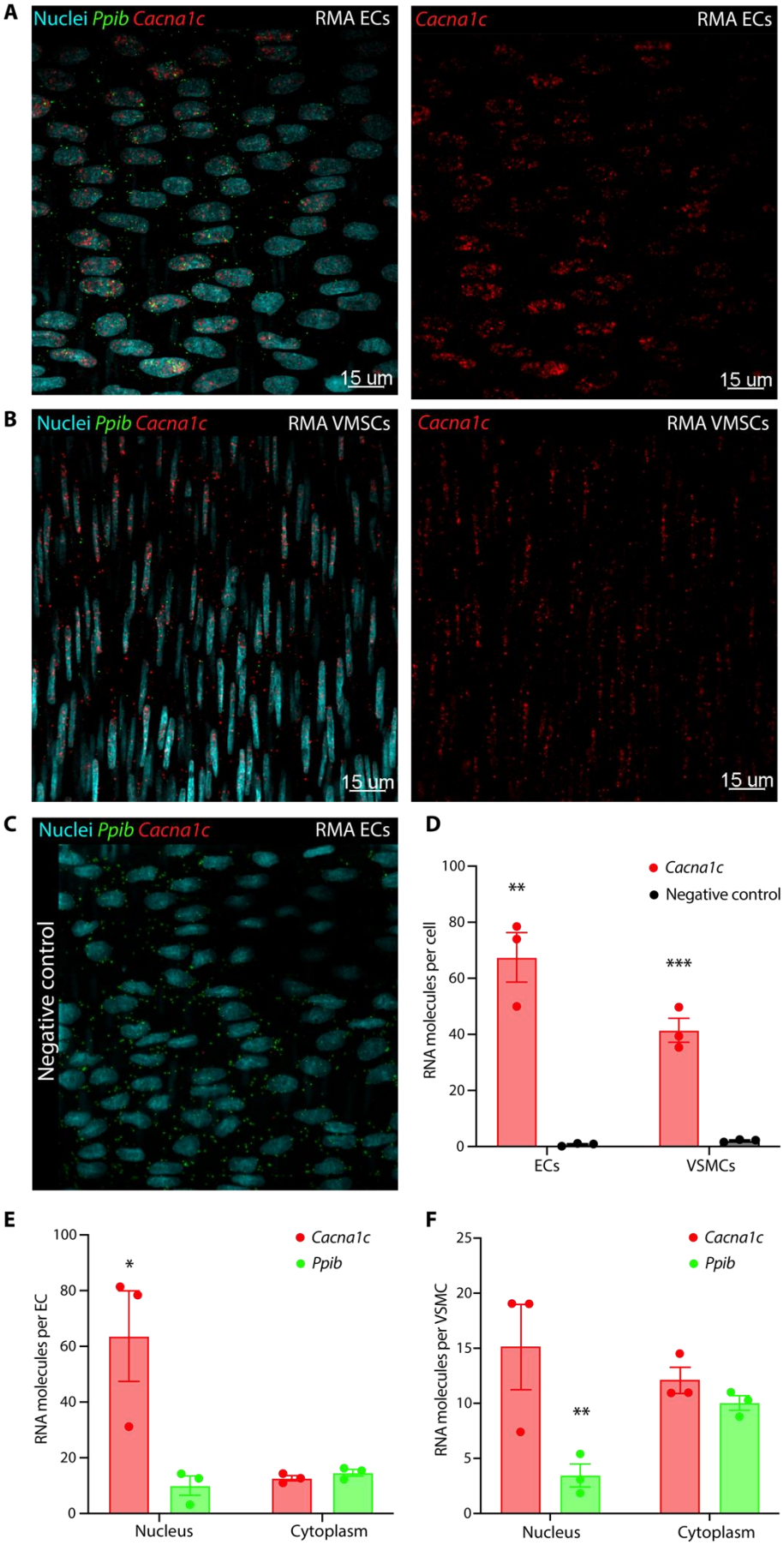
A
Nuclei Ppib Cacna1c
RMA ECs
15 um
Cacna1c
RMA ECs
15 um
B
Nuclei Ppib Cacna1c
RMA VMSCs
15 um
Cacna1c
RMA VMSCs
15 um
C
Nuclei Ppib Cacna1c
RMA ECs
Negative control
D
Cacna1c
Negative control
RNA molecules per cell
100
80
60
40
20
0
**
***
ECs
VSMCs
E
Cacna1c
Ppib
RNA molecules per EC
100
80
60
40
20
0
*
Nucleus
Cytoplasm
F
Cacna1c
Ppib
RNA molecules per VSMC
25
20
15
10
5
0
**
Nucleus
Cytoplasm

Figure 4.3.1. Expression of *Cacna1c* mRNA (encoding $Ca_V1.2$) by rat mesenteric arteries (RMAs). RNAscope was used to determine *Cacna1c* expression (red) by endothelial cells (ECs, **A**) and vascular smooth muscle cells (VSMCs, **B**) of wire-myograph mounted mesenteric arteries. *Ppib* (green) was used as a positive control. (**C**) Negative control where target probes were omitted from the RNAscope protocol. (**D**) Quantification of *Cacna1c*, expressed as molecules per cell and compared against the negative control. Data are means ± SEM; n = 3 rats. **P = 0.0017 vs EC negative control and ***P = 0.0008 vs VMSC negative control, using unpaired student's t test. (**E**) Localisation of *Cacna1c* and *Ppib* transcripts in ECs. Data are means of 3 cells per artery ± SEM; n = 3 rats. *P = 0.0100 vs *Cacna1c* cytoplasmic localisation and P = 0.2765 for *Ppib* nuclear vs cytoplasmic localisation, using unpaired student's t test. (**F**) Localisation of *Cacna1c* and *Ppib* transcripts in VSMCs. Data are means of 3 cells per artery ± SEM; n = 3 rats. P = 0.7000 for *Cacna1c* nuclear vs cytoplasmic localisation and **P = 0.0060 vs *Ppib* cytoplasmic localisation, using Mann-Whitney U test and unpaired student's t test, respectively.

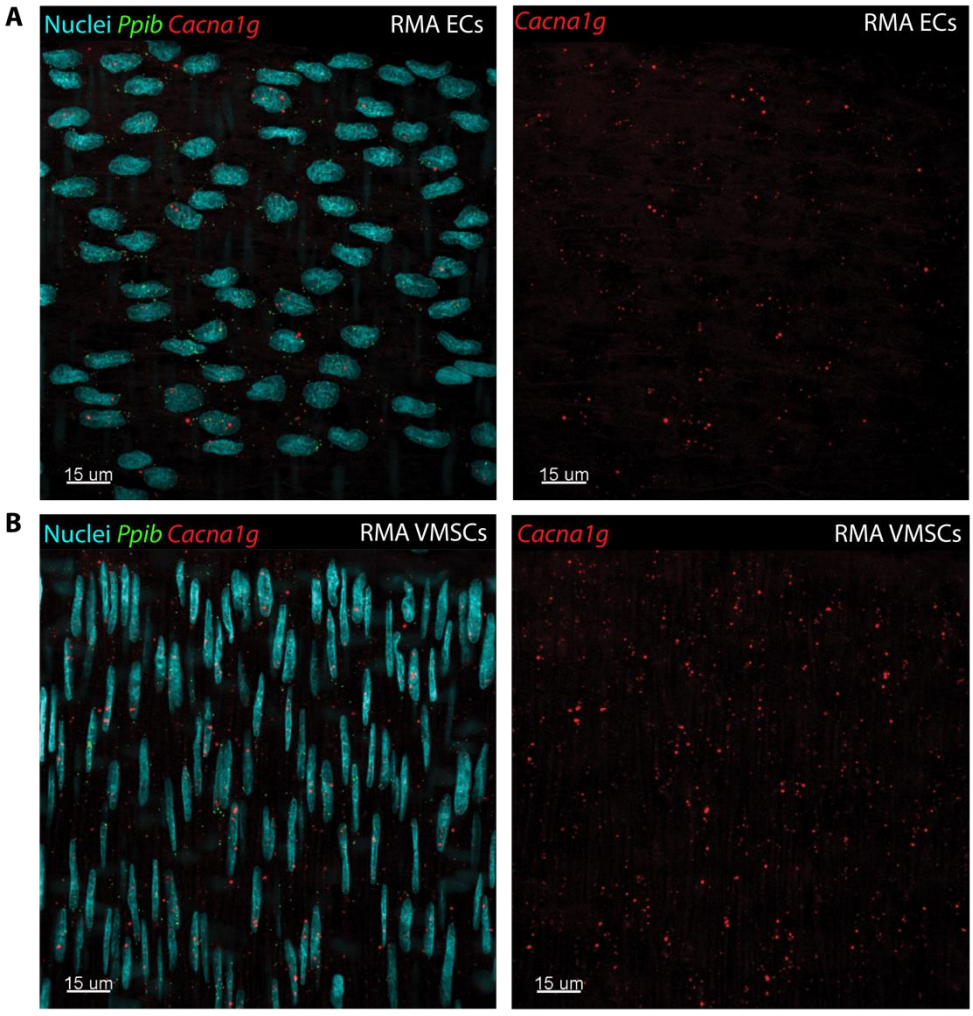
A
Nuclei Ppib Cacna1g
RMA ECs
15 um
Cacna1g
RMA ECs
15 um
B
Nuclei Ppib Cacna1g
RMA VMSCs
15 um
Cacna1g
RMA VMSCs
15 um

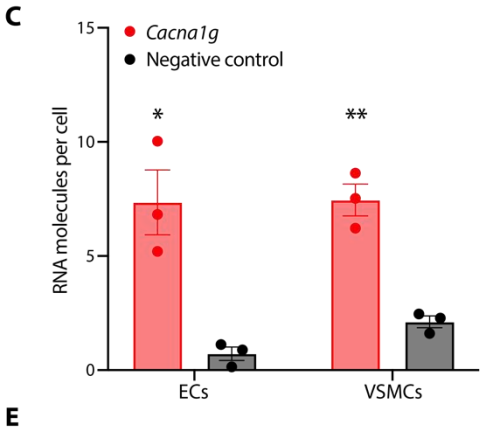
C
Cacna1g
Negative control
RNA molecules per cell
15
10
5
0
*
**
ECs
VSMCs

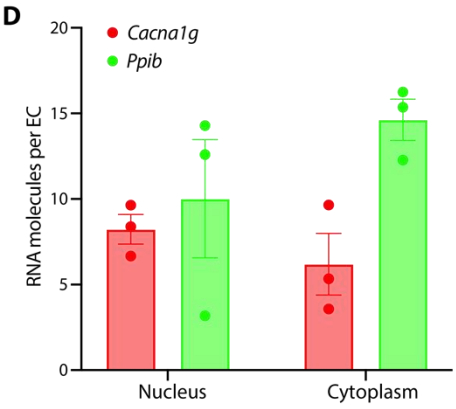
D
Cacna1g
Ppib
RNA molecules per EC
20
15
10
5
0
Nucleus
Cytoplasm

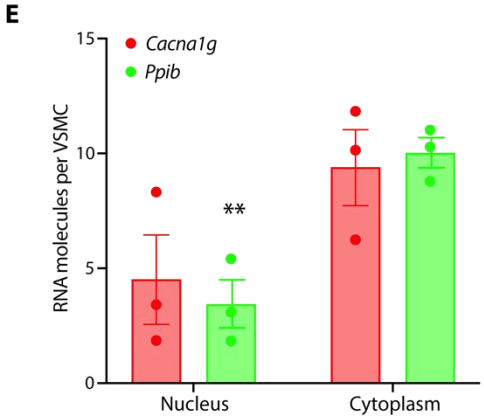
E
Cacna1g
Ppib
RNA molecules per VSMC
15
10
5
0
**
Nucleus
Cytoplasm

Figure 4.3.2. Expression of *Cacna1g* mRNA (encoding $Ca_V3.1$) by rat mesenteric arteries (RMAs). RNAscope was used to determine *Cacna1g* expression (red) by endothelial cells (ECs, **A**) and vascular smooth muscle cells (VSMCs, **B**) of wire-myograph mounted mesenteric arteries. *Ppib* (green) was used as a positive control. (**C**) Quantification of *Cacna1g*, expressed as molecules per cell and compared against a negative control where target probes were omitted from the RNAscope protocol. Data are means ± SEM; n = 3 rats. *P = 0.0103 vs EC negative control and **P = 0.002 vs VSMC negative control using unpaired student's t test. (**D**) Localisation of *Cacna1g* and *Ppib* transcripts in ECs. Data are means of 3 cells per artery ± SEM; n = 3 rats. P = 0.3653 for *Cacna1g* nuclear vs cytoplasmic localisation and P = 0.2765 for *Ppib* nuclear vs cytoplasmic localisation, using unpaired student's t test. (**E**) Localisation of *Cacna1g* and *Ppib* transcripts in VSMCs. Data are means of 3 cells per artery ± SEM; n = 3 rats. P = 0.1288 for *Cacna1g* nuclear vs cytoplasmic localisation and **P = 0.0060 vs *Ppib* cytoplasmic localisation, using unpaired student's t test.

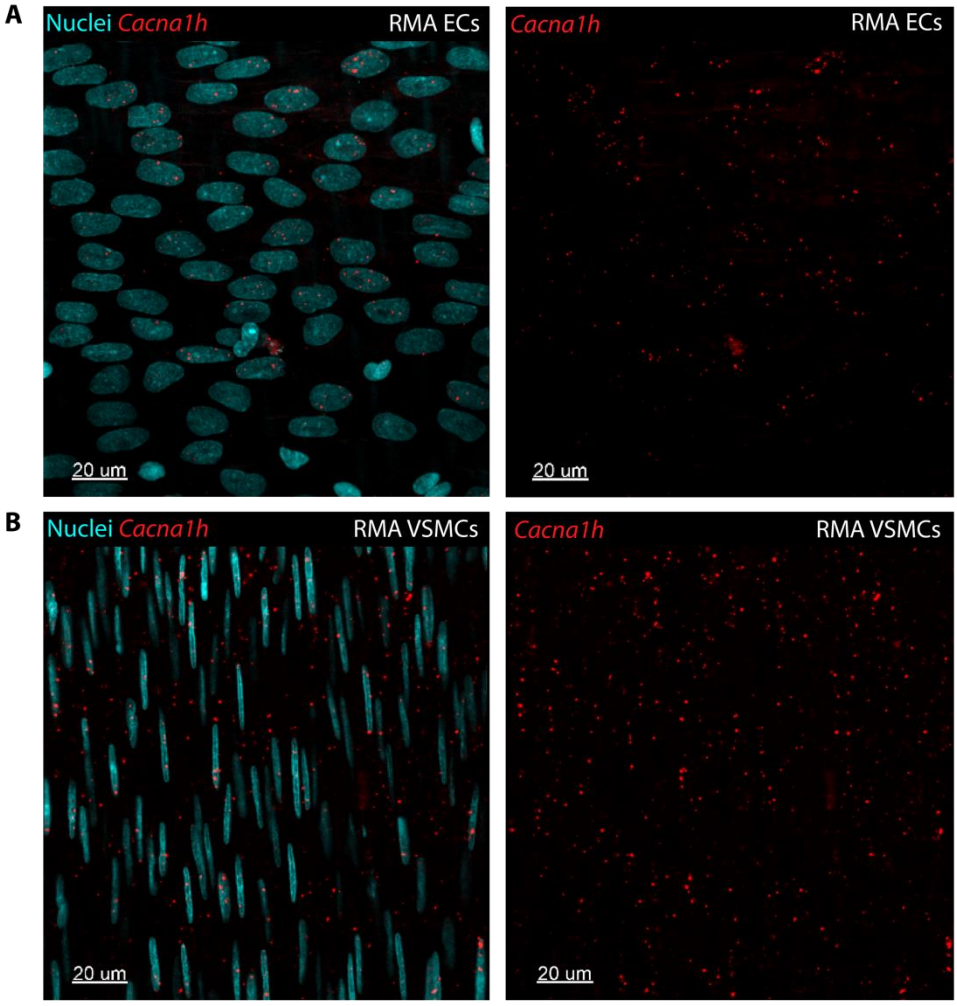
A
Nuclei Cacna1h
RMA ECs
20 um
Cacna1h
RMA ECs
20 um
B
Nuclei Cacna1h
RMA VSMCs
20 um
Cacna1h
RMA VSMCs
20 um

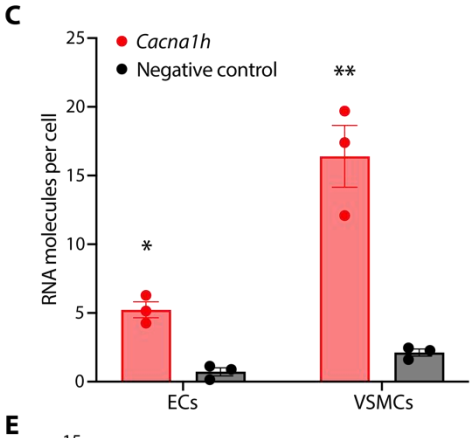
C
Cacna1h
Negative control
RNA molecules per cell
25
20
15
10
5
0
*
**
ECs
VSMCs

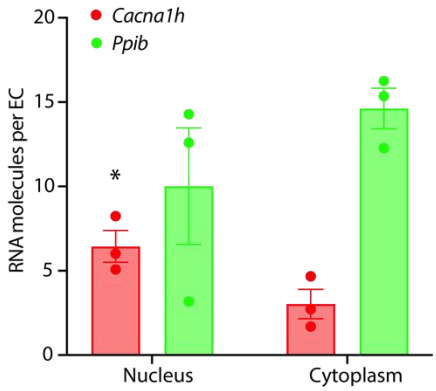
D
Cacna1h
Ppib
RNA molecules per EC
20
15
10
5
0
*
Nucleus
Cytoplasm

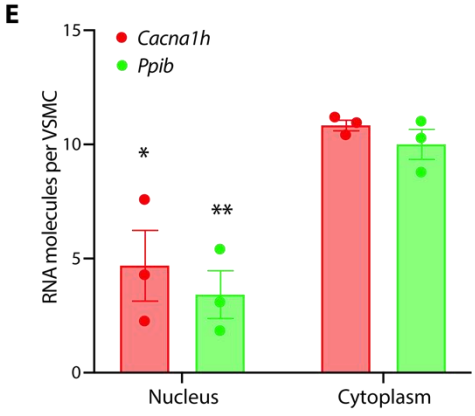
E
Cacna1h
Ppib
RNA molecules per VSMC
15
10
5
0
*
**
Nucleus
Cytoplasm

Figure 4.3.3. Expression of *Cacna1h* mRNA (encoding $Ca_V3.2$) by rat mesenteric arteries (RMAs). RNAscope was used to determine *Cacna1h* expression (red) by endothelial cells (ECs, **A**) and vascular smooth muscle cells (VSMCs, **B**) of wire-myograph mounted mesenteric arteries. (**C**) Quantification of *Cacna1h*, expressed as molecules per cell and compared against a negative control where target probes were omitted from the RNAscope protocol. Data are means ± SEM; n = 3 rats. *P = 0.0103 vs EC negative control and **P = 0.002 vs VSMC negative control, using unpaired student's t test. (**D**) Localisation of *Cacna1h* and *Ppib* transcripts in ECs. Data are means of 3 cells per artery ± SEM; n = 3 rats. **P = 0.0382 vs *Cacna1h* cytoplasmic localisation, P = 0.2765 for *Ppib* nuclear vs cytoplasmic localisation, using unpaired student's t test. (**E**) Localisation of *Cacna1h* and *Ppib* transcripts in VSMCs. Data are means of 3 cells per artery ± SEM; n = 3 rats. *P = 0.0173 for *Cacna1h* nuclear vs cytoplasmic localisation and **P = 0.0060 vs *Ppib* cytoplasmic localisation, using unpaired student's t test.

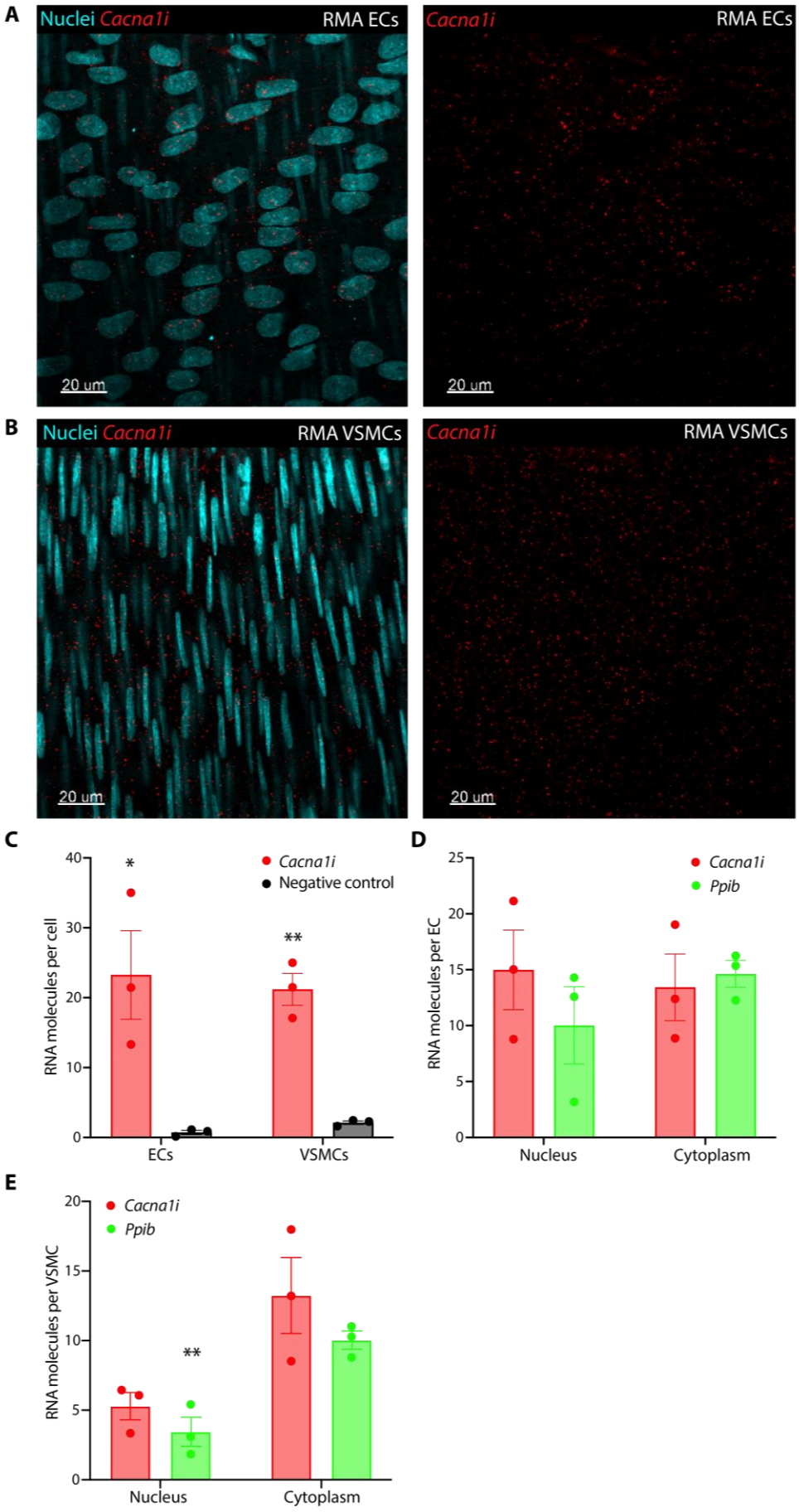
A
Nuclei Cacna1i
RMA ECs
20 um
Cacna1i
RMA ECs
20 um
B
Nuclei Cacna1i
RMA VSMCs
20 um
Cacna1i
RMA VSMCs
20 um
C
RNA molecules per cell
Cacna1i
Negative control
*
**
ECs
VSMCs
D
RNA molecules per EC
Cacna1i
Ppib
Nucleus
Cytoplasm
E
RNA molecules per VSMC
Cacna1i
Ppib
**
Nucleus
Cytoplasm

Figure 4.3.4. Expression of *Cacna1i* mRNA (encoding $Ca_V3.3$) by rat mesenteric arteries (RMAs). RNAscope was used to determine *Cacna1i* expression (red) by endothelial cells (ECs, **A**) and vascular smooth muscle cells (VSMCs, **B**) of wire-myograph mounted mesenteric arteries. (**C**) Quantification of *Cacna1i*, expressed as molecules per cell and compared against a negative control where target probes were omitted from the RNAscope protocol. Data are means ± SEM; n = 3 rats. *P = 0.0238 vs EC negative control and **P = 0.0012 vs VSMC negative control, using unpaired student's t test. (**D**) Localisation of *Cacna1i* and *Ppib* transcripts in ECs. Data are means of 3 cells per artery ± SEM; n = 3 rats. P = 0.7544 for *Cacna1i* nuclear vs cytoplasmic localisation and P = 0.2765 for *Ppib* nuclear vs cytoplasmic localisation, using unpaired student's t test. (**E**) Localisation of *Cacna1i* and *Ppib* transcripts in VSMCs. Data are means of 3 cells per artery ± SEM; n = 3 rats. P = 0.0519 for *Cacna1i* nuclear vs cytoplasmic localisation and **P = 0.0060 vs *Ppib* cytoplasmic localisation, using unpaired student's t test.

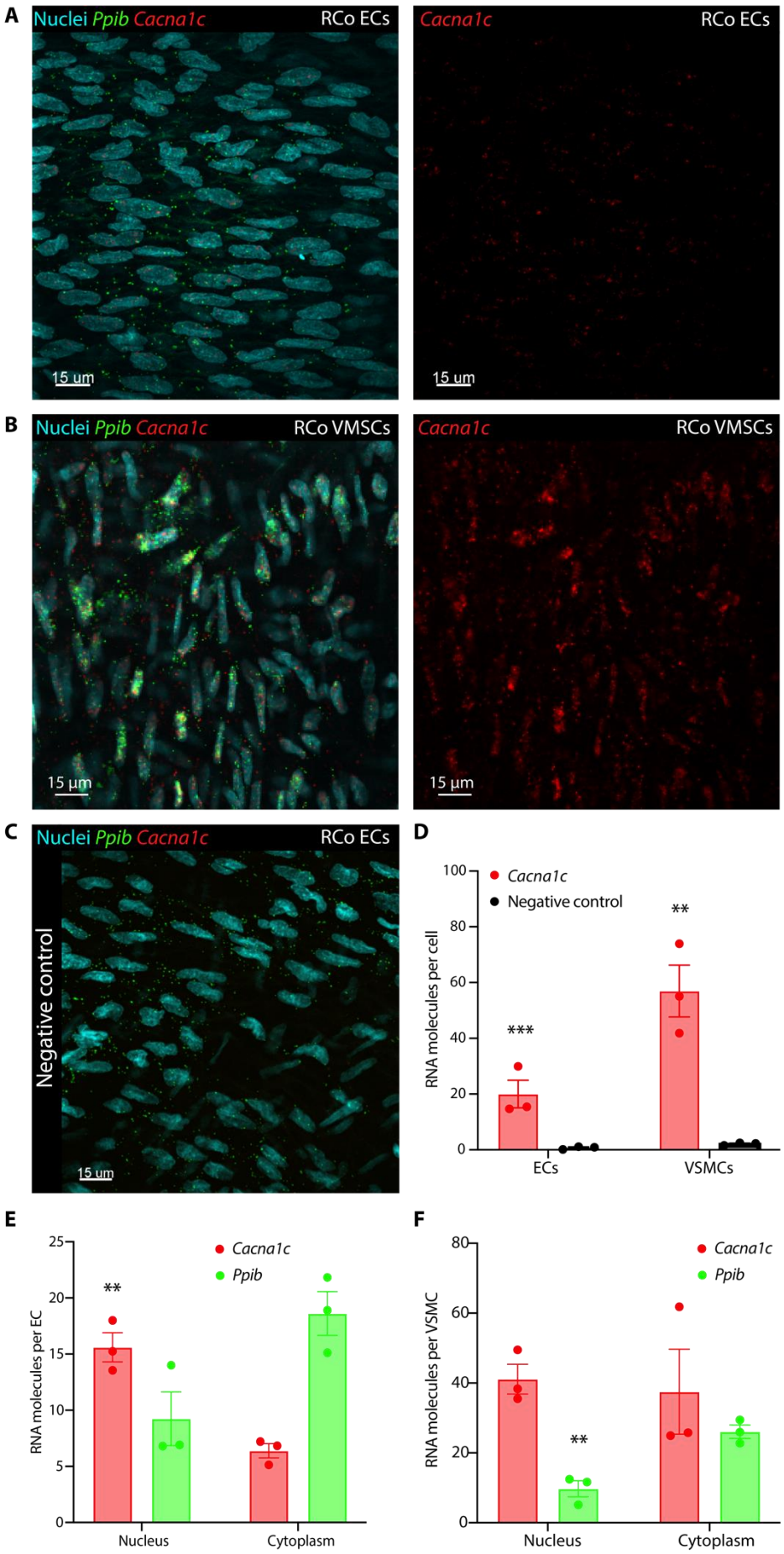
A
Nuclei Ppib Cacna1c
RCo ECs
15 um
Cacna1c
RCo ECs
15 um
B
Nuclei Ppib Cacna1c
RCo VMSCs
15 µm
Cacna1c
RCo VMSCs
15 µm
C
Nuclei Ppib Cacna1c
RCo ECs
Negative control
15 um
D
Cacna1c
Negative control
RNA molecules per cell
100
80
60
40
20
0
***
**
ECs
VSMCs
E
Cacna1c
Ppib
RNA molecules per EC
25
20
15
10
5
0
**
Nucleus
Cytoplasm
F
Cacna1c
Ppib
RNA molecules per VSMC
80
60
40
20
0
**
Nucleus
Cytoplasm

Figure 4.3.5. Expression of *Cacna1c* mRNA (encoding $Ca_V1.2$) by rat coronary arteries (RCos). RNAscope was used to determine *Cacna1c* expression (red) by endothelial cells (ECs, **A**) and vascular smooth muscle cells (VSMCs, **B**) of wire-myograph mounted coronary arteries. *Ppib* (green) was used as a positive control. (**C**) Negative control where target probes were omitted from the RNAscope protocol. (**D**) Quantification of *Cacna1c*, expressed as molecules per cell and compared against the negative control. Data are means ± SEM; n = 3 rats. ***P = 0.0001 vs EC negative control and **P = 0.0043 vs VSMC negative control, using unpaired student's t test. (**E**) Localisation of *Cacna1c* and *Ppib* transcripts in ECs. Data are means of 3 cells per artery ± SEM; n = 3 rats. **P = 0.0031 vs *Cacna1c* cytoplasmic localisation and P = 0.1000 for *Ppib* nuclear vs cytoplasmic localisation, using unpaired student's t test and Mann-Whitney U test, respectively. (**F**) Localisation of *Cacna1c* and *Ppib* transcripts in VSMCs. Data are means of 3 cells per artery ± SEM; n = 3 rats. P = 0.7000 for *Cacna1c* nuclear vs cytoplasmic localisation and **P = 0.0056 vs *Ppib* cytoplasmic localisation, using Mann-Whitney U test and unpaired student's t test, respectively.

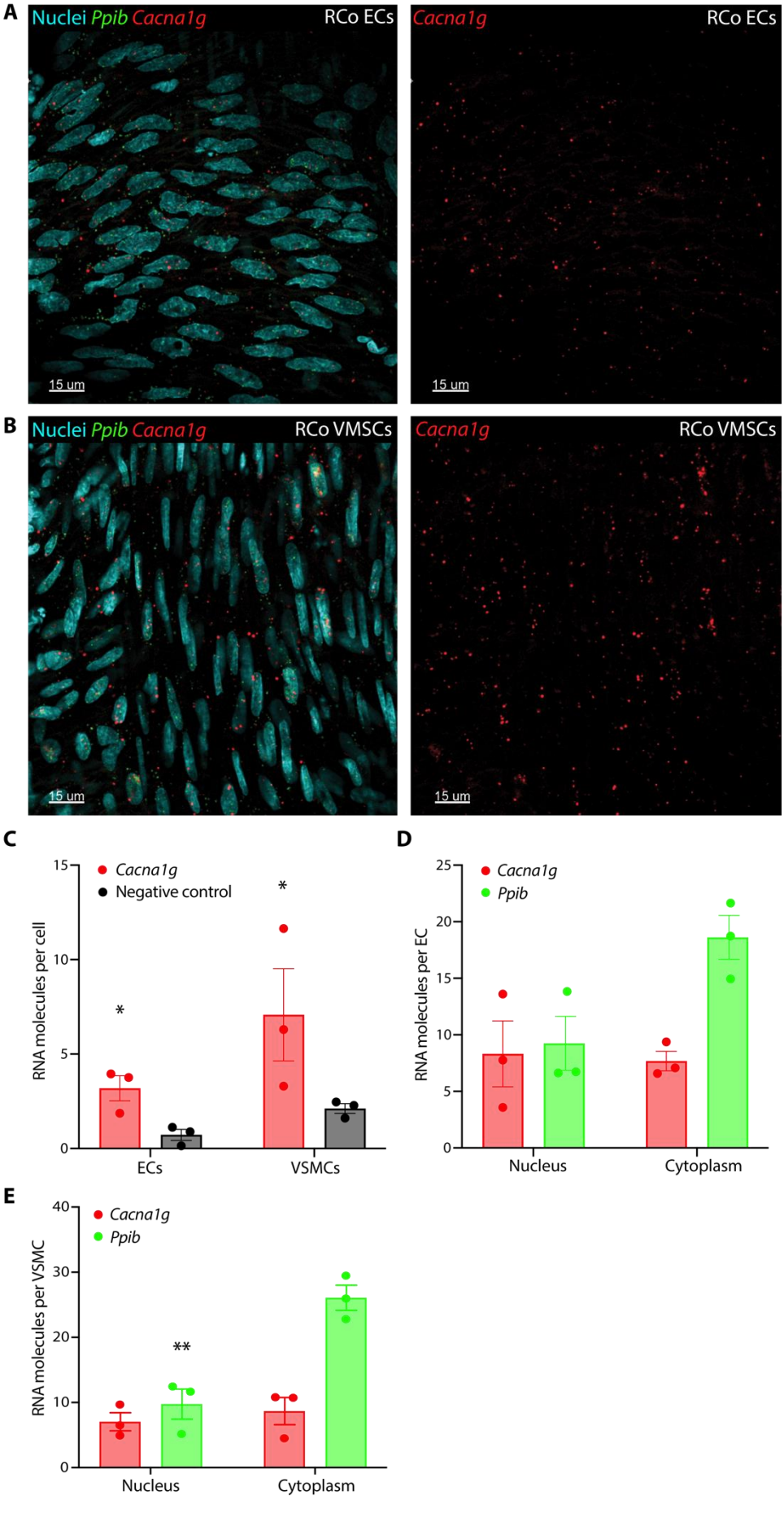
A
Nuclei Ppib Cacna1g
RCo ECs
15 um
Cacna1g
RCo ECs
15 um
B
Nuclei Ppib Cacna1g
RCo VMSCs
15 um
Cacna1g
RCo VMSCs
15 um
C
Cacna1g
Negative control
RNA molecules per cell
ECs
VSMCs
D
Cacna1g
Ppib
RNA molecules per EC
Nucleus
Cytoplasm
E
Cacna1g
Ppib
RNA molecules per VSMC
Nucleus
Cytoplasm

Figure 4.3.6. Expression of *Cacna1g* mRNA (encoding $Ca_V3.1$) by rat coronary arteries (RCos). RNAscope was used to determine *Cacna1g* expression (red) by endothelial cells (ECs, **A**) and vascular smooth muscle cells (VSMCs, **B**) of wire-myograph mounted coronary arteries. *Ppib* (green) was used as a positive control. (**C**) Quantification of *Cacna1g*, expressed as molecules per cell and compared against a negative control where target probes were omitted from the RNAscope protocol. Data are means ± SEM; n = 3 rats. *P = 0.0274 vs EC negative control and *P = 0.0176 vs VSMC negative control, using unpaired student's t test. (**D**) Localisation of *Cacna1g* and *Ppib* transcripts in ECs. Data are means of 3 cells per artery ± SEM; n = 3 rats. P = 0.8439 for *Cacna1g* nuclear vs cytoplasmic localisation and P = 0.1000 for *Ppib* nuclear vs cytoplasmic localisation, using unpaired student's t test and Mann-Whitney U test, respectively. (**E**) Localisation of *Cacna1g* and *Ppib* transcripts in VSMCs. Data are means of 3 cells per artery ± SEM; n = 3 rats. P = 0.7000 for *Cacna1g* nuclear vs cytoplasmic localisation and **P = 0.0056 vs *Ppib* cytoplasmic localisation, using Mann-Whitney U test and paired student's t test, respectively.

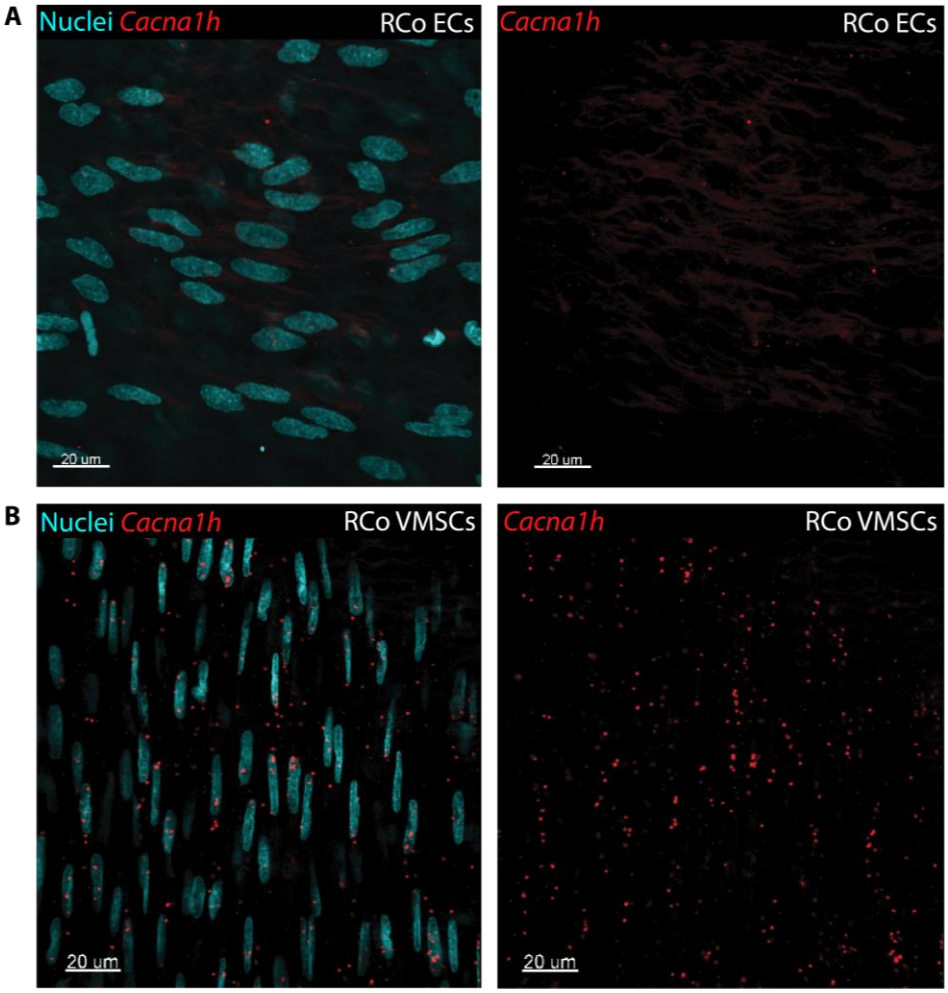
A
Nuclei Cacna1h
RCo ECs
20 um
Cacna1h
RCo ECs
20 um
B
Nuclei Cacna1h
RCo VMSCs
20 um
Cacna1h
RCo VMSCs
20 um

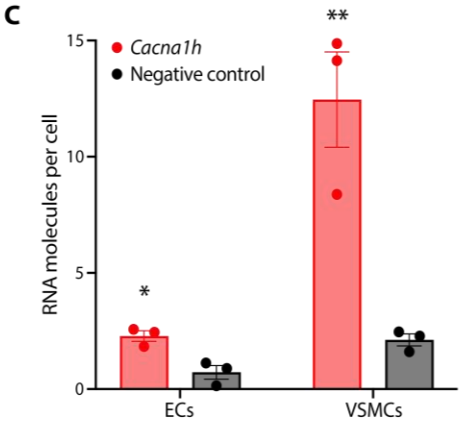
C
Cacna1h
Negative control
RNA molecules per cell
15
10
5
0
*
**
ECs
VSMCs

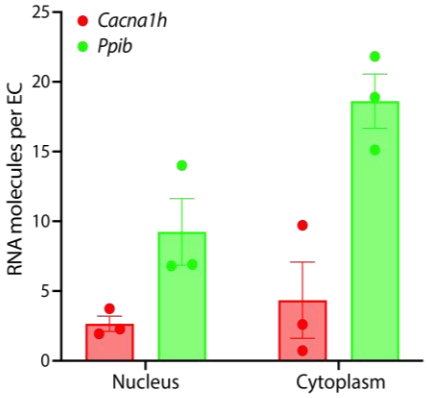
D
Cacna1h
Ppib
RNA molecules per EC
25
20
15
10
5
0
Nucleus
Cytoplasm

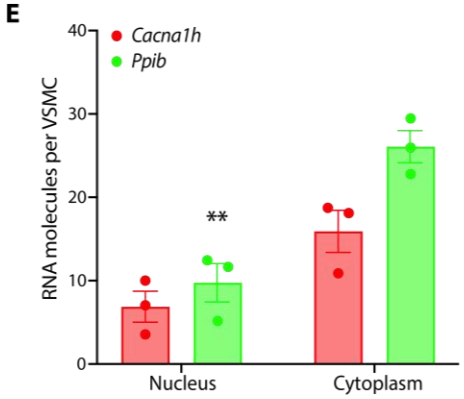
E
Cacna1h
Ppib
RNA molecules per VSMC
40
30
20
10
0
**
Nucleus
Cytoplasm

Figure 4.3.7. Expression of *Cacna1h* mRNA (encoding $Ca_V3.2$) by rat coronary arteries (RCos). RNAscope was used to determine *Cacna1h* expression (red) by endothelial cells (ECs, **A**) and vascular smooth muscle cells (VSMCs, **B**) of wire-myograph mounted coronary arteries. (**C**) Quantification of *Cacna1h*, expressed as molecules per cell and compared against a negative control where target probes were omitted from the RNAscope protocol. Data are means ± SEM; n = 3 rats. *P = 0.0138 vs EC negative control and **P = 0.0075 vs VSMC negative control, using unpaired student's t test. (**D**) Localisation of *Cacna1h* and *Ppib* transcripts in ECs. Data are means of 3 cells per artery ± SEM; n = 3 rats. P = 0.5777 for *Cacna1h* nuclear vs cytoplasmic localisation and P = 0.1000 for *Ppib* nuclear vs cytoplasmic localisation, using unpaired student's t test and Mann-Whitney U test, respectively. (**E**) Localisation of *Cacna1h* and *Ppib* transcripts in VSMCs. Data are means of 3 cells per artery ± SEM; n = 3 rats. P = 0.1117 for *Cacna1h* nuclear vs cytoplasmic localisation and **P = 0.0056 vs *Ppib* cytoplasmic localisation, using unpaired student's t test.

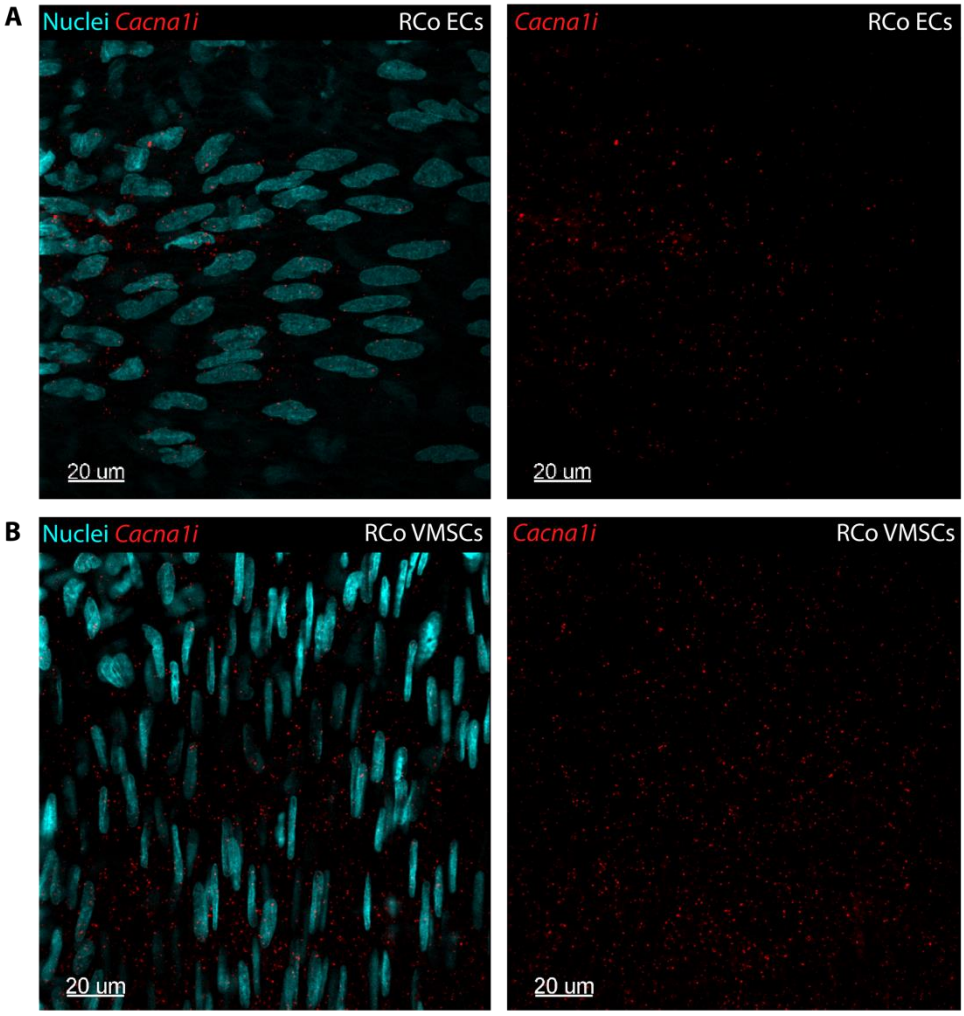
A
Nuclei Cacna1i
RCo ECs
20 um
Cacna1i
RCo ECs
20 um
B
Nuclei Cacna1i
RCo VMSCs
20 um
Cacna1i
RCo VMSCs
20 um

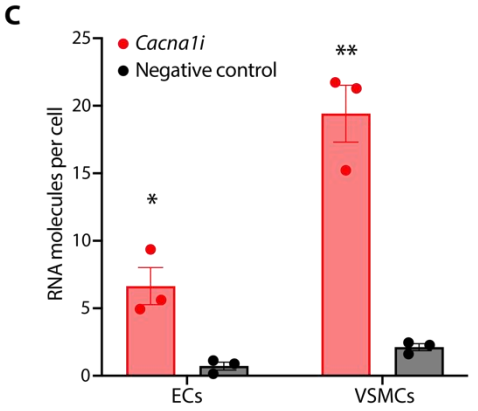
C
Cacna1i
Negative control
RNA molecules per cell
25
20
15
10
5
0
*
**
ECs
VSMCs

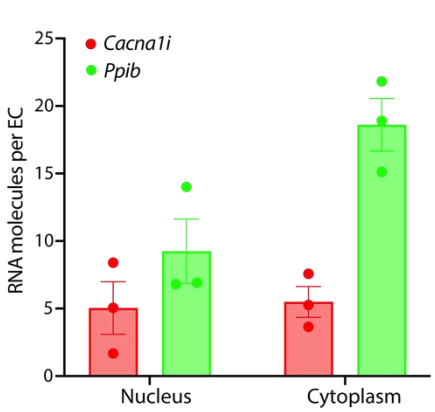
D
Cacna1i
Ppib
RNA molecules per EC
25
20
15
10
5
0
Nucleus
Cytoplasm

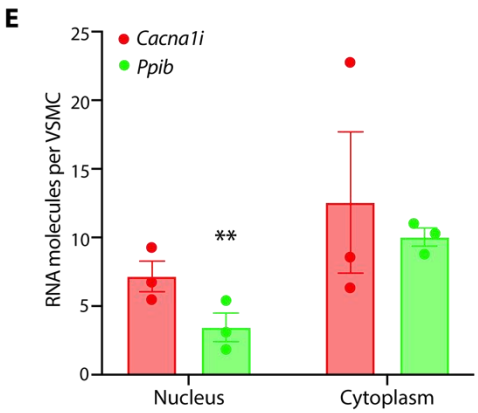
E
Cacna1i
Ppib
RNA molecules per VSMC
25
20
15
10
5
0
**
Nucleus
Cytoplasm

Figure 4.3.8. Expression of *Cacna1i* mRNA (encoding $Ca_V3.3$) by rat coronary arteries (RCos). RNAscope was used to determine *Cacna1i* expression (red) by endothelial cells (ECs, **A**) and vascular smooth muscle cells (VSMCs, **B**) of wire-myograph mounted coronary arteries. (**C**) Quantification of *Cacna1i*, expressed as molecules per cell and compared against a negative control where target probes were omitted from the RNAscope protocol. Data are means ± SEM; n = 3 rats. *P = 0.0137 vs EC negative control and **P = 0.0012 vs VSMC negative control, using unpaired student's t test. (**D**) Localisation of *Cacna1i* and *Ppib* transcripts in ECs. Data are means of 3 cells per artery ± SEM; n = 3 rats. P = 0.8502 for *Cacna1i* nuclear vs cytoplasmic localisation and P = 0.1000 for *Ppib* nuclear vs cytoplasmic localisation, using unpaired student's t test and Mann-Whitney U test, respectively. (**E**) Localisation of *Cacna1i* and *Ppib* transcripts in VSMCs. Data are means of 3 cells per artery ± SEM; n = 3 rats. P = 0.3638 for *Cacna1i* nuclear vs cytoplasmic localisation and **P = 0.0056 vs *Ppib* cytoplasmic localisation, using unpaired student's t test.

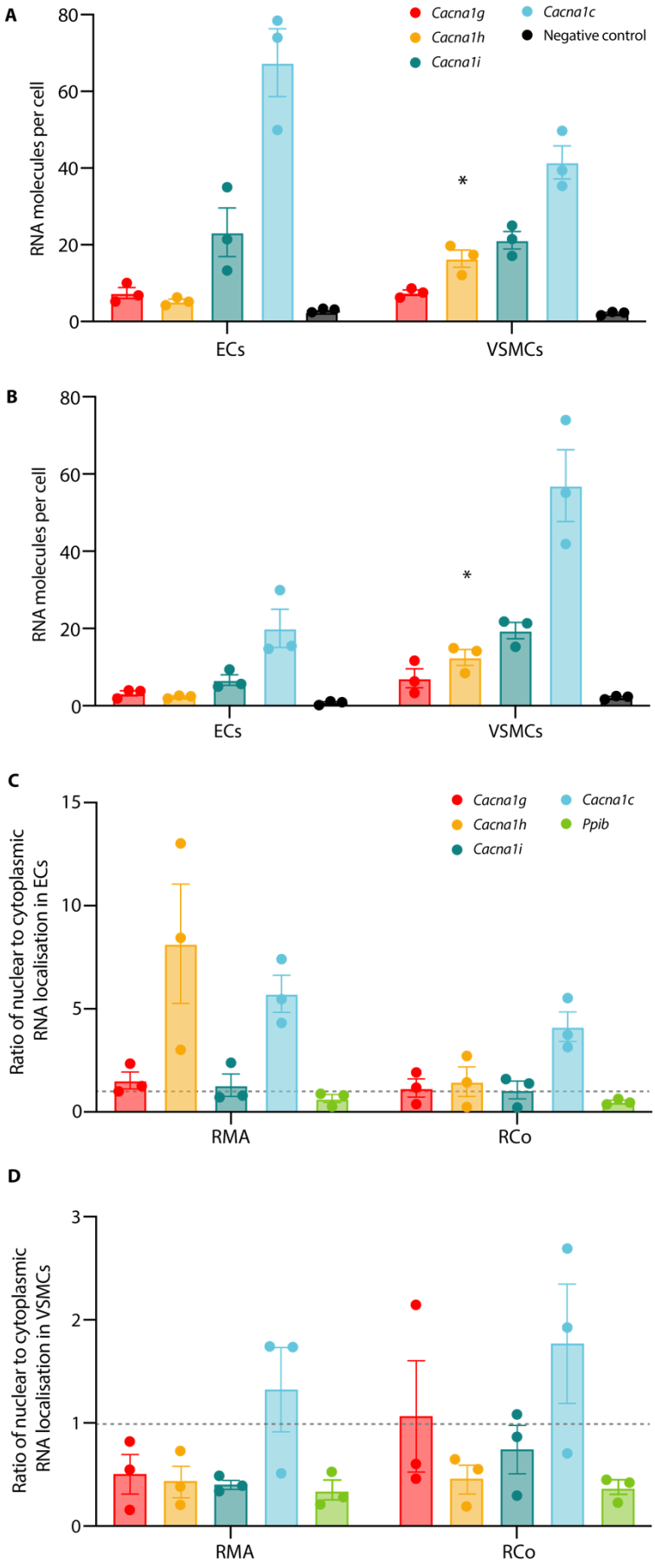
A
RNA molecules per cell
80
60
40
20
0
Cacna1g
Cacna1h
Cacna1i
Cacna1c
Negative control
*
ECs
VSMCs
B
RNA molecules per cell
80
60
40
20
0
*
ECs
VSMCs
C
Ratio of nuclear to cytoplasmic RNA localisation in ECs
15
10
5
0
Cacna1g
Cacna1h
Cacna1i
Cacna1c
Ppib
RMA
RCo
D
Ratio of nuclear to cytoplasmic RNA localisation in VSMCs
3
2
1
0
RMA
RCo

Figure 4.3.9. Quantification and localisation of voltage gated calcium channel (VGCC) mRNA. Quantification of VGCC mRNA in endothelial cells (ECs) and vascular smooth muscle cells (VSMCs) of rat mesenteric arteries (RMAs, **A**) and coronary arteries (RCos, **B**). To generate negative controls, the RNAscope protocol was carried out minus the addition of target RNA probes. Data are means ± SEM; n = 3 for each. For RMAs, *P = 0.0341 vs *Cacna1i* using ordinary one-way ANOVA with Bonferroni's correction. For RCos, *P = 0.0146 vs *Cacna1i* using ordinary one-way ANOVA with Bonferroni's correction. Statistical comparisons of each transcript against the negative control are included in previous figures. Ratio of nuclear to cytoplasmic localisation of VGCC and *Ppib* control probe mRNA transcripts in ECs (**C**) and VSMCs (**D**) of rat mesenteric and coronary arteries. The grey dashed line at a ratio of 1 indicates equally distributed RNA expression across the nucleus and cytoplasm. For each artery, the average number of RNA molecules in the nucleus and cytoplasm was determined from 3 cells, and this was repeated for 3 separate arteries (n = 3 rats). Data are means ± SEM. No statistically significant differences were detected using ordinary one-way ANOVA with Bonferroni's correction.

4.3.2 Rat mesenteric and coronary arteries express T-type voltage-gated calcium channel protein

Next, immunohistochemistry was used to label T-type VGCC proteins in wire-fixed RMAs (**Figure 4.3.10**) and RCos (**Figure 4.3.11**). Western blotting was used to demonstrate specificity of the antibodies used, where brain tissue was used as a positive control (**Figure 4.3.12**). For each T-type channel subtype, the fragments detected in RMAs (band at ~70 KDa for $Ca_V3.1$, band at ~90 kDa for $Ca_V3.2$ and band at ~70 kDa for $Ca_V3.3$) were smaller than expected (~250 kDa for all 3 subtypes). Smaller than expected bands for $Ca_V3.1$ and $Ca_V3.3$ have previously been detected in western blots from mouse, rat, and human brain homogenates, which the authors proposed were a result of alternative splicing (Yunker *et al.*, 2003).

All 3 T-type VGCC subtypes were present in ECs and VSMCs of both artery types. There was punctate labelling of T-type VGCCs in VSMCs of both artery types, and weaker labelling in the endothelium. In RMAs, T-type VGCCs occasionally aligned with holes in the IEL (white arrow heads in **Figure 4.3.10**). In reconstructed Z-stacks of these arteries, the fluorescent signal was more intense at the basolateral surface of the endothelium, indicating that these VGCCs were expressed at the interface between ECs and VSMCs, perhaps on or near MEPs. The same Ca_V/MEP alignment may also occur in RCos, but the sparse arrangement of elastin fibres in the IEL made this difficult to identify. Negative controls indicate that the primary antibodies used in this immunohistochemistry protocol were specific to their respective targets (**Figure 4.3.13**).

L-type ($Ca_V1.2$) VGCC expression was investigated using IHC, but the data are not included herein due to inconsistencies in patterns of labelling, likely due to non-specific primary antibody binding (details of the primary antibody tested included in Section 4.2.2). Optimising the immunohistochemistry protocol for $Ca_V1.2$ channel detection was not prioritised in this

study as the literature has reached a consensus that $Ca_V1.2$ channels are expressed in resistance artery VSMCs but not in ECs. This conclusion is supported by data across species and vascular beds, obtained using a variety of experimental techniques (previously discussed in Section 1.4).

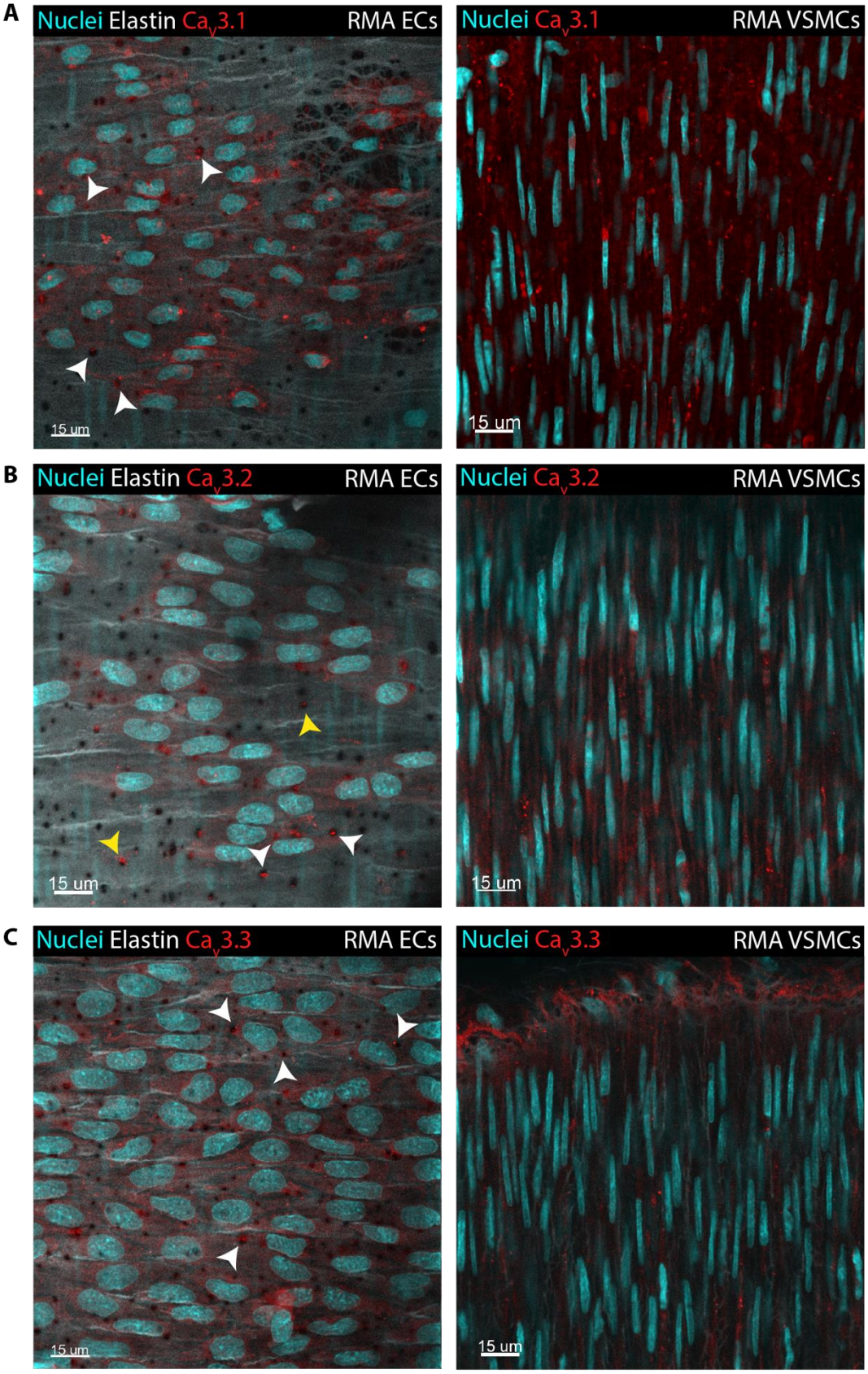
A
Nuclei Elastin Cav3.1
RMA ECs
15 um
Nuclei Cav3.1
RMA VSMCs
15 um
B
Nuclei Elastin Cav3.2
RMA ECs
15 um
Nuclei Cav3.2
RMA VSMCs
15 um
C
Nuclei Elastin Cav3.3
RMA ECs
15 um
Nuclei Cav3.3
RMA VSMCs
15 um

Figure 4.3.10. Expression of T-type voltage gated calcium channels (VGCCs) by rat mesenteric arteries (RMAs). Immunohistochemistry was used to determine $Ca_V3.1$ (**A**), $Ca_V3.2$ (**B**), and $Ca_V3.3$ expression (**C**) by endothelial cells (ECs) and vascular smooth muscle cells (VSMCs), shown in red, in wire-myograph mounted mesenteric arteries. Selected areas where Ca_V expression aligns with holes in the internal elastic lamina are indicated using white arrow heads. Yellow arrow heads indicate this alignment where the endothelium is damaged, suggesting these proteins may be expressed by underlying VSMCs. Images are representative of n = 3 rats.

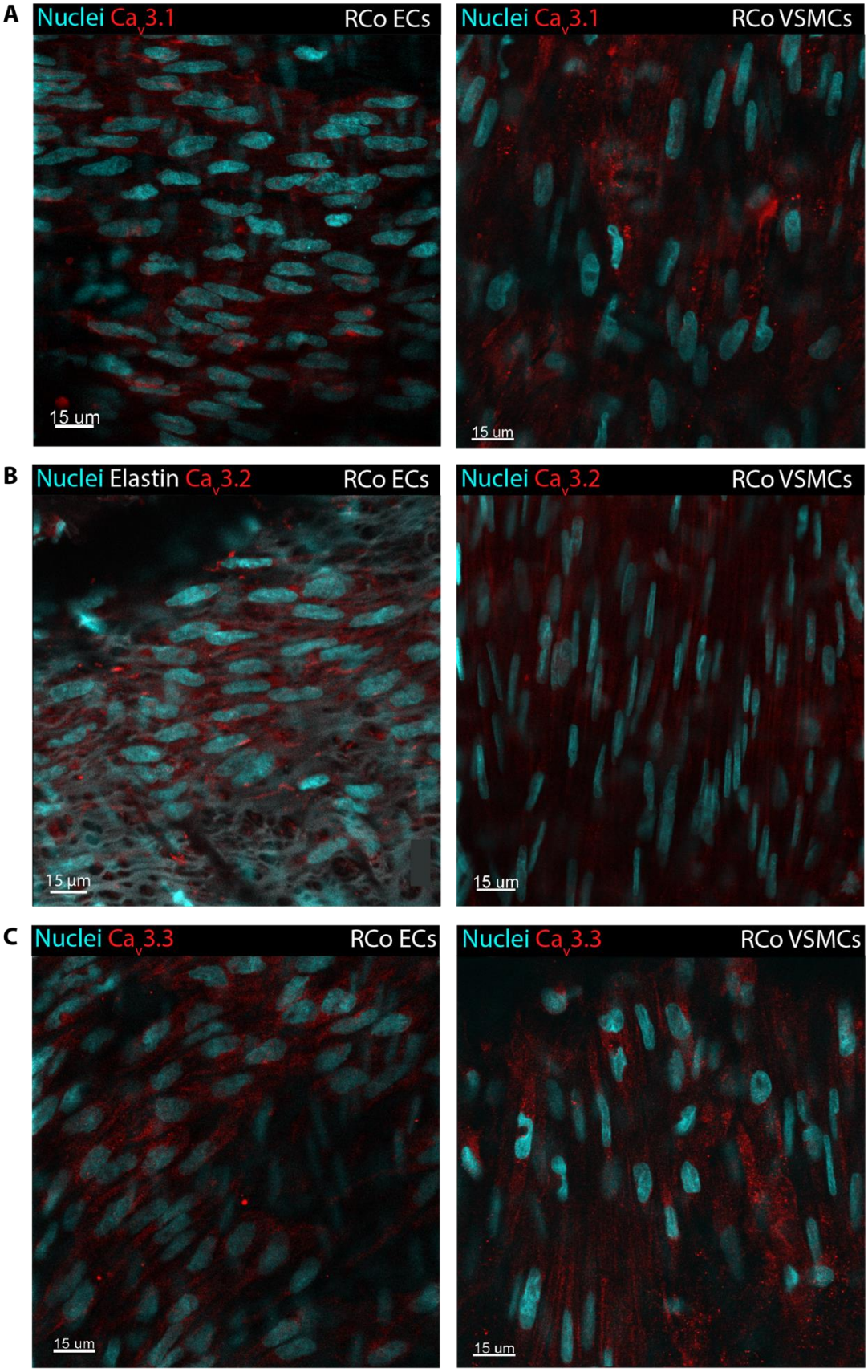
A
Nuclei Cav3.1
RCo ECs
15 um
Nuclei Cav3.1
RCo VSMCs
15 um
B
Nuclei Elastin Cav3.2
RCo ECs
15 µm
Nuclei Cav3.2
RCo VSMCs
15 um
C
Nuclei Cav3.3
RCo ECs
15 um
Nuclei Cav3.3
RCo VSMCs
15 um

Figure 4.3.11. Expression of T-type voltage gated calcium channels (VGCCs) by rat coronary arteries (RCos). Immunohistochemistry was used to determine $Ca_V3.1$ (**A**), $Ca_V3.2$ (**B**), and $Ca_V3.3$ expression (**C**) by endothelial cells (ECs) and vascular smooth muscle cells (VSMCs), shown in red, in wire-myograph mounted coronary arteries. Images are representative of n = 3 rats.

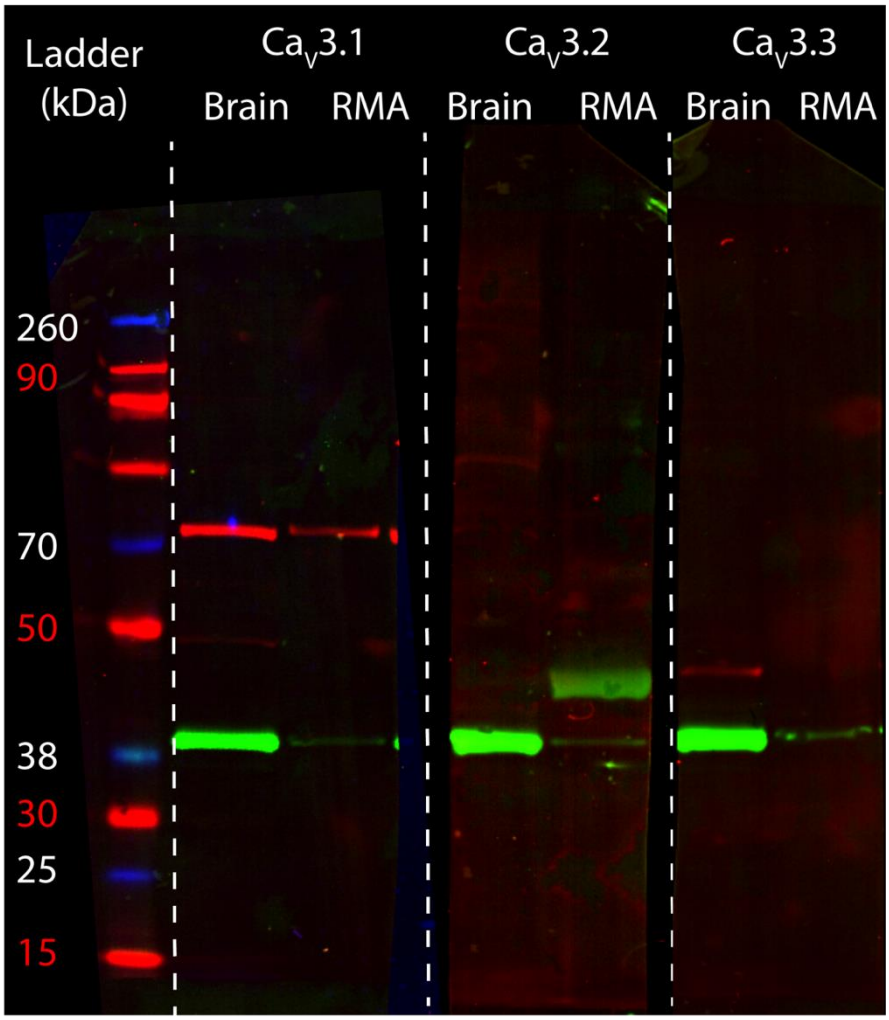

Figure 4.3.12. Western blot analysis of T-type voltage-gated calcium channels (VGCCs) from rat brain and mesenteric artery (RMA) lysates. Western blotting was used to validate the antibodies used in immunolabelling: anti-$Ca_V3.1$ (ACC-021; Alomone), anti-$Ca_V3.2$ (C1868; Sigma), and anti-$Ca_V3.3$ (ACC-009; Alomone), using rat brain as a positive control. The molecular weight of all 3 channel subtypes is ~250 kDa, and the smaller fragments observed for all 3 channel subtypes (shown in red) may be a result of alternative splicing or protein degradation during processing. The green bands at ~38 kDa represent positive GAPDH detection.

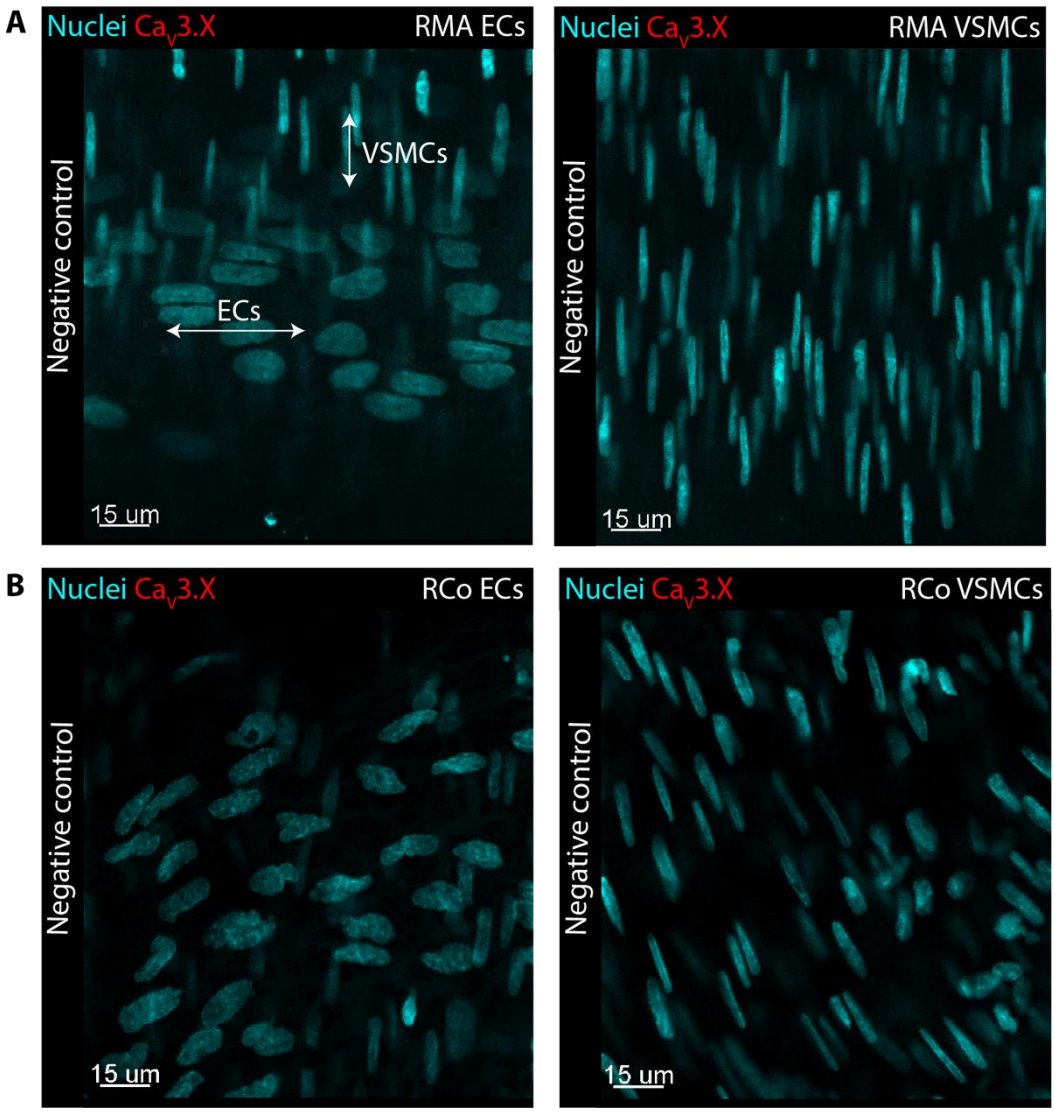

Figure 4.3.13. Negative controls of voltage-gated calcium channel (VGCC) immunolabelling in endothelial cells (ECs) and vascular smooth muscle cells (VSMCs) of rat mesenteric (A) and coronary arteries (B). Primary antibodies were omitted from the immunohistochemistry protocol, and only the secondary antibody (AlexaFluor™ 488 goat anti-rabbit) was applied. Images are representative of n = 3 rats.

4.3.3 T-type voltage-gated calcium channels overlap with myoendothelial projections

To better understand the localisation of T-type VGCCs in relation to MEPs, confocal microscopy was employed using pressurised arteries. Building on a technique first developed in the Dora/Garland laboratory (published in Garland *et al.*, 2011), ECs of live, pressurised arteries were selectively loaded with calcium indicator calcein AM, which acts as a cytoplasmic marker. Calcein remains in ECs post-fixation, allowing MEPs and immunolabelled proteins to be imaged simultaneously. High-resolution confocal microscopy allows serial Z-stacks through the artery wall to be reconstructed in 3D, where orthogonal cross-sections show the endothelium, MEPs, and underlying layers of VSMCs.

Using this technique, MEPs were identified in second-order RMAs (**Figure 4.3.14**) and intraseptal RCos (**Figure 4.3.15**). In RMAs, there were 3.05 ± 0.29 projections per EC, and 82.59 % ± 6.30 of holes in the IEL housed a projection (n = 5; **Figure 4.3.16**). In the one RCo imaged, there were 1.61 projections per EC; the number of holes in the IEL was not quantified due to their poorly defined structure (**Figure 4.3.17**).

In pressurised RMAs loaded with calcein AM and immunolabelled against T-type VGCCs, $Ca_V3.1$, $Ca_V3.2$, and $Ca_V3.3$ were all expressed diffusely throughout the cytoplasm of ECs and VSMCs (**Figures 4.3.18 – 4.3.20**). Additionally, for all 3 VGCCs, there were clusters of intense fluorescence which often aligned with holes in the IEL and MEPs (See **Table 4.3.3** for summary).

To identify whether the T-type VGCCs expressed near MEPs were on ECs or VSMCs, orthogonal cross-sections through MEPs in RMAs were analysed. Figure **4.3.18 C** shows overlapping $Ca_V3.1$ channels and MEPs through holes in the IEL. The fluorescence corresponding to $Ca_V3.1$ channels overlapped with the distal portion of MEPs, suggesting that either $Ca_V3.1$ channels are expressed by ECs in MEPs, or they are expressed by VSMCs near

points where MEPs make contact. This same pattern of expression was true for both $Ca_V3.2$ (**Figure 4.3.19 C**) and $Ca_V3.3$ channels (**Figure 4.3.20 C**).

Channel subtype	IEL holes with Ca_V only (%)	IEL holes with MEP and Ca_V (%)	MEPS aligned with Ca_V (%)	Corresponding figure
$Ca_V3.1$	20.97 ± 2.79 (n = 2)	58.75 ± 0.34 (n = 2)	73.78 ± 2.70 (n = 2)	4.3.18
$Ca_V3.2$	0 (n = 1)	11.01 (n = 1)	13.18 (n = 1)	4.3.19
$Ca_V3.3$	1.16 (n = 1)	24.41 (n = 1)	28.00 (n = 1)	4.3.20

Table 4.3.3. Table summarising the alignment between T-type voltage-gated calcium channels (VGCCs), holes in the internal elastic lamina (IEL) and myoendothelial projections (MEPs) in rat mesenteric arteries.

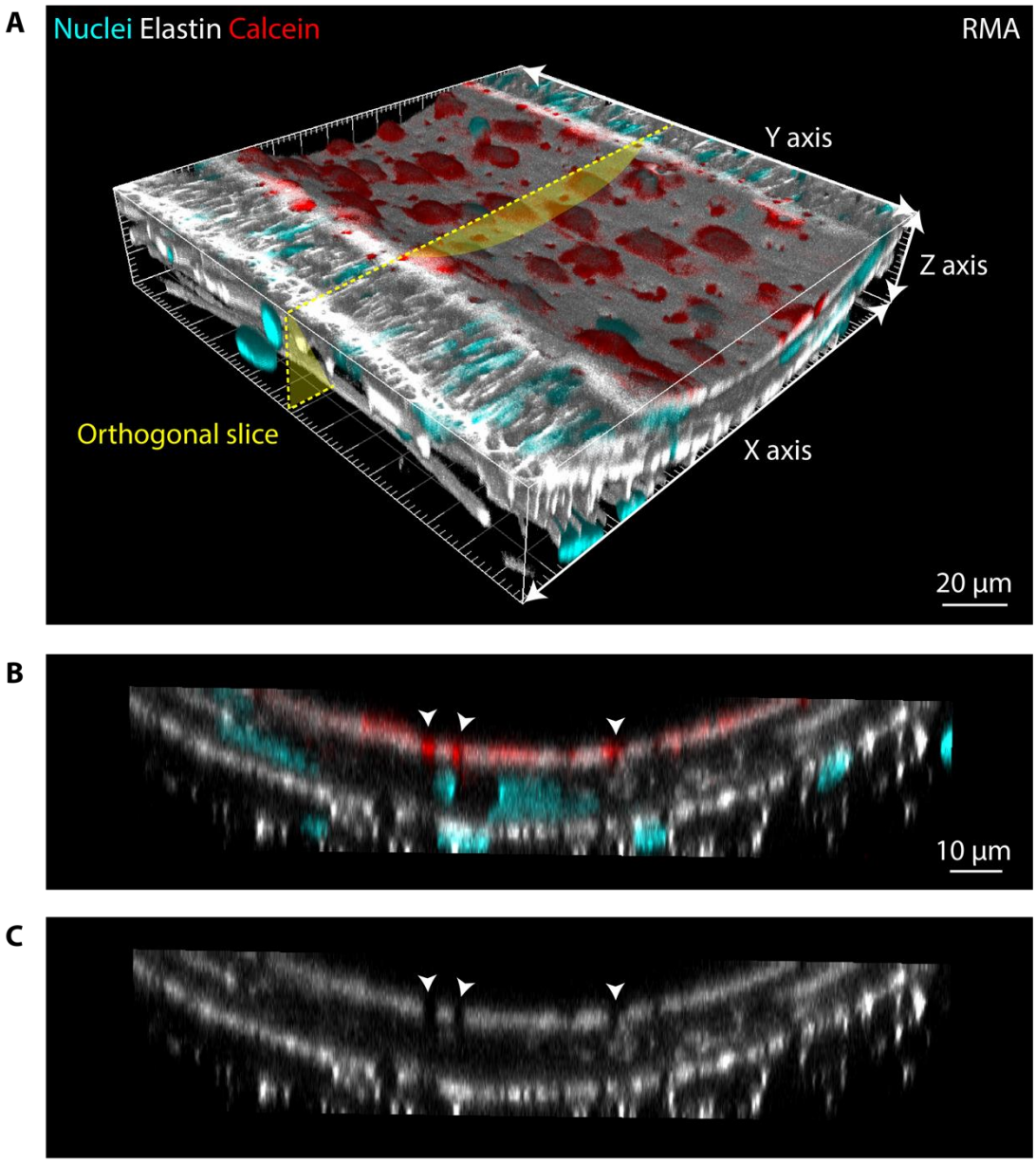

Figure 4.3.14. Confocal micrographs of pressurised mesenteric artery showing myoendothelial projections (MEPs). Endothelial cells (ECs) were selectively loaded with fluorescent indicator calcein AM, which enables visualization of their cytoplasm. **(A)** 3D reconstruction of the artery wall with region used for XZ orthogonal cross section (2.15 µm depth) indicated. (**B**) XZ slice through artery wall showing MEPs (white arrow heads) originating from the basolateral surface of ECs and protruding towards vascular smooth muscle cells (VSMCs) through holes in the internal elastic lamina (IEL). (**C**) XZ slice with holes in IEL clearly visible (white arrow heads). Images representative of n = 5 rats.

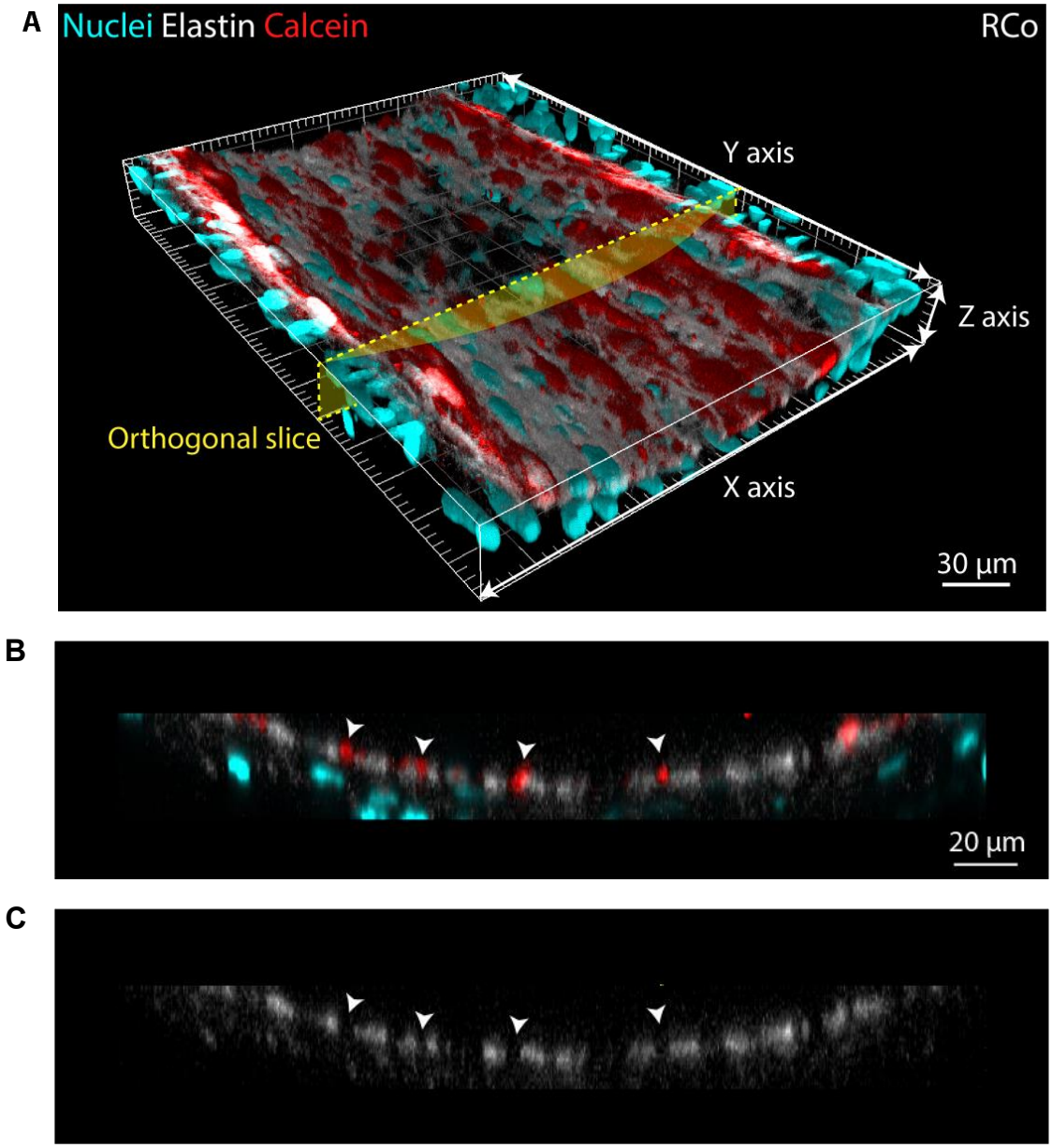

Figure 4.3.15. Confocal micrographs of pressurised coronary artery showing myoendothelial projections (MEPs). Endothelial cells (ECs) were selectively loaded with fluorescent indicator calcein AM, which enables visualization of their cytoplasm. **(A)** 3D reconstruction of the artery wall with region used for XZ orthogonal cross section (2.15 µm depth) indicated. (**B**) XZ slice through artery wall showing MEPs (white arrow heads) originating from the basolateral surface of ECs and protruding towards vascular smooth muscle cells (VSMCs) through holes in the internal elastic lamina (IEL). (**C**) XZ slice with holes in IEL clearly visible (white arrow heads). Images representative of n = 1 rat.

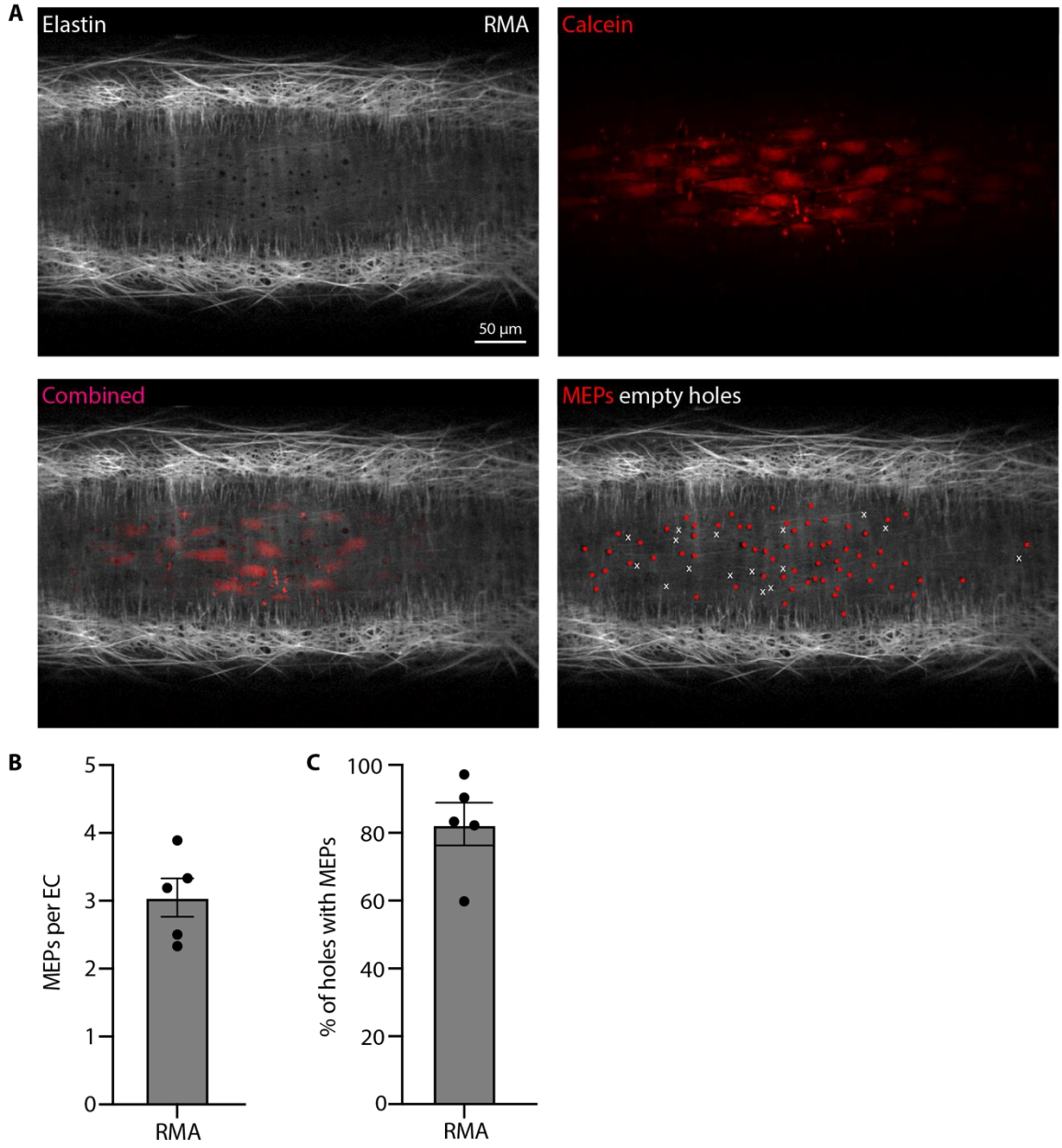

Figure 4.3.16. Quantification of myoendothelial projections (MEPs) in pressurised mesenteric arteries (RMAs). (A) Confocal micrographs of artery where endothelial cells (ECs) were selectively loaded with fluorescent indicator calcein AM (red) and elastin was stained with AF hydrazide 633 (white). MEPs are indicated using red dots (bottom right). **(B)** Bar graph showing the number of MEPs per EC. Data are means; n = 5 rats. (**C**) Bar graph showing the proportion of holes in the IEL housing a MEP (expressed as a percentage). Data are means; n = 5 rats.

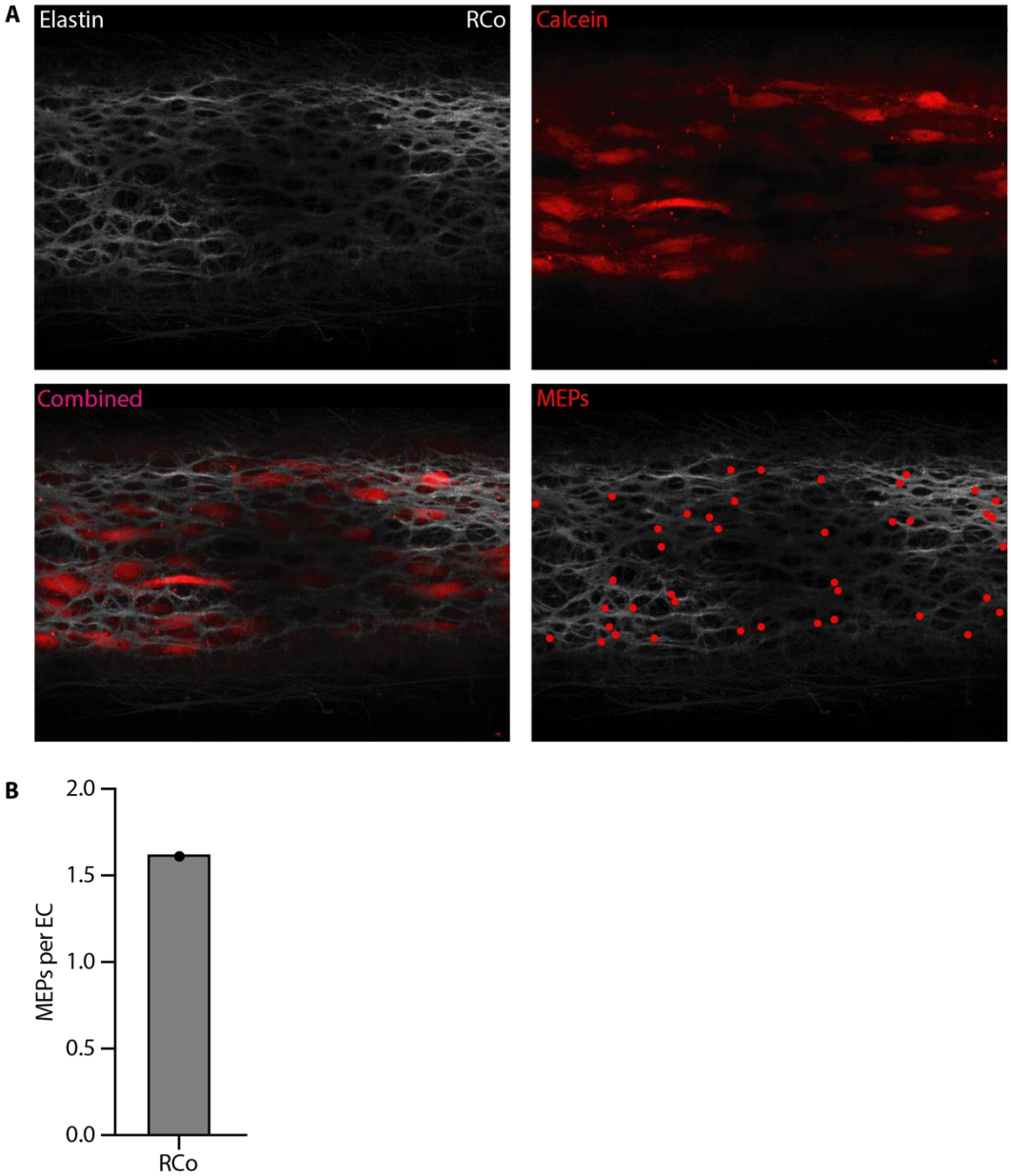

Figure 4.3.17. Quantification of myoendothelial projections (MEPs) in pressurised coronary artery. (A) Confocal micrographs of artery where endothelial cells (ECs) were selectively loaded with fluorescent indicator calcein AM (red) and elastin was stained with AF hydrazide 633 (white). MEPs are indicated using red dots (bottom right). **(B)** Bar graph showing the number of MEPs per EC. Data are means; n = 1 rat.

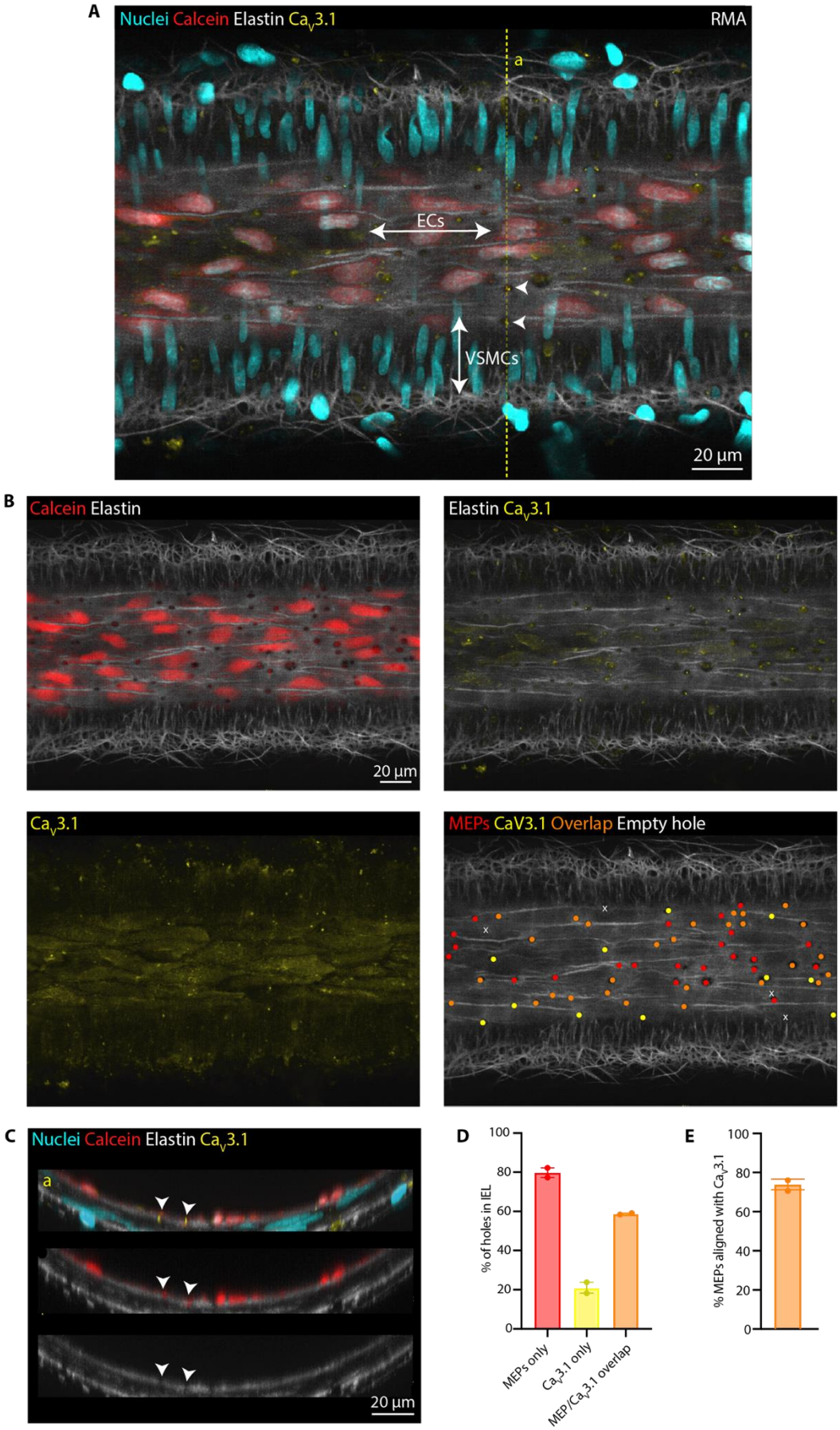
A
Nuclei Calcein Elastin $Ca_V3.1$
RMA
a
ECs
VSMCs
20 µm
B
Calcein Elastin
20 µm
Elastin $Ca_V3.1$
$Ca_V3.1$
MEPs CaV3.1 Overlap Empty hole
C
Nuclei Calcein Elastin $Ca_V3.1$
a
20 µm
D
% of holes in IEL
100
80
60
40
20
0
MEPs only
$Ca_V3.1$ only
MEP/$Ca_V3.1$ overlap
E
% MEPs aligned with $Ca_V3.1$
100
80
60
40
20
0

Figure 4.3.18. Alignment of $Ca_V3.1$ channels with myoendothelial projections (MEPs) in pressurised mesenteric arteries. (**A, B**) Confocal merged images (5 x 0.5 µm Z-axis planes) of artery wall where endothelial cells (ECs) were selectively loaded with calcein AM to reveal MEPs (red) and $Ca_V3.1$ channels were immunolabelled (yellow). $Ca_V3.1$ channels are expressed ubiquitously throughout ECs, with areas of increased protein density aligning with holes in the internal elastic lamina (IEL, yellow dots, bottom right) and often MEPs (orange dots). Empty holes are indicated using white crosses, and holes housing MEPs are indicated using red dots. (**C**) Orthogonal cross sections of reconstructed Z-stacks through artery wall corresponding to vertical dashed yellow line (a) in **A**. Overlapping $Ca_V3.1$ channels and MEPs align with holes in the IEL (white arrow heads). (**D**) Bar graph showing the proportion of holes in the IEL housing either MEPs, $Ca_V3.1$ channels, or both overlapping. (**E**) Bar graph showing the proportion of MEPs aligned with $Ca_V3.1$ channels. Error bars represent SEM; n = 2 rats.

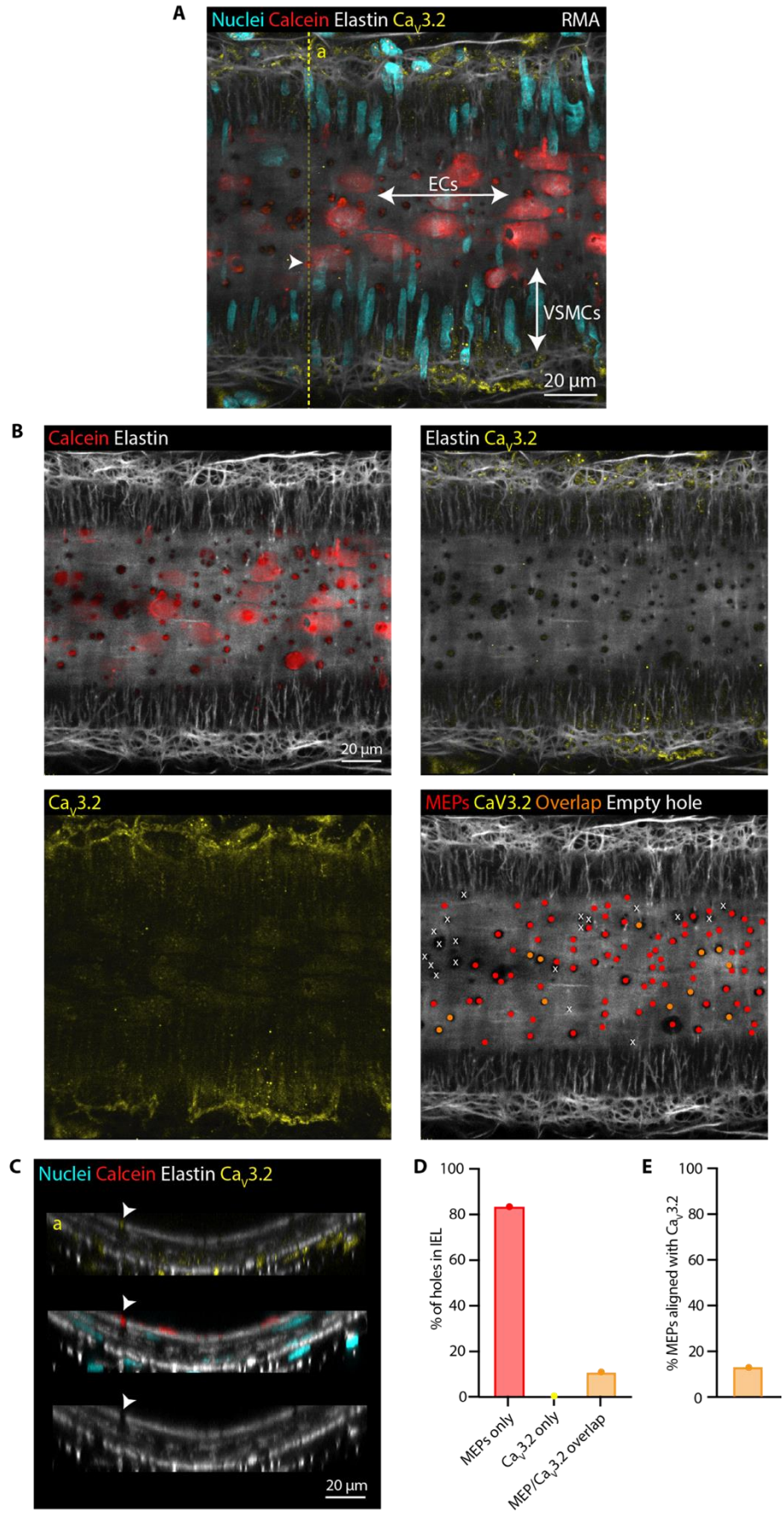
A
Nuclei Calcein Elastin Cav3.2
RMA
a
ECs
VSMCs
20 µm
B
Calcein Elastin
20 µm
Elastin Cav3.2
Cav3.2
MEPs CaV3.2 Overlap Empty hole
C
Nuclei Calcein Elastin Cav3.2
a
20 µm
D
% of holes in IEL
100
80
60
40
20
0
MEPs only
Cav3.2 only
MEP/Cav3.2 overlap
E
% MEPs aligned with Cav3.2
100
80
60
40
20
0

Figure 4.3.19. Alignment of $Ca_V3.2$ channels with myoendothelial projections (MEPs) in pressurised mesenteric arteries. (**A, B**) Confocal merged images (5 x 0.5 µm Z-axis planes) of artery wall where endothelial cells (ECs) were selectively loaded with calcein AM to reveal MEPs (red) and $Ca_V3.2$ channels were immunolabelled (yellow). $Ca_V3.2$ channels are weakly expressed throughout ECs, with some areas of increased protein density aligning with MEPs (orange dots). Empty holes are indicated using white crosses, and holes housing EPs are indicated using red dots. (**C**) Orthogonal cross sections of reconstructed Z-stacks through artery wall corresponding to vertical dashed yellow line (a) in **A**. Overlapping $Ca_V3.2$ channels and MEPs align with holes in the IEL (white arrow heads). (**D**) Bar graph showing the proportion of holes in the IEL housing either MEPs, $Ca_V3.2$ channels, or both overlapping. (**E**) Bar graph showing the proportion of MEPs aligned with $Ca_V3.2$ channels. n = 1 rat.

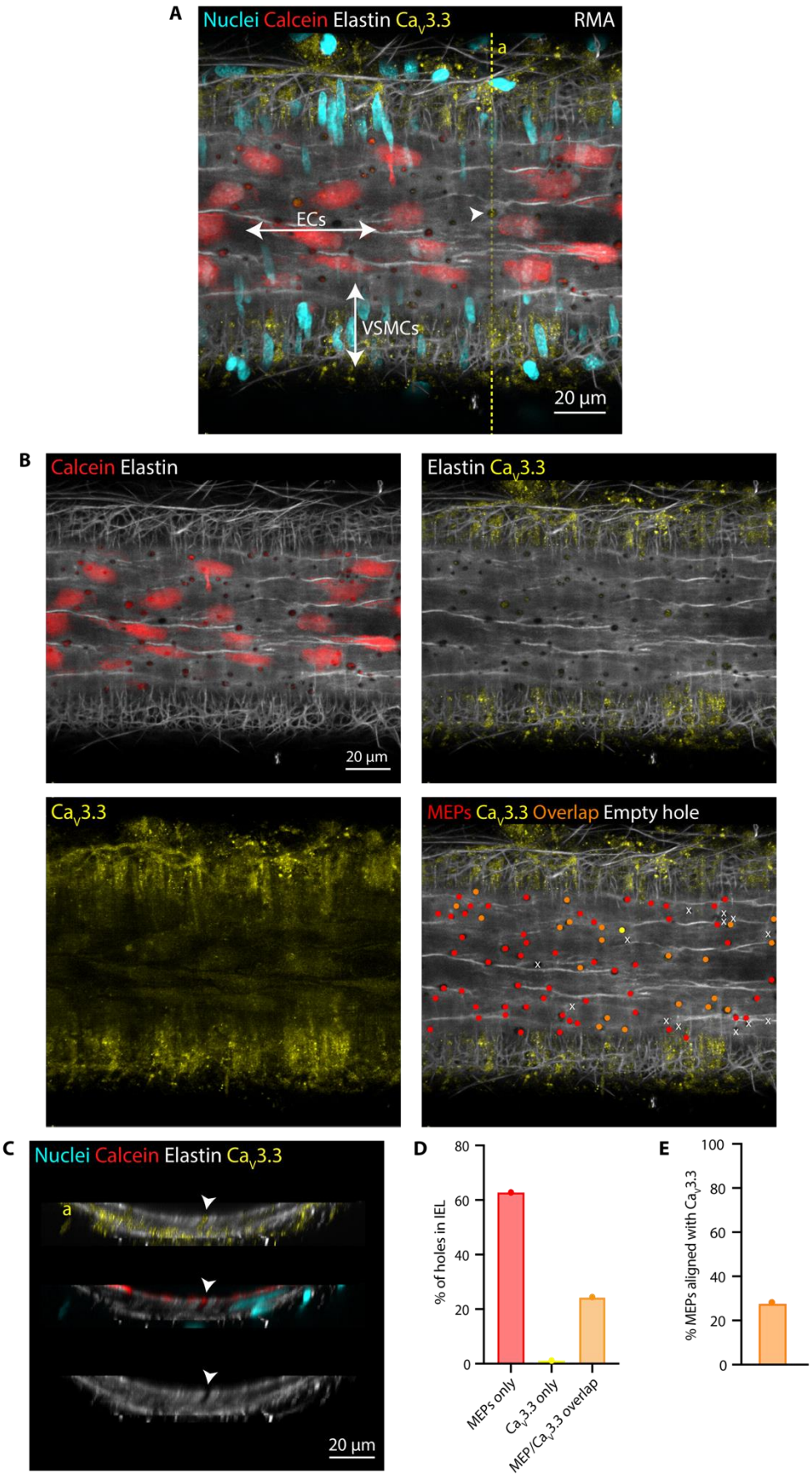
A
Nuclei Calcein Elastin $Ca_V3.3$
RMA
a
ECs
VSMCs
20 µm
B
Calcein Elastin
20 µm
Elastin $Ca_V3.3$
$Ca_V3.3$
MEPs $Ca_V3.3$ Overlap Empty hole
C
Nuclei Calcein Elastin $Ca_V3.3$
a
20 µm
D
% of holes in IEL
80
60
40
20
0
MEPs only
$Ca_V3.3$ only
MEP/$Ca_V3.3$ overlap
E
% MEPs aligned with $Ca_V3.3$
100
80
60
40
20
0

Figure 4.3.20. Alignment of $Ca_V3.3$ channels with myoendothelial projections (MEPs) in pressurised mesenteric arteries. (**A, B**) Confocal merged images (5 x 0.5 µm Z-axis planes) of artery wall where endothelial cells (ECs) were selectively loaded with calcein AM to reveal MEPs (red) and $Ca_V3.3$ channels were immunolabelled (yellow). $Ca_V3.3$ channels are weakly expressed throughout ECs, with some areas of increased protein density aligning with MEPs (orange dots). Empty holes are indicated using white crosses, and holes housing EPs are indicated using red dots. (**C**) Orthogonal cross sections of reconstructed Z-stacks through artery wall corresponding to vertical dashed yellow line (a) in **A**. Overlapping $Ca_V3.3$ channels and MEPs align with holes in the IEL (white arrow heads). (**D**) Bar graph showing the proportion of holes in the IEL housing either MEPs, $Ca_V3.3$ channels, or both overlapping. (**E**) Bar graph showing the proportion of MEPs aligned with $Ca_V3.2$ channels. n = 1 rat.

4.3.4 There are no functional L- or T-type voltage-gated calcium channels in mesenteric endothelial cells

Isolated mesenteric EC tubes were loaded with calcium indicator Calbryte 520 AM and fluorescence responses to pharmacological agents were measured (**Figure 4.3.21**). This was to determine whether the T-type VGCCs seemingly expressed by ECs contribute to intracellular calcium signalling, and also whether functional L-type VGCCs were expressed by ECs.

Figure **4.3.21 D** shows that over a 30 second baseline, there were no spontaneous Ca^{2+} events in ECs. This contrasts with findings in intact, pressurised RMAs, where ECs typically display spontaneous Ca^{2+} waves at rest, at an average frequency of 0.015 Hz per cell (Kansui *et al.*, 2008). In EC tubes, neither the addition of L-type VGCC activator Bay K 8644 (30 nM; mean F/F_0 = 0.98 ± 0.03; P = 0.94; n = 5) nor depolarising agent KCl (45 mM; mean F/F_0 = 1.02 ± 0.03; P = 0.92; n = 5) increased local Ca^{2+} events or global intracellular [Ca^{2+}] above baseline. In contrast, ACh (100 nM) added at the end of each experiment triggered Ca^{2+} waves (peak F/F_0 = 2.21 ± 0.25; P = 0.026 vs baseline; n = 5) in 82.60 ± 4.27 % of cells, indicating that cells remained viable following tube extraction and throughout each experiment. These results suggest that any VGCCs expressed by RMA ECs are not functional and do not contribute to EC Ca^{2+} dynamics.

In these experiments, isotonic KCl was used to prevent cells from shrinking or swelling, as such changes could affect fluorescence responses. In initial trials, 2 M KCl solution was added to the perfusion buffer already in the chamber, resulting in a solution with a greater osmolarity than that of the cells. This caused the cells to shrink, leading to a marked increase in fluorescence. This increase was not due to the opening of VGCCs and subsequent Ca^{2+} influx, but rather because the effective cytoplasmic [Ca^{2+}] increased as cell volume decreased.

Considering this observation, a separate stock of perfusion buffer containing 45 mM KCl was used in future experiments, with an osmolarity of ~300 mOsm/L to match that of the cells.

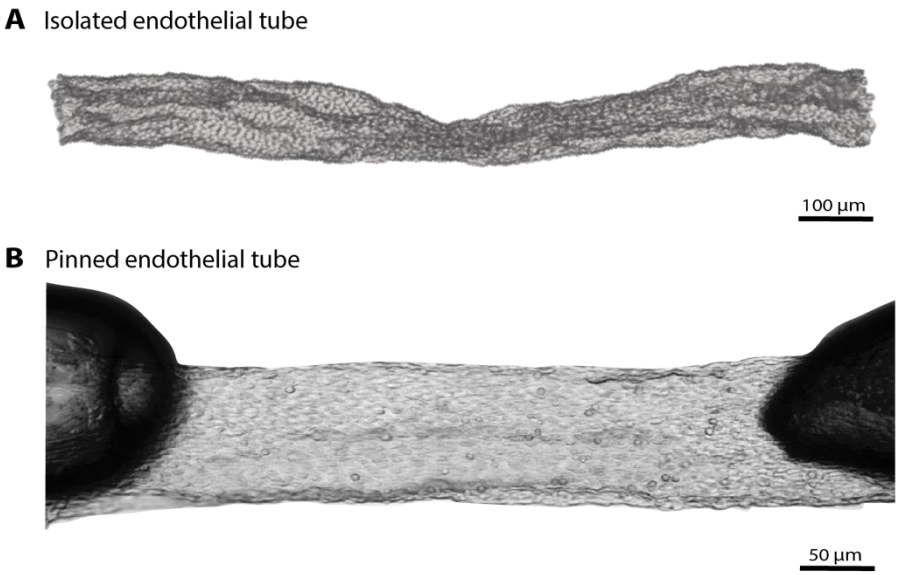
A Isolated endothelial tube
100 µm
B Pinned endothelial tube
50 µm
C Ca2+ indicator-loaded endothelial cells
15 µm
D
100 nM ACh
30 nM Bay K
45 mM KCl
F/F0
Time (seconds)
E
Mean F/F0
30 nM BayK
45 mM KCl
100 nM ACh

Figure 4.3.21. The effect of voltage gated calcium channel (VGCC) activation in isolated endothelial cell (EC) tubes from mesenteric arteries. (**A**) Enzymatic and mechanical dissociation of mesenteric artery media and adventitia reveals tube of ECs with homocellular connections intact. (**B**) EC tubes can be pinned and stretched in an imaging chamber using polished glass micropipettes visible in the image. (**C**) Pinned ECs loaded with calcium indicator Calbryte 520 AM (50 nM) with red region of interest outlining a single cell. The white line corresponds to the kymograph in D. (**D**) Fluorescence time course corresponding to red region of interest. Neither activation of L-type VGCCs with Bay K 8644 (30 nM) or membrane depolarization using 45 mM KCl evoked an increase in global EC [Ca^{2+}] (drug additions indicated using red dots). Agents were not washed out between additions due to the fragility of the preparation. 100 nM ACh was added at the end of each experiment to confirm cell viability. (**E**) Bar graph summarising the effects of Bay K 8644, KCl and ACh on EC calcium activity. For Bay K and KCl, mean fluorescence (F) was taken over 10 frames at 3 Hz immediately preceding the addition of the next agent. For ACh, the peak fluorescence was taken. The dashed black line represents mean F/F_0 = 1, where there is no change in fluorescence. Data are means ± SEM of at 3 cells per tube, n = 5 tubes from different rats. *P = 0.0135 and 0.0188 vs Bay K 8644 and KCl, respectively, using repeated measures one-way ANOVA with Bonferroni correction.

4.3.5 Selective blockade of vascular smooth muscle $Ca_V3.2$ channels in rat coronary arteries increases EC Ca^{2+} events

To determine whether the activation of T-type VGCCs expressed by VSMCs contributes to EC [Ca^{2+}], EC calcium imaging was carried out in pressurised RCos (**Figure 4.3.22**). The technical challenges associated with pressurising RCos means that only one successful experiment was completed. To maximise the data generated from this technically demanding experimental set up, drugs were added sequentially. Whilst this means the effects of inhibitors on basal EC Ca^{2+} events cannot be determined, the data still provides valuable insights into the relative effects of these inhibitors on Ca^{2+} dynamics.

After developing stable myogenic tone of ~25 %, spontaneous Ca^{2+} events at an average frequency of ~0.017 Hz per cell (mean of 8 cells from one artery) were observed in ~60 % ECs, shown in Figure **4.3.22 C**. These events, referred to as Ca^{2+} pulsars or VGCC-dependent endothelial calcium transients (VECTors) in the literature, occurred in highly localised sub-cellular regions and did not trigger cell-wide Ca^{2+} waves.

Selective blockade of $Ca_V3.2$ channels with 50 μM Ni^{2+} resulted in a 2.4-fold increase in EC Ca^{2+} event frequency (from 0.72 events per minute to 1.75 events per minute; n = 1; **Figure 4.3.22 D**). This indicates that VSMC $Ca_V3.2$ channels are open in unstimulated, myogenically-active RCos, and they have a paradoxical effect of limiting Ca^{2+} influx into VSMCs, which in turn means that less Ca^{2+} diffuses into ECs through MEPs. The addition of 300 nM NNC 55-0396 to block all T-type VGCCs resulted in a 1.15-fold reduction in Ca^{2+} event frequency (from 1.75 events per minute to 1.53 events per minute, n = 1), which was reduced 1.19-fold further by L-type VGCC blocker nifedipine (1 μM; from 1.53 events per minute to 1.28 events per minute; n = 1). This suggests that VSMC $Ca_V3.1$ and $Ca_V3.3$ channels, along with $Ca_V1.2$ channels, are at least partly responsible for the increased EC Ca^{2+} events observed following $Ca_V3.2$ blockade.

Interestingly, the addition of Ni^{2+} did not change the percentage of active ECs (defined as cells displaying at least one Ca^{2+} event during recording; **Figure 4.3.22 E**) observed at baseline. Blocking $Ca_V3.1$ and $Ca_V3.3$ channels with NNC 55-0396 reduced the percentage of active ECs from 64.71 % to 37.50 % (n = 1), whilst the addition of nifedipine increased the percentage of active ECs to 62.50.

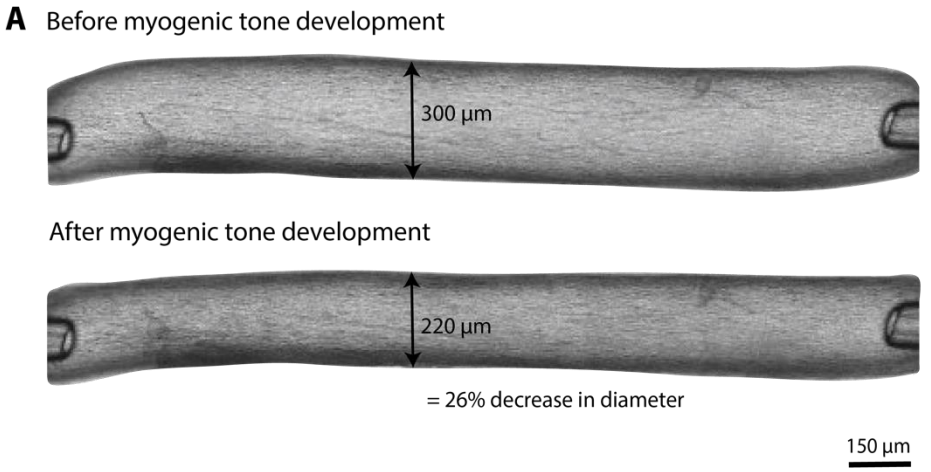
A
Before myogenic tone development
300 µm
After myogenic tone development
220 µm
= 26% decrease in diameter
150 µm
B
Ca2+ indicator-loaded endothelial cells
10 µm
C
2.0
1.5
1.0
0.5
F/F0
Sub-cellular region
Whole cell
0
60
120
180
Time (seconds)
D
Calcium events / cell / min
2.0
1.5
1.0
0.5
0.0
Baseline
50 µM Ni 2+
300 nM NNC
1 µM nifedipine
E
% active cells
80
60
40
20
0
Baseline
50 µM Ni 2+
300 nM NNC
1 µM nifedipine

Figure 4.3.22. The effect of T- and L-type voltage gated calcium channel (VGCC) blockade on endothelial cell (EC) calcium events in a coronary artery with myogenic tone. (**A**) Pressurised coronary artery before and after myogenic tone development. After the artery developed stable myogenic tone, ECs were selectively loaded with calcium indicator Calbryte 520 AM (50 nM) and imaged using confocal microscopy. (**B**) Calcium indicator-loaded ECs with region of interest (red circle) indicated. The white line corresponds to the kymograph in C. (**C**) Fluorescence time course corresponding to red region of interest in EC from coronary artery with myogenic tone. Note the spatially restricted calcium spark activity compared to the mean fluorescence response of the whole cell (grey line). (**D**) Bar graph summarising localised calcium activity at baseline (with myogenic tone), and in the sequential presence of Ni^{2+} (50 μM), NNC 55-0396 (300 nM), and nifedipine (1 μM), expressed as calcium events per cell per minute. Drugs were added at least 60 seconds apart and were not washed out between additions. (**E**) Bar graph summarising localised calcium activity expressed as % of active cells. Data are means of at least 8 cells, all of which responded to 100 nM ACh added at the end of the run, from a single artery.

Endothelium-independent vasodilation

4.3.6 Characterisation of NNC 55-0396 and nifedipine in rat coronary arteries

Despite the vasodilatory effects of non-selective T-type VGCC blocker NNC 55-0396 and L-type VGCC blocker nifedipine being widely demonstrated in the literature, their effects on RCos with myogenic tone are poorly characterised.

Addition of 300 nM NNC 55-0396 resulted in near-complete relaxation of RCos from myogenic tone (76.63 ± 20.1 % relaxation; n = 5; **Figure 4.3.23 C**), which was irreversible following wash out. Arteries that did not spontaneously develop myogenic tone were either incubated with L-NAME (10 μM) or L-NAME and NS 6180 (1 μM). The similar IC_{50} values calculated for NNC 55-0396 in these arteries confirms that T-type VGCC blockade mediates vasodilation independently of NO and EDH (see **Table 4.3.6** for values).

Similarly, nifedipine evoked robust vasodilation in RCos, both from myogenic tone and from contraction caused by L-NAME and NS 6180. Nifedipine was highly potent, resulting in complete relaxation at approximately 10 pM (95.54 ± 2.61 % relaxation; n = 4; **Figure 4.3.23 D**; see **Table 4.3.6** for additional values). Upon washing out, myogenic tone was immediately reestablished to similar levels observed before adding the inhibitor. Like NNC 55-0396, IC_{50} values for nifedipine were similar in arteries with myogenic tone and in arteries preconstricted with L-NAME and NS 6180 (**Table 4.3.6**). This suggests that nifedipine-mediated vasodilation occurs exclusively via VSMCs.

Inhibitor	IC_{50} (MT)	IC_{50} (L-N)	IC_{50} (L-N + NS 6180)	Corresponding figure
NNC 55-0396	40.7 nM (n =6)	109.0 nM (n = 5)	87.4 nM (n = 5)	4.3.23 C
Nifedipine	597 fM (n = 5)	-	986 fM (n = 7)	4.3.23 D

Table 4.3.6. Summary of the pharmacological properties of voltage-gated calcium channel inhibitors NNC 55-0396 and nifedipine in rat coronary arteries. The vasodilatory effects of the inhibitors were assessed in arteries with myogenic tone (MT) or following pre-incubation with L-NAME (L-N; 10 μM) or L-N and NS 6180 (1 μM).

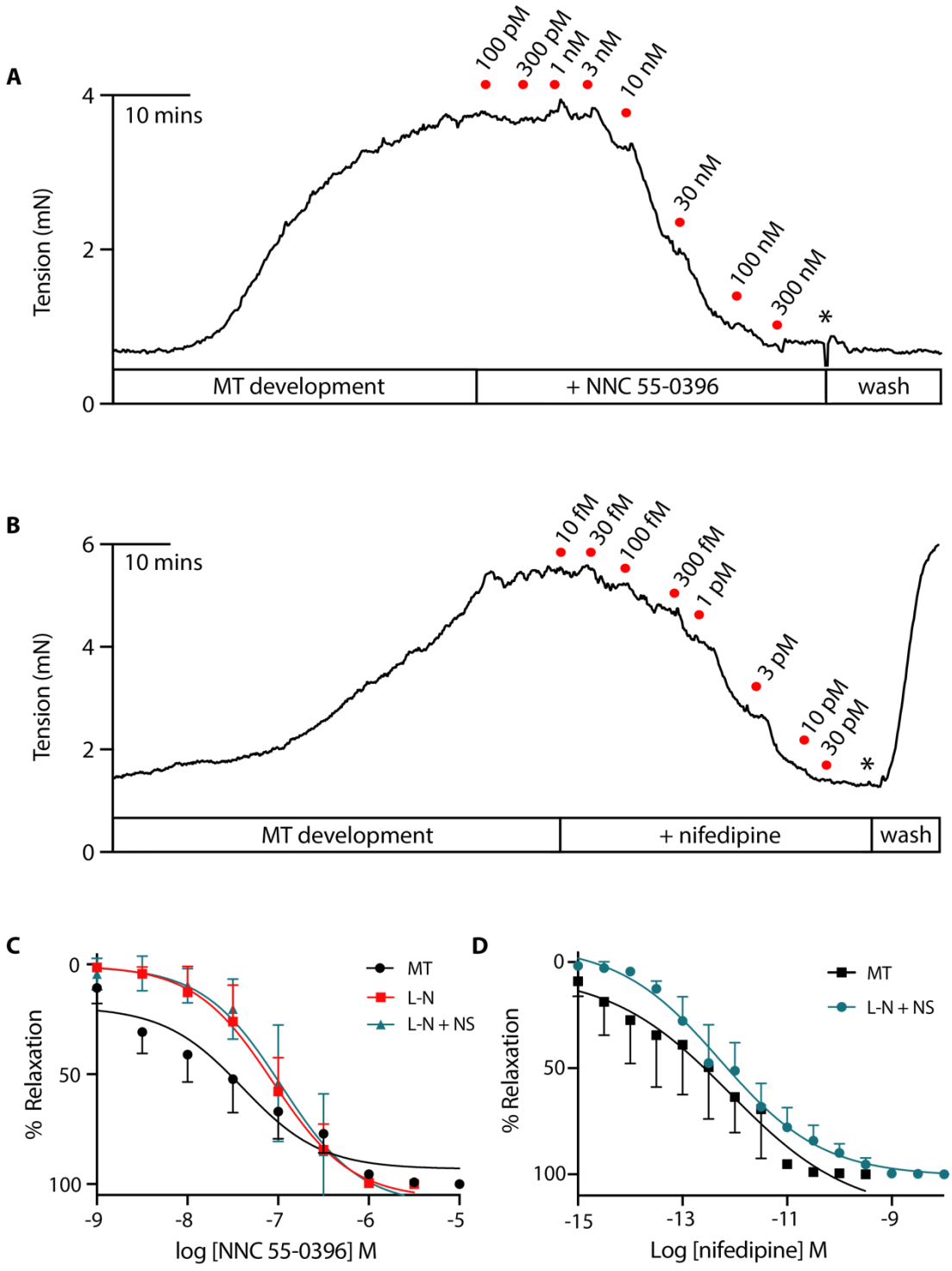
A
10 mins
Tension (mN)
100 pM
300 pM
1 nM
3 nM
10 nM
30 nM
100 nM
300 nM
*
MT development
+ NNC 55-0396
wash
B
10 mins
Tension (mN)
10 fM
30 fM
100 fM
300 fM
1 pM
3 pM
10 pM
30 pM
*
MT development
+ nifedipine
wash
C
% Relaxation
MT
L-N
L-N + NS
log [NNC 55-0396] M
D
% Relaxation
MT
L-N + NS
Log [nifedipine] M

Figure 4.3.23. Effect of T- and L-type voltage-gated calcium channel (VGCC) blockade on wire-mounted coronary artery tension. Representative traces showing the concentration-dependent relaxation of coronary arteries with myogenic tone (MT) in response to T-type VGCC blocker NNC 55-0396 (**A**) and L-type VGCC blocker nifedipine (**B**). Following wash out (indicated using asterisks), NNC 55-0396 relaxation persisted, whereas nifedipine was fully reversible. (**C**) Summary dose-response curve comparing relaxation to NNC 55-0396 in myogenically-active coronary arteries (IC_{50} = 40.7 nM) vs coronary arteries preconstricted with 10 μM L-NAME (L-N; IC_{50} = 109.0 nM) or 10 μM L-N + 1 μM NS 6180 (IC_{50} = 87.4 nM). Data are means ± SEM; n = 5-6. P = 0.3030 for IC_{50} values for MT vs L-N and P = 0.3983 for MT vs L-N + NS using Mann-Whitney U test. (**D**) Summary dose-response curve comparing relaxation to nifedipine in myogenically-active coronary arteries (IC_{50} = 597.2 fM) vs coronary arteries preconstricted with 10 μM L-N + 1 μM NS 6180 (IC_{50} = 986.1 fM). Data are means ± SEM; n = 4-8. P = 0.2677 for IC_{50} values using Mann-Whitney U test.

4.3.7 $Ca_V3.2$ channels negatively regulate myogenic tone development in rat coronary arteries

To determine whether the $Ca_V3.2$ channel/RyR/BK_{Ca} channel signaling microdomain identified in cerebral and mesenteric arteries is present in RCos, isometric tension responses in the presence of different pharmacological blockers were measured (**Figure 4.3.24**).

In arteries with myogenic tone, blocking $Ca_V3.2$ channels with Ni^{2+} (50 μM) enhanced contraction almost 2-fold, from a mean of 2.88 ± 0.94 mN/mm to 4.49 ± 0.06 mN/mm (P = 0.0042; n = 6) This response was irreversible, although arteries did relax when ACh was added (1 μM ACh caused ~70 % relaxation; data not shown).

Figure 4.3.24 B shows that Ni^{2+} caused a similar amount of contraction in arteries with myogenic tone (an increase of 1.33 ± 0.38 mN/mm; n = 6) to arteries incubated with L-NAME and NS 6180 (an increase of 1.80 ± 0.38 mN/mm; n = 5) and arteries where the endothelium had been removed (an increase of 2.30 ± 0.87 mN/mm; n = 5). This reveals that the increased number of endothelial Ca^{2+} events observed in pressurised RCos following $Ca_V3.2$ channel blockade are not sufficient to regulate arterial tension by stimulating NO/EDH production, and that the VSMC $Ca_V3.2$ signaling microdomain opposes excess vasoconstriction independently of the endothelium. As the development of myogenic tone in RCos is believed to be underpinned by calcium influx through VSMC VGCCs, the contraction caused by Ni^{2+} was surprising. An explanation for this paradoxical response is that the calcium current through $Ca_V3.2$ channels activates nearby calcium-activated potassium channels, such as BK_{Ca} channels, thus providing negative feedback control to prevent over-constriction.

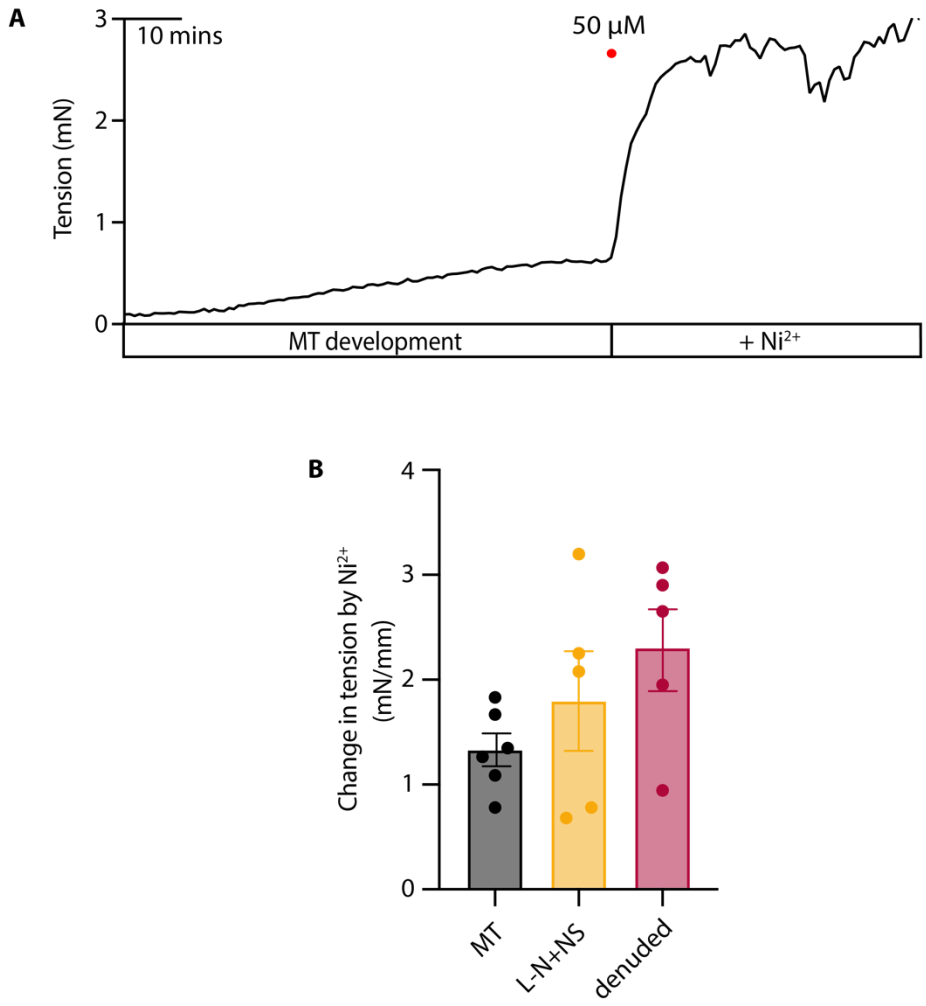

Figure 4.3.24. Effect of $Ca_V3.2$ voltage gated calcium channel (VGCC) blocker Ni^{2+} on wire-mounted coronary artery tension. (**A**) Representative trace showing the contractile effect of Ni^{2+} on a coronary artery with myogenic tone (MT). The red dot indicates when Ni^{2+} was added. (**B**) Summary bar chart showing the effect of 50 µM Ni^{2+} on artery tension either from MT, following preconstriction to L-NAME (L-N; 10 µM) + NS 6190 (1 µM), or in denuded arteries. Data are means ± SEM; n = 5-6 rats. P > 0.9999 for MT vs L-N + NS, P = 0.1963 for MT vs denuded, and P = > 0.9999 for L-N + NS vs denuded, using ordinary one-way AVOVA with Bonferroni's correction.

4.3.8 $Ca_V3.2$ channels form a signaling microdomain with BK_{Ca} channels in rat coronary artery smooth muscle cells

Next, the BK_{Ca} channel blocker paxilline was also found to elicit vasoconstriction in myogenically-active arteries, albeit to a lesser extent than Ni^{2+}, from a mean of 3.17 ± 1.09 mN/mm to 4.15 ± 1.07 mN/mm (P = 0.0154; n = 5; **Figure 4.3.25 B**). Furthermore, the diminished (but not statistically significant) contractile effect of Ni^{2+} in the presence of paxilline (a difference of 1.33 mN/mm ± 0.38 with paxilline compared to 1.00 mN/mm ± 0.33 without; P = 0.1678; n = 5-6; **Figure 4.3.25 A**) suggests that BK_{Ca} channels are involved in the $Ca_V3.2$ channel signaling microdomain. Although paxilline attenuated Ni^{2+}-induced vasoconstriction, Ni^{2+} still evoked further contraction, increasing from a mean of 4.15 ± 1.01 mN/mm to 5.16 ± 0.77 mN/mm (P = 0.0279; n = 5; **Figure 4.3.25 B**). This suggests that, in addition to BK_{Ca} channels, there may be additional calcium-activated potassium channels involved in the $Ca_V3.2$ signaling microdomain in rat coronary arteries which have not yet been recognised in the literature.

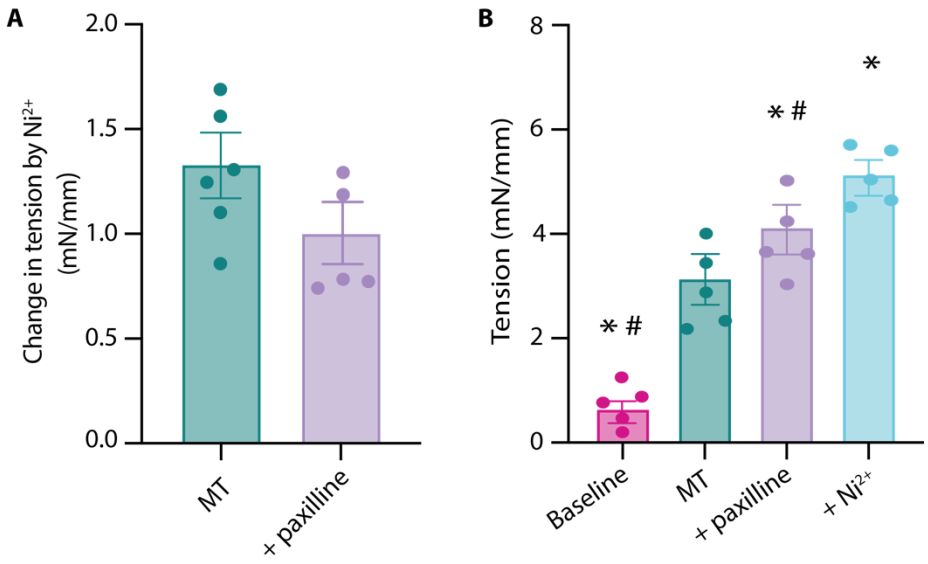

Figure 4.3.25. Effect of BK_{Ca} channel blocker paxilline on Ni^{2+}-induced contraction of rat coronary arteries. (**A**) Summary bar chart showing the effect of 50 μM Ni^{2+} on artery tension either from MT or following incubation with BK_{Ca} channel blocker paxilline (1μM). Data are means ± SEM; n = 5-6 rats. P = 0.1678 for MT vs paxilline, using unpaired student's t test. (**B**) Summary bar chart showing the sequential effects of paxilline (1 μM) and Ni^{2+} (50 μM) on coronary artery tension from MT. Ni^{2+} was added in the presence of paxilline once artery tension had stabilised. Data are means ± SEM; n = 5 rats. *P = 0.0154 for baseline vs paxilline and #P = 0.0021 for baseline vs Ni^{2+}, *P = 0.0228 for MT vs paxilline and #P = 0.0012 for MT vs Ni^{2+}, and *P = 0.0279 for paxilline vs Ni^{2+}, using repeated measures one-way ANOVA with Bonferroni's correction.

4.4 Discussion

The current study investigated the expression of T-type VGCCs in ECs and VSMCs of rat resistance mesenteric and coronary arteries, and the function of T-type VGCCs in rat resistance coronary arteries. These data support the hypothesis that these channels are involved in vasodilation of coronary resistance arteries, with channels expressed by VSMCs, but not ECs, being responsible for their effects.

For the first time, RNAscope was used to detect and quantify VGCC mRNA expression in RCos and RMAs. The present study shows that mRNA encoding L-type VGCCs and all 3 T-type channel subtypes is expressed by ECs and VSMCs of both artery types (**Figures 4.3.1 – 4.3.8**). Previous studies employing molecular biology techniques such as RT-PCR and gel electrophoresis also found mRNA encoding VGCCs expressed in arteries (see **Table 4.4.1** for summary). There were some inconsistencies in the mRNA identified in whole artery homogenates compared to in isolated VSMCs; for example, all 4 VGCC mRNA transcripts were present in whole rat cerebral arteries, whereas only *Cacna1g* and *Cacna1h* transcripts (encoding $Ca_V3.1$ and $Ca_V3.2$) were identified in isolated VSMCs (El-Rahman *et al.*, 2013). This may indicate that $Ca_V1.2$ and $Ca_V3.3$ channels were expressed by other vascular cells such as ECs or perivascular nerve cells, or that mRNA levels in VSMCs were too low to be detected. The technical difficulties associated with extracting sufficient amounts of RNA from ECs to perform molecular analysis means that the expression of VGCCs mRNA transcripts in ECs has not been extensively investigated. This issue is addressed by using RNAscope as it allows individual mRNA molecules to be visualised in the different cell types of whole arteries.

The presence of L- and T-type VGCC mRNA in ECs was unexpected, given that these cells are generally considered non-excitable. Nonetheless, *Cacna1c* mRNA (encoding $Ca_V1.2$) was highly expressed in mesenteric and coronary ECs, though predominantly localised within the

nuclei (**Figure 4.3.1 E** and **4.3.5 E**). This pattern contrasts with *Cacna1c* mRNA expression in RMA and RCo VSMCs, which was distributed evenly between the nucleus and cytoplasm (**Figure 4.3.1 F and 4.3.5 F**). The differential localisation of *Cacna1c* mRNA in ECs and VSMCs suggests a key regulatory distinction between these two cell types. The nuclear retention of *Cacna1c* mRNA in ECs may allow for its controlled export into the cytoplasm and subsequent translation into $Ca_V1.2$ protein under specific conditions. Reports demonstrate that translation of $Ca_V1.2$ protein increases during acute hypoxia, as the accumulation of hypoxia-inducible factors (HIFs) leads to degradation of microRNAs which usually cleave and destabilise *Cacna1c* mRNA (Xing *et al.*, 2022). This may also account for the observations of L-type I_{Ca} in cultured, but not native ECs, as cultured ECs may be exposed to environmental stressors which alter their characteristics (Bossu *et al.*, 1989; Wu *et al.*, 2003; Olschewski *et al.*, 2001). In contrast, VSMCs lack this nuclear mRNA 'store', potentially limiting their ability to rapidly upregulate $Ca_V1.2$ protein in response to external stimuli. Indeed, mRNA and protein corresponding to L-type VGCCs was upregulated in mesenteric VSMCs from adult, but not juvenile, spontaneously hypertensive rats, compared to VSMCs from age-matched controls (Pratt *et al.*, 2002). The difference in time taken by ECs and VSMCs to upregulate $Ca_V1.2$ expression under pathophysiological conditions requires further investigation, especially in native cells, where $Ca_V1.2$ channels may contribute to vasodilation through enhancing EDH/NO production.

Citation	Species / vascular bed	VGCC mRNA identified	Notes
Gustafsson *et al.* (2001)	Rat mesenteric arterioles	Cacna1g, Cacna1h	
Hansen *et al.* (2001)	Rat renal arteries	Cacna1c, Cacna1g, Cacna1h	
Jensen *et al.* (2004)	Rat mesenteric arterioles	Cacna1g	*Cacna1h* and *Cacna1i* not investigated
Nikitina *et al.* (2007)	Dog cerebral arteries	Cacna1c, Cacna1g, Cacna1i	*Cacna1h* not investigated
Kuo *et al.* (2010)	Rat cerebral arteries	Cacna1c, Cacna1g, Cacna1h	
El-Rahman *et al.* (2013)	Rat cerebral arteries	Cacna1c, Cacna1g, Cacna1h, Cacna1i	
Smith *et al.* (2020)	Rat mesenteric arteries	Cacna1c, Cacna1g, Cacna1h	*Cacna1i* not investigated

Table 4.4.1. Summary of literature reporting expression of voltage-gated calcium channel (VGCC) mRNA in whole vessels using molecular biology techniques.

While the present study detected weak expression of T-type VGCC protein in ECs (**Figure 4.3.10** and **4.3.11**), calcium imaging experiments in isolated tubes of endothelium from RMAs revealed that these channels do not underpin Ca^{2+} influx **(Figure 4.3.21**). Assuming that the primary antibodies used were specific for cleaved fragments of their targets, the $Ca_V3.1$, $Ca_V3.2$, and $Ca_V3.3$ channels detected by immunolabelling may not be functional for various reasons, including protein misfolding, a lack of essential post-translational modifications, or incorrect trafficking to the plasma membrane. Disparities between protein expression and function have previously been observed, most notably in cystic fibrosis, where mutated, non-functional chloride channels are detected by immunoprecipitation/SDS-PAGE and immunolabelling (Cheng *et al.*, 1990). This is believed to be a result of defective intracellular transport and processing of channels due to incomplete glycosylation, resulting in them being retained in the endoplasmic reticulum where they are subsequently degraded. A similar mechanism may be responsible for the non-functional VGCCs expressed by ECs, as

glycosylation of these channels is critical for their proper functional expression (Lazniewska and Weiss, 2017).

The endothelial expression of T-type VGCCs, specifically $Ca_V3.1$ and $Ca_V3.2$, is supported by functional and RT-PCR data from cultured bovine and rat ECs (Bossu *et al.*, 1989; Wu *et al.*, 2003), immunohistochemistry in rat mesenteric and cerebral ECs *in situ* (Braunstein *et al.*, 2009; Kuo *et al.*, 2010), and functional data from *ex vivo* arteries from knock out mice (Svenningsen *et al.*, 2014; Gilbert *et al.*, 2017). Due to the paucity of evidence for the role of endothelial T-type VGCCs in wild-type arteries, the EC tube data presented herein is particularly insightful. This evidence is strengthened by the fact that EC tubes likely reflect *in situ* EC Ca^{2+} dynamics more accurately than previous studies involving cultured or freshly isolated ECs due to the preservation of homocellular connections. It is tempting to speculate that coronary artery ECs also lack VGCCs, although due to the variability in VGCC expression across different vascular beds from the same species, it will be important to replicate these experiments in coronary artery EC tubes.

Immunolabelling of T-type VGCCs in pressurised RMAs showed that expression of all 3 channel subtypes is enriched around MEPs (**Figures 4.3.18 – 4.3.20**). Careful analysis of reconstructed 3D images through the artery wall, combined with EC tube Ca^{2+} imaging, revealed that these channels were expressed by VSMCs at the points where MEPs made contact. Interestingly, there was a substantial number of holes in the IEL that did not house a MEP yet did show signal for T-type VGCCs. This may indicate that MEPs are primed to form in these locations. The dynamic formation of MEPs has been demonstrated in pathological states, for example, the number of MEPs in the vasculature increases during ligation-induced hypertension (Michel *et al.*, 1995). This upregulation may allow resistance arteries to compensate for pathological vascular remodelling and maintain EDH-mediated vasodilation. Whilst the processes governing MEP formation in arteries are poorly understood, the findings

presented herein hint that dynamic formation of MEPs may occur in healthy resistance arteries, perhaps rapidly in response to acute, local changes in oxygen demand.

The close proximity of VSMC T-type VGCCs and MEPs in RMAs suggests that Ca^{2+} conducted by these channels may promote endothelium-mediated feedback vasodilation. A similar mechanism has been demonstrated in cremaster arterioles, where Ca^{2+} entering through L-type VGCCs expressed by depolarised VSMCs also diffuses into adjacent ECs via MEGJs to trigger IK_{Ca} channel-mediated hyperpolarisation and vasodilation (Garland *et al.*, 2017). The present study found that blocking VSMC $Ca_V3.2$ channels in pressurised coronary arteries increased the frequency of EC Ca^{2+} events which were sensitive to both NNC 55-0396 and nifedipine (**Figure 4.3.22**). These events closely resembled the highly localised Ca^{2+} events recorded in ECs of pressurised cremaster arterioles, which aligned with MEPs and were termed VECTors (Garland *et al.*, 2017). Unlike in cremaster ECs, the VECTors observed in this study did not appear to evolve into Ca^{2+} puffs or cell-wide Ca^{2+} waves, a process believed to rely on the activation of endothelial IP_3 receptors (IP_3Rs). Taken together with the EC tube data, this suggests that the EC Ca^{2+} events observed in RCos were driven by T- and L-type VGCCs expressed by VSMCs, with the initial increase in intracellular [Ca^{2+}] in these cells subsequently diffusing into ECs via MEPs (see **Figure 4.4.1**). The close proximity of VSMC T-type VGCCs to MEPs is likely important for their contribution to EC Ca^{2+} as their currents are tiny and transient, thus channel opening only allows a small amount of Ca^{2+} into the cell at once. The effective range over which Ca^{2+} can exert its effects is limited by its short diffusion constant of ~38 $\mu m^2/s$ (Allbritton *et al.*, 1992), so for T-type I_{Ca} to impact EC Ca^{2+}, it follows that T-type channels must be expressed close to MEGJs.

Moreover, this study provides further support for Ca^{2+} being the principal signal involved in myoendothelial feedback following VSMC depolarisation, as IP_3 is not generated following VGCC opening; phospholipase C, which produces IP_3, is autoinhibited in the absence of G_q receptor stimulation (Zhang and Neer, 2001). It remains uncertain whether the increased EC

Ca^{2+} events in RCos in this study directly contribute to feedback vasodilation. Although removing the endothelium's influence did enhance the vasoconstrictive effect of Ni^{2+}, the difference was not statistically significant compared to in intact arteries (**Figure 4.3.24**). Additionally, the vasodilatory effects of NNC 55-0396 and nifedipine were similar in control vs L-NAME + NS 6180 treated arteries. Overall, it appears that depolarisation-driven feedback vasodilation does not occur in RCos, perhaps because VECTors alone do not sufficiently elevate EC Ca^{2+} to activate NO/EDH pathways.

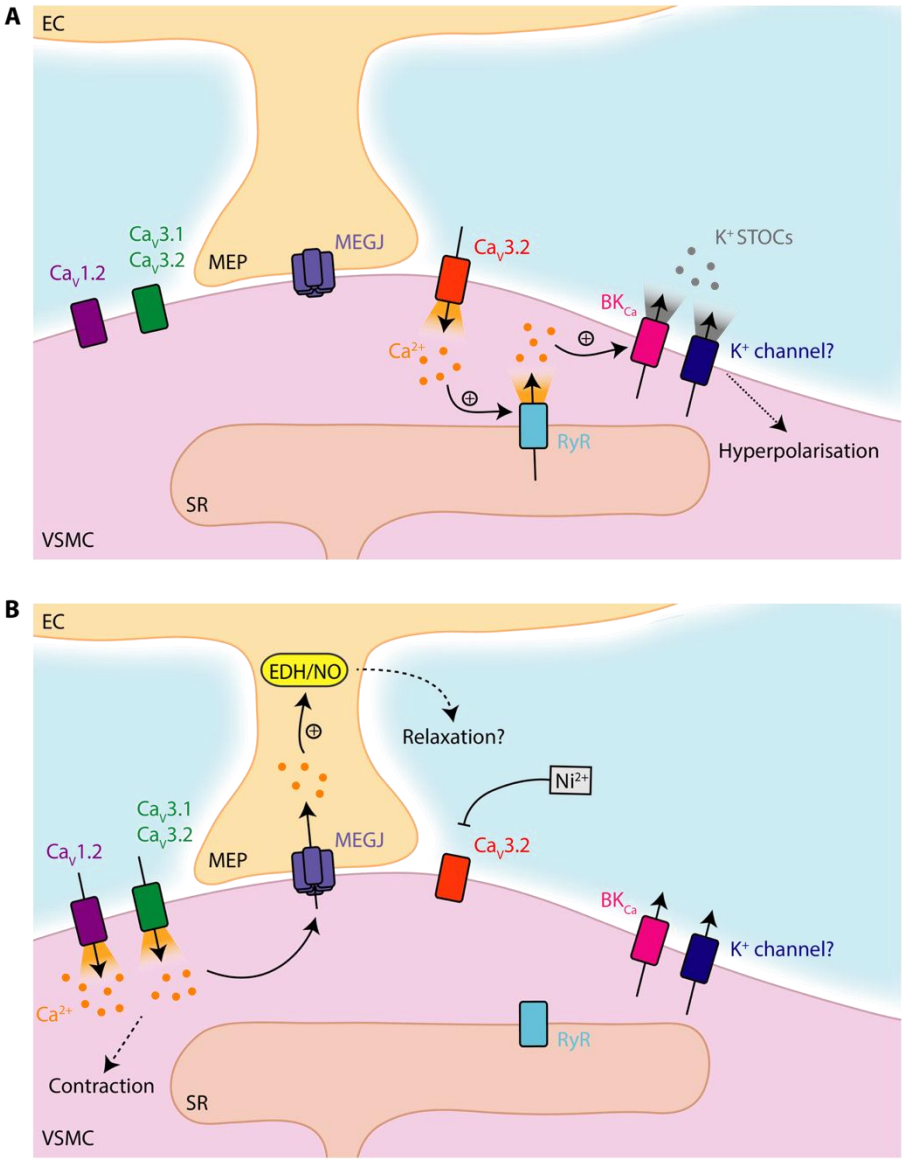

Figure 4.4.1. Proposed mechanism of Ni^{2+}-induced vasoconstriction in coronary resistance arteries. (A) Ca^{2+} influx through vascular smooth muscle cell (VSMC) $Ca_V3.2$ channels activates nearby ryanodine receptors (RyRs) located on the sarcoplasmic reticulum (SR), resulting in Ca^{2+} release and activation of calcium-activated K^+ channels, including BK_{Ca} channels. The opening of K^+ results in spontaneous transient outward currents (STOCs), which hyperpolarise the cell membrane and oppose opening of voltage-gated calcium channels (VGCCs), preventing excess vasoconstriction from occurring. (**B**) Blocking $Ca_V3.2$ channels with 50 μM Ni^{2+} removes the hyperpolarising influence of K^+ channel activation, resulting in depolarisation driven VGCC opening and Ca^{2+} influx into VSMCs. Due to the close proximity of L- and T-type VGCCs to myoendothelial projections (MEPs), this Ca^{2+} signal diffuses into endothelial cells (ECs) via myoendothelial gap junctions (MEGJs) to increase the frequency of Ca^{2+} events in ECs. These localised Ca^{2+} events may stimulate nitric oxide (NO) or endothelium-dependent hyperpolarisation (EDH) to produce feedback vasodilation.

The observation that Ca^{2+} influx into VSMCs via VGCCs did not trigger feedback vasodilation in RCos does not necessarily imply that this mechanism is absent. It is possible that myoendothelial feedback does occur in coronary arteries but requires the transfer of IP_3 into ECs to initiate Ca^{2+} waves and subsequent NO/EDH generation. Some studies suggest that IP_3, which is generated in VSMCs upon activation of G_q-coupled receptors by endogenous agonists, is the predominant myoendothelial signalling molecule (Lamboley *et al.*, 2005; Nausch *et al.*, 2012; Tran *et al.*, 2012). However, the interdependence of Ca^{2+} and IP_3, as well as technical limitations associated with measuring the two signals within the confined space of MEPs, made attempts to isolate their contributions to myoendothelial feedback difficult. Acknowledging this, later studies found that Ca^{2+} was also directly involved in myoendothelial feedback (Dora *et al.*, 1997; Oishi *et al.*, 2001; Garland *et al.*, 2017). Overall, our current understanding of myoendothelial feedback highlights a complex interplay between both Ca^{2+} and IP_3, with the precise contributions of these signalling molecules likely varying between vascular beds.

In the coronary microcirculation, the activation of feedback vasodilation may require the combined increase of IP_3 and Ca^{2+} in VSMCs e.g., following noradrenaline release from adventitial sympathetic nerves. This may be important during exercise to maintain adequate coronary blood flow and to prevent vasospasm from occurring. Indeed, this been demonstrated in pig coronary arteries, where vasodilation caused by myoendothelial feedback was more pronounced when VSMCs were stimulated with a G_q-receptor agonist compared to high $[K^+]$ solution (Budel *et al.*, 2001). Although the present study suggests that both signals are required to activate feedback vasodilation in coronary arteries, due to the small sample sizes used, further investigations will be required to elucidate the mechanisms leading to feedback vasodilation in these arteries.

Next, the interaction of $Ca_V3.2$ channels with BK_{Ca} channels was investigated to determine whether the increase in EC Ca^{2+} event frequency upon application of Ni^{2+} was a result of

blocking the $Ca_V3.2$/RyR/BK_{Ca} channel signalling microdomain (**Figure 4.3.24**). In agreement with studies using rat and human cerebral arteries, mouse mesenteric arteries (Harraz *et al.*, 2014a; Harraz *et al.*, 2015), and mouse epigastric arteries (Mullan *et al.*, 2017), the present study indicates that Ni^{2+}, at a concentration that should selectively block $Ca_V3.2$ channels (50 μM; Zamponi *et al.*, 1996), produced vasoconstriction in RCos with myogenic tone. Blocking BK_{Ca} channels with paxilline (1 μM) also induced vasoconstriction, albeit to a lesser extent than Ni^{2+}, and applying Ni^{2+} in the presence of paxilline evoked further vasoconstriction (**Figure 4.3.25**). Both these findings contrast with those reported by Harraz *et al.* (2014a), who found that paxilline evoked a similar level of vasoconstriction to Ni^{2+}, and that addition of Ni^{2+} following paxilline did not produce additive vasoconstriction. In RCos, it therefore appears that some of the vasoconstriction evoked by Ni^{2+} is due to BK_{Ca} channel blockade, though it is likely that additional Ca^{2+}-activated K^+ channels are involved such as SK_{Ca} or IK_{Ca} channels (See **Figure 4.4.1** for suggested mechanism). Although it is generally accepted that the only Ca^{2+}-activated K^+ channels expressed by VSMCs are BK_{Ca} channels (Ledoux *et al.*, 2006), further research would be required in coronary arteries to rule out their role in in Ni^{2+}-mediated vasoconstriction.

Intriguingly, the effects of Ni^{2+} on STOC frequency reported in rat cerebral arteries and mouse epigastric arteries were opposite; STOCs decreased in rat cerebral arteries, whereas they increased in mouse epigastric arteries (Harraz *et al.*, 2014a; Mullan *et al.*, 2017). In mouse epigastric arteries, contraction to Ni^{2+} was not reduced when arteries were pre-incubated with paxilline, which deviates from previous findings in rat cerebral and mouse mesenteric arteries and in RCos presented herein. Whilst the present study did not investigate STOCs in VSMCs, the similar effects of paxilline to rat cerebral and mouse mesenteric arteries makes it likely that Ni^{2+} produces vasoconstriction in RCos by decreasing STOC frequency.

In order to conclude that part of the vasoconstriction caused by Ni^{2+} is a result of removing the stimulatory effect of $Ca_V3.2$ channels on nearby BK_{Ca} channels, it is important to determine

the specificity of Ni^{2+} as a pharmacological tool. Early molecular cloning studies revealed that of the VGCC isoforms, $Ca_V3.2$ channels are most sensitive to Ni^{2+} (IC_{50} = 13 μM in *Xenopus* oocytes and HEK-293 cells; Lee *et al.*, 1999) . The concentrations of Ni^{2+} used in studies to maximally inhibit $Ca_V3.2$ channels (30 – 50 μM) fall far below the amount required to block $Ca_V1.3$, $Ca_V3.3$, and $Ca_V1.2$ channels, providing support for Ni^{2+}'s $Ca_V3.2$ selectivity. Furthermore, the EC_{50} of Ni^{2+} for constricting mouse epigastric arteries was between 1 – 2.5 μM, which is consistent with block of $Ca_V3.2$ channels (Mullan *et al.*, 2017). Despite its apparent selectivity for $Ca_V3.2$ channels, Mullan *et al.* (2017) speculate that Ni^{2+} evokes vasoconstriction by activating transient receptor potential vanilloid 1 (TRPV1) channels. While this may explain the increased STOC frequency they observed following application of 30 μM Ni^{2+}, it is unlikely as TRPV1 channels require ~1,000-fold higher concentrations of Ni^{2+} for maximal activation (Luebbert *et al.*, 2010). Overall, it appears that the concentrations of Ni^{2+} used in the present study and previous studies do indeed selectively block $Ca_V3.2$ channels. The inconsistencies in Ni^{2+}'s effects on STOC frequency may instead reflect differences depending on artery size, vascular bed, or species, which have yet to be elucidated.

Finally, the unexpectedly high potency of nifedipine in causing vasodilation in small, myogenically-active coronary arteries is worth discussing due to its clinical relevance. The present study found that nifedipine had an IC_{50} of ~600 fM, which is considerably lower than published IC_{50} values in large arteries including coronary arteries (3-9 nM; Chen and Wang, 1997; Cobine *et al.*, 2007), internal thoracic arteries (6 nM; Brixius *et al.*, 2005), and renal arteries (130 nM; Eckert *et al.*, 2000), and resistance arteries from renal and mesenteric vascular beds (both ~1 nM; van der Lee *et al.*, 1999; Figure 22). It is not understood why nifedipine is most potent in the coronary circulation, however, it could be a result of regional differences in expression of L-type VGCCs, or expression of a specific L-type VGCC splice variant with higher affinity for dihydropyridines. Indeed, there is evidence supporting the existence of a smooth muscle $Ca_V1.2$ channel splice variant lacking exon 33, which is more sensitive to nifedipine blockade than the established clone (Liao *et al.*, 2007). These

possibilities, and others, should be investigated further as elucidating mechanisms of vasoconstriction unique to the coronary microcirculation could aid the development of novel vasodilators which selectively target these arteries. This would be particularly useful for treating non-obstructive coronary artery disease and vasospastic angina, especially in individuals without hypertension, who represent approximately half of all affected patients (Berge *et al.*, 2022).

4.5 Conclusions

This study provides novel insights into the expression and function of T-type VGCCs in rat mesenteric and coronary resistance arteries. Our findings demonstrate that mRNA encoding all 3 T-type VGCC subtypes ($Ca_V3.1$, $Ca_V3.2$, and $Ca_V3.3$) is expressed in both ECs and VSMCs of these arteries. Surprisingly, despite the presence of mRNA and protein, functional studies revealed no evidence of T-type VGCC activity in ECs, highlighting the complex post-transcriptional regulation of these channels in the vasculature.

A key novel finding of this research is the localisation of T-type VGCCs near MEPs in mesenteric arteries, which is also likely to occur in coronary arteries. Our data indicate that these channels are primarily expressed on VSMCs and often at points of contact with MEPs, so may contribute to endothelial Ca^{2+} events termed VECTors. This arrangement may facilitate myoendothelial feedback, although the direct contribution to vasodilation in coronary arteries appears limited. Interestingly, blockade of $Ca_V3.2$ channels with Ni^{2+} increased the frequency of EC Ca^{2+} events, suggesting a complex interplay between VSMC T-type VGCCs and EC Ca^{2+} dynamics. This may occur via activation of other VGCCs on VSMCs, as their open probability increases when BK_{Ca} channels close.

Furthermore, we provide evidence for the existence of a $Ca_V3.2/BK_{Ca}$ channel signalling microdomain in rat coronary arteries, which appears to play a role in regulating myogenic tone. Selective blockade of $Ca_V3.2$ channels with Ni^{2+} enhanced vasoconstriction, an effect partially attenuated by pre-incubation with the BK_{Ca} channel blocker paxilline. This suggests that $Ca_V3.2$ channels paradoxically oppose vasoconstriction, likely by activating nearby BK_{Ca} channels.

In conclusion, this study advances our understanding of T-type VGCC function in the microcirculation, particularly in coronary resistance arteries. The findings presented herein not only contribute to the growing body of knowledge on vascular physiology but also open new

avenues for future research. The development of a new methodological approach to study microdomain associations and differences in cellular gene and protein expression will bring new insights to light, especially in the future when the antibodies available for immunohistochemistry improve. As we continue to unravel the intricacies of calcium signalling in the vasculature, these insights may ultimately inform therapeutic strategies for cardiovascular diseases involving microvascular dysfunction, potentially through the development of novel pharmacological agents targeting T-type VGCCs or the $Ca_V3.2/BK_{Ca}$ signalling axis.

5. The Role of Endothelial HCN Channels in Vasodilation of Rat Resistance Arteries

5.1 Introduction

EDH involves the spread of hyperpolarisation from ECs to underlying VSMCs, opposing VGCC activity and maintaining low intracellular [Ca^{2+}]. The EDH mechanism is primarily mediated by two processes: the action of extracellular K^+ originating from ECs, and the direct conduction of hyperpolarisation via MEGJs (Edwards *et al.*, 1998; Yamamoto *et al.*, 1999). This hyperpolarisation is initiated by the activation of endothelial calcium-sensitive K^+ channels, specifically SK_{Ca} and IK_{Ca} channels (Crane *et al.*, 2003a). The resulting K^+ efflux creates localised "K^+ clouds" in the arterial wall, which activate K_{ir} channels and Na^+/K^+-ATPases on VSMCs, leading to their hyperpolarisation and subsequent relaxation.

In addition to this local effect, hyperpolarisation can spread axially along the endothelium in a process known as conducted vasodilation. This phenomenon allows for coordinated vasodilation of upstream arteries which is important for regulating blood flow distribution within tissues, particularly during functional hyperaemia. The spread of hyperpolarisation occurs primarily through homocellular EC-EC gap junctions, with Cxs (Cx37, Cx40, and Cx43) playing a vital role in this process (Emerson and Segal, 2000; Sandow *et al.*, 2006).

While the generation of hyperpolarisation in EDH is well understood, the mechanism by which it is sustained over long distances remains unclear. Current research suggests the involvement of an amplification process, potentially mediated by K_{ir} channels, Na^+/K^+-ATPases, or HCN channels (Goto *et al.*, 2004; Bondarenko and Sagach, 2006; Dora and Garland, 2013). Of particular interest are HCN channels, which are activated by hyperpolarisation and cyclic nucleotides, and conduct cations including Ca^{2+} (Michels *et al.*, 2008). The activation of HCN channels expressed by ECs could lead to Ca^{2+} influx, triggering NO production and/or activation of SK_{Ca} and IK_{Ca} channels, thereby amplifying the spread of hyperpolarisation (see **Figure 1.5.7.2**). However, the expression and function of HCN channels in the native vasculature remains largely unexplored, with limited evidence from HUVECs suggesting the presence of HCN1 and HCN2 isoforms (Civil Urkmez *et al.*, 2024).

Although ivabradine, a non-selective HCN channel blocker, is not believed affect large-scale haemodynamic changes through modulating vascular ion conductance (Drouin *et al.*, 2008; Hohneck *et al.*, 2019), unpublished results from the Dora/Garland group show that a different HCN channel blocker, ZD 7288, prevents endothelial Ca^{2+} influx evoked by hyperpolarisation in cremaster arterioles (**Figure 5.1.1**). This raises the possibility that HCN channels are involved in propagating conducted vasodilation over considerable distances in resistance arteries. To investigate this further, the expression profile of HCN channels in native resistance arteries must be characterised, which is the aim of this chapter. As HCN channels are typically associated with triggering action potentials in the SAN and neurones, demonstrating their expression in arteries will lend key support to existing functional data.

Understanding any potential role of HCN channels in conducted vasodilation is important as this mechanism is impaired in various cardiovascular diseases including hypertension (Kurjiaka, 2004) and diabetes (Sato *et al.*, 2002). Restoring or enhancing conducted vasodilation may therefore be a successful strategy in improving symptoms associated with these diseases. If endothelial HCN channels do indeed facilitate the propagation of conducted vasodilation, drugs which activate these channels may be effective treatments. Moreover, elucidating which specific HCN channel isoforms are expressed in the vasculature may lead to the identification of channel subtypes that are preferentially expressed in blood vessels but not in the heart. This could pave the way for the development of novel drugs that selectively activate vascular HCN channels without affecting cardiac function. This could overcome limitations of current non-selective HCN channel blockers like ivabradine, which may disrupt normal blood flow regulation due to their effects on conducted vasodilation.

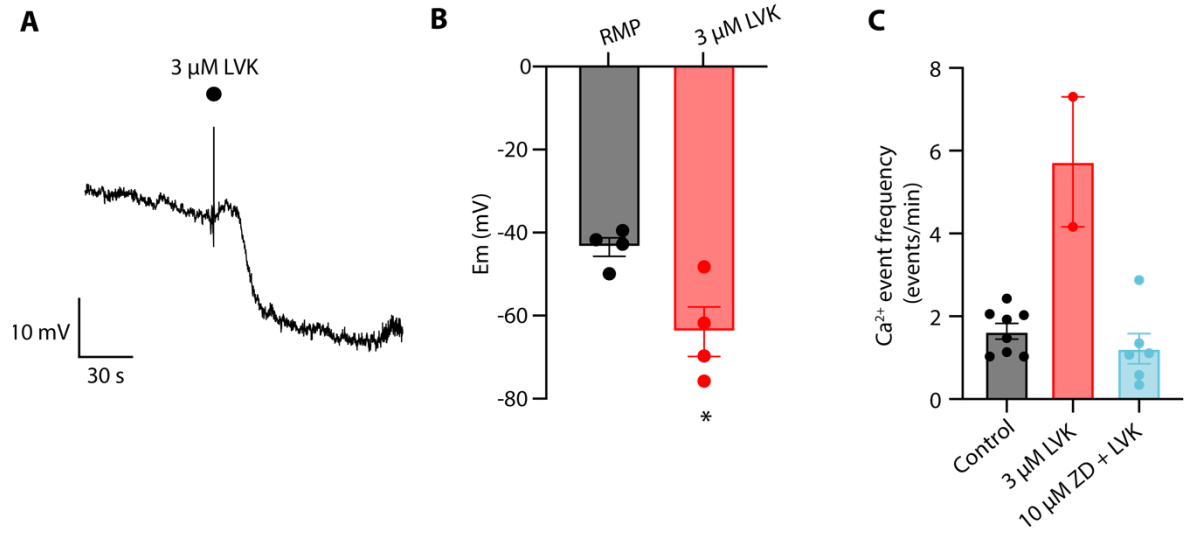

Figure 5.1.1. Unpublished data from the Dora/Garland group showing that hyperpolarisation of endothelial cells (ECs) in pressurised rat cremaster arterioles leads to more frequent Ca^{2+} events. (**A, B**) Application of K_{ATP} channel opener levcromakalim (LVK, 3 µM) results in hyperpolarisation of ECs (black dot represents addition of drug). Data are means ± SEM; n = 4. *P = 0.0298 vs resting membrane potential (RMP) using paired student's t test. (**C**) EC Ca^{2+} event frequency increases upon application of LVK and is reduced back to baseline levels by the sequential addition of HCN channel blocker ZD 7288 (10 µM, ZD). Data are means ± SEM; n = 2 – 8. Data collected by Professor Chris Garland and analysed by Professor Kim Dora.

5.1.1 Aim and hypothesis

Based on unpublished results from the Dora/Garland group, it was hypothesised that endothelial HCN channels may be involved in propagating conducted vasodilation in resistance arteries.

The aim of the present study was to characterise the expression of HCN channels in mesenteric, coronary, and cremaster resistance arteries at the mRNA and protein level.

5.2 Materials and methods

5.2.1 RNAscope

RNAscope was used to detect and quantify *Hcn* channel (*Hcn1-4*) mRNA expression in mesenteric, coronary, and cremaster arteries, as described in Section 2.7. Arteries were fixed whilst isometrically stretched on a wire myograph, where they were normalised to a resting tension equivalent to that generated at 90% of the diameter of the artery at 70 mmHg (mesenteric) or 80 mmHg (cremaster and coronary). Arteries were imaged as described in Section 2.7.2. The method used to determine the nuclear: cytoplasmic localisation of mRNA transcripts is detailed in Section 2.7.3.

5.2.2 Immunohistochemistry

Immunohistochemistry was used to detect protein-level expression of HCN channels in wire myograph-fixed mesenteric, cremaster and coronary arteries (see Section 2.6). Sections of SAN were used as positive controls to test antibody specificity. Following dissection, SAN tissue was fixed and stained in the same way as arteries. The following antibodies were used to label HCN channels:

Target protein	Primary antibody	Immunogen
HCN1	• Alomone APC-056 • Polyclonal • Raised in rabbit • 4.25 µg/mL	Amino acid residues 6-24 of rat HCN1, N-terminus
HCN2	• Alomone APC-030 • Polyclonal • Raised in rabbit • 4 µg/mL	Amino acid residues 147-161 of human HCN2, N-terminus
HCN3	• Invitrogen PA5-104434 • Polyclonal • Raised in rabbit • 5 µg/mL	Amino acid residues 720-770 of human HCN3, C-terminus
HCN4	• Sigma SAB5200035 • Monoclonal	Amino acid residues 1019-1198 of rat HCN4, C-terminus

• Raised in mouse • 5 µg/mL

For HCN 1-3 channels, the same secondary antibody was used, which was a polyclonal anti-rabbit IgG antibody raised in goat and conjugated to Alexa Fluor 633 (2 µg/mL; A21070, Invitrogen; excitation wavelength = 630 nm, emitted light detected at ≥ 650 nm). For HCN4 channels, the secondary antibody was a polyclonal anti-mouse IgG antibody raised in goat and conjugated to Alexa Fluor 633 (2 µg/mL; A11030, Invitrogen; excitation wavelength = 560 nm, emitted light detected at ≥ 570 nm). Arteries were imaged as described in Section 2.6.3.

For immunofluorescence analysis, distinct punctate fluorescent signal was considered positive staining, whereas diffuse areas of weaker fluorescence were excluded as potential imaging artefacts or non-specific binding.

5.3 Results

5.3.1 Rat mesenteric, coronary, and cremaster arteries express *Hcn* mRNA

To better understand the expression profile of HCN channels in resistance arteries, RNAscope was used to detect mRNA transcripts in ECs and VSMCs of small mesenteric, coronary, and cremaster arteries following fixation in a wire myograph.

Hcn mRNA transcripts were detected in ECs of RMAs (**Figures 5.3.1 – 5.3.4**), RCos (**Figures 5.3.5 – 5.3.8**) and rat cremaster arteries (RCres; **Figures 5.3.9 – 5.3.12**). *Hcn2* was the most highly expressed transcript in mesenteric ECs (34.15 ± 5.51 molecules per cell; P < 0.0001 vs negative control; n = 3 rats; **Figure 5.3.2 A and C**), followed by *Hcn1 (*22.61 ± 0.13 molecules per cell; n = 2; **Figure 5.3.1 A and C**)*, Hcn3 (*11.41 ± 5.27 molecules per cell; P = 0.0252 vs negative control; n = 3; **Figure 5.3.3 A and C**), and *Hcn4 (*10.47 ± 3.46 molecules per cell; P = 0.0085 vs negative control; n = 3; **Figure 5.3.4 A and C**). In coronary ECs, the most highly expressed transcript was *Hcn3* (18.85 ± 2.56 molecules per cell; P = 0.0003 vs negative control; n = 3; **Figure 5.3.7 A and C**), followed by *Hcn4* (14.82 ± 1.43 molecules per cell; P < 0.0001 vs negative control; n = 3; **Figure 5.3.8 A and C**) and *Hcn2* (4.27 ± 0.62 molecules per cell; P = 0.0008 vs negative control; n = 3; **Figure 5.3.6 A and C**). *Hcn1* expression was not detected above background levels in RCo ECs (0.72 ± 0.38 molecules per cell; P = 0.0865 vs negative control; n = 3; **Figure 5.3.5 A and C**). Finally, in cremaster ECs, *Hcn4* was the most highly expressed transcript (47.21 ± 20.64 molecules per cell; P = 0.0176 vs negative control; n = 3; **Figure 5.3.12 A and C**), followed by *Hcn3* (36.50 ± 12.31 molecules per cell; P = 0.0074 vs negative control; n = 3; **Figure 5.3.11 A and C**), then *Hcn2* (5.12 ± 1.78 molecules per cell; P = 0.0140 vs negative control; n = 3; **Figure 5.3.10 A and C**). Again, *Hcn1* expression was not detected above background levels in RCre ECs (2.26 ± 1.00 molecules per cell; P = 0.0691 vs negative control; n = 3; **Figure 5.3.9 A and C**).

Similarly, *Hcn* mRNA transcripts were also detected in VSMCs of mesenteric, coronary and cremaster arteries. *Hcn1* was the most highly expressed transcript in RMAs (22.07 ± 7.32 molecules per cell; P = 0.0067 vs negative control; n = 3; **Figure 5.3.1 B and C**), followed by *Hcn2* (13.15 ± 2.11 molecules per cell; P = 0.0005 vs negative control; n = 3; **Figure 5.3.2 B and C**), *Hcn3* (12.88 ± 3.82 molecules per cell; P = 0.0046 vs negative control; n = 3; **Figure 5.3.3 B and C**), then *Hcn4* (9.81 ± 1.96 molecules per cell; P = 0.0011 vs negative control; n = 3; **Figure 5.3.4 B and C**). In RCo VSMCs, *Hcn3* was the most highly expressed transcript (24.34 ± 0.48 molecules per cell; P = 0.0005 vs negative control; n = 3; **Figure 5.3.7 B and C**), followed by *Hcn4* (21.01 ± 3.57 molecules per cell; P = 0.0005 vs negative control; n = 3; **Figure 5.3.8 B and C**) then *Hcn2* (4.95 ± 1.75 molecules per cell; n = 0.0099 vs negative control; n = 3; **Figure 5.3.6 B and C**). *Hcn1* expression was not detected above background levels (2.74 ± 1.89 molecules per cell; P = 0.0865 vs negative control; n = 3; **Figure 5.3.5 B and C**). The relative abundance of mRNA corresponding to each HCN isoform in cremaster VSMCs was opposite to that in mesenteric VSMCs. In RCre VSMCs, *Hcn4* was the most highly expressed (18.69 ± 5.59 molecules per cell; P = 0.0047 vs negative control; n = 3; **Figure 5.3.12 B and C)**, followed by *Hcn3* (10.97 ± 5.29 molecules per cell; P = 0.0248 vs negative control; **Figure 5.3.11 B and C**). mRNA corresponding to both *Hcn2* and *Hcn1* was present at low levels in RCre VSMCs (2.47 ± 1.27 and 1.25 ± 0.56 molecules per cell, respectively, P = 0.0406 and P = 0.0415 vs negative control, respectively; **Figures 5.3.10 B and C and 5.3.9 B and C**). A summary of this RNAscope data is provided in **Figure 5.3.13.**

Further analysis of the RNAscope data was carried out to determine whether there were any differences in the sub-cellular localisation of the mRNA transcripts. In RMA ECs, *Hcn2* transcripts localised more extensively in the nucleus than the cytoplasm (~3.5-fold difference, 14.09 ± 3.18 nuclear mRNA molecules per cell compared to 4.39 ± 0.48 in the cytoplasm; P = 0.0110; n = 3; **Figure 5.3.2 D**). In RCos, *Hcn3* transcripts were differentially localised in both ECs and VSMCs. In ECs, there was ~3 times more mRNA in the cytoplasm than the nucleus

(15.80 ± 1.19 cytoplasmic mRNA molecules per cell compared to 5.93 in the nucleus; P = 0.0003; n = 3; **Figure 5.3.7 D**). Similarly, in VSMCs, there was ~6 times more mRNA in the cytoplasm than the nucleus (19.37 ± 0.48 cytoplasmic mRNA molecules per cell compared to 3.32 ± 0.98 in the nucleus; P < 0.0001; n = 3; **Figure 5.3.7 E**). Finally, in RCres, *Hcn2* mRNA was localised more to the nucleus in ECs (5.85 ± 1.97 nuclear mRNA molecules per cell compared to 1.67 ± 0.59 in the cytoplasm; P = 0.0244; n = 3; **Figure 5.3.10 D**). In the same arteries, *Hcn3* mRNA was also distributed unevenly across ECs and VSMCs. In ECs, there was significantly more mRNA in the nucleus (over 5-fold difference, 36.42 ± 4.38 nuclear mRNA molecules per cell compared to 7.43 ± 2.62 in the cytoplasm; P = 0.0006; n = 3; **Figure 5.3.11 D**). In VSMCs, the cytoplasm contained ~3 times more mRNA than the nucleus (5.87 ± 0.91 cytoplasmic molecules per cell compared to 1.73 ± 0.25 in the nucleus; P = 0.0016; n = 3; **Figure 5.3.11 E**). All other *Hcn* transcripts studied were evenly distributed across both cellular compartments of ECs and VSMCs. A summary of this RNAscope data is provided in **Figure 5.3.14**.

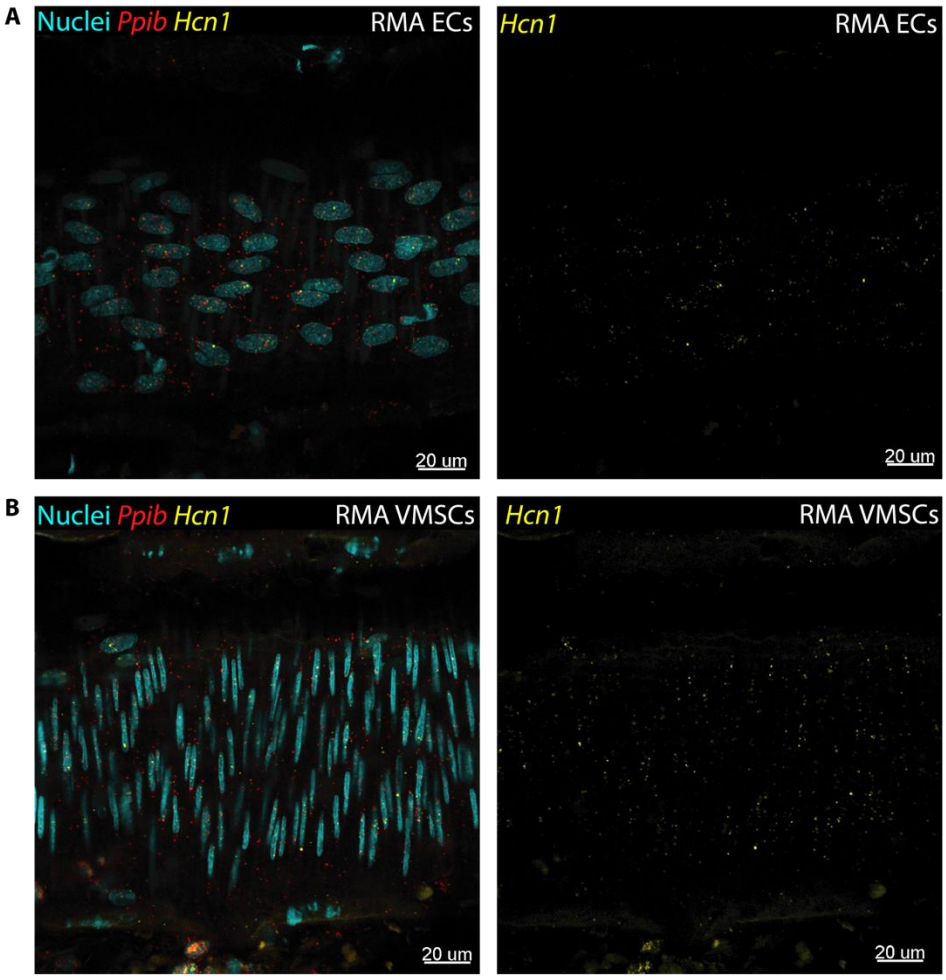
A
Nuclei Ppib Hcn1
RMA ECs
20 um
Hcn1
RMA ECs
20 um
B
Nuclei Ppib Hcn1
RMA VMSCs
20 um
Hcn1
RMA VMSCs
20 um

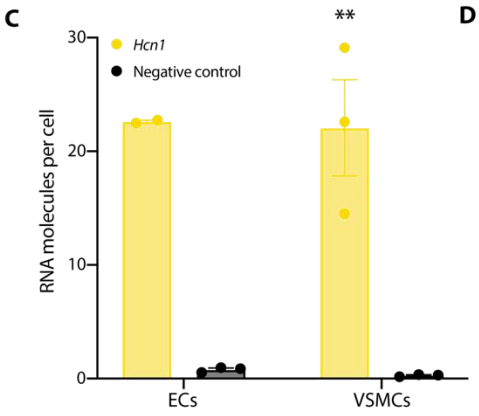
C
**
Hcn1
Negative control
RNA molecules per cell
30
20
10
0
ECs
VSMCs

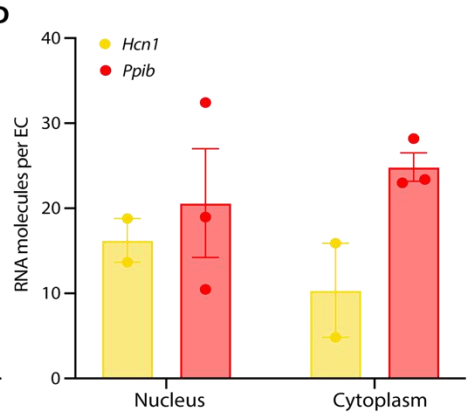
D
Hcn1
Ppib
RNA molecules per EC
40
30
20
10
0
Nucleus
Cytoplasm

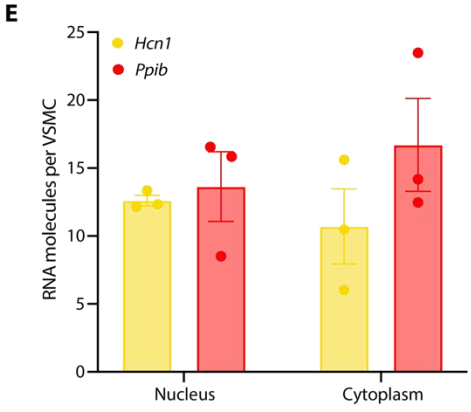
E
Hcn1
Ppib
RNA molecules per VSMC
25
20
15
10
5
0
Nucleus
Cytoplasm

Figure 5.3.1. Expression of *Hcn1* mRNA by rat mesenteric arteries (RMAs). RNAscope was used to determine *Hcn1* expression (yellow) by endothelial cells (ECs, **A**) and vascular smooth muscle cells (VSMCs, **B**) of wire-myograph mounted mesenteric arteries. *Ppib* (red) was used as a positive control. (**C**) Quantification of *Hcn1*, expressed as molecules per cell and compared against the negative control. Data are means ± SEM; n = 2-3 rats. **P = 0.0067 vs VSMC negative control using unpaired student's t test. (**D**) Localisation of *Hcn1* and *Ppib* transcripts in ECs. Data are means of 3 cells per artery ± SEM; n = 2- 3 rats. P = 0.5562 for *Ppib* nuclear vs cytoplasmic localisation using unpaired student's t test. (**E**) Localisation of *Hcn1* and *Ppib* transcripts in VSMCs. Data are means of 3 cells per artery ± SEM, n = 3 rats. P = 0.5334 for *Hcn1* nuclear vs cytoplasmic localisation and P = 0.5126 for *Ppib* nuclear vs cytoplasmic localisation, using unpaired student's t test.

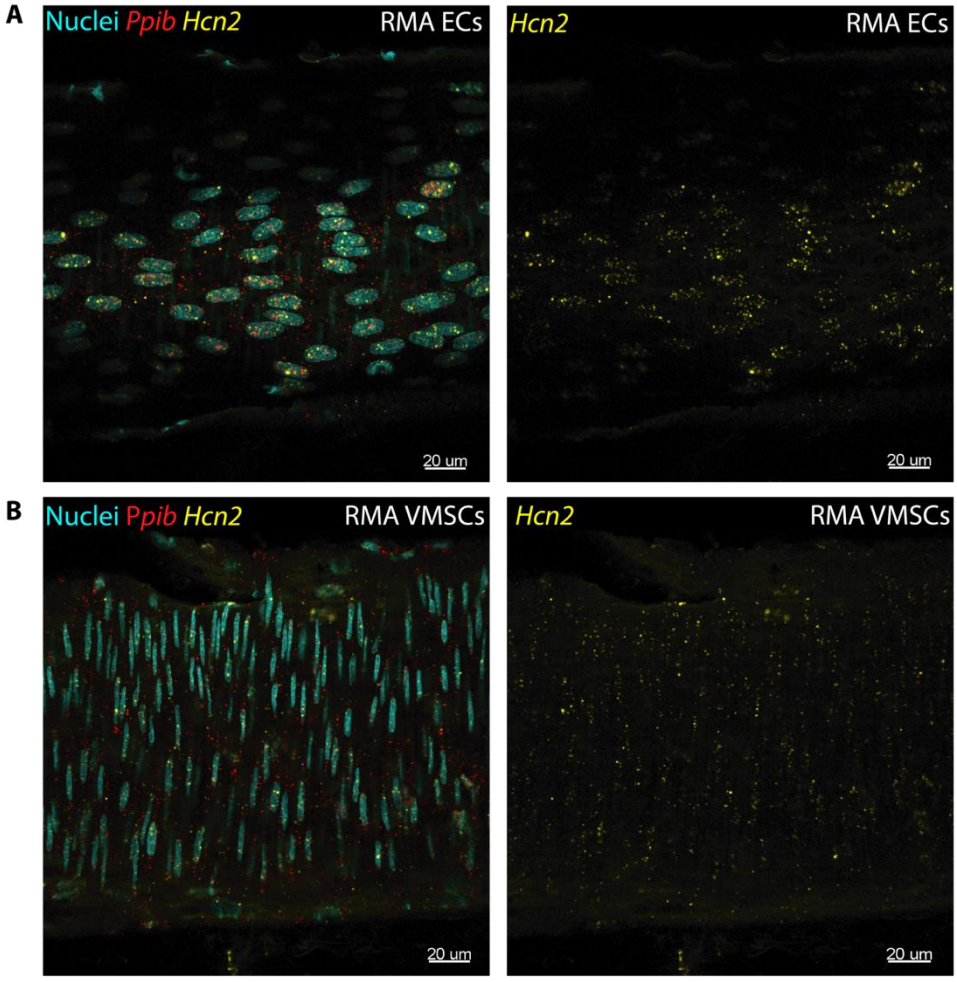
A
Nuclei Ppib Hcn2
RMA ECs
20 um
Hcn2
RMA ECs
20 um
B
Nuclei Ppib Hcn2
RMA VMSCs
20 um
Hcn2
RMA VMSCs
20 um

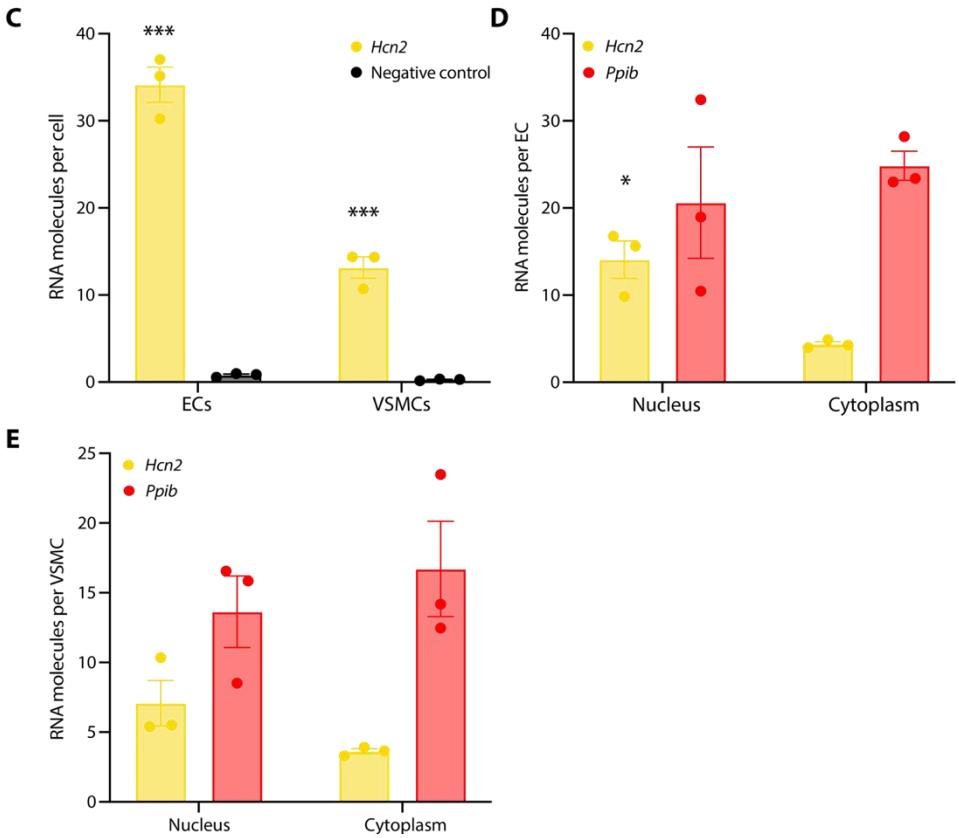
C
RNA molecules per cell
40
30
20
10
0
***
***
Hcn2
Negative control
ECs
VSMCs
D
RNA molecules per EC
40
30
20
10
0
*
Hcn2
Ppib
Nucleus
Cytoplasm
E
RNA molecules per VSMC
25
20
15
10
5
0
Hcn2
Ppib
Nucleus
Cytoplasm

Figure 5.3.2. Expression of *Hcn2* mRNA by rat mesenteric arteries (RMAs). RNAscope was used to determine *Hcn2* expression (yellow) by endothelial cells (ECs, **A**) and vascular smooth muscle cells (VSMCs, **B**) of wire-myograph mounted mesenteric arteries. *Ppib* (red) was used as a positive control. (**C**) Quantification of *Hcn2*, expressed as molecules per cell and compared against the negative control. Data are means ± SEM; n = 3. ***P < 0.0001 vs EC negative control and ***P = 0.0005 vs VMSC negative control, using unpaired student's t test. (**D**) Localisation of *Hcn2* and *Ppib* transcripts in ECs. Data are means of 3 cells per artery ± SEM; n = 3 rats. *P = 0.0110 for *Hcn2* nuclear vs cytoplasmic localisation and P = 0.5562 for *Ppib* nuclear vs cytoplasmic localisation, using unpaired student's t test. (**E**) Localisation of *Hcn2* and *Ppib* transcripts in VSMCs. Data are means of 3 cells per artery ± SEM, n = 3 rats. P = 0.1000 for *Hcn2* nuclear vs cytoplasmic localisation and P = 0.5126 for *Ppib* nuclear vs cytoplasmic localisation, using Mann-Whitney U test and unpaired student's t test, respectively.

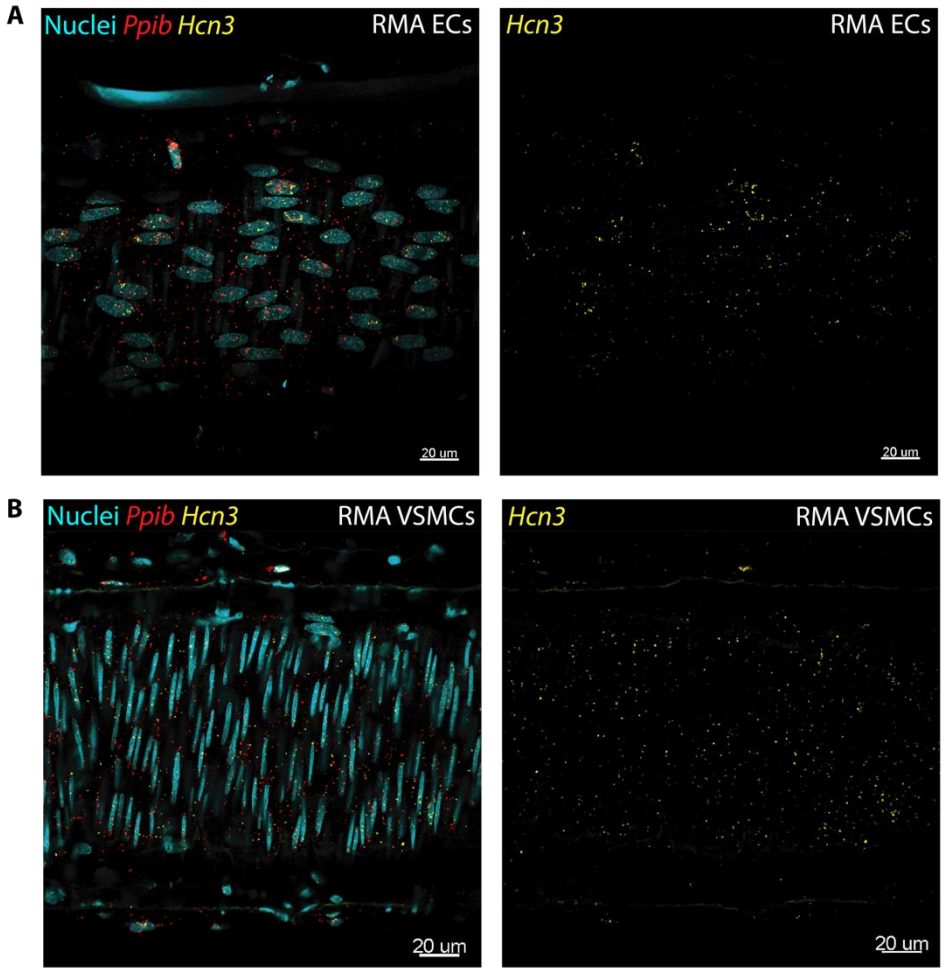
A
Nuclei Ppib Hcn3
RMA ECs
20 um
Hcn3
RMA ECs
20 um
B
Nuclei Ppib Hcn3
RMA VSMCs
20 um
Hcn3
RMA VSMCs
20 um

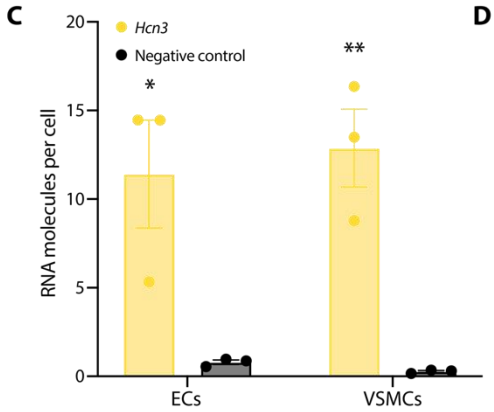
C
Hcn3
Negative control
*
**
RMA molecules per cell
20
15
10
5
0
ECs
VSMCs

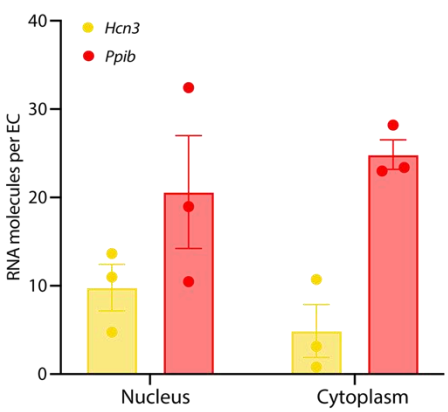
D
Hcn3
Ppib
RMA molecules per EC
40
30
20
10
0
Nucleus
Cytoplasm

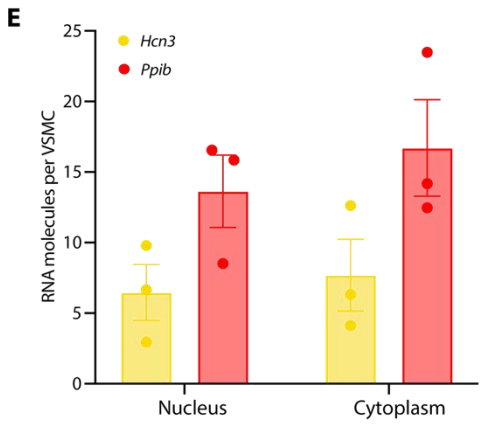
E
Hcn3
Ppib
RMA molecules per VSMC
25
20
15
10
5
0
Nucleus
Cytoplasm

Figure 5.3.3. Expression of *Hcn3* mRNA by rat mesenteric arteries (RMAs). RNAscope was used to determine *Hcn3* expression (yellow) by endothelial cells (ECs, **A**) and vascular smooth muscle cells (VSMCs, **B**) of wire-myograph mounted mesenteric arteries. *Ppib* (red) was used as a positive control. (**C**) Quantification of *Hcn3*, expressed as molecules per cell and compared against the negative control. Data are means ± SEM; n = 3. *P = 0.0252 vs EC negative control and **P = 0.0046 vs VMSC negative control, using unpaired student's t test. (**D**) Localisation of *Hcn3* and *Ppib* transcripts in ECs. Data are means of 3 cells per artery ± SEM; n = 3 rats. P = 0.2862 for *Hcn3* nuclear vs cytoplasmic localisation and P = 0.5562 for *Ppib* nuclear vs cytoplasmic localisation, using unpaired student's t test. (**E**) Localisation of *Hcn3* and *Ppib* transcripts in VSMCs. Data are means of 3 cells per artery ± SEM, n = 3 rats. P = 0.7229 for *Hcn3* nuclear vs cytoplasmic localisation and P = 0.5126 for *Ppib* nuclear vs cytoplasmic localisation, using unpaired student's t test.

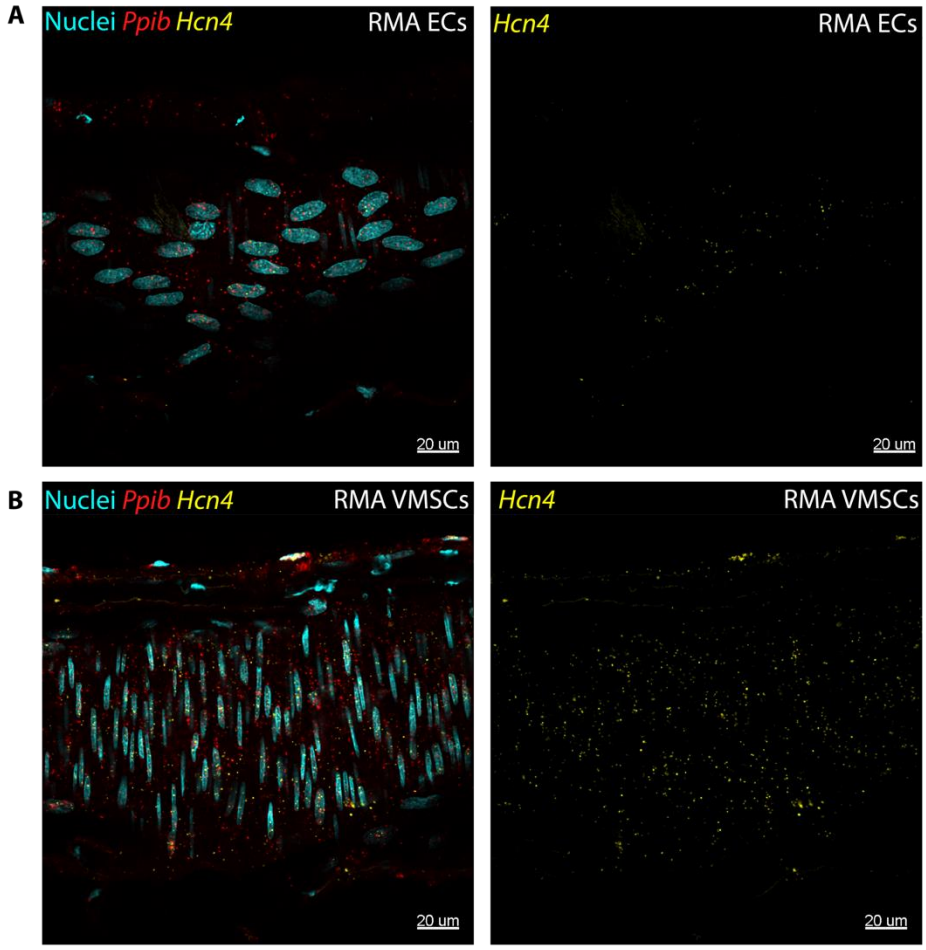
A
Nuclei Ppib Hcn4
RMA ECs
20 um
Hcn4
RMA ECs
20 um
B
Nuclei Ppib Hcn4
RMA VMSCs
20 um
Hcn4
RMA VMSCs
20 um

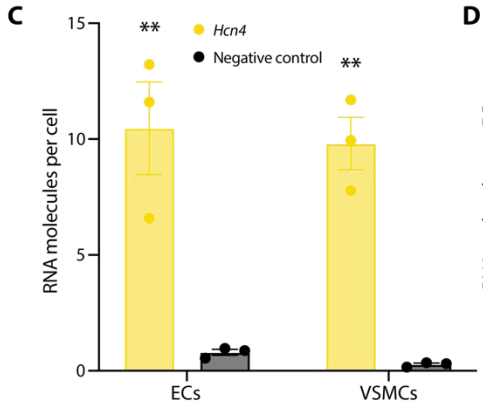
C
RNA molecules per cell
15
10
5
0
**
**
Hcn4
Negative control
ECs
VSMCs

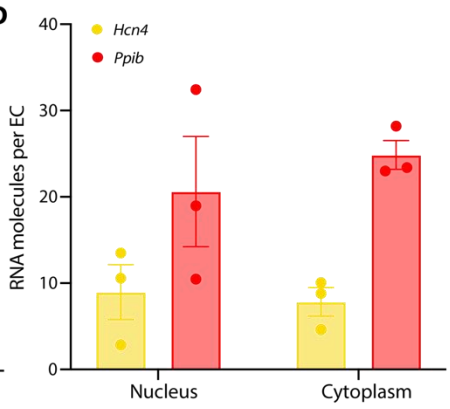
D
RNA molecules per EC
40
30
20
10
0
Hcn4
Ppib
Nucleus
Cytoplasm

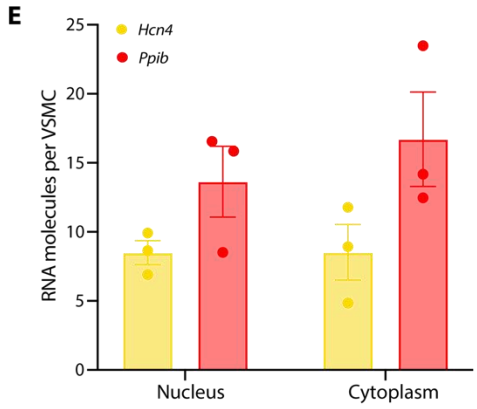
E
RNA molecules per VSMC
25
20
15
10
5
0
Hcn4
Ppib
Nucleus
Cytoplasm

Figure 5.3.4. Expression of *Hcn4* mRNA by rat mesenteric arteries (RMAs). RNAscope was used to determine *Hcn4* expression (yellow) by endothelial cells (ECs, **A**) and vascular smooth muscle cells (VSMCs, **B**) of wire-myograph mounted mesenteric arteries. *Ppib* (red) was used as a positive control. (**C**) Quantification of *Hcn4*, expressed as molecules per cell and compared against the negative control. Data are means ± SEM; n = 3. **P = 0.0085 vs EC negative control and **P = 0.0011 vs VMSC negative control, using unpaired student's t test. (**D**) Localisation of *Hcn4* and *Ppib* transcripts in ECs. Data are means of 3 cells per artery ± SEM; n = 3 rats. P = 0.7664 for *Hcn4* nuclear vs cytoplasmic localisation and P = 0.5562 for *Ppib* nuclear vs cytoplasmic localisation, using unpaired student's t test. (**E**) Localisation of *Hcn4* and *Ppib* transcripts in VSMCs. Data are means of 3 cells per artery ± SEM, n = 3 rats. P = 0.9916 for *Hcn4* nuclear vs cytoplasmic localisation and P = 0.5126 for *Ppib* nuclear vs cytoplasmic localisation, using unpaired student's t test.

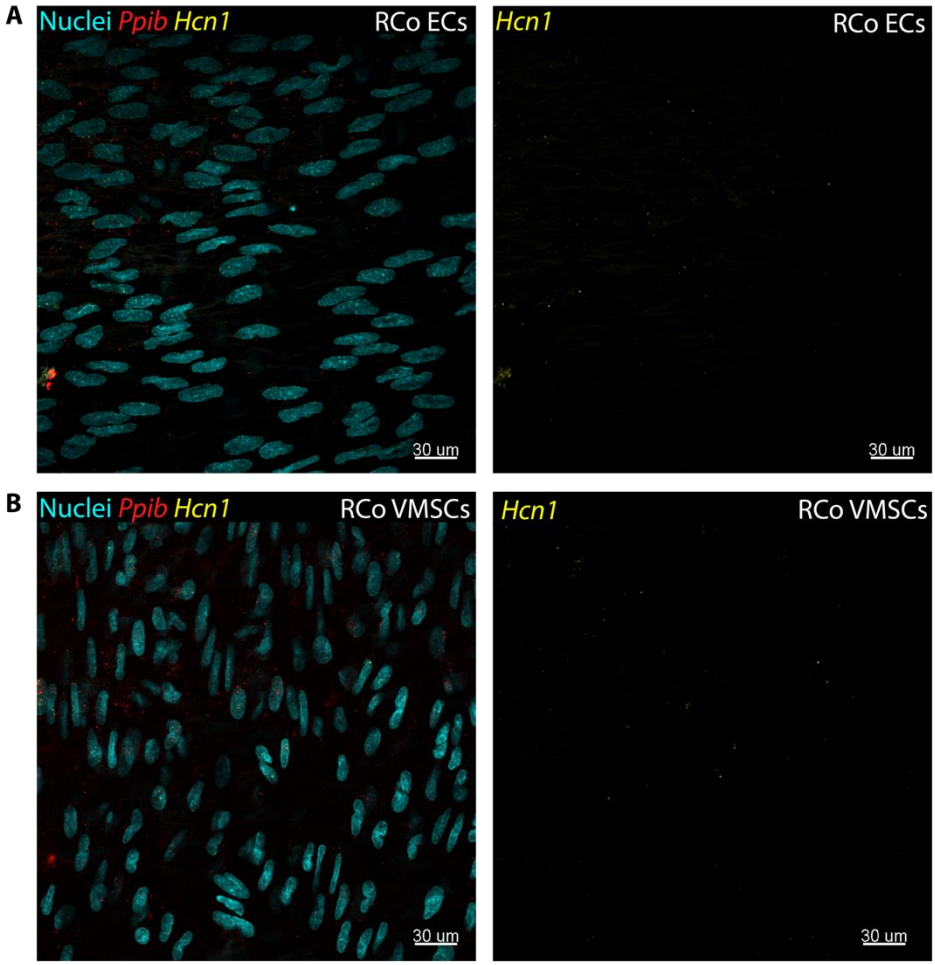
A
Nuclei Ppib Hcn1
RCo ECs
30 um
Hcn1
RCo ECs
30 um
B
Nuclei Ppib Hcn1
RCo VMSCs
30 um
Hcn1
RCo VMSCs
30 um

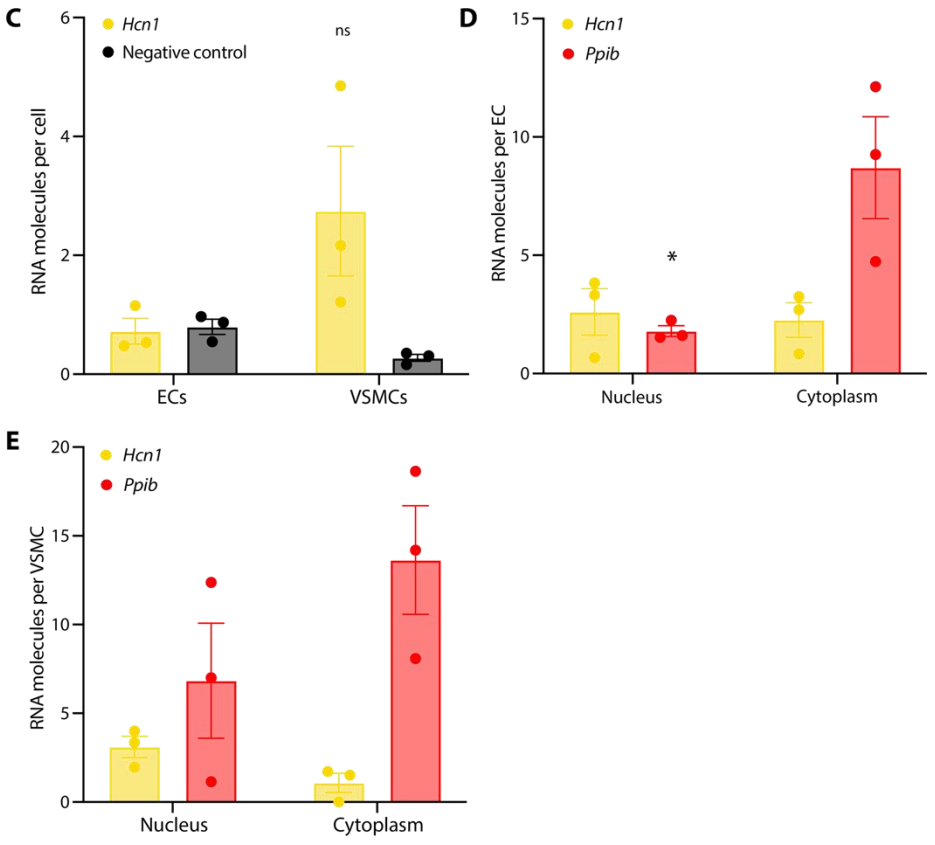
C
Hcn1
Negative control
ns
RNA molecules per cell
0
2
4
6
ECs
VSMCs
D
Hcn1
Ppib
RNA molecules per EC
0
5
10
15
*
Nucleus
Cytoplasm
E
Hcn1
Ppib
RNA molecules per VSMC
0
5
10
15
20
Nucleus
Cytoplasm

Figure 5.3.5. Expression of *Hcn1* mRNA by rat coronary arteries (RCos). RNAscope was used to determine *Hcn1* expression (yellow) by endothelial cells (ECs, **A**) and vascular smooth muscle cells (VSMCs, **B**) of wire-myograph mounted coronary arteries. *Ppib* (red) was used as a positive control. (**C**) Quantification of *Hcn1*, expressed as molecules per cell and compared against the negative control. Data are means ± SEM; n = 3. P = 0.0865 vs VSMC negative control using unpaired student's t test. (**D**) Localisation of *Hcn1* and *Ppib* transcripts in ECs. Data are means of 3 cells per artery ± SEM; n = 3 rats. P = 0.7928 for *Hcn1* nuclear vs cytoplasmic localisation and *P = 0.0332 for *Ppib* nuclear vs cytoplasmic localisation, using unpaired student's t test. (**E**) Localisation of *Hcn1* and *Ppib* transcripts in VSMCs. Data are means of 3 cells per artery ± SEM, n = 3 rats. P = 0.0674 for *Hcn1* nuclear vs cytoplasmic localisation and P = 0.2021 for *Ppib* nuclear vs cytoplasmic localisation, using unpaired student's t test.

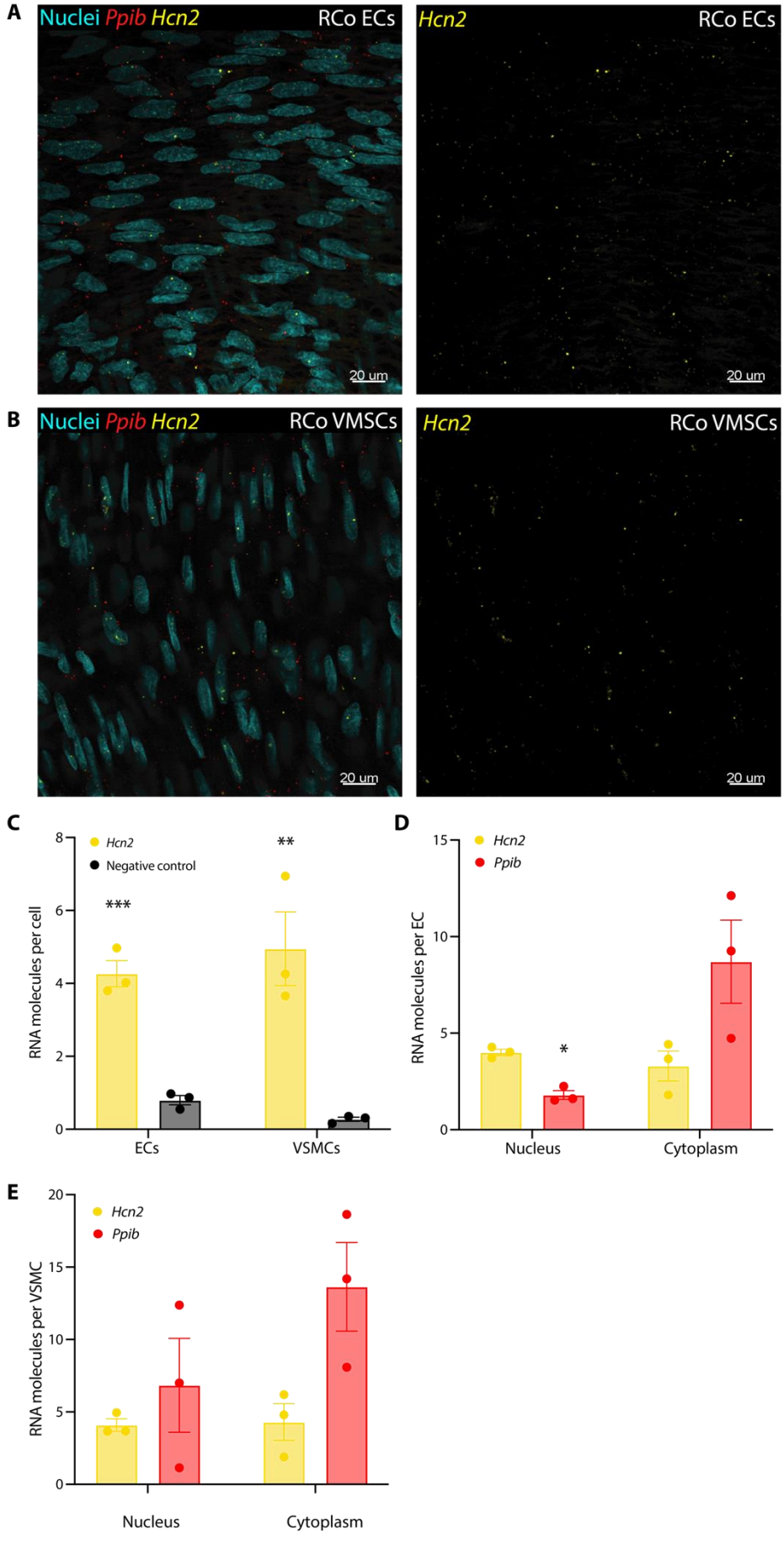
A
Nuclei Ppib Hcn2
RCo ECs
20 um
Hcn2
RCo ECs
20 um
B
Nuclei Ppib Hcn2
RCo VMSCs
20 um
Hcn2
RCo VMSCs
20 um
C
Hcn2
Negative control
***
**
RNA molecules per cell
0
2
4
6
8
ECs
VSMCs
D
Hcn2
Ppib
*
RNA molecules per EC
0
5
10
15
Nucleus
Cytoplasm
E
Hcn2
Ppib
RNA molecules per VSMC
0
5
10
15
20
Nucleus
Cytoplasm

Figure 5.3.6. Expression of *Hcn2* mRNA by rat coronary arteries (RCos). RNAscope was used to determine *Hcn2* expression (yellow) by endothelial cells (ECs, **A**) and vascular smooth muscle cells (VSMCs, **B**) of wire-myograph mounted coronary arteries. *Ppib* (red) was used as a positive control. (**C**) Quantification of *Hcn2*, expressed as molecules per cell and compared against the negative control. Data are means ± SEM; n = 3. ***P = 0.0008 vs EC negative control and **P = 0.0099 vs VMSC negative control, using unpaired student's t test. (**D**) Localisation of *Hcn2* and *Ppib* transcripts in ECs. Data are means of 3 cells per artery ± SEM; n = 3 rats. P = 0.7928 for *Hcn2* nuclear vs cytoplasmic localisation and *P = 0.0332 for *Ppib* nuclear vs cytoplasmic localisation, using unpaired student's t test. (**E**) Localisation of *Hcn2* and *Ppib* transcripts in VSMCs. Data are means of 3 cells per artery ± SEM, n = 3 rats. P = 0.8862 for *Hcn2* nuclear vs cytoplasmic localisation and P = 0.2021 for *Ppib* nuclear vs cytoplasmic localisation, using unpaired student's t test.

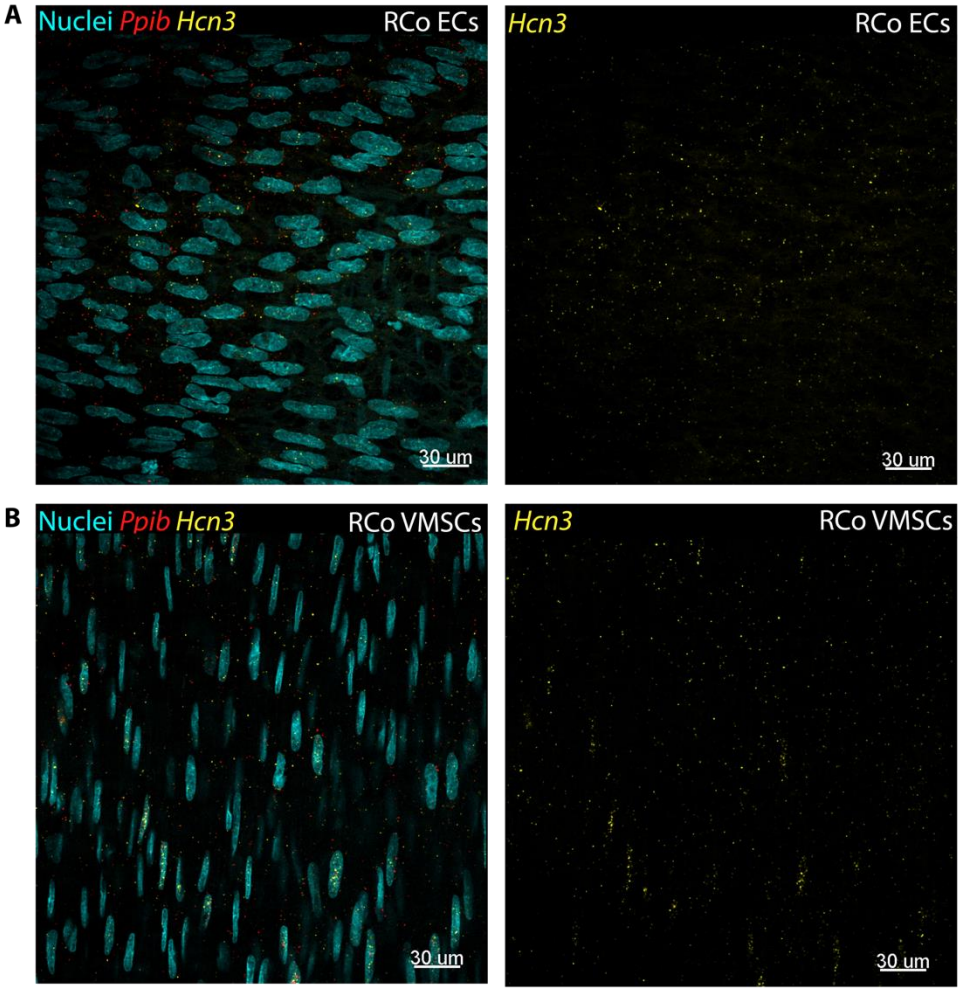
A
Nuclei Ppib Hcn3
RCo ECs
30 um
Hcn3
RCo ECs
30 um
B
Nuclei Ppib Hcn3
RCo VMSCs
30 um
Hcn3
RCo VMSCs
30 um

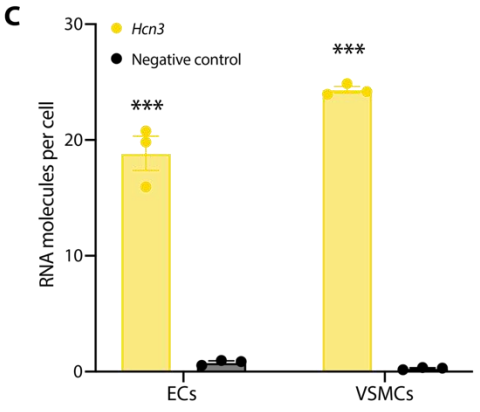
C
Hcn3
Negative control
RNA molecules per cell
30
20
10
0
***
***
ECs
VSMCs

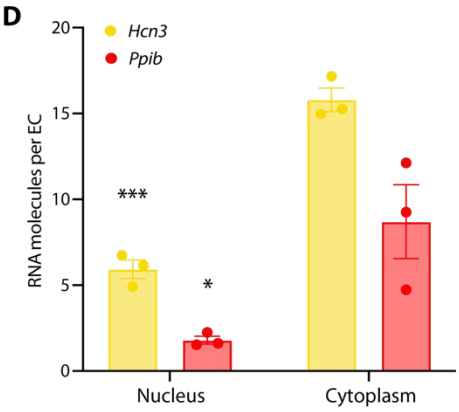
D
Hcn3
Ppib
RNA molecules per EC
20
15
10
5
0
***
*
Nucleus
Cytoplasm

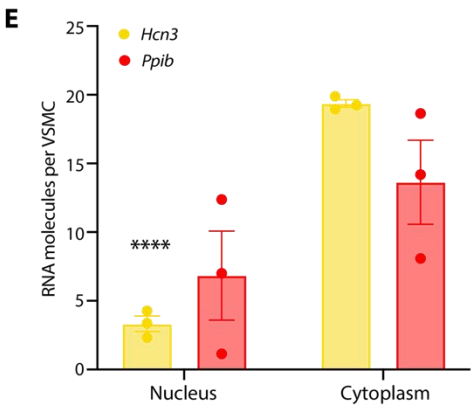
E
Hcn3
Ppib
RNA molecules per VSMC
25
20
15
10
5
0
****
Nucleus
Cytoplasm

Figure 5.3.7. Expression of *Hcn3* mRNA by rat coronary arteries (RCos). RNAscope was used to determine *Hcn3* expression (yellow) by endothelial cells (ECs, **A**) and vascular smooth muscle cells (VSMCs, **B**) of wire-myograph mounted coronary arteries. *Ppib* (red) was used as a positive control. (**C**) Quantification of *Hcn3*, expressed as molecules per cell and compared against the negative control. Data are means ± SEM; n = 3. ***P = 0.0003 vs EC negative control and ***P = 0.0005 vs VMSC negative control, using unpaired student's t test. (**D**) Localisation of *Hcn3* and *Ppib* transcripts in ECs. Data are means of 3 cells per artery ± SEM; n = 3 rats. ***P = 0.0003 for *Hcn3* nuclear vs cytoplasmic localisation and *P = 0.0332 for *Ppib* nuclear vs cytoplasmic localisation, using unpaired student's t test. (**E**) Localisation of *Hcn3* and *Ppib* transcripts in VSMCs. Data are means of 3 cells per artery ± SEM, n = 3 rats. ****P < 0.0001 for *Hcn3* nuclear vs cytoplasmic localisation and P = 0.2021 for *Ppib* nuclear vs cytoplasmic localisation, using unpaired student's t test.

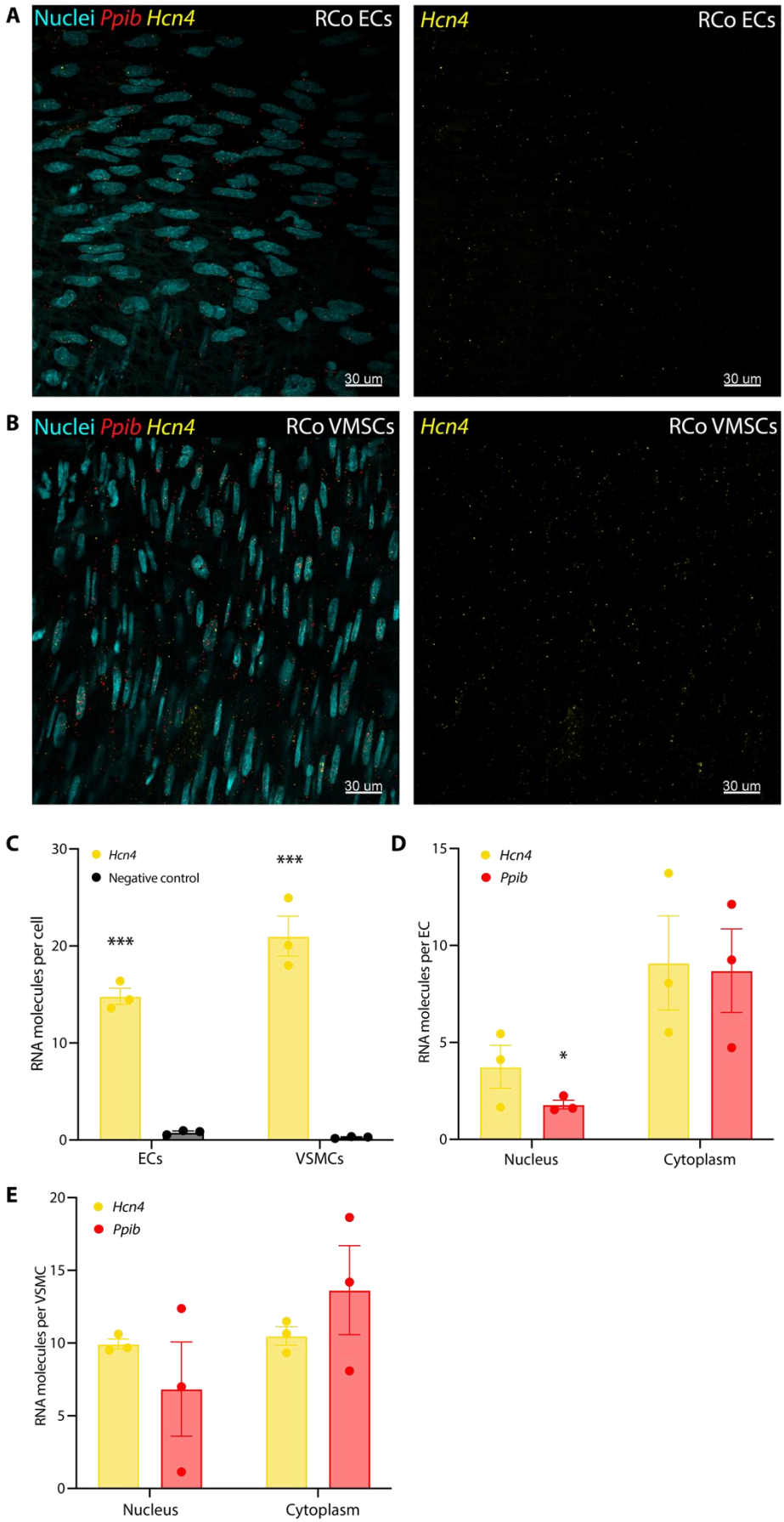
A
Nuclei Ppib Hcn4
RCo ECs
30 um
Hcn4
RCo ECs
30 um
B
Nuclei Ppib Hcn4
RCo VMSCs
30 um
Hcn4
RCo VMSCs
30 um
C
Hcn4
Negative control
RNA molecules per cell
30
20
10
0
***
***
ECs
VSMCs
D
Hcn4
Ppib
RNA molecules per EC
15
10
5
0
*
Nucleus
Cytoplasm
E
Hcn4
Ppib
RNA molecules per VSMC
20
15
10
5
0
Nucleus
Cytoplasm

Figure 5.3.8. Expression of *Hcn4* mRNA by rat coronary arteries (RCos). RNAscope was used to determine *Hcn4* expression (yellow) by endothelial cells (ECs, **A**) and vascular smooth muscle cells (VSMCs, **B**) of wire-myograph mounted coronary arteries. *Ppib* (red) was used as a positive control. (**C**) Quantification of *Hcn4*, expressed as molecules per cell and compared against the negative control. Data are means ± SEM; n = 3. ***P < 0.0001 vs EC negative control and ***P = 0.0005 vs VMSC negative control, using unpaired student's t test. (**D**) Localisation of *Hcn4* and *Ppib* transcripts in ECs. Data are means of 3 cells per artery ± SEM; n = 3 rats. P = 0.1151 for *Hcn4* nuclear vs cytoplasmic localisation and *P = 0.0332 for *Ppib* nuclear vs cytoplasmic localisation, using unpaired student's t test. (**E**) Localisation of *Hcn4* and *Ppib* transcripts in VSMCs. Data are means of 3 cells per artery ± SEM, n = 3 rats. P = 0.4812 for *Hcn4* nuclear vs cytoplasmic localisation and P = 0.2021 for *Ppib* nuclear vs cytoplasmic localisation, using unpaired student's t test.

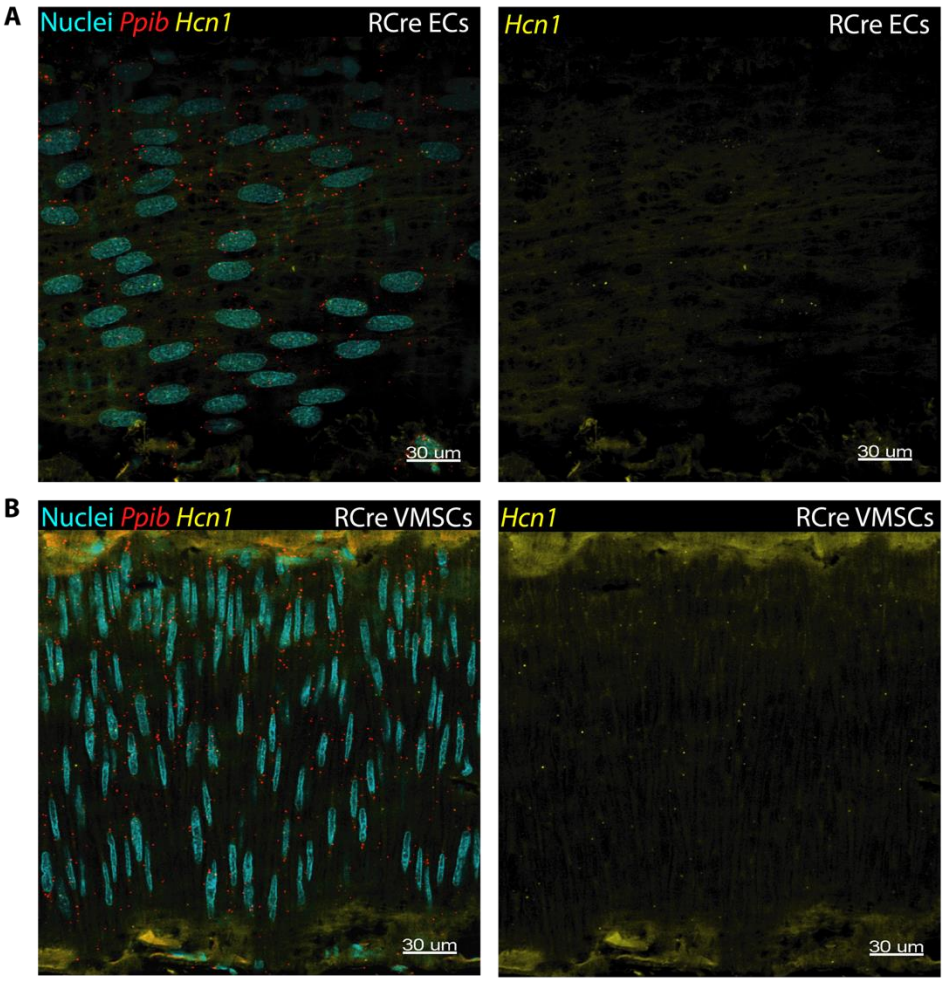
A
Nuclei Ppib Hcn1
RCre ECs
30 um
Hcn1
RCre ECs
30 um
B
Nuclei Ppib Hcn1
RCre VMSCs
30 um
Hcn1
RCre VMSCs
30 um

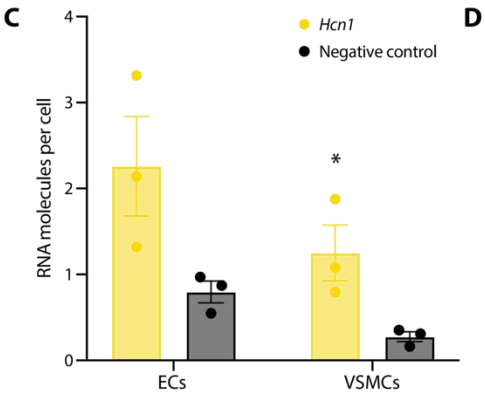
C
Hcn1
Negative control
RNA molecules per cell
4
3
2
1
0
*
ECs
VSMCs

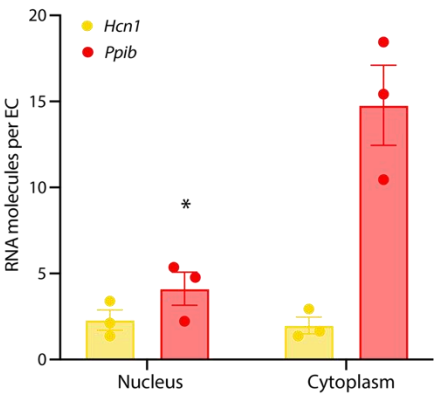
D
Hcn1
Ppib
RNA molecules per EC
20
15
10
5
0
*
Nucleus
Cytoplasm

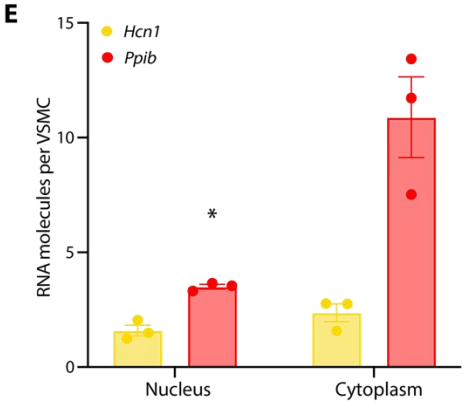
E
Hcn1
Ppib
RNA molecules per VSMC
15
10
5
0
*
Nucleus
Cytoplasm

Figure 5.3.9. Expression of *Hcn1* mRNA by rat cremaster arteries (RCres). RNAscope was used to determine *Hcn1* expression (yellow) by endothelial cells (ECs, **A**) and vascular smooth muscle cells (VSMCs, **B**) of wire-myograph mounted cremaster arteries. *Ppib* (red) was used as a positive control. (**C**) Quantification of *Hcn1*, expressed as molecules per cell and compared against the negative control. Data are means ± SEM; n = 3. P = 0.0691 vs EC negative control and *P = 0.0415 vs VMSC negative control, using unpaired student's t test. (**D**) Localisation of *Hcn1* and *Ppib* transcripts in ECs. Data are means of 3 cells per artery ± SEM; n = 3 rats. P = 0.6990 for *Hcn1* nuclear vs cytoplasmic localisation and *P = 0.0135 for *Ppib* nuclear vs cytoplasmic localisation, using unpaired student's t test. (**E**) Localisation of *Hcn1* and *Ppib* transcripts in VSMCs. Data are means of 3 cells per artery ± SEM, n = 3 rats. P = 0.2000 for *Hcn1* nuclear vs cytoplasmic localisation and P = *0.0137 for *Ppib* nuclear vs cytoplasmic localisation, using Mann-Whitney U test and unpaired student's t test, respectively.

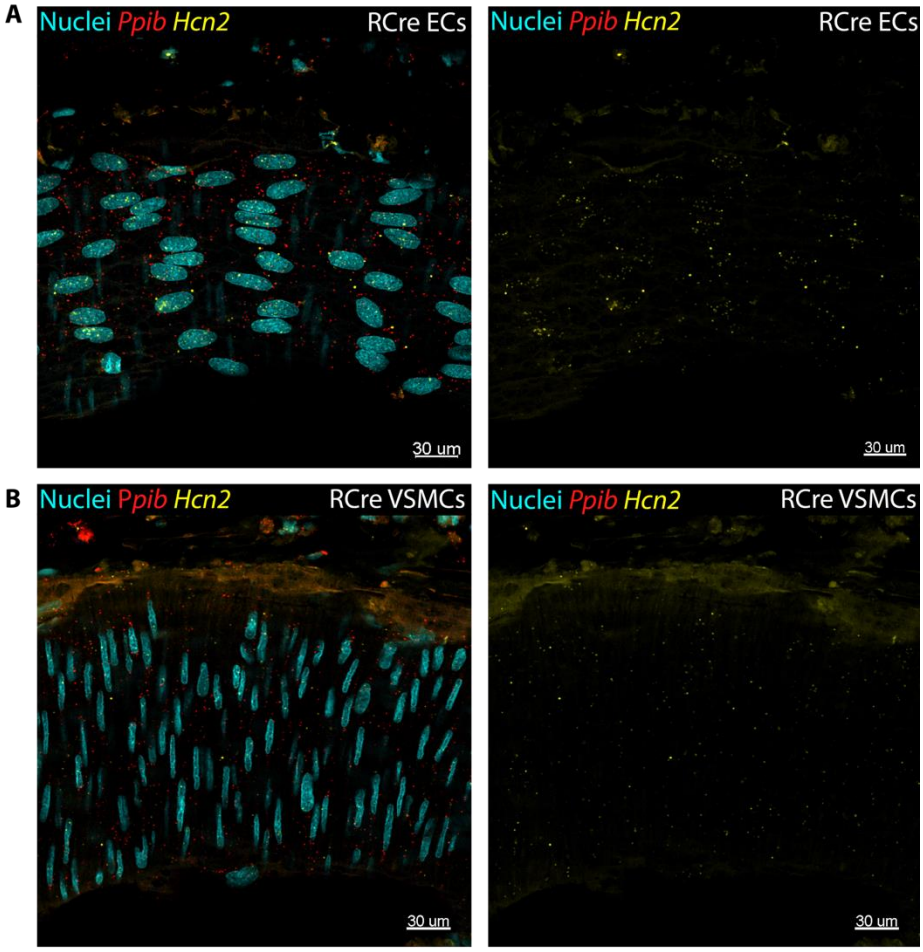
A
Nuclei Ppib Hcn2
RCre ECs
30 um
Nuclei Ppib Hcn2
RCre ECs
30 um
B
Nuclei Ppib Hcn2
RCre VSMCs
30 um
Nuclei Ppib Hcn2
RCre VSMCs
30 um

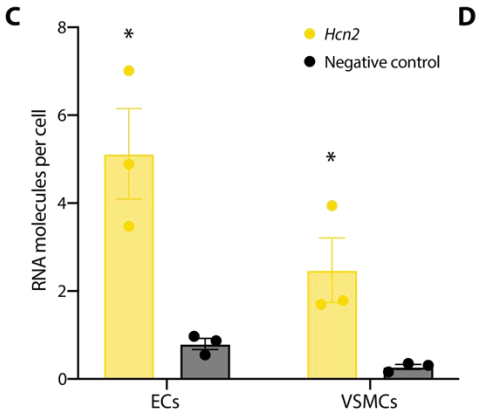
C
Hcn2
Negative control
RNA molecules per cell
0
2
4
6
8
*
*
ECs
VSMCs

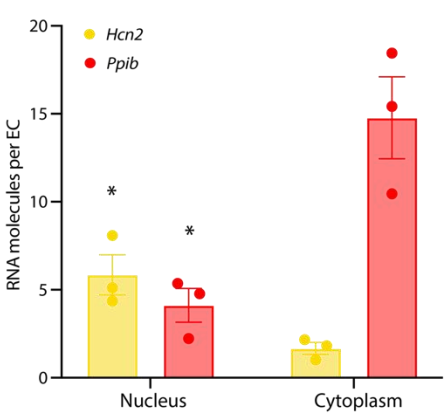
D
Hcn2
Ppib
RNA molecules per EC
0
5
10
15
20
*
*
Nucleus
Cytoplasm

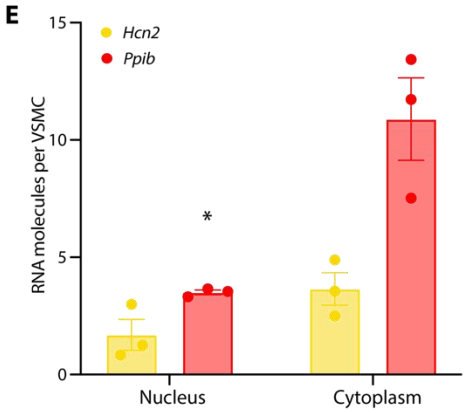
E
Hcn2
Ppib
RNA molecules per VSMC
0
5
10
15
*
Nucleus
Cytoplasm

Figure 5.3.10. Expression of *Hcn2* mRNA by rat cremaster arteries (RCres). RNAscope was used to determine *Hcn2* expression (yellow) by endothelial cells (ECs, **A**) and vascular smooth muscle cells (VSMCs, **B**) of wire-myograph mounted cremaster arteries. *Ppib* (red) was used as a positive control. (**C**) Quantification of *Hcn2*, expressed as molecules per cell and compared against the negative control. Data are means ± SEM; n = 3. *P = 0.0140 vs EC negative control and *P = 0.0406 vs VMSC negative control, using unpaired student's t test. (**D**) Localisation of *Hcn2* and *Ppib* transcripts in ECs. Data are means of 3 cells per artery ± SEM; n = 3 rats. *P = 0.0244 for *Hcn2* nuclear vs cytoplasmic localisation and *P = 0.0135 for *Ppib* nuclear vs cytoplasmic localisation, using unpaired student's t test. (**E**) Localisation of *Hcn2* and *Ppib* transcripts in VSMCs. Data are means of 3 cells per artery ± SEM, n = 3 rats. P = 0.1101 for *Hcn2* nuclear vs cytoplasmic localisation and P = *0.0137 for *Ppib* nuclear vs cytoplasmic localisation, using unpaired student's t test.

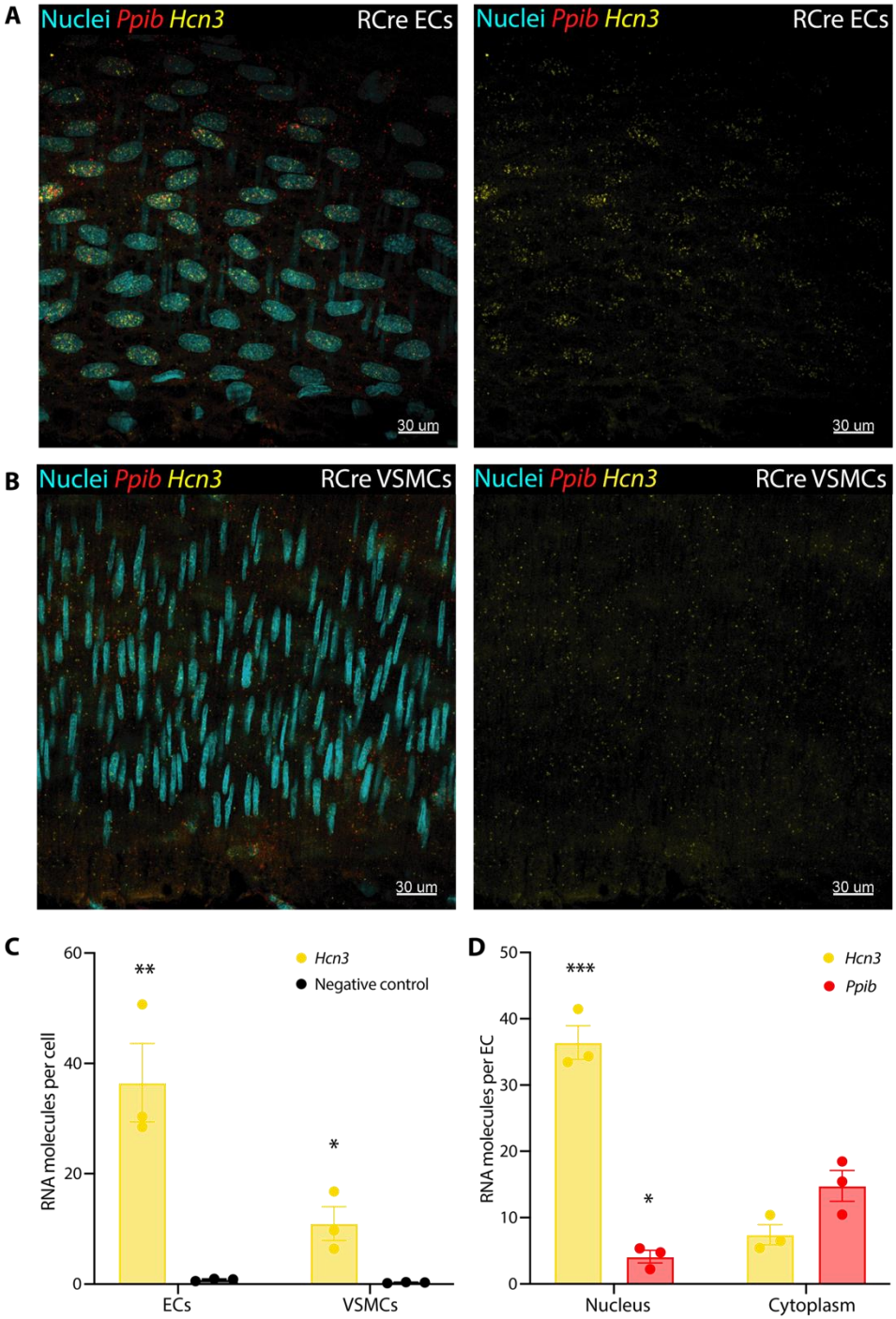
A
Nuclei Ppib Hcn3
RCre ECs
30 um
Nuclei Ppib Hcn3
RCre ECs
30 um
B
Nuclei Ppib Hcn3
RCre VSMCs
30 um
Nuclei Ppib Hcn3
RCre VSMCs
30 um
C
RNA molecules per cell
60
40
20
0
**
*
Hcn3
Negative control
ECs
VSMCs
D
RNA molecules per EC
50
40
30
20
10
0
***
*
Hcn3
Ppib
Nucleus
Cytoplasm
E
RNA molecules per VSMC
15
10
5
0
**
*
Hcn3
Ppib
Nucleus
Cytoplasm

Figure 5.3.11. Expression of *Hcn3* mRNA by rat cremaster arteries (RCres). RNAscope was used to determine *Hcn3* expression (yellow) by endothelial cells (ECs, **A**) and vascular smooth muscle cells (VSMCs, **B**) of wire-myograph mounted cremaster arteries. *Ppib (*red) was used as a positive control. (**C**) Quantification of *Hcn3*, expressed as molecules per cell and compared against the negative control. Data are means ± SEM; n = 3. **P = 0.0074 vs EC negative control and *P = 0.0248 vs VMSC negative control, using unpaired student's t test. (**D**) Localisation of *Hcn3* and *Ppib* transcripts in ECs. Data are means of 3 cells per artery ± SEM; n = 3 rats. ***P = 0.0006 for *Hcn3* nuclear vs cytoplasmic localisation and *P = 0.0135 for *Ppib* nuclear vs cytoplasmic localisation, using unpaired student's t test. (**E**) Localisation of *Hcn3* and *Ppib* transcripts in VSMCs. Data are means of 3 cells per artery ± SEM, n = 3 rats. **P = 0.0016 for *Hcn3* nuclear vs cytoplasmic localisation and P = *0.0137 for *Ppib* nuclear vs cytoplasmic localisation, using unpaired student's t test.

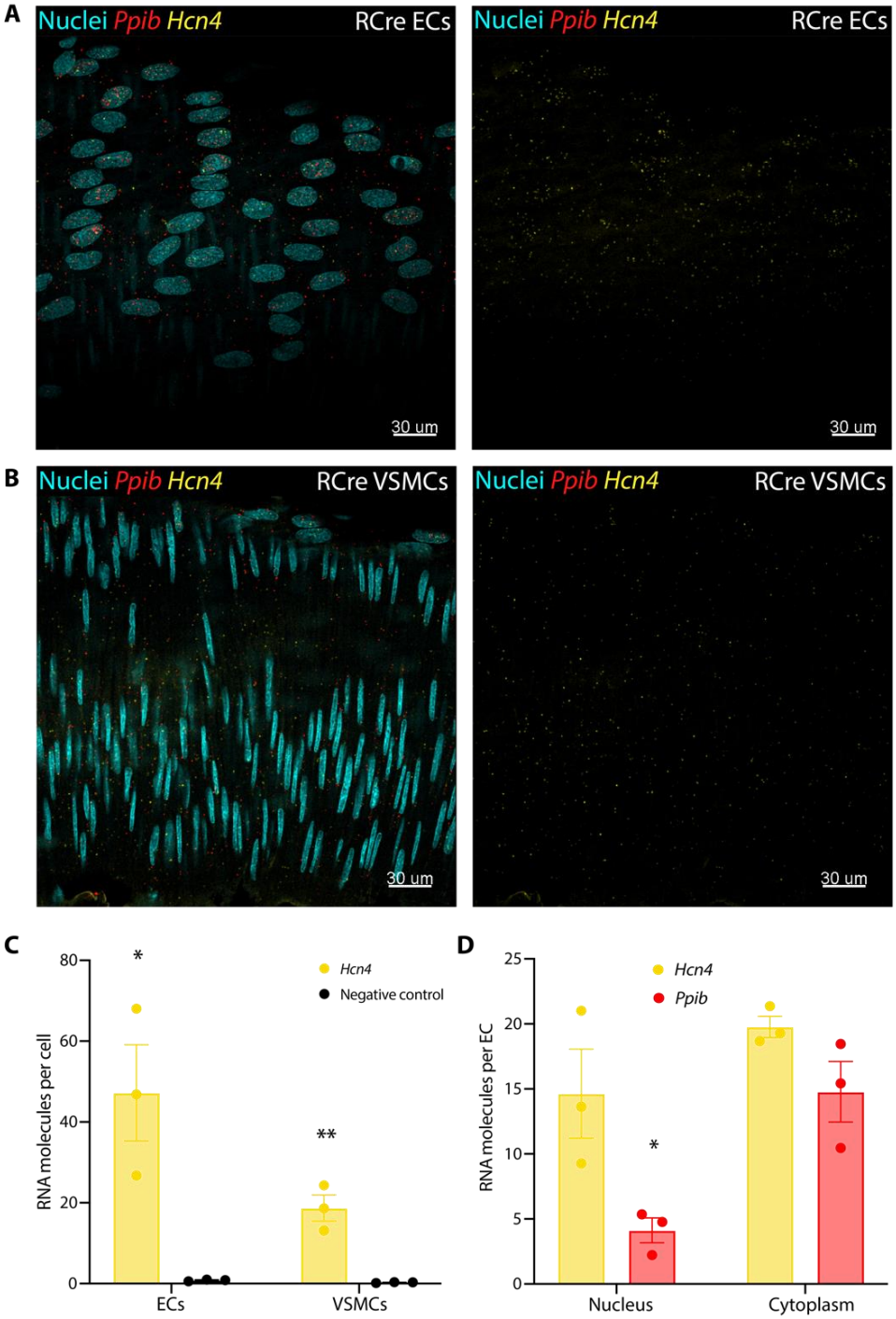
A
Nuclei Ppib Hcn4
RCre ECs
30 um
Nuclei Ppib Hcn4
RCre ECs
30 um
B
Nuclei Ppib Hcn4
RCre VSMCs
30 um
Nuclei Ppib Hcn4
RCre VSMCs
30 um
C
RNA molecules per cell
Hcn4
Negative control
ECs
VSMCs
D
RNA molecules per EC
Hcn4
Ppib
Nucleus
Cytoplasm
E
RNA molecules per VSMC
Hcn4
Ppib
Nucleus
Cytoplasm

Figure 5.3.12. Expression of *Hcn4* mRNA by rat cremaster arteries (RCres). RNAscope was used to determine *Hcn4* expression (yellow) by endothelial cells (ECs, **A**) and vascular smooth muscle cells (VSMCs, **B**) of wire-myograph mounted cremaster arteries. *Ppib* (red) was used as a positive control. (**C**) Quantification of *Hcn4*, expressed as molecules per cell and compared against the negative control. Data are means ± SEM; n = 3. *P = 0.0176 vs EC negative control and **P = 0.0047 vs VMSC negative control, using unpaired student's t test. (**D**) Localisation of *Hcn4* and *Ppib* transcripts in ECs. Data are means of 3 cells per artery ± SEM; n = 3 rats. P = 0.2188 for *Hcn4* nuclear vs cytoplasmic localisation and *P = 0.0135 for *Ppib* nuclear vs cytoplasmic localisation, using unpaired student's t test. (**E**) Localisation of *Hcn4* and *Ppib* transcripts in VSMCs. Data are means of 3 cells per artery ± SEM, n = 3 rats. P = 0.0565 for *Hcn4* nuclear vs cytoplasmic localisation and P = *0.0137 for *Ppib* nuclear vs cytoplasmic localisation, using unpaired student's t test.

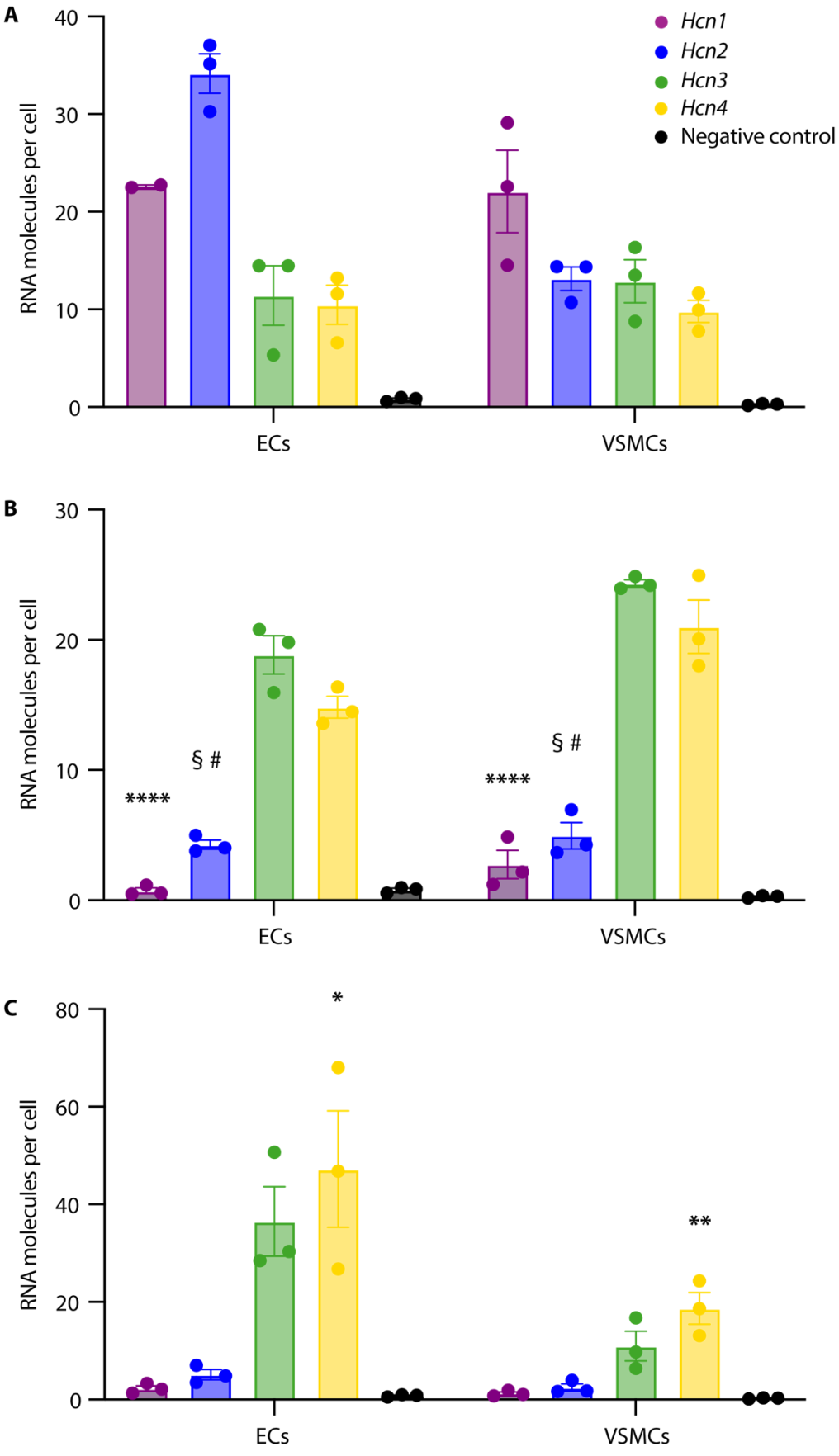
A
B
C
RNA molecules per cell
Hcn1
Hcn2
Hcn3
Hcn4
Negative control
ECs
VSMCs
****
§ #
*
**

Figure 5.3.13. Quantification of hyperpolarization-activated cyclic nucleotide-gated (HCN) channel mRNA. Quantification of *Hcn* mRNA in endothelial cells (ECs) and vascular smooth muscle cells (VSMCs) of rat mesenteric arteries (RMAs, **A**), coronary arteries (RCos, **B**), and cremaster arteries (RCres, **C**). To generate negative controls, the RNAscope protocol was carried out minus the addition of target RNA probes. Data are means ± SEM; n = 3 for each. For RCo ECs, ****P < 0.0001 vs *Hcn3* and *Hcn4*, §P < 0.0001 vs *Hcn3*, and $^{\#}$P = 0.0002 vs *Hcn4*, using ordinary one-way ANOVA with Bonferroni's correction. For RCo VSMCs, ****P < 0.0001 vs *Hcn3* and *Hcn4*, §P < 0.0001 vs *Hcn3*, and $^{\#}$P = 0.0001 vs *Hcn4*, using ordinary one-way ANOVA with Bonferroni's correction. For RCre ECs, *P = 0.0110 and 0.0162 vs *Hcn1* and *Hcn2*, respectively, using ordinary one-way ANOVA with Bonferroni's correction. For RCre VSMCs, **P = 0.0036 and 0.0057 vs *Hcn1* and *Hcn2*, respectively, using ordinary one-way ANOVA with Bonferroni's correction. Statistical comparisons of each transcript against the negative control are included in previous figures.

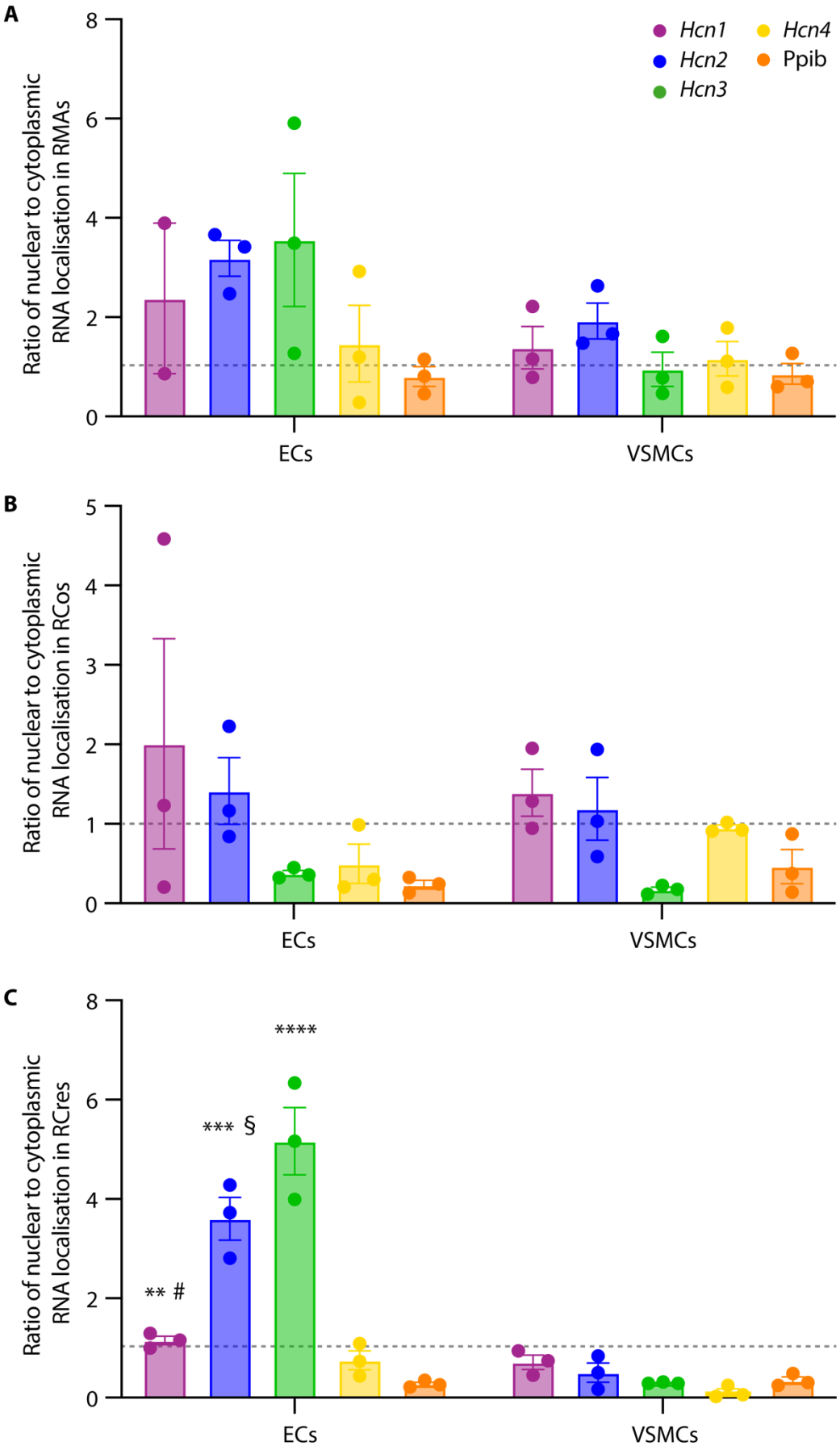
A
Ratio of nuclear to cytoplasmic RNA localisation in RMAs
Hcn1
Hcn2
Hcn3
Hcn4
Ppib
ECs
VSMCs
B
Ratio of nuclear to cytoplasmic RNA localisation in RCos
ECs
VSMCs
C
Ratio of nuclear to cytoplasmic RNA localisation in RCres
** #
*** §
****
ECs
VSMCs

Figure 5.3.14. Localisation of hyperpolarization-activated cyclic nucleotide-gated (HCN) channel mRNA. Ratio of nuclear to cytoplasmic localisation of *Hcn* and *Ppib* mRNA transcripts in endothelial cells (ECs) and vascular smooth muscle cells (VSMCs) of rat mesenteric (RMA, **A**), coronary (RCo, **B**), and cremaster arteries (RCre, **C**). The grey dashed line at a ratio of 1 indicates equally distributed RNA expression across the nucleus and cytoplasm. For each artery, the average number of RNA molecules in the nucleus and cytoplasm was determined from 3 cells, and this was repeated for 3 separate arteries (n = 3 rats). Data are means ± SEM. For RMAs and RCos, no statistically significant differences were detected using ordinary one-way ANOVA with Bonferroni's correction. For RCre ECs, **P = 0.0088 vs *Hcn2*, $^{\#}$P = 0.0002 vs *Hcn3,* ***P = 0.0008 vs *Ppib*, §P = 0.0029 vs *Hcn4,* and ****P < 0.0001 vs *Hcn4* and *Ppib*, using ordinary one-way ANOVA with Bonferroni's correction.

5.3.2 Rat mesenteric, coronary, and cremaster arteries express HCN channel protein

Next, immunohistochemistry was used to label HCN channel proteins in wire-fixed RMAs (**Figure 5.3.15**), RCos (**Figure 5.3.16**), and RCres (**Figure 5.3.17**). To test the specificity of the antibodies, they were first validated using rat SAN tissue as a positive control (**Figure 5.3.18**). In this positive control, all 4 HCN channel isoforms were detected using specific antibodies. While this differs slightly from a previous report which detected HCN2 and HCN4 (but not HCN1 or HCN3) using western blotting in rat SAN (Huang *et al.*, 2016), the additional detection of HCN1 and HNC3 channels in the present study may reflect the increased sensitivity of immunohistochemical analysis compared to western blotting. Negative controls indicate that the primary antibodies used in this immunohistochemistry protocol were specific to their respective targets (**Figure 5.3.19**).

For all 3 artery types, HCN channels were present in the endothelium but not the smooth muscle layer. In RMAs, there was punctate labelling of all 4 HCN channel isoforms in ECs, which was distributed evenly across the cells (**Figure 5.3.15**). HCN1 and HCN2 were more highly expressed than HCN3 and HCN4, where only a few puncta were visible. In RCos, only HCN1, HCN2, and HCN3 channels were detected in the endothelium (**Figure 5.3.16).** HCN1 channels were the most highly expressed, followed by HCN2 then HCN3. Finally, in RCres, punctate labelling for all 4 HCN channel isoforms was present in ECs, with HCN4 channels being the most highly expressed, followed by HCN1, HCN3 and then HCN2 (**Figure 5.3.17**)

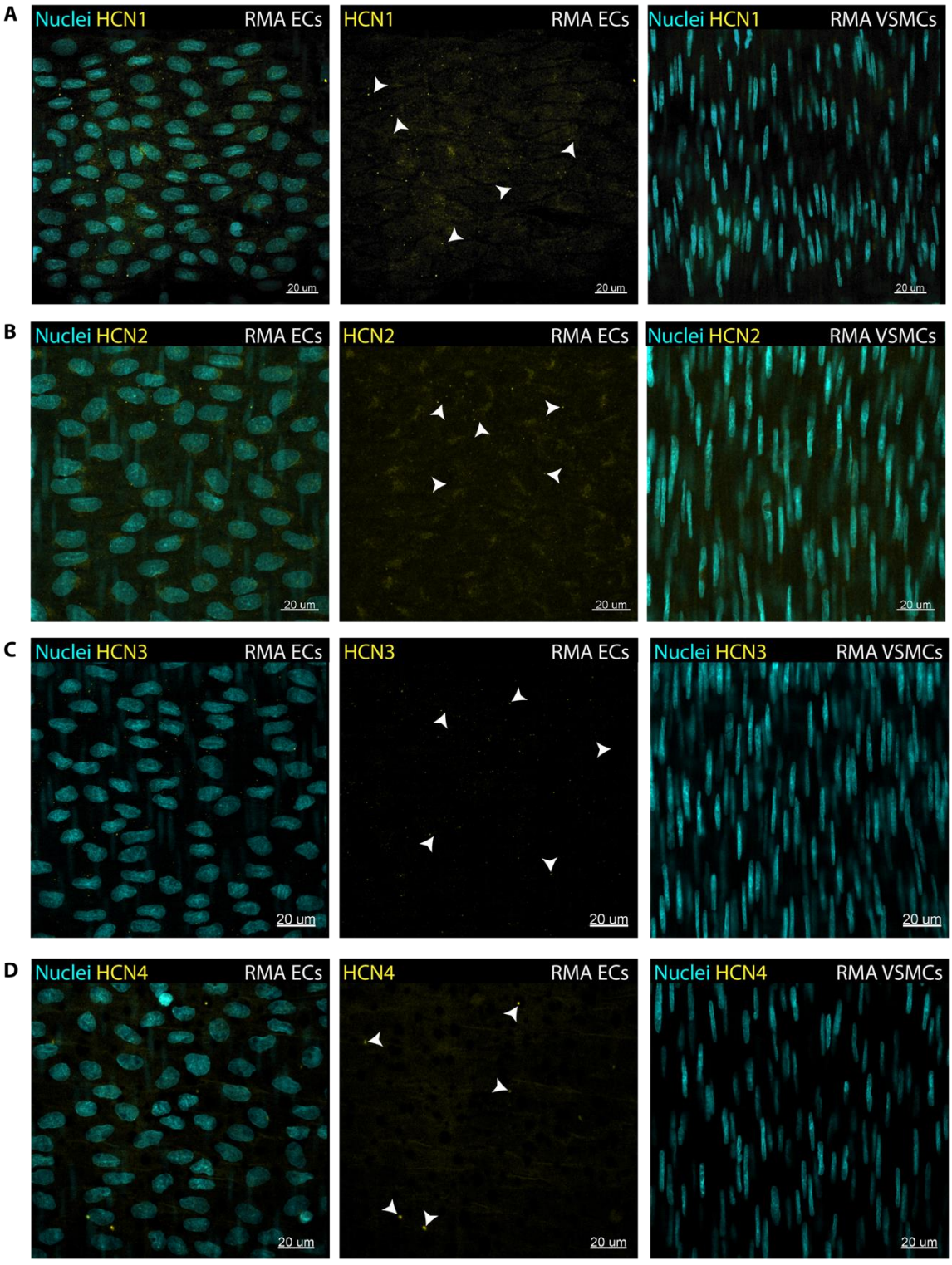
A
Nuclei HCN1
RMA ECs
20 um
HCN1
RMA ECs
20 um
Nuclei HCN1
RMA VSMCs
20 um
B
Nuclei HCN2
RMA ECs
20 um
HCN2
RMA ECs
20 um
Nuclei HCN2
RMA VSMCs
20 um
C
Nuclei HCN3
RMA ECs
20 um
HCN3
RMA ECs
20 um
Nuclei HCN3
RMA VSMCs
20 um
D
Nuclei HCN4
RMA ECs
20 um
HCN4
RMA ECs
20 um
Nuclei HCN4
RMA VSMCs
20 um

Figure 5.3.15. Expression of hyperpolarization-activated cyclic nucleotide-gated (HCN) channel proteins by rat mesenteric arteries (RMAs). Immunohistochemistry was used to determine expression of HCN1 (**A**), HCN2 (**B**), HCN3 (**C**), and HCN4 (**D**) by endothelial cells (ECs) and vascular smooth muscle cells (VSMCs), shown in yellow, in wire-myograph mounted mesenteric arteries. For all 4 channels, punctate expression was visible in the endothelium, with selected puncta indicated using white arrow heads. There was no HCN expression in VSMCs. Images are representative of n = 3 rats.

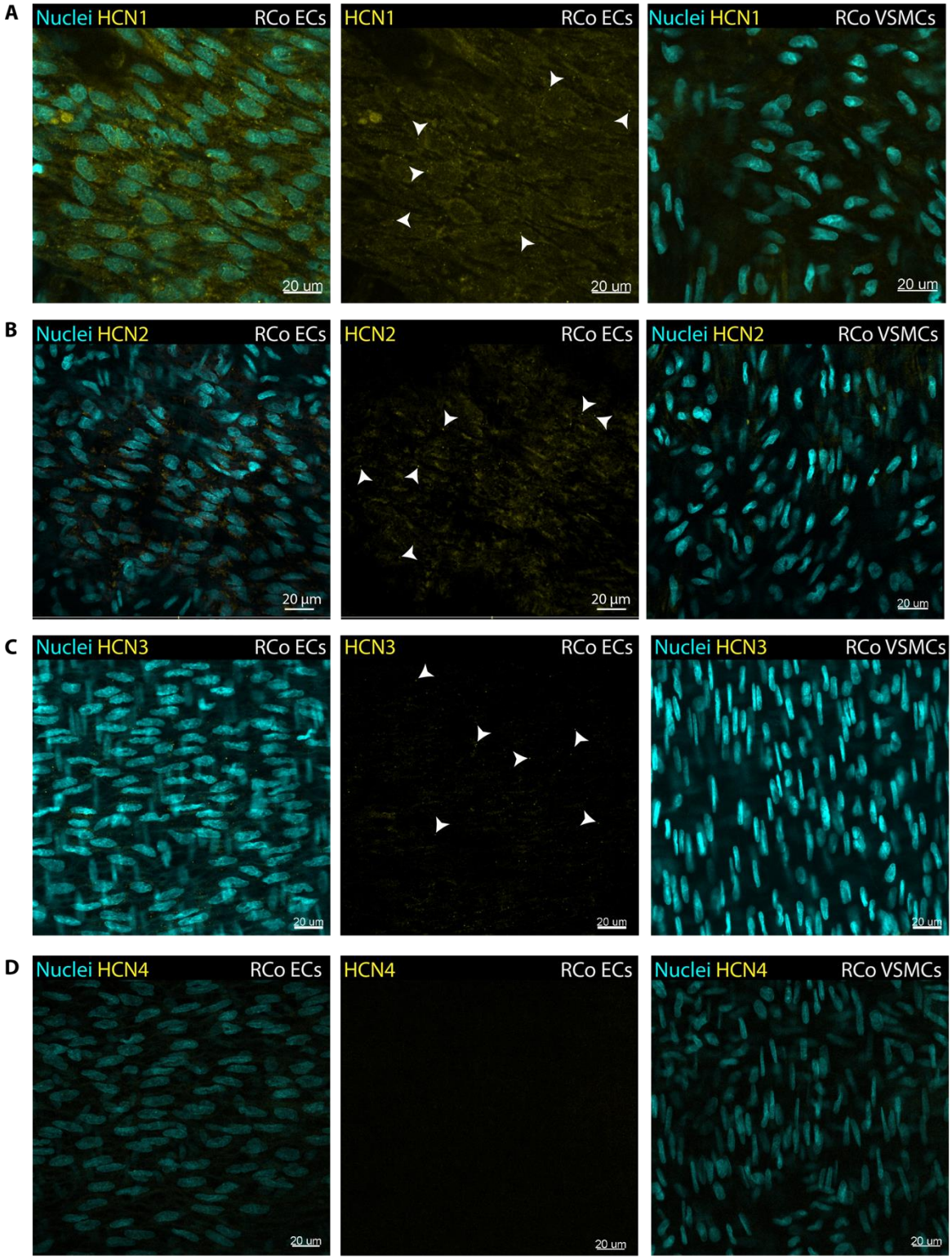
A
Nuclei HCN1
RCo ECs
20 um
HCN1
RCo ECs
20 um
Nuclei HCN1
RCo VSMCs
20 um
B
Nuclei HCN2
RCo ECs
20 µm
HCN2
RCo ECs
20 µm
Nuclei HCN2
RCo VSMCs
20 um
C
Nuclei HCN3
RCo ECs
20 um
HCN3
RCo ECs
20 um
Nuclei HCN3
RCo VSMCs
20 um
D
Nuclei HCN4
RCo ECs
20 um
HCN4
RCo ECs
20 um
Nuclei HCN4
RCo VSMCs
20 um

Figure 5.3.16. Expression of hyperpolarization-activated cyclic nucleotide-gated (HCN) channel proteins by rat coronary arteries (RCos). Immunohistochemistry was used to determine expression of HCN1 (**A**), HCN2 (**B**), HCN3 (**C**), and HCN4 (**D**) by endothelial cells (ECs) and vascular smooth muscle cells (VSMCs), shown in yellow, in wire-myograph mounted coronary arteries. For HCN1-3, punctate expression was visible in the endothelium, with selected puncta indicated using white arrow heads. There was no HCN4 expression in the endothelium, and no HCN isoforms were present in VSMCs. Images are representative of n = 3 rats.

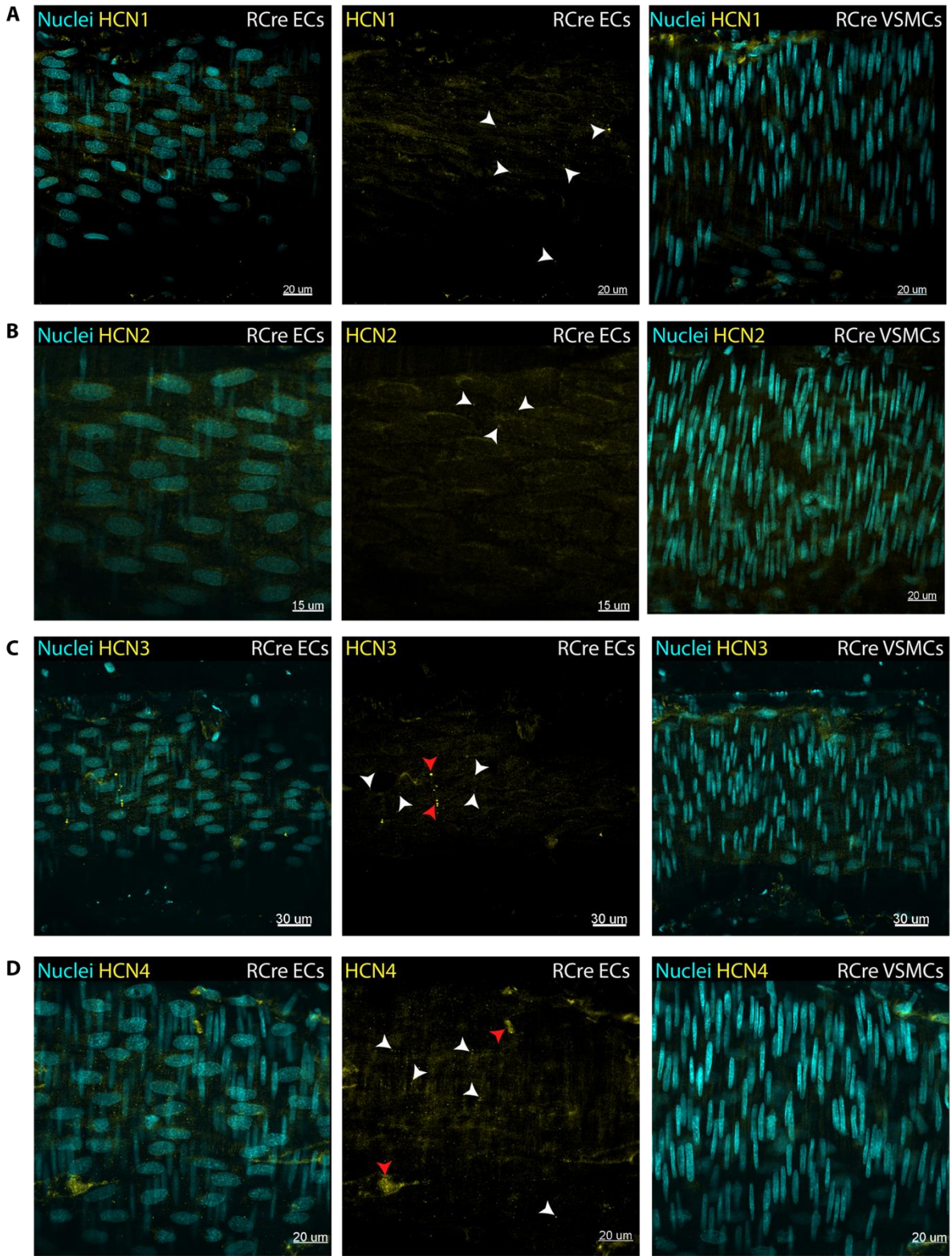
A
Nuclei HCN1
RCre ECs
20 um
HCN1
RCre ECs
20 um
Nuclei HCN1
RCre VSMCs
20 um
B
Nuclei HCN2
RCre ECs
15 um
HCN2
RCre ECs
15 um
Nuclei HCN2
RCre VSMCs
20 um
C
Nuclei HCN3
RCre ECs
30 um
HCN3
RCre ECs
30 um
Nuclei HCN3
RCre VSMCs
30 um
D
Nuclei HCN4
RCre ECs
20 um
HCN4
RCre ECs
20 um
Nuclei HCN4
RCre VSMCs
20 um

Figure 5.3.17. Expression of hyperpolarization-activated cyclic nucleotide-gated (HCN) channel proteins by rat cremaster arteries (RCres). Immunohistochemistry was used to determine expression of HCN1 (**A**), HCN2 (**B**), HCN3 (**C**), and HCN4 (**D**) by endothelial cells (ECs) and vascular smooth muscle cells (VSMCs), shown in yellow, in wire-myograph mounted mesenteric arteries. For all 4 channels, punctate expression was visible in the endothelium, with selected puncta indicated using white arrow heads. Labelling artefacts are indicated using red arrowheads. There was no HCN expression in VSMCs. Images are representative of n = 3 rats.

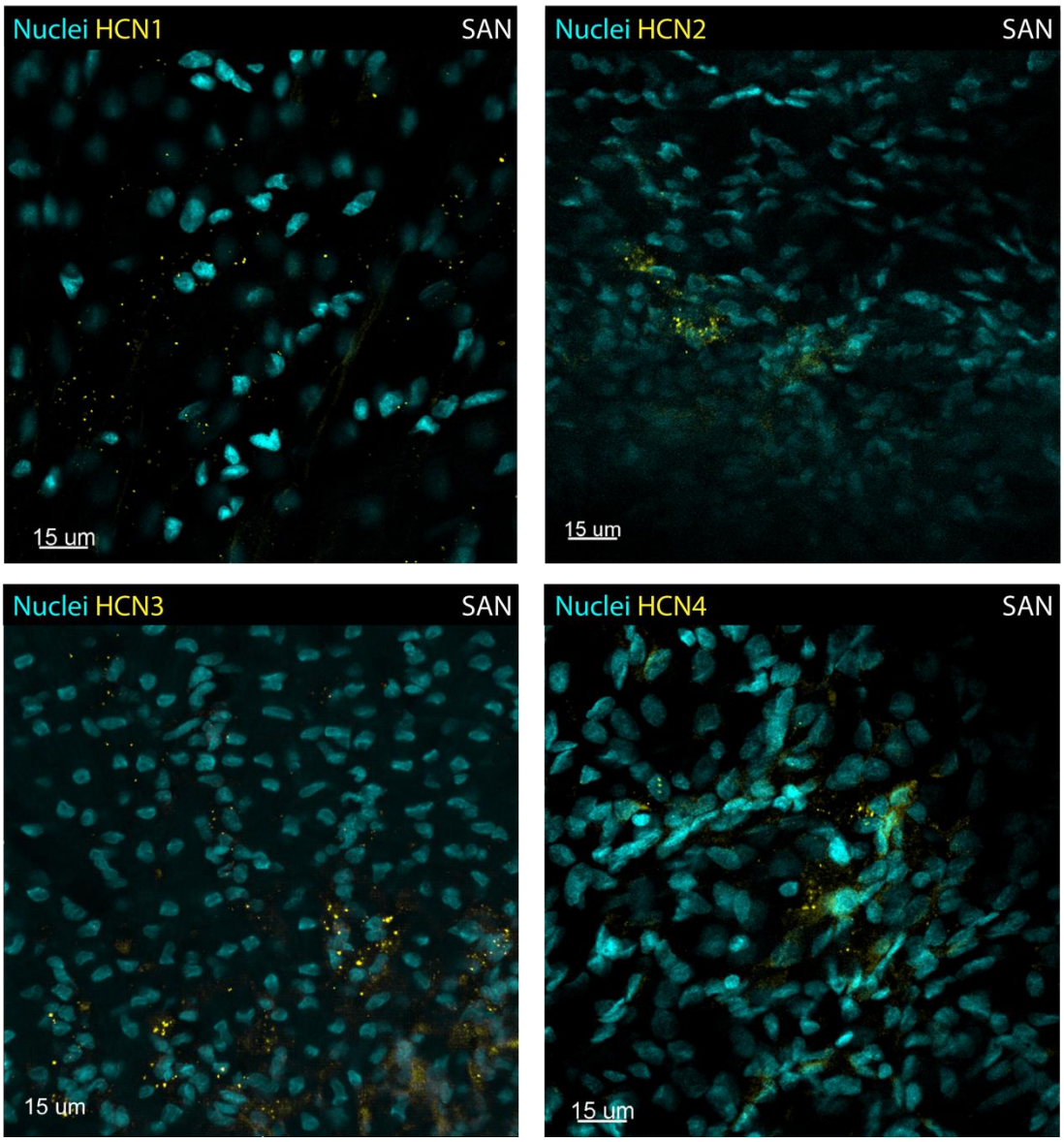

Figure 5.3.18. Expression of hyperpolarization-activated cyclic nucleotide-gated (HCN) channel proteins in rat sinoatrial node (SAN). The SAN was used as a positive control due to previous reports of HCN channel expression in this tissue. For all four channels, punctate expression was visible throughout the tissue (yellow). Images are representative of n = 3 rats.

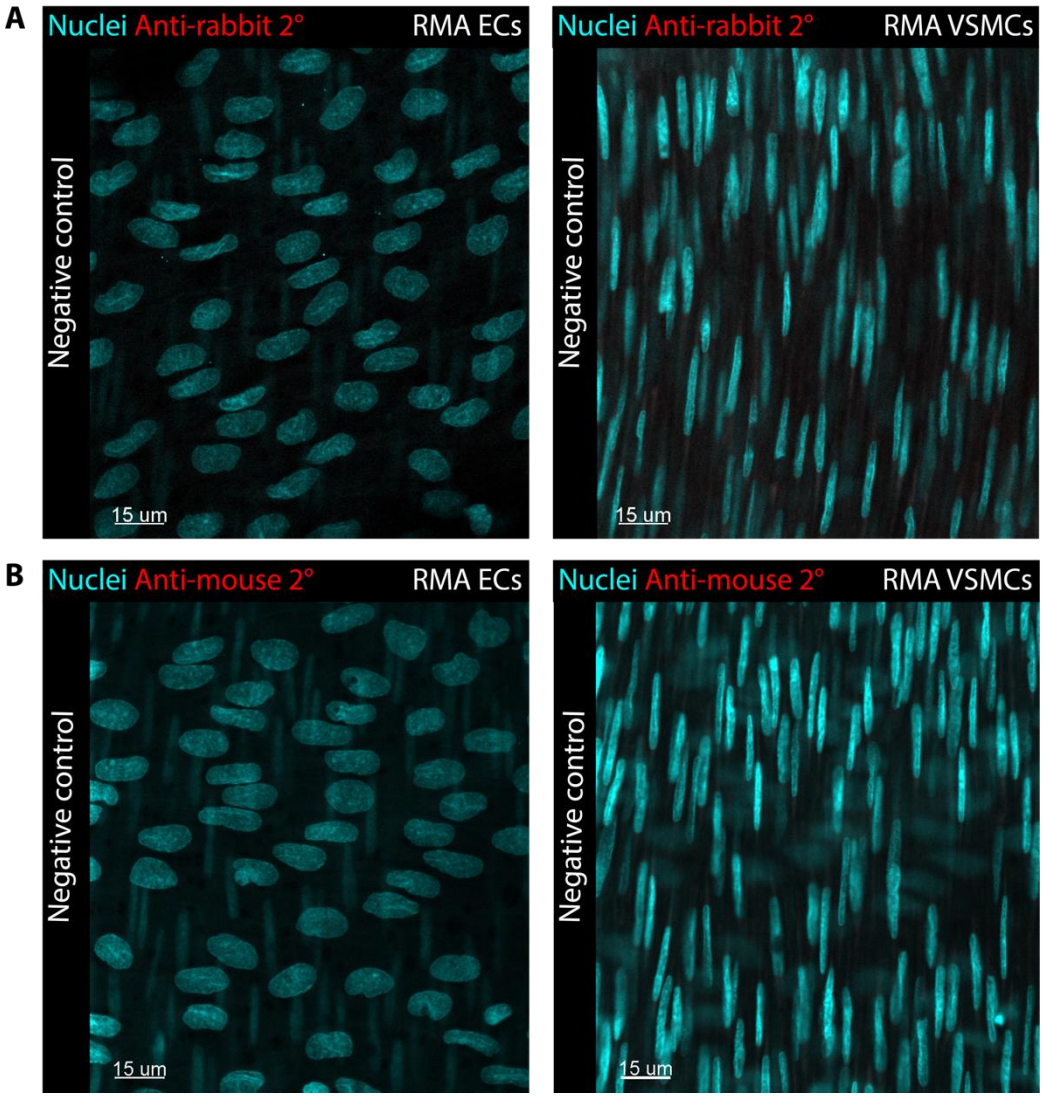

Figure 5.3.19. Negative controls of hyperpolarization-activated cyclic nucleotide-gated (HCN) channel immunolabelling in endothelial cells (ECs) and vascular smooth muscle cells (VSMCs) of rat mesenteric arteries (RMAs). Primary antibodies were omitted from the immunohistochemistry protocol, and only the secondary antibodies (AlexaFluor™ 633 goat anti-rabbit, **A**; or AlexaFluor™ 633 goat anti-mouse, **B**) were applied. Images are representative of n = 3 rats.

5.4 Discussion

The current study investigated the expression of HCN channels in rat resistance mesenteric, coronary, and cremaster arteries, using a combined approach of RNAscope and immunohistochemistry. For the first time, HCN channels were identified in the endothelium of these arteries at both mRNA (**Figures 5.3.1 - 5.3.13**) and protein levels (**Figures 5.3.15 – 5.3.17**), a finding which supports the hypothesis that HCN channels are involved in the propagation of conducted vasodilation.

Whilst HCN mRNA was largely consistent with protein expression in the endothelium, there were discrepancies in VSMCs. mRNA transcripts encoding all 4 HCN channels were present in VSMCs of mesenteric and cremaster arteries, and transcripts encoding HCN2-4 were present in VSMCs from coronary arteries. Immunohistochemical analysis revealed that no HCN channels were present in VSMCs at the protein level in any of the artery types, indicating that the mRNA detected using RNAscope was not translated in these cells. This could be a result of VSMC-specific post-transcriptional regulation, such as miRNA-mediated suppression of *Hcn* mRNA translation, or rapid degradation of HCN channels due to proteolysis mechanisms. It could also be that the antibodies used to label HCN channels detected different splice variants than the ones expressed by these arteries, although the existence of HCN splice variants has yet to be reported. Alternatively, the disparity could reflect the differing sensitivities of the two methods used to assess HCN expression. RNAscope is considered to be more sensitive than immunohistochemistry as it allows visualisation of single RNA molecules (Wang *et al.*, 2012), which may explain the detection of mRNA in the absence of detectable protein. In any case, these findings underscore the importance of combining RNAscope with protein detection methods such as immunohistochemistry when investigating gene expression. While RNAscope offers high sensitivity for RNA detection, it does not provide information on protein expression, which is crucial for informing our understanding of the functional relevance of gene transcripts.

While increases in EC Ca^{2+} following hyperpolarisation induced by K^+ channel openers have previously been reported in isolated cells (Luckhoff and Busse, 1990; Langheinrich *et al.*, 1998), this phenomenon has not yet been demonstrated in intact arteries. Unpublished data from the Dora/Garland group using rat cremaster arterioles indicates that opening K_{ATP} channels using levcromakalim (3 μM) results in hyperpolarisation and Ca^{2+} influx into ECs at both the site of stimulation and ~500 μm upstream. This increase in EC [Ca^{2+}] was blocked by ZD 7288 (10 μM), demonstrating that HCN channels may be responsible for Ca^{2+} influx into hyperpolarised ECs and the propagation of conducted vasodilation (See **Figure 1.5.7.2** for proposed mechanism). Combining the findings of the present investigation with the unpublished functional data from the Dora/Garland group provides compelling evidence for HCN channels being key players in coordinating vascular responses along the arterial tree.

This could have implications for both current drug treatments and the development of treatments in the future. Blocking these channels with ivabradine, which is often prescribed for heart failure and angina, could result in perturbed EDH and conducted vasodilation. Ivabradine is effective in the treatment of these disorders due to its negative chronotropic effects, which reduces myocardial oxygen consumption (Cober *et al.*, 2011). However, if ivabradine does impair conducted vasodilation, especially of coronary resistance arteries, its beneficial effects may be limited by its impairment of vasodilation. This will be most apparent in situations where the heart's workload is increased, such as during exercise, as coronary arteries may not dilate sufficiently to provide enough blood flow to match the myocardium's demands. Developing a next-generation HCN channel blocker which selectively targets channels in the SAN and not in ECs would avoid this limitation, likely resulting in enhanced therapeutic effects. Furthermore, developing drugs which selectively activate vascular HCN channels may be beneficial in restoring conducted vasodilation responses which have been impaired. There are currently no dedicated HCN channel activators available for clinical use, although a few drugs which potentiate HCN currents have been characterised experimentally. For example, fisetin is a naturally occurring flavonoid found in fruits and vegetables, which

potentiates HCN2 mediated currents by binding to the CNBD and right-shifting the channel's current-voltage curve (Carlson *et al.*, 2013). Further development of this compound, plus other candidates, may produce a drug which selectively activates vascular HCN channels, thereby improving EDH and conducted vasodilation.

The role of HCN channels in endothelium-dependent vasodilation may not just be restricted to sustaining EDH; Ca^{2+} influx through these channels may also stimulate eNOS, resulting in NO production in hyperpolarised ECs. Studies using arteries from varied vascular beds and species show that hyperpolarised ECs can produce NO. For example, stimulation of endothelial muscarinic receptors with ACh results in hyperpolarisation and Ca^{2+}-dependent eNOS activation (Busse *et al.*, 1988; Chen *et al.*, 1988; Cohen *et al.*, 1997). This occurs via the release of Ca^{2+} from intracellular stores, although it is possible that HCN channels may contribute to the elevated intracellular [Ca^{2+}], further enhancing NO production. Due to the limited studies acknowledging the presence of HCN channels in ECs, their potential role in NO production is poorly understood and requires further investigation.

Interestingly, there is evidence to suggest that a regulatory relationship exists between NO and HCN channels, demonstrated using cultured rat cerebral ECs (Janigro *et al.*, 1994) and isolated guinea pig atria (Musialek *et al.*, 1997). These studies found that NO can enhance HCN channel conductance by elevating levels of cGMP, a cyclic nucleotide known to gate these channels, especially the HCN2 subtype (Wahl-Schott and Biel, 2009). If HCN channels do contribute to NO production, this regulatory mechanism could result in a positive-feedback loop of NO production. The functional significance of this potential mechanism is not immediately obvious, therefore further investigations should be made into whether it occurs in intact arteries and its effects on arterial tone.

5.5. Conclusions

This study provides the first evidence for the expression of HCN channels in resistance arteries at the mRNA and protein level. Taken together with unpublished data from the Dora/Garland group, the data presented herein strengthens the hypothesis that endothelial HCN channels facilitate Ca^{2+} entry into hyperpolarised ECs, which may be important in the propagation of conducted vasodilation.

This may have important implications for pharmacological interventions, particularly regarding the use of HCN channel blockers like ivabradine. The potential impact on vascular function identifies the need for developing more selective HCN channel modulators which can differentiate between cardiac and vascular tissue.

In conclusion, this study provides new insights into HCN channel expression in resistance arteries, laying the groundwork for future investigations into their role in vascular physiology.

6. Summary and Future Directions

6.1 Summary

This thesis advances our understanding of vascular physiology through several key contributions. First, by developing and validating a protocol for loading intact, pressurised resistance arteries with DAR-4M AM, a highly sensitivity NO-specific fluorescent indicator. Chapter 3 marks the first successful validation of DAR-4M AM in a near-physiological artery preparation, opening up new avenues for NO research. While a different NO dye, Cu_2FL2E, has previously been validated in intact arteries, the present study found it to be ineffective under the conditions tested.

Next, this research investigated two mechanisms of rat resistance artery vasodilation, one involving T-type VGCCs, and the other involving HCN channels. The findings in Chapter 4 confirm the absence of functional VGCCs in ECs, and that T-type VGCCs expressed by VSMCs are enriched at the sites where MEPs make contact. This localisation suggests that these channels may contribute to EC Ca^{2+} events and the generation of EDH/NO. The vasodilatory effect of VSMC $Ca_V3.2$ channels in rat coronary arteries was also probed in detail, where they were found to functionally couple with BK_{Ca} channels to paradoxically oppose vasoconstriction. This is the first time that a $Ca_V3.2/BK_{Ca}$ channel microdomain has been identified in coronary resistance arteries, which is important as alterations in this channel interaction could contribute to the coronary microvascular dysfunction often observed in cardiovascular disorders.

Finally, Chapter 5 provides the first evidence for the endothelial expression of HCN channels in resistance arteries. This links to unpublished functional data showing that Ca^{2+} influx through these channels contributes to EC Ca^{2+} events and possibly conducted vasodilation. As the mechanism underpinning the propagation of conducted vasodilation over long

distances (1-2 mm) is currently unknown, the data presented herein supports the notion that HCN channels may be important in this process.

6.2 Future directions

6.2.1 Enhancing DAR-4M AM for detecting NO

In Chapter 3, DAR-4M AM was validated for detecting NO released by arteries, where its response to ACh was measured under control conditions and in the presence of L-NAME. Initially, the fluorescence response of DAR-4M to ACh was inhibited by L-NAME for up to 60 minutes; however, after this, fluorescence increased to levels similar to those observed under control conditions, i.e., when L-NAME was absent. This rebound in fluorescence may be attributed to unexpected effects of L-NAME, such as its incomplete inhibition of eNOS (Cohen *et al.*, 1997), a gradual reduction its inhibitory capacity of eNOS (Pechanova *et al.*, 2020), or even its gradual release of NO over time (Liu *et al.*, 2019). Further studies of DAR-4M AM in intact artery preparations should investigate whether the rebound in fluorescence after 60 minutes persists when using higher concentrations of L-NAME (>100 μM) or alternative eNOS inhibitors such as asymmetric dimethylarginine (ADMA) or L-thiocitrulline. This will help determine if the observed effect is due to the accumulation of NO produced by uninhibited eNOS, or NO originating from L-NAME itself. If these measures do not prevent the increase in fluorescence evoked by ACh 60 minutes after its application, it may reflect an inherent limitation of DAR-4M AM in detecting NO over extended periods.

Although this research indicates that DAR-4M AM is effective at detecting NO in intact arteries, we propose several modifications to enhance its utility for future studies. Currently, DAR-4M only detects one form of NO, the uncharged free radical (NO•), meaning it does not reflect the levels of other physiologically-relevant nitrogen species produced by ECs, such as HNO.

Studies suggest that HNO can be formed endogenously, where it mediates vasodilation via the sGC/cGMP pathway (Yuill *et al.*, 2011). Therefore, modifying DAR-4M AM so that it detects both NO• and HNO would provide a more complete picture of NO signalling in the vasculature, the extent of which is likely underestimated by the detection of just one nitrogen species alone. Additionally, modifying DAR-4M AM to reversibly bind NO (and HNO) would be advantageous as it would enable real-time monitoring of rapid and transient changes in NO levels, offering insights into the dynamics of NO signalling that are currently difficult to capture. It would also allow repeated measurements within the same artery preparation, maximising data collection from these technically challenging experimental set ups and reducing the number of animals required for research. Reducing the extent to which DAR-4M AM binds to elastin is also desirable, as this binding might interfere with its ability to report NO levels.

Finally, we propose developing an advanced protocol for using DAR-4M AM in pressurised arteries which eliminates the need for nifedipine to prevent movement artefacts. This would provide important insights into basal NO release in arteries with myogenic tone or during vasoconstriction. To minimise movement artefacts due to changes in artery diameter, midplane imaging through a section of the artery wall could be utilised. This configuration is more tolerant for movement in the Z-axis, and would allow ECs, VSMCs, and the lumen to be visualised at once. As midplane imaging requires deeper laser penetration into the tissue, multiphoton microscopy may be required, instead of the single-photon confocal microscopy used in the present study. Adapting the current protocol to incorporate midplane multiphoton microscopy may require additional optimisation, such as adjusting dye loading times and laser power, and will need to be validated against our current method.

6.2.2 Investigating voltage-gated calcium channel expression in endothelial cells

Chapter 4 found that mRNA for T-type ($Ca_V3.1$, 3.2, and 3.3) and L-type ($Ca_V1.2$) channels was present in ECs of mesenteric and coronary arteries, with *Cacna1c* mRNA ($Ca_V1.2$) being

the most abundantly expressed. *Cacna1c* transcripts were mostly restricted to EC nuclei, suggesting a mechanism might exist where they are released into the cytoplasm under specific pathological conditions, such as hypoxia or oxidative stress, to facilitate protein translation. This unidentified mechanism may explain the observations of L-type I_{Ca} in cultured, but not native ECs (Bossu *et al.*, 1989; Wu *et al.*, 2003; Olschewski *et al.*, 2001), which are often exposed to non-physiological conditions like increased oxidative stress which are associated with pathological conditions *in vivo* (Halliwell, 2003). The possible stimuli which trigger the export and translation of *Cacna1c* mRNA into $Ca_V1.2$ protein should be further investigated in arteries, as it is possible that functional $Ca_V1.2$ channels are expressed by ECs in certain disease states, altering normal artery function. For example, EC I_{Ca} could be studied in arteries where oxidative stress has been induced by free-radical generating compounds such as hydrogen peroxide, or in arteries from genetic animal models with perturbed antioxidant defence mechanisms such as superoxide dismutase knockouts (Li *et al.*, 1995). These arteries could also be fixed following experimentation, where RNAscope and immunohistochemistry could be performed to support the functional data.

6.2.3 Exploring myoendothelial projection dynamics

When investigating the relationship between T-type VGCC expression and MEPs in RMAs, we found that the two were often aligned. Interestingly, there were a number of holes in the IEL that did not house a MEP but did show signal for T-type VGCCs, perhaps suggesting that MEPs were primed to form in these locations. While there is evidence of increased MEPs in hypertension (Michel *et al.*, 1995), whether they form and retract dynamically under physiological conditions is less well understood and requires further investigation. This could involve loading live pressurised arteries with calcein to visualise MEPs and observing their positioning over time. If MEPs do indeed form and retract dynamically under physiological conditions, it could be a way of ‘resetting’ modifications to gap junctions which alter their permeability. Straub *et al.* showed that *S*-nitrosylation of Cx43, which comprises heterocellular

gap junctions in MEPs, increases permeability and promotes vasodilation, whilst denitrosylation does the opposite (Straub *et al.*, 2011). Additionally, the triggers for MEP formation, such as local changes in oxygen demand, should be investigated further, which may lead to the development of treatments which preserve or enhance MEP formation and thus vasodilation.

6.2.4 Characterising coronary artery sensitivity to nifedipine

When characterising the effects of nifedipine in myogenically-active coronary arteries, we found that it was extremely potent (IC_{50} of ~600 fM) when compared to arteries from other vascular beds. The reason for this increased potency should be further investigated, perhaps starting with a comparison of $Ca_V1.2$ protein expression in arteries from a range of vascular beds and species, including humans. This should be combined with functional studies to correlate $Ca_V1.2$ expression levels with nifedipine sensitivity. Additional studies may also investigate whether specific $Ca_V1.2$ splice variants are preferentially expressed in coronary arteries. This could be achieved through RT-PCR analysis using primers specific to known splice variants, or by employing RNA sequencing to comprehensively identify all transcripts, including novel splice variants. The identification of a coronary artery-specific splice variant may lead to the development of drugs which specifically target this part of the circulation, which would be useful in treating patients with non-obstructive coronary artery disease and vasospastic angina with otherwise normal systemic blood pressure.

6.2.5 Investigating the $Ca_V3.2$ channel signalling microdomain

Chapter 4 found that VSMC $Ca_V3.2$ channels in coronary arteries functionally couple with BK_{Ca} channels, and their activity in arteries with myogenic tone prevents excess vasoconstriction. This is the first time that a $Ca_V3.2/BK_{Ca}$ channel microdomain has been identified in coronary resistance arteries, and it mirrors a similar microdomain which has been identified in rat

cerebral (Harraz *et al.*, 2014a) and mouse mesenteric resistance arteries (Harraz *et al.*, 2015). We propose that as well as BK_{Ca} channels, other calcium-activated K^+ channels are activated by $Ca_V3.2$-mediated Ca^{2+} influx, such as IK_{Ca} or SK_{Ca} channels. This is due to fact that addition of Ni^{2+} in the presence of BK_{Ca} channel blocker paxilline resulted in further contraction. Further experiments are required to determine whether IK_{Ca}/SK_{Ca} channels are involved in the $Ca_V3.2$ microdomain, such as investigating whether Ni^{2+} causes further contraction of coronary arteries in the combined presence of paxilline with NS 6180/TRAM-34 (IK_{Ca} channel blockers) or apamin (SK_{Ca} channel blocker). Additionally, the role of RyRs in the coronary VSMC $Ca_V3.2$/BK_{Ca} signalling microdomain should be probed further. Although we did not determine whether RyRs were activated by Ca^{2+} influx via $Ca_V3.2$ channels, the literature agrees that RyR-mediated Ca^{2+} sparks are required to activate BK_{Ca} channels and trigger vasodilation (Harraz *et al.*, 2014a; Harraz *et al.*, 2015). We could investigate the potential role of RyRs in the coronary VSMC microdomain by monitoring Ca^{2+} spark frequency in VSMCs; if RyRs are involved in the signalling microdomain, Ni^{2+} should reduce the frequency of sparks observed. Finally, measuring STOC frequency in coronary VSMCs would be useful as the effect of Ni^{2+} on STOCs is inconsistent between vascular beds. Harraz *et al.* (2014a) reported that Ni^{2+} decreased STOC frequency in rat cerebral arteries, however, Mullan *et al.* (2017) found the opposite in mouse superior epigastric arteries. It therefore appears that Ni^{2+}'s effects on STOC frequency are not universal across species and vascular beds and so should be probed further in coronary VSMCs.

6.2.6 The role of T-type voltage-gated calcium channels in disease

Surprisingly, no studies have yet been carried out to determine whether T-type VGCCs directly contribute to the development of cardiovascular disease. Initial experiments should determine whether arterial T-type VGCC expression and function changes in cardiovascular disease models such as hypertension, atherosclerosis, or diabetes. It has already been established that RyRs uncouple from BK_{Ca} channels in hypertension (Amberg *et al.*, 2003), but little is

known about whether changes also occur between $Ca_V3.2$/RyR coupling. Evidence shows that Ca^{2+} spark frequency is decreased at high intraluminal pressures (80 mmHg) in mesenteric arteries from mice with obesity-induced hypertension, compared to controls (Greenstein *et al.*, 2020). There was no change in Ca^{2+} spark frequency in arteries from hypertensive mice when observed at low intraluminal pressure (20 mmHg). This suggests that the increased activation of RyRs relies on a voltage-dependent mechanism, perhaps involving $Ca_V3.2$ channels, which might be lost in hypertension. A loss of $Ca_V3.2$ channel input, either through reduced expression of uncoupling from RyRs, is more likely to be responsible for the depressed Ca^{2+} spark activity in hypertensive arteries than changes in L-type I_{Ca}. Although Ca^{2+} influx through $Ca_V1.2$ channels is considered the primary driver of RyR activation (Essin *et al.*, 2007), evidence suggests that these channels are upregulated in hypertension (Pesic *et al.*, 2004). This not only brings into the question the importance of $Ca_V1.2$ I_{Ca} in activating RyRs in the signalling microdomain, but also suggests that other VGCCs, such as $Ca_V3.2$, may contribute to arterial dysregulation in hypertension.

6.2.7 The role of HCN channels in conducted vasodilation

In Chapter 5, we demonstrated that HCN channels are expressed in ECs of mesenteric, coronary, and cremaster arteries, which supports unpublished functional data from the Dora/Garland group. Taken together, it appears that endothelial HCN channels underpin Ca^{2+} influx into hyperpolarised ECs in pressurised cremaster arterioles. Although this opens up the possibility of these channels in propagating conducted vasodilation, further studies are required to fully support this theory. These experiments could determine if conducted vasodilation, e.g., triggered by the focal application of ACh or bradykinin, still propagates upstream in pressurised arteries in the presence of an HCN channel blocker, such as ivabradine or ZD 7288. Furthermore, demonstrating a role for endothelial HCN channels in conducted vasodilation in arteries from other vascular beds, including coronary arteries, will

be important. This is because ivabradine, which is widely used to treat angina and heart failure, may unknowingly impair vasodilation responses, limiting its therapeutic benefits.

7. References

Aalkjær, C., Nilsson, H. & Mey, J. G. R. D. 2021. Sympathetic and sensory-motor nerves in peripheral small arteries. *Physiological Reviews,* 101**,** 495-544.

Adeagbo, A. S. O. & Triggle, C. R. 1993. Varying Extracellular [K+] - a Functional-Approach to Separating Edhf-Related and Edno-Related Mechanisms in Perfused Rat Mesenteric Arterial Bed. *Journal of Cardiovascular Pharmacology,* 21**,** 423-429.

Afshar, Y., Ma, F., Quach, A., Jeong, A., Sunshine, H. L., Freitas, V., Jami-Alahmadi, Y., Helaers, R., Li, X., Pellegrini, M., Wohlschlegel, J. A., Romanoski, C. E., Vikkula, M. & Iruela-Arispe, M. L. 2023. Transcriptional drifts associated with environmental changes in endothelial cells. *eLife,* 12:e81370.

Allbritton, N. L., Meyer, T. & Stryer, L. 1992. Range of messenger action of calcium ion and inositol 1,4,5-trisphosphate. *Science,* 258**,** 1812-5.

Amberg, G. C., Bonev, A. D., Rossow, C. F., Nelson, M. T. & Santana, L. F. 2003. Modulation of the molecular composition of large conductance, Ca^{2+} activated K^{+} channels in vascular smooth muscle during hypertension. *Journal of Clinical Investigation,* 112**,** 717-24.

Ball, C. J., Wilson, D. P., Turner, S. P., Saint, D. A. & Beltrame, J. F. 2009. Heterogeneity of L- and T-Channels in the Vasculature. *Hypertension,* 53**,** 654-60.

Baruscotti, M., Bucchi, A. & Difrancesco, D. 2005. Physiology and pharmacology of the cardiac pacemaker ("funny") current. *Pharmacology and Therapeutics,* 107**,** 59-79.

Bayliss, W. M. 1902. On the local reactions of the arterial wall to changes of internal pressure. *The Journal of Physiology,* 28**,** 220-231.

Berge, C. A., Eskerud, I., Almeland, E. B., Larsen, T. H., Pedersen, E. R., Rotevatn, S. & Lonnebakken, M. T. 2022. Relationship between hypertension and non-obstructive coronary artery disease in chronic coronary syndrome (the NORIC registry). *PLoS ONE,* 17**,** e0262290.

Bijlenga, P., Liu, J. H., Espinos, E., Haenggeli, C. A., Fischer-Lougheed, J., Bader, C. R. & Bernheim, L. 2000. T-type alpha 1H Ca^{2+} channels are involved in Ca^{2+} signaling during terminal differentiation (fusion) of human myoblasts. *Proceedings of the National Academy of Sciences of the United States of America,* 97**,** 7627-32.

Bolivar, J. J., Tapia, D., Arenas, G., Castanon-Arreola, M., Torres, H. & Galarraga, E. 2008. A hyperpolarization-activated, cyclic nucleotide-gated, (Ih-like) cationic current and HCN gene expression in renal inner medullary collecting duct cells. *American Journal of Physiology - Cell Physiology,* 294**,** C893-906.

Bolotina, V. M., Najibi, S., Palacino, J. J., Pagano, P. J. & Cohen, R. A. 1994. Nitric oxide directly activates calcium-dependent potassium channels in vascular smooth muscle. *Nature,* 368**,** 850-853.

Bolton, T. B., Lang, R. J. & Takewaki, T. 1984. Mechanisms of Action of Noradrenaline and Carbachol on Smooth-Muscle of Guinea-Pig Anterior Mesenteric-Artery. *Journal of Physiology-London,* 351**,** 549-572.

Bondarenko, A. & Sagach, V. 2006. Na-K-ATPase is involved in the sustained ACh-induced hyperpolarization of endothelial cells from rat aorta. *British Journal of Pharmacology,* 149**,** 958-965.

Boric, M. P., Figueroa, X. F., Donoso, M. V., Paredes, A., Poblete, I. & Huidobro-Toro, J. P. 1999. Rise in endothelium-derived NO after stimulation of rat perivascular sympathetic mesenteric nerves. *American Journal of Physiology-Heart and Circulatory Physiology,* 277**,** H1027-H1035.

Bossu, J. L., Feltz, A., Rodeau, J. L. & Tanzi, F. 1989. Voltage-dependent transient calcium currents in freshly dissociated capillary endothelial cells. *FEBS Letters,* 255**,** 377-80.

Braunstein, T. H., Inoue, R., Cribbs, L., Oike, M., Ito, Y., Holstein-Rathlou, N. H. & Jensen, L. J. 2009. The Role of L- and T-Type Calcium Channels in Local and Remote Calcium Responses in Rat Mesenteric Terminal Arterioles. *Journal of Vascular Research,* 46**,** 138-151.

Brixius, K., Gross, T., Tossios, P., Geissler, H. J., Mehlhorn, U., Schwinger, R. H. & Hekmat, K. 2005. Increased vascular selectivity and prolonged pharmacological efficacy of the L-type Ca^{2+} channel antagonist lercanidipine in human cardiovascular tissue. *Clinical and Experimental Pharmacology and Physiology,* 32**,** 708-13.

Broillet, M.-C., Randin, O. & Chatton, J.-Y. 2001. Photoactivation and calcium sensitivity of the fluorescent NO indicator 4,5-diaminofluorescein (DAF-2): implications for cellular NO imaging. *FEBS Letters,* 491**,** 227-232.

Brown, H. F., DiFrancesco, D. & Noble, S. J. 1979. How does adrenaline accelerate the heart? *Nature,* 280**,** 235-6.

Budel, S., Schuster, A., Stergiopoulos, N., Meister, J. J. & Beny, J. L. 2001. Role of smooth muscle cells on endothelial cell cytosolic free calcium in porcine coronary arteries. *American Journal of Physiology - Heart and Circulatory Physiology,* 281**,** H1156-62.

Busse, R., Fichtner, H., Luckhoff, A. & Kohlhardt, M. 1988. Hyperpolarization and increased free calcium in acetylcholine-stimulated endothelial cells. *American Journal of Physiology,* 255**,** H965-9.

Busse, R., Lückhoff, A. & Mülsch, A. 1991. Cellular mechanisms controlling EDRF/NO formation in endothelial cells. *Endothelial Mechanisms of Vasomotor Control,* 82**,** 7-16.

Calejo, A. I., Reverendo, M., Silva, V. S., Pereira, P. M., Santos, M. A., Zorec, R. & Goncalves, P. P. 2014. Differences in the expression pattern of HCN isoforms among mammalian tissues: sources and implications. *Molecular Biology Reports,* 41**,** 297-307.

Carlson, A. E., Rosenbaum, J. C., Brelidze, T. I., Klevit, R. E. & Zagotta, W. N. 2013. Flavonoid regulation of HCN2 channels. *Journal of Biological Chemistry,* 288**,** 33136-45.

Chaytor, A. T., Evans, W. H. & Griffith, T. M. 1998. Central role of heterocellular gap junctional communication in endothelium-dependent relaxations of rabbit arteries. *The Journal of Physiology,* 508**,** 561-73.

Chemin, J., Monteil, A., Dubel, S., Nargeot, J. & Lory, P. 2001. The alpha1I T-type calcium channel exhibits faster gating properties when overexpressed in neuroblastoma/glioma NG 108-15 cells. *European Journal of Neuroscience,* 14**,** 1678-86.

Chen, C.-C., Lamping, K. G., Nuno, D. W., Barresi, R., Prouty, S. J., Lavoie, J. L., Cribbs, L. L., England, S. K., Sigmund, C. D., Weiss, R. M., Williamson, R. A., Hill, J. A. & Campbell, K. P. 2003. Abnormal Coronary Function in Mice Deficient in α 1H T-type Ca^{2+} Channels. *Science,* 302**,** 1416-1418.

Chen, G., Suzuki, H. & Weston, A. H. 1988. Acetylcholine releases endothelium-derived hyperpolarizing factor and EDRF from rat blood vessels. *British Journal of Pharmacology,* 95**,** 1165–1174.

Chen, Q. & Wang, X. L. 1997. Effects of nifedipine and cromakalim on isolated rat bladder tissue and aorta strip. *Yao Xue Xue Bao,* 32**,** 740-3.

Cheng, S. H., Gregory, R. J., Marshall, J., Paul, S., Souza, D. W., White, G. A., Oriordan, C. R. & Smith, A. E. 1990. Defective Intracellular-Transport and Processing of Cftr Is the Molecular-Basis of Most Cystic-Fibrosis. *Cell,* 63**,** 827-834.

Chowdhury, R. A., Debney, M. T., Protti, A., Handa, B. S., Patel, K. H. K., Lyon, A. R., Shah, A. M., Ng, F. S. & Peters, N. S. 2021. Rotigaptide Infusion for the First 7 Days After Myocardial Infarction-Reperfusion Reduced Late Complexity of Myocardial Architecture of the Healing Border-Zone and Arrhythmia Inducibility. *Journal of the American Heart Association,* 10**,** e020006.

Civil Urkmez, Y., Avci, B., Gunaydin, C., Celik, Z. B. & Urkmez, S. S. 2024. Investigation of hyperpolarization-activated cyclic nucleotide-gated (HCN) channels in vitro inflammation model at molecular level. *Molecular and Cellular Biochemistry,* 479**,** 1223-1229.

Clarke, T. C., Thomas, D., Petersen, J. S., Evans, W. H. & Martin, P. E. 2006. The antiarrhythmic peptide rotigaptide (ZP123) increases gap junction intercellular communication in cardiac myocytes and HeLa cells expressing connexin 43. *British Journal of Pharmacology,* 147**,** 486-95.

Cober, R. E., Schober, K. E., Buffington, T. C., Li, X., Riesen, S. C. & Bonagura, J. D. 2011. Pharmacodynamic effects of ivabradine, a negative chronotropic agent, in healthy cats. *Journal of Veterinary Cardiology,* 13**,** 231-42.

Cobine, C. A., Callaghan, B. P. & Keef, K. D. 2007. Role of L-type calcium channels and PKC in active tone development in rabbit coronary artery. *American Journal of Physiology - Heart and Circulatory Physiology,* 292**,** H3079-88.

Cohen, R. A., Plane, F., Najibi, S., Huk, I., Malinski, T. & Garland, C. J. 1997. Nitric oxide is the mediator of both endothelium-dependent relaxation and hyperpolarization of the rabbit carotid artery. *Proceedings of the National Academy of Sciences of the United States of America,* 94**,** 4193-8.

Crane, G. J., Gallagher, N., Dora, K. A. & Garland, C. J. 2003a. Small- and intermediate-conductance calcium-activated K channels provide different facets of endothelium-dependent hyperpolarization in rat mesenteric artery. *Journal of Physiology-London,* 553**,** 183-189.

Crane, G. J., Walker, S. D., Dora, K. A. & Garland, C. J. 2003b. Evidence for a differential cellular distribution of inward rectifier K channels in the rat isolated mesenteric artery. *Journal of Vascular Research,* 40**,** 159-168.

Dalal, P. J., Muller, W. A. & Sullivan, D. P. 2020. Endothelial Cell Calcium Signaling during Barrier Function and Inflammation. *The American Journal of Pathology,* 190**,** 535-542.

Daut, J., Mehrke, G., Nees, S. & Newman, W. H. 1988. Passive electrical properties and electrogenic sodium transport of cultured guinea-pig coronary endothelial cells. *The Journal of Physiology,* 402**,** 237-54.

de Wit, C. & Griffith, T. M. 2010. Connexins and gap junctions in the EDHF phenomenon and conducted vasomotor responses. *Pflugers Arch,* 459**,** 897-914.

Dicks, A. P. & Williams, D. L. 1996. Generation of nitric oxide from S-nitrosothiols using protein-bound Cu^{2+} sources. *Chemical Biology,* 3**,** 655-9.

DiFrancesco, D., Ferroni, A., Mazzanti, M. & Tromba, C. 1986. Properties of the hyperpolarizing-activated current (if) in cells isolated from the rabbit sino-atrial node. *The Journal of Physiology,* 377**,** 61-88.

Dora, K., Doyle, M. P. & Duling, B. 1997. Elevation of intracellular calcium in smooth muscle causes endothelial cell generation of NO in arterioles. *Proceedings of the National Academy of Sciences of the United States of America,* 94**,** 6529-34.

Dora, K. A. & Garland, C. J. 2013. Linking hyperpolarization to endothelial cell calcium events in arterioles. *Microcirculation,* 20**,** 248-56.

Dora, K. A., Ings, N. T. & Garland, C. J. 2002. K(Ca) channel blockers reveal hyperpolarization and relaxation to K^+ in rat isolated mesenteric artery. *American Journal of Physiology - Heart and Circulatory Physiology,* 283**,** H606-14.

Drouin, A., Gendron, M. E., Thorin, E., Gillis, M. A., Mahlberg-Gaudin, F. & Tardif, J. C. 2008. Chronic heart rate reduction by ivabradine prevents endothelial dysfunction in dyslipidaemic mice. *British Journal of Pharmacology,* 154**,** 749-57.

Duling, B. R., Gore, R. W., Dacey, R. G., Jr. & Damon, D. N. 1981. Methods for isolation, cannulation, and in vitro study of single microvessels. *American Journal of Physiology,* 241**,** H108-116.

Eckert, R. E., Karsten, A. J., Utz, J. & Ziegler, M. 2000. Regulation of renal artery smooth muscle tone by alpha1-adrenoceptors: role of voltage-gated calcium channels and intracellular calcium stores. *Urology Research and Practice,* 28**,** 122-7.

Edwards, G., Dora, K. A., Gardener, M. J., Garland, C. J. & Weston, A. H. 1998. K^+ is an endothelium-derived hyperpolarizing factor in rat arteries. *Nature,* 396**,** 269-272.

El-Lakany, M. A., Haghbin, N., Arora, N., Hashad, A. M., Mironova, G. Y., Sancho, M., Gros, R. & Welsh, D. G. 2023. CaV3.1 channels facilitate calcium wave generation and myogenic tone development in mouse mesenteric arteries. *Scientific Reports,* 13**,** 20407.

El-Rahman, Abd, R. R., Harraz, O. F., Brett, S. E., Anfinogenova, Y., Mufti, R. E., Goldman, D. & Welsh, D. G. 2013. Identification of L- and T-type Ca^{2+} channels in rat cerebral arteries: role in myogenic tone development. *American Journal of Physiology-Heart and Circulatory Physiology,* 304**,** H58-H71.

Emerson, G. G., Neild, T. O. & Segal, S. S. 2002. Conduction of hyperpolarization along hamster feed arteries: augmentation by acetylcholine. *American Journal of Physiology-Heart and Circulatory Physiology,* 283**,** H102-H109.

Emerson, G. G. & Segal, S. S. 2000. Endothelial cell pathway for conduction of hyperpolarization and vasodilation along hamster feed artery. *Circulation Research,* 86**,** 94-100.

Epstein, M. 2007. Resistant hypertension: prevalence and evolving concepts. *American Journal of Hypertension,* 9**,** 2-6.

Essin, K., Welling, A., Hofmann, F., Luft, F. C., Gollasch, M. & Moosmang, S. 2007. Indirect coupling between Cav1.2 channels and ryanodine receptors to generate Ca^{2+} sparks in murine arterial smooth muscle cells. *The Journal of Physiology,* 584**,** 205-19.

Feelisch, M. 1991. The Biochemical Pathways of Nitric-Oxide Formation from Nitrovasodilators - Appropriate Choice of Exogenous No Donors and Aspects of Preparation and Handling of Aqueous No Solutions. *Journal of Cardiovascular Pharmacology,* 17**,** S25-S33.

Figueroa, X. F., Poblete, M. I., Boric, M. P., Mendizábal, V. E., Adler-Graschinsky, E. & Huidobro-Toro, J. P. 2001. Clonidine-induced nitric oxide-dependent vasorelaxation mediated by endothelial α-adrenoceptor activation. *British Journal of Pharmacology,* 134**,** 957-968.

Fleming, I. & Busse, R. 1999. Signal transduction of eNOS activation. *Cardiovascular Research,* 43**,** 532-41.

Fleming, I., Fisslthaler, B., Dimmeler, S., Kemp, B. E. & Busse, R. 2001. Phosphorylation of Thr(495) regulates Ca(2+)/calmodulin-dependent endothelial nitric oxide synthase activity. *Circ Res,* 88**,** E68-75.

Förstermann, U., Mülsch, A., Böhme, E. & Busse, R. 1986. Stimulation of soluble guanylate cyclase by an acetylcholine-induced endothelium-derived factor from rabbit and canine arteries. *Circulation Research,* 58**,** 531-8.

Furchgott, R. F. & Zawadzki, J. V. 1980. The obligatory role of endothelial cells in the relaxation of arterial smooth muscle by acetylcholine. *Nature,* 288**,** 373-376.

Garcia, J. & Beam, K. G. 1994. Calcium transients associated with the T type calcium current in myotubes. *The Journal of General Physiology,* 104**,** 1113-28.

Garcia, S. R. & Bund, S. J. 1998. Nitric oxide modulation of coronary artery myogenic tone in spontaneously hypertensive and Wistar-Kyoto rats. *Clinical Science,* 94**,** 225-9.

Garland, C. J. 1985. Endothelial cells and the electrical and mechanical responses of the rabbit coronary artery to 5-hydroxytryptamine. *Journal of Pharmacology and Experimental Therapeutics,* 233**,** 158-62.

Garland, C. J., Bagher, P., Powell, C., Ye, X., Lemmey, H. A. L., Borysova, L. & Dora, K. A. 2017. Voltage-dependent Ca^{2+} entry into smooth muscle during contraction promotes endothelium-mediated feedback vasodilation in arterioles. *Science Signaling,* 10**,** eaal3806.

Garland, C. J., Hiley, C. R. & Dora, K. A. 2011. EDHF: spreading the influence of the endothelium. *British Journal of Pharmacology,* 164**,** 839-52.

Garland, C. J. & McPherson, G. A. 1992. Evidence that nitric oxide does not mediate the hyperpolarization and relaxation to acetylcholine in the rat small mesenteric artery. *British Journal of Pharmacology,* 105**,** 429-35.

Ghosh, M., van den Akker, N. M. S., Wijnands, K. A. P., Poeze, M., Weber, C., McQuade, L. E., Pluth, M. D., Lippard, S. J., Post, M. J., Molin, D. G. M. & van Zandvoort, M. A. M. J. 2013. Specific Visualization of Nitric Oxide in the Vasculature with Two-Photon Microscopy Using a Copper Based Fluorescent Probe. *PLoS ONE,* 8**,** e75331-e75331.

Gilbert, G., Courtois, A., Dubois, M., Cussac, L.-A., Ducret, T., Lory, P., Marthan, R., Savineau, J.-P. & Quignard, J.-F. 2017. T-type voltage gated calcium channels are involved in

endothelium-dependent relaxation of mice pulmonary artery. *Biochemical Pharmacology,* 138**,** 61-72.

Goto, K., Rummery, N. M., Grayson, T. H. & Hill, C. E. 2004. Attenuation of conducted vasodilatation in rat mesenteric arteries during hypertension: role of inwardly rectifying potassium channels. *Journal of Physiology-London,* 561**,** 215-231.

Greenstein, A. S., Kadir, S., Csato, V., Sugden, S. A., Baylie, R. A., Eisner, D. A. & Nelson, M. T. 2020. Disruption of Pressure-Induced Ca^{2+} Spark Vasoregulation of Resistance Arteries, Rather Than Endothelial Dysfunction, Underlies Obesity-Related Hypertension. *Hypertension,* 75**,** 539-548.

Greenwood, I. A. & Prestwich, S. A. 2002. Characteristics of hyperpolarization-activated cation currents in portal vein smooth muscle cells. *American Journal of Physiology - Cell Physiology,* 282**,** C744-53.

Greif, D. M., Sacks, D. B. & Michel, T. 2004. Calmodulin phosphorylation and modulation of endothelial nitric oxide synthase catalysis. *Proceedings of the National Academy of Sciences of the United States of America,* 101**,** 1165-1170.

Gryglewski, R. J., Botting, R. M. & Vane, J. R. 1988. Mediators produced by the endothelial cell. *Hypertension,* 12**,** 530-48.

Gustafsson, F., Andreasen, D., Salomonsson, M., Jensen, B. L. & Holstein-Rathlou, N.-H. 2001. Conducted vasoconstriction in rat mesenteric arterioles: role for dihydropyridine-insensitive Ca^{2+} channels. *American Journal of Physiology-Heart and Circulatory Physiology,* 280**,** H582-H590.

Haefliger, J. A., Meda, P., Formenton, A., Wiesel, P., Zanchi, A., Brunner, H. R., Nicod, P. & Hayoz, D. 1999. Aortic connexin43 is decreased during hypertension induced by inhibition of nitric oxide synthase. *Arteriosclerosis, Thrombosis, and Vascular Biology,* 19**,** 1615-22.

Halcox, J. P., Schenke, W. H., Zalos, G., Mincemoyer, R., Prasad, A., Waclawiw, M. A., Nour, K. R. & Quyyumi, A. A. 2002. Prognostic value of coronary vascular endothelial dysfunction. *Circulation,* 106**,** 653-8.

Halliwell, B. 2003. Oxidative stress in cell culture: an under-appreciated problem? *FEBS Letters,* 540**,** 3-6.

Halliwell, J. V. & Adams, P. R. 1982. Voltage-clamp analysis of muscarinic excitation in hippocampal neurons. *Brain Research,* 250**,** 71-92.

Hansen, P. B., Jensen, B. L., Andreasen, D. & Skøtt, O. 2001. Differential Expression of T- and L-Type Voltage-Dependent Calcium Channels in Renal Resistance Vessels. *Circulation Research,* 89**,** 630-638.

Harraz, O. F., Abd El-Rahman, R. R., Bigdely-Shamloo, K., Wilson, S. M., Brett, S. E., Romero, M., Gonzales, A. L., Earley, S., Vigmond, E. J., Nygren, A., Menon, B. K., Mufti, R. E., Watson, T., Starreveld, Y., Furstenhaupt, T., Muellerleile, P. R., Kurjiaka, D. T., Kyle, B. D., Braun, A. P. & Welsh, D. G. 2014a. CaV3.2 channels and the induction of negative feedback in cerebral arteries. *Circulation Research,* 115**,** 650-61.

Harraz, O. F., Brett, S. E. & Welsh, D. G. 2014b. Nitric oxide suppresses vascular voltage-gated T-type Ca^{2+} channels through cGMP/PKG signaling. *American Journal of Physiology - Heart and Circulatory Physiology,* 306**,** H279-85.

Harraz, O. F., Brett, S. E., Zechariah, A., Romero, M., Puglisi, J. L., Wilson, S. M. & Welsh, D. G. 2015. Genetic ablation of CaV3.2 channels enhances the arterial myogenic response by modulating the RyR-BKCa axis. *Arteriosclerosis, Thrombosis, and Vascular Biology,* 35**,** 1843-51.

Hayashi, K., Ozawa, Y., Wakino, S., Kanda, T., Homma, K., Takamatsu, I., Tatematsu, S. & Saruta, T. 2003. Cellular mechanism for mibefradil-induced vasodilation of renal microcirculation - Studies in the isolated perfused hydronephrotic kidney. *Journal of Cardiovascular Pharmacology,* 42**,** 697-702.

He, W. & Frost, M. C. 2016. Direct measurement of actual levels of nitric oxide (NO) in cell culture conditions using soluble NO donors. *Redox Biology,* 9**,** 1-14.

Hilton, S. M. 1959. A peripheral arterial conducting mechanism underlying dilatation of the femoral artery and concerned in functional vasodilatation in skeletal muscle. *The Journal of Physiology,* 149**,** 93-111.

Hirano, Y., Fozzard, H. A. & January, C. T. 1989. Characteristics of L- and T-type Ca^{2+} currents in canine cardiac Purkinje cells. *American Journal of Physiology-Heart and Circulatory Physiology,* 256**,** H1478-H1492.

Hofmann, F. & Sold, G. 1972. A protein kinase activity from rat cerebellum stimulated by guanosine-3':5'-monophosphate. *Biochemical and Biophysical Research Communications,* 49**,** 1100-7.

Hohneck, A. L., Fries, P., Stroder, J., Schneider, G., Wagenpfeil, S., Schirmer, S. H., Bohm, M., Laufs, U. & Custodis, F. 2019. Effects of heart rate reduction with ivabradine on vascular stiffness and endothelial function in chronic stable coronary artery disease. *Journal of hypertension,* 37**,** 1023-1031.

Holzmann, S. 1982. Endothelium-induced relaxation by acetylcholine associated with larger rises in cyclic GMP in coronary arterial strips. *Journal of cyclic nucleotide research,* 8**,** 409–419.

Howitt, L., Kuo, I. Y., Ellis, A., Chaston, D. J., Shin, H.-S., Hansen, P. B. & Hill, C. E. 2013. Chronic deficit in nitric oxide elicits oxidative stress and augments T-type calcium-channel contribution to vascular tone of rodent arteries and arterioles. *Cardiovascular Research,* 98**,** 449-457.

Hu, Z. Q., Xiong, Y., Han, X. F., Geng, C. Y., Jiang, B. B., Huo, Y. Q. & Luo, J. C. 2013. Acute Mechanical Stretch Promotes eNOS Activation in Venous Endothelial Cells Mainly via PKA and Akt Pathways. *PLoS ONE,* 8**,** e71359.

Huang, L., Keyser, B. M., Tagmose, T. M., Hansen, J. B., Taylor, J. T., Zhuang, H., Zhang, M., Ragsdale, D. S. & Li, M. 2004. NNC 55-0396 [(1S,2S)-2-(2-(N-[(3-benzimidazol-2-yl)propyl]-N-methylamino)ethyl)-6-fluoro-1,2,3,4-tetrahydro-1-isopropyl-2-naphtyl cyclopropanecarboxylate dihydrochloride]: a new selective inhibitor of T-type calcium channels. *Journal of Pharmacology and Experimental Therapeutics,* 309**,** 193-9.

Huang, X., Yang, P., Yang, Z., Zhang, H. & Ma, A. 2016. Age-associated expression of HCN channel isoforms in rat sinoatrial node. *Experimental Biology and Medicine,* 241**,** 331-9.

Ignarro, L. J., Buga, G. M., Wood, K. S., Byrns, R. E. & Chaudhuri, G. 1987. Endothelium-derived relaxing factor produced and released from artery and vein is nitric oxide. *Proceedings of the National Academy of Sciences of the United States of America,* 84**,** 9265-9269.

Ingerman-Wojenski, C., Silver, M. J., Smith, J. B. & Macarak, E. 1981. Bovine endothelial cells in culture produce thromboxane as well as prostacyclin. *The Journal of clinical investigation,* 67**,** 1292-6.

Isakson, B. E., Ramos, S. I. & Duling, B. R. 2007. Ca^{2+} and inositol 1,4,5-trisphosphate-mediated signaling across the myoendothelial junction. *Circulation Research,* 100**,** 246-54.

Jackson, W. F. 2017. Potassium Channels in Regulation of Vascular Smooth Muscle Contraction and Growth. *Advances in pharmacology,* 78**,** 89-144.

Janigro, D., West, G. A., Nguyen, T. S. & Winn, H. R. 1994. Regulation of blood-brain barrier endothelial cells by nitric oxide. *Circulation Research,* 75**,** 528-38.

Jantzi, M. C., Brett, S. E., Jackson, W. F., Corteling, R., Vigmond, E. J. & Welsh, D. G. 2006. Inward rectifying potassium channels facilitate cell-to-cell communication in hamster retractor muscle feed arteries. *American Journal of Physiology-Heart and Circulatory Physiology,* 291**,** H1319-H1328.

Jensen, L. J., Salomonsson, M., Jensen, B. L. & Holstein-Rathlou, N. H. 2004. Depolarization-induced calcium influx in rat mesenteric small arterioles is mediated exclusively via mibefradil-sensitive calcium channels. *British Journal of Pharmacology,* 142**,** 709-18.

Jia, L., Bonaventura, C., Bonaventura, J. & Stamler, J. S. 1996. S-nitrosohaemoglobin: a dynamic activity of blood involved in vascular control. *Nature,* 380**,** 221-6.

Johns, A., Lategan, T. W., Lodge, N. J., Ryan, U. S., Van Breemen, C. & Adams, D. J. 1987. Calcium entry through receptor-operated channels in bovine pulmonary artery endothelial cells. *Tissue Cell,* 19**,** 733-45.

Joksovic, P. M., Doctor, A., Gaston, B. & Todorovic, S. M. 2007. Functional regulation of T-type calcium channels by s-nitrosothiols in the rat thalamus. *Journal of Neurophysiology,* 97**,** 2712-21.

Joseph, B. K., Thakali, K. M., Moore, C. L. & Rhee, S. W. 2013. Ion channel remodeling in vascular smooth muscle during hypertension: Implications for novel therapeutic approaches. *Pharmacology Research,* 70**,** 126-38.

Kansui, Y., Garland, C. J. & Dora, K. A. 2008. Enhanced spontaneous Ca^{2+} events in endothelial cells reflect signalling through myoendothelial gap junctions in pressurized mesenteric arteries. *Cell calcium,* 44**,** 135-46.

Klöckner, U., Lee, J. H., Cribbs, L. L., Daud, A., Hescheler, J., Pereverzev, A., Perez-Reyes, E. & Schneider, T. 1999. Comparison of the Ca^{2+} currents induced by expression of three cloned alpha1 subunits, alpha1G, alpha1H and alpha1I, of low-voltage-activated T-type Ca^{2+} channels. *European Journal of Neuroscience,* 11**,** 4171-8.

Knot, H. J. & Nelson, M. T. 1998. Regulation of arterial diameter and wall Ca^{2+} in cerebral arteries of rat by membrane potential and intravascular pressure. *Journal of Physiology,* 508**,** 199-209.

Kojima, H., Hirotani, M., Nakatsubo, N., Kikuchi, K., Urano, Y., Higuchi, T., Hirata, Y. & Nagano, T. 2001. Bioimaging of Nitric Oxide with Fluorescent Indicators Based on the Rhodamine Chromophore. *Analytical Chemistry,* 73**,** 1967-1973.

Kopincova, J., Puzserova, A. & Bernatova, I. 2012. L-NAME in the cardiovascular system - nitric oxide synthase activator? *Pharmacological Reports,* 64**,** 511-20.

Krogh, A. 1920. Studies on the capillariometer mechanism: I. The reaction to stimuli and the innervation of the blood vessels in the tongue of the frog. *The Journal of Physiology,* 53**,** 399-419.

Kuchan, M. J. & Frangos, J. A. 1994. Role of Calcium and Calmodulin in Flow-Induced Nitric-Oxide Production in Endothelial-Cells. *American Journal of Physiology,* 266**,** C628-C636.

Kuebler, W. M., Uhlig, U., Goldmann, T., Schael, G., Kerem, A., Exner, K., Martin, C., Vollmer, E. & Uhlig, S. 2003. Stretch activates nitric oxide production in pulmonary vascular endothelial cells. *American Journal of Respiratory and Critical Care Medicine,* 168**,** 1391-1398.

Kuo, I. Y., Ellis, A., Seymour, V. A. L., Sandow, S. L. & Hill, C. E. 2010. Dihydropyridine-Insensitive Calcium Currents Contribute to Function of Small Cerebral Arteries. *Journal of Cerebral Blood Flow & Metabolism,* 30**,** 1226-1239.

Kurjiaka, D. T. 2004. The conduction of dilation along an arteriole is diminished in the cremaster muscle of hypertensive hamsters. *Journal of Vascular Research,* 41**,** 517-24.

Lacy, P. S., Pilkington, G., Hanvesakul, R., Fish, H. J., Boyle, J. P. & Thurston, H. 2000. Evidence against potassium as an endothelium-derived hyperpolarizing factor in rat mesenteric small arteries. *British Journal of Pharmacology,* 129**,** 605-611.

Lacza, Z., Horvath, E. M., Pankotai, E., Csordas, A., Kollai, M., Szabo, C. & Busija, D. W. 2005. The novel red-fluorescent probe DAR-4M measures reactive nitrogen species rather than NO. *Journal of Pharmacological and Toxicological Methods,* 52**,** 335-40.

Lamboley, M., Pittet, P., Koenigsberger, M., Sauser, R., Beny, J. L. & Meister, J. J. 2005. Evidence for signaling via gap junctions from smooth muscle to endothelial cells in rat mesenteric arteries: possible implication of a second messenger. *Cell calcium,* 37**,** 311-20.

Lancaster, J. R., Jr. 1994. Simulation of the diffusion and reaction of endogenously produced nitric oxide. *Proceedings of the National Academy of Sciences of the United States of America,* 91**,** 8137-41.

Langheinrich, U., Mederos y Schnitzler, M. & Daut, J. 1998. Ca^{2+}-transients induced by K^{+} channel openers in isolated coronary capillaries. *Pflügers Archiv,* 435**,** 435-8.

Langton, P. D. & Standen, N. B. 1993. Calcium currents elicited by voltage steps and steady voltages in myocytes isolated from the rat basilar artery. *The Journal of Physiology,* 469**,** 535-48.

Lawton, P. F., Lee, M. D., Saunter, C. D., Girkin, J. M., McCarron, J. G. & Wilson, C. 2019. VasoTracker, a Low-Cost and Open Source Pressure Myograph System for Vascular Physiology. *Frontiers in Physiology,* 10**,** 99.

Lazniewska, J. & Weiss, N. 2017. Glycosylation of voltage-gated calcium channels in health and disease. *Biochimica et Biophysica Acta (BBA) - Biomembranes,* 1859**,** 662-668.

Ledoux, J., Werner, M. E., Brayden, J. E. & Nelson, M. T. 2006. Calcium-Activated Potassium Channels and the Regulation of Vascular Tone. *Physiology,* 21**,** 69-78.

Lee, J., Nelson, M. T., Rose, K. E. & Todorovic, S. M. 2013. Redox mechanism of S-nitrosothiol modulation of neuronal CaV3.2 T-type calcium channels. *Molecular Neurobiology,* 48**,** 274-80.

Lee, J. H., Gomora, J. C., Cribbs, L. L. & Perez-Reyes, E. 1999. Nickel block of three cloned T-type calcium channels: low concentrations selectively block alpha1H. *Biophysical Journal,* 77**,** 3034-42.

Lee, M. 2014. Z944: a first in class T-type calcium channel modulator for the treatment of pain. *Journal of the Peripheral Nervous System,* 19 Suppl 2**,** S11-2.

Lemmey, H. A. L., Ye, X., Ding, H. C., Triggle, C. R., Garland, C. J. & Dora, K. A. 2018. Hyperglycaemia disrupts conducted vasodilation in the resistance vasculature of db/db mice. *Vascular Pharmacology,* 103-105**,** 29-35.

Leo, F., Suvorava, T., Heuser, S. K., Li, J., LoBue, A., Barbarino, F., Piragine, E., Schneckmann, R., Hutzler, B., Good, M. E., Fernandez, B. O., Vornholz, L., Rogers, S., Doctor, A., Grandoch, M., Stegbauer, J., Weitzberg, E., Feelisch, M., Lundberg, J. O., Isakson, B. E., Kelm, M. & Cortese-Krott, M. M. 2021. Red Blood Cell and Endothelial eNOS Independently Regulate Circulating Nitric Oxide Metabolites and Blood Pressure. *Circulation,* 144**,** 870-889.

Lerman, A. & Zeiher, A. M. 2005. Endothelial function: cardiac events. *Circulation,* 111**,** 363-8.

Li, Y., Huang, T. T., Carlson, E. J., Melov, S., Ursell, P. C., Olson, J. L., Noble, L. J., Yoshimura, M. P., Berger, C., Chan, P. H., Wallace, D. C. & Epstein, C. J. 1995. Dilated cardiomyopathy and neonatal lethality in mutant mice lacking manganese superoxide dismutase. *Nature Genetics,* 11**,** 376-81.

Liao, P., Yu, D., Li, G., Yong, T. F., Soon, J. L., Chua, Y. L. & Soong, T. W. 2007. A smooth muscle Cav1.2 calcium channel splice variant underlies hyperpolarized window current and enhanced state-dependent inhibition by nifedipine. *Journal of Biological Chemistry,* 282**,** 35133-42.

Lidington, D., Ouellette, Y. & Tyml, K. 2002. Communication of agonist-induced electrical responses along 'capillaries' in vitro can be modulated by lipopolysaccharide, but not nitric oxide. *Journal of Vascular Research,* 39**,** 405-13.

Liu, T., Zhang, M., Mukosera, G. T., Borchardt, D., Li, Q., Tipple, T. E., Ishtiaq Ahmed, A. S., Power, G. G. & Blood, A. B. 2019. L-NAME releases nitric oxide and potentiates subsequent nitroglycerin-mediated vasodilation. *Redox Biology,* 26**,** 101238.

Lu, D. & Kassab, G. S. 2011. Role of shear stress and stretch in vascular mechanobiology. *Journal of The Royal Society Interface,* 8**,** 1379-85.

Luckhoff, A. & Busse, R. 1990. Calcium influx into endothelial cells and formation of endothelium-derived relaxing factor is controlled by the membrane potential. *Pflügers Archiv,* 416**,** 305-11.

Luebbert, M., Radtke, D., Wodarski, R., Damann, N., Hatt, H. & Wetzel, C. H. 2010. Direct activation of transient receptor potential V1 by nickel ions. *Pflügers Archiv,* 459**,** 737-50.

Lundberg, J. O., Gladwin, M. T. & Weitzberg, E. 2015. Strategies to increase nitric oxide signalling in cardiovascular disease. *Nature Reviews Drug Discovery,* 14**,** 623-41.

Majgaard, J., Skov, F. G., Kim, S., Hjortdal, V. E. & Boedtkjer, D. M. B. 2022. Positive chronotropic action of HCN channel antagonism in human collecting lymphatic vessels. *Physiological Reports,* 10**,** e15401.

Malinski, T., Taha, Z., Grunfeld, S., Patton, S., Kapturczak, M. & Tomboulian, P. 1993. Diffusion of Nitric-Oxide in the Aorta Wall Monitored in-Situ by Porphyrinic Microsensors. *Biochemical and Biophysical Research Communications,* 193**,** 1076-1082.

McNeish, A. J., Dora, K. A. & Garland, C. J. 2005. Possible role for K^+ in endothelium-derived hyperpolarizing factor-linked dilatation in rat middle cerebral artery. *Stroke,* 36**,** 1526-32.

McQuade, L. E., Ma, J., Lowe, G., Ghatpande, A., Gelperin, A. & Lippard, S. J. 2010. Visualization of nitric oxide production in the mouse main olfactory bulb by a cell-trappable copper(II) fluorescent probe. *Proceedings of the National Academy of Sciences of the United States of America,* 107**,** 8525-8530.

Michel, R. P., Hu, F. & Meyrick, B. O. 1995. Myoendothelial junctional complexes in postobstructive pulmonary vasculopathy: a quantitative electron microscopic study. *Experimental Lung Research,* 21**,** 437-52.

Michels, G., Brandt, M. C., Zagidullin, N., Khan, I. F., Larbig, R., van Aaken, S., Wippermann, J. & Hoppe, U. C. 2008. Direct evidence for calcium conductance of hyperpolarization-activated cyclic nucleotide-gated channels and human native If at physiological calcium concentrations. *Cardiovascular Research,* 78**,** 466-75.

Mistry, D. K. & Garland, C. J. 1998. Nitric oxide (NO)-induced activation of large conductance Ca^{2+}-dependent K^+ channels (BK(Ca)) in smooth muscle cells isolated from the rat mesenteric artery. *British Journal of Pharmacology,* 124**,** 1131-40.

Mittman, S., Guo, J. & Agnew, W. S. 1999. Structure and alternative splicing of the gene encoding alpha1G, a human brain T calcium channel alpha1 subunit. *Neuroscience Letters,* 274**,** 143-6.

Möller, M. N., Rios, N., Trujillo, M., Radi, R., Denicola, A. & Alvarez, B. 2019. Detection and quantification of nitric oxide–derived oxidants in biological systems. *Journal of Biological Chemistry,* 294**,** 14776-14802.

Moosmang, S., Biel, M., Hofmann, F. & Ludwig, A. 1999. Differential distribution of four hyperpolarization-activated cation channels in mouse brain. *Journal of Biological Chemistry,* 380**,** 975-80.

Morita, H., Cousins, H., Onoue, H., Ito, Y. & Inoue, R. 1999. Predominant distribution of nifedipine-insensitive, high voltage-activated Ca^{2+} channels in the terminal mesenteric artery of guinea pig. *Circulation Research,* 85**,** 596-605.

Mufti, R. E., Brett, S. E., Tran, C. H., Abd El-Rahman, R., Anfinogenova, Y., El-Yazbi, A., Cole, W. C., Jones, P. P., Chen, S. R. & Welsh, D. G. 2010. Intravascular pressure augments cerebral arterial constriction by inducing voltage-insensitive Ca^{2+} waves. *The Journal of Physiology,* 588**,** 3983-4005.

Mullan, B., Pettis, J. & Jackson, W. F. 2017. T-type voltage-gated Ca^{2+} channels do not contribute to the negative feedback regulation of myogenic tone in murine superior epigastric arteries. *Pharmacology Research & Perspectives,* 5**,** e00320.

Mulvany, M. J. & Halpern, W. 1976. Mechanical properties of vascular smooth muscle cells in situ. *Nature,* 260**,** 617-9.

Murata, T., Sato, K., Hori, M., Ozaki, H. & Karaki, H. 2002. Decreased endothelial nitric-oxide synthase (eNOS) activity resulting from abnormal interaction between eNOS and its regulatory proteins in hypoxia-induced pulmonary hypertension. *Journal of Biological Chemistry,* 277**,** 44085-92.

Murbartián, J., Arias, J. M., Lee, J.-H., Gomora, J. C. & Perez-Reyes, E. 2002. Alternative splicing of the rat CaV3.3 T-type calcium channel gene produces variants with distinct functional properties *FEBS Letters,* 528**,** 272-278.

Musialek, P., Lei, M., Brown, H. F., Paterson, D. J. & Casadei, B. 1997. Nitric oxide can increase heart rate by stimulating the hyperpolarization-activated inward current, I(f). *Circulation Research,* 81**,** 60-8.

Nam, G. 2018. T-type calcium channel blockers: a patent review (2012-2018). *Expert Opinion on Therapeutic Patents,* 28**,** 883-901.

Nausch, L. W., Bonev, A. D., Heppner, T. J., Tallini, Y., Kotlikoff, M. I. & Nelson, M. T. 2012. Sympathetic nerve stimulation induces local endothelial Ca^{2+} signals to oppose vasoconstriction of mouse mesenteric arteries. *American Journal of Physiology - Heart and Circulatory Physiology,* 302**,** H594-602.

Nelson, M. T., Patlak, J. B., Worley, J. F. & Standen, N. B. 1990. Calcium channels, potassium channels, and voltage dependence of arterial smooth muscle tone. *American Journal of Physiology-Cell Physiology,* 259**,** C3-C18.

Nikitina, E., Zhang, Z. D., Kawashima, A., Jahromi, B. S., Bouryi, V. A., Takahashi, M., Xie, A. & Macdonald, R. L. 2007. Voltage-dependent calcium channels of dog basilar artery. *Journal of Physiology-London,* 580**,** 523-541.

Nishikawa, Y. & Ogawa, S. 1997. Importance of nitric oxide in the coronary artery at rest and during pacing in humans. *Journal of the American College of Cardiology,* 29**,** 85-92.

Ohishi, M., Takagi, T., Ito, N., Terai, M., Tatara, Y., Hayashi, N., Shiota, A., Katsuya, T., Rakugi, H. & Ogihara, T. 2007. Renal-protective effect of T-and L-type calcium channel blockers in hypertensive patients: an Amlodipine-to-Benidipine Changeover (ABC) study. *Hypertension Research,* 30**,** 797-806.

Oishi, H., Budel, S., Schuster, A., Stergiopulos, N., Meister, J. J. & Beny, J. L. 2001. Cytosolic-free calcium in smooth-muscle and endothelial cells in an intact arterial wall from rat mesenteric artery in vitro. *Cell calcium,* 30**,** 261-7.

Olschewski, A., Olschewski, H., Brau, M. E., Hempelmann, G., Vogel, W. & Safronov, B. V. 2001. Basic electrical properties of in situ endothelial cells of small pulmonary arteries during postnatal development. *American Journal of Respiratory Cell and Molecular Biology,* 25**,** 285-90.

Papapetropoulos, S., Lee, M. S., Versavel, S., Newbold, E., Jinnah, H. A., Pahwa, R., Lyons, K. E., Elble, R., Ondo, W., Zesiewicz, T., Hedera, P., Handforth, A., Elder, J. & Versavel, M. 2021. A Phase 2 Proof-of-Concept, Randomized, Placebo-Controlled Trial of CX-8998 in Essential Tremor. *Movement Disorders,* 36**,** 1944-1949.

Pechanova, O., Vrankova, S. & Cebova, M. 2020. Chronic L-Name-Treatment Produces Hypertension by Different Mechanisms in Peripheral Tissues and Brain: Role of Central eNOS. *Pathophysiology,* 27**,** 46-54.

Pedersen, C. M., Venkatasubramanian, S., Vase, H., Hyldebrandt, J. A., Contractor, H., Schmidt, M. R., Botker, H. E., Cruden, N. L., Newby, D. E., Kharbanda, R. K. & Lang, N. N. 2016. Rotigaptide protects the myocardium and arterial vasculature from ischaemia reperfusion injury. *British Journal of Clinical Pharmacology,* 81**,** 1037-45.

Perez-Reyes, E. 2003. Molecular physiology of low-voltage-activated T-type calcium channels. *Physiological Reviews,* 83**,** 117-161.

Perez-Reyes, E., Cribbs, L. L., Daud, A., Lacerda, A. E., Barclay, J., Williamson, M. P., Fox, M., Rees, M. & Lee, J. H. 1998. Molecular characterization of a neuronal low-voltage-activated T-type calcium channel. *Nature,* 391**,** 896-900.

Pesic, A., Madden, J. A., Pesic, M. & Rusch, N. J. 2004. High Blood Pressure Upregulates Arterial L-Type Ca^{2+} Channels. *Circulation Research,* 94**,** e97-104.

Piazza, M., Guillemette, J. G. & Dieckmann, T. 2015. Dynamics of Nitric Oxide Synthase-Calmodulin Interactions at Physiological Calcium Concentrations. *Biochemistry,* 54**,** 1989-2000.

Picard, E., Kerckhove, N., Francois, A., Boudieu, L., Billard, E., Carvalho, F. A., Bogard, G., Gosset, P., Bourdier, J., Aissouni, Y., Bourinet, E., Eschalier, A., Daulhac, L. & Mallet, C. 2023. Role of T CD4(+) cells, macrophages, C-low threshold mechanoreceptors and spinal Ca(v) 3.2 channels in inflammation and related pain-like symptoms in murine inflammatory models. *British Journal of Pharmacology,* 180**,** 385-400.

Postea, O. & Biel, M. 2011. Exploring HCN channels as novel drug targets. *Nature Reviews Drug Discovery,* 10**,** 903-914.

Pratt, P. F., Bonnet, S., Ludwig, L. M., Bonnet, P. & Rusch, N. J. 2002. Upregulation of L-type Ca^{2+} channels in mesenteric and skeletal arteries of SHR. *Hypertension,* 40**,** 214-9.

Presta, A., Liu, J. W., Sessa, W. C. & Stuehr, D. J. 1997. Substrate binding and calmodulin binding to endothelial nitric oxide synthase coregulate its enzymatic activity. *Nitric Oxide-Biology and Chemistry,* 1**,** 74-87.

Quignard, J. F., Frapier, J. M., Harricane, M. C., Albat, B., Nargeot, J. & Richard, S. 1997. Voltage-gated calcium channel currents in human coronary myocytes. Regulation by cyclic GMP and nitric oxide. *Journal of Clinical Investigation,* 99**,** 185-193.

Quyyumi, A. A., Dakak, N., Andrews, N. P., Husain, S., Arora, S., Gilligan, D. M., Panza, J. A. & Cannon, R. O. 1995. Nitric-Oxide Activity in the Human Coronary Circulation - Impact of Risk-Factors for Coronary Atherosclerosis. *Journal of Clinical Investigation,* 95**,** 1747-1755.

Rae, G. A. & Calixto, J. B. 1989. Interactions of calcium antagonists and the calcium channel agonist Bay K 8644 on neurotransmission of the mouse isolated vas deferens. *British Journal of Pharmacology,* 96**,** 333-40.

Rapoport, R. M., Draznln, M. B. & Murad, F. 1983. Endothelium-dependent relaxation in rat aorta may be mediated through cyclic GMP-dependent protein phosphorylation. *Nature,* 306**,** 174-6.

Rees, D. D., Palmer, R. M. & Moncada, S. 1989. Role of endothelium-derived nitric oxide in the regulation of blood pressure. *Proceedings of the National Academy of Sciences of the United States of America,* 86**,** 3375-8.

Rhodin, J. A. 1967. The ultrastructure of mammalian arterioles and precapillary sphincters. *Journal of Ultrastructure Research,* 18**,** 181-223.

Richard, M., Kaufmann, P., Kornberger, R. & Dingemanse, J. 2019. First-in-man study of ACT-709478, a novel selective triple T-type calcium channel blocker. *Epilepsia,* 60**,** 968-978.

Rivers, R. J., Hein, T. W., Zhang, C. H. & Kuo, L. 2001. Activation of barium-sensitive inward rectifier potassium channels mediates remote dilation of coronary arterioles. *Circulation,* 104**,** 1749-1753.

Robertson, B. E., Schubert, R., Hescheler, J. & Nelson, M. T. 1993. cGMP-dependent protein kinase activates Ca-activated K channels in cerebral artery smooth muscle cells. *American Journal of Physiology-Cell Physiology,* 265**,** C299-303.

Sanchez, M. & McManus, O. B. 1996. Paxilline inhibition of the alpha-subunit of the high-conductance calcium-activated potassium channel. *Neuropharmacology,* 35**,** 963-8.

Sandow, S. L. & Hill, C. E. 2000. Incidence of myoendothelial gap junctions in the proximal and distal mesenteric arteries of the rat is suggestive of a role in endothelium-derived hyperpolarizing factor-mediated responses. *Circulation Research,* 86**,** 341-346.

Sandow, S. L., Neylon, C. B., Chen, M. X. & Garland, C. J. 2006. Spatial separation of endothelial small- and intermediate-conductance calcium-activated potassium channels (K(Ca)) and connexins: possible relationship to vasodilator function? *Journal of Anatomy,* 209**,** 689-98.

Santoro, B. & Shah, M. M. 2020. Hyperpolarization-Activated Cyclic Nucleotide-Gated Channels as Drug Targets for Neurological Disorders. *Annual Review of Pharmacology and Toxicology, Vol 60,* 60**,** 109-131.

Sato, T., Haimovici, R., Kao, R., Li, A. F. & Roy, S. 2002. Downregulation of connexin 43 expression by high glucose reduces gap junction activity in microvascular endothelial cells. *Diabetes,* 51**,** 1565-71.

Schachinger, V., Britten, M. B. & Zeiher, A. M. 2000. Prognostic impact of coronary vasodilator dysfunction on adverse long-term outcome of coronary heart disease. *Circulation,* 101**,** 1899-906.

Schiffrin, E. L. 1992. Reactivity of small blood vessels in hypertension: relation with structural changes. *Hypertension,* 19**,** 1-9.

Segal, S. S. & Duling, B. R. 1986. Flow control among microvessels coordinated by intercellular conduction. *Science,* 234**,** 868-70.

Segal, S. S. & Duling, B. R. 1989. Conduction of vasomotor responses in arterioles: a role for cell-to-cell coupling? *American Journal of Physiology-Heart and Circulatory Physiology,* 256.

Shibuki, K. 1990. An Electrochemical Microprobe for Detecting Nitric-Oxide Release in Brain-Tissue. *Neuroscience Research,* 9**,** 69-76.

Shimokawa, H., Yasutake, H., Fujii, K., Owada, M. K., Nakaike, R., Fukumoto, Y., Takayanagi, T., Nagao, T., Egashira, K., Fujishima, M. & Takeshita, A. 1996. The importance of the hyperpolarizing mechanism increases as the vessel size decreases in endothelium-dependent relaxations in rat mesenteric circulation. *Journal of Cardiovascular Pharmacology,* 28**,** 703-11.

Si, H., Heyken, W. T., Wolfle, S. E., Tysiac, M., Schubert, R., Grgic, I., Vilianovich, L., Giebing, G., Maier, T., Gross, V., Bader, M., de Wit, C., Hoyer, J. & Kohler, R. 2006. Impaired endothelium-derived hyperpolarizing factor-mediated dilations and increased blood pressure in mice deficient of the intermediate-conductance Ca^{2+}-activated K^+ channel. *Circulation Research,* 99**,** 537-44.

Simon, L., Ghaleh, B., Puybasset, L., Giudicelli, J. F. & Berdeaux, A. 1995. Coronary and hemodynamic effects of S 16257, a new bradycardic agent, in resting and exercising conscious dogs. *Journal of Pharmacology and Experimental Therapeutics,* 275**,** 659-66.

Simonsen, U., Wadsworth, R. M., Buus, N. H. & Mulvany, M. J. 1999. In vitro simultaneous measurements of relaxation and nitric oxide concentration in rat superior mesenteric artery. *The Journal of Physiology,* 516 (Pt 1)**,** 271-82.

Smirnov, S. V., Loutzenhiser, K. & Loutzenhiser, R. 2013. Voltage-activated Ca^{2+} channels in rat renal afferent and efferent myocytes: no evidence for the T-type Ca^{2+} current. *Cardiovascular Research,* 97**,** 293-301.

Smith, J. F., Lemmey, H. A. L., Borysova, L., Hiley, C. R., Dora, K. A. & Garland, C. J. 2020. Endothelial Nitric Oxide Suppresses Action-Potential-Like Transient Spikes and Vasospasm in Small Resistance Arteries. *Hypertension,* 76**,** 785-794.

Stamler, J. S., Loh, E., Roddy, M. A., Currie, K. E. & Creager, M. A. 1994. Nitric oxide regulates basal systemic and pulmonary vascular resistance in healthy humans. *Circulation,* 89**,** 2035-40.

Stork, A. P. & Cocks, T. M. 1994. Pharmacological reactivity of human epicardial coronary arteries: phasic and tonic responses to vasoconstrictor agents differentiated by nifedipine. *British Journal of Pharmacology,* 113**,** 1093-8.

Straub, A. C., Billaud, M., Johnstone, S. R., Best, A. K., Yemen, S., Dwyer, S. T., Looft-Wilson, R., Lysiak, J. J., Gaston, B., Palmer, L. & Isakson, B. E. 2011. Compartmentalized connexin 43 s-nitrosylation/denitrosylation regulates heterocellular communication in the vessel wall. *Arteriosclerosis, Thrombosis, and Vascular Biology,* 31**,** 399-407.

Svenningsen, P., Andersen, K., Thuesen, A. D., Shin, H.-S., Vanhoutte, P. M., Skøtt, O., Jensen, B. L., Hill, C. & Hansen, P. B. L. 2014. T-type Ca^{2+} channels facilitate NO-formation, vasodilatation and NO-mediated modulation of blood pressure. *Pflügers Archiv,* 466**,** 2205-2214.

Szekeres, M., Nadasy, G. L., Kaley, G. & Koller, A. 2004. Nitric oxide and prostaglandins modulate pressure-induced myogenic responses of intramural coronary arterioles. *Journal of Cardiovascular Pharmacology,* 43**,** 242-9.

Takano, H., Dora, K. A., Spitaler, M. M. & Garland, C. J. 2004. Spreading dilatation in rat mesenteric arteries associated with calcium-independent endothelial cell hyperpolarization. *Journal of Physiology-London,* 556**,** 887-903.

Takeda, K., Schini, V. & Stoeckel, H. 1987. Voltage-activated potassium, but not calcium currents in cultured bovine aortic endothelial cells. *Pflügers Archiv,* 410**,** 385-93.

Tewari, K. & Simard, J. M. 1997. Sodium nitroprusside and cGMP decrease Ca^{2+} channel availability in basilar artery smooth muscle cells. *Pflügers Archiv,* 433**,** 304-11.

Tran, C. H., Taylor, M. S., Plane, F., Nagaraja, S., Tsoukias, N. M., Solodushko, V., Vigmond, E. J., Furstenhaupt, T., Brigdan, M. & Welsh, D. G. 2012. Endothelial Ca^{2+} wavelets and the induction of myoendothelial feedback. *American Journal of Physiology-Cell Physiology,* 302**,** C1226-42.

Tschudi, M., Richard, V., Buhler, F. R. & Luscher, T. F. 1991. Importance of endothelium-derived nitric oxide in porcine coronary resistance arteries. *American Journal of Physiology,* 260**,** H13-20.

Vallance, P., Patton, S., Bhagat, K., Macallister, R., Radomski, M., Moncada, S. & Malinski, T. 1995. Direct Measurement of Nitric-Oxide in Human-Beings. *Lancet,* 346**,** 153-154.

van der Lee, R., Pfaffendorf, M. & van Zwieten, P. A. 1999. Comparative effects of mibefradil and other calcium antagonists on resistance arteries of different end organs. *Fundamental & Clinical Pharmacology,* 13**,** 198-203.

Wahl-Schott, C. & Biel, M. 2009. HCN channels: structure, cellular regulation and physiological function. *Cell Mol Life Sci,* 66**,** 470-94.

Waldron, C. G. & Garland, C. J. 1994. Effect of potassium channel blockers on the L-NAME insensitive relaxations in rat small mesenteric artery (Abstract). *Canadian Journal of Physiology and Pharmacology,* 72.

Wang, F., Flanagan, J., Su, N., Wang, L. C., Bui, S., Nielson, A., Wu, X., Vo, H. T., Ma, X. J. & Luo, Y. 2012. RNAscope: a novel in situ RNA analysis platform for formalin-fixed, paraffin-embedded tissues. *The Journal of Molecular Diagnostics,* 14**,** 22-9.

Weiss, N. & Zamponi, G. W. 2019. T-type calcium channels: From molecule to therapeutic opportunities. *The International Journal of Biochemistry & Cell Biology,* 108**,** 34-39.

Williams, D. L. H. 1999. The chemistry of S-nitrosothiols. *Accounts of Chemical Research,* 32**,** 869-876.

Wolfe, L., Francis, S. H., Landiss, L. R. & Corbin, J. D. 1987. Interconvertible cGMP-free and cGMP-bound forms of cGMP-dependent protein kinase in mammalian tissues. *Journal of Biological Chemistry,* 262**,** 16906-13.

Wu, S. W., Haynes, J., Taylor, J. T., Obiako, B. O., Stubbs, J. R., Li, M. & Stevens, T. 2003. CaV3.1 T-type Ca^{2+} channels mediate vaso-occlusion of sickled erythrocytes in lung microcirculation. *Circulation Research,* 93**,** 346-353.

Xiao, J., Nguyen, T. V., Ngui, K., Strijbos, P. J., Selmer, I. S., Neylon, C. B. & Furness, J. B. 2004. Molecular and functional analysis of hyperpolarisation-activated nucleotide-gated (HCN) channels in the enteric nervous system. *Neuroscience,* 129**,** 603-14.

Xing, Y., Zheng, X., Fu, Y., Qi, J., Li, M., Ma, M., Wang, S., Li, S. & Zhu, D. 2022. Long Noncoding RNA-Maternally Expressed Gene 3 Contributes to Hypoxic Pulmonary Hypertension. *Molecular Therapy,* 30**,** 501.

Yamamoto, Y., Imaeda, K. & Suzuki, H. 1999. Endothelium-dependent hyperpolarization and intercellular electrical coupling in guinea-pig mesenteric arterioles. *Journal of Physiology-London,* 514**,** 505-513.

Yeh, H. I., Lee, P. Y., Su, C. H., Tian, T. Y., Ko, Y. S. & Tsai, C. H. 2006. Reduced expression of endothelial connexins 43 and 37 in hypertensive rats is rectified after 7-day carvedilol treatment. *American Journal of Hypertension,* 19**,** 129-35.

Yi, X., Liu, M., Luo, Q., Zhuo, H., Cao, H., Wang, J. & Han, Y. 2017. Toxic effects of dimethyl sulfoxide on red blood cells, platelets, and vascular endothelial cells in vitro. *FEBS Open Bio,* 7**,** 485-494.

Yoshida, Y., Sun, H. T., Cai, Q. & Imai, S. 1991. Cyclic GMP-dependent protein kinase stimulates the plasma membrane Ca^{2+} pump ATPase of vascular smooth muscle via phosphorylation of a 240-kDa protein. *Journal of Biological Chemistry,* 266**,** 19819-25.

Yu, X., Duan, K. L., Shang, C. F., Yu, H. G. & Zhou, Z. 2004. Calcium influx through hyperpolarization-activated cation channels (I(h) channels) contributes to activity-evoked neuronal secretion. *Proceedings of the National Academy of Sciences of the United States of America,* 101**,** 1051-6.

Yuill, K. H., Yarova, P., Kemp-Harper, B. K., Garland, C. J. & Dora, K. A. 2011. A novel role for HNO in local and spreading vasodilatation in rat mesenteric resistance arteries. *Antioxidants & Redox Signaling,* 14**,** 1625-35.

Yunker, A. M., Sharp, A. H., Sundarraj, S., Ranganathan, V., Copeland, T. D. & McEnery, M. W. 2003. Immunological characterization of T-type voltage-dependent calcium channel CaV3.1 (alpha 1G) and CaV3.3 (alpha 1I) isoforms reveal differences in their localization, expression, and neural development. *Neuroscience,* 117**,** 321-35.

Zamponi, G. W., Bourinet, E. & Snutch, T. P. 1996. Nickel block of a family of neuronal calcium channels: subtype- and subunit-dependent action at multiple sites. *The Journal of Membrane Biology,* 151**,** 77-90.

Zhang, W. & Neer, E. J. 2001. Reassembly of phospholipase C-β from separated domains: Analysis of basal and G protein-stimulated activities. *Journal of Biological Chemistry,* 276**,** 2503-2508.

Zhong, X., Liu, J. R., Kyle, J. W., Hanck, D. A. & Agnew, W. S. 2006. A profile of alternative RNA splicing and transcript variation of CACNA1H, a human T-channel gene candidate for idiopathic generalized epilepsies. *Human Molecular Genetics,* 15**,** 1497-512.

Zong, X. G., Krause, S., Chen, C. C., Krüger, J., Gruner, C., Cao-Ehlker, X., Fenske, S., Wahl-Schott, C. & Biel, M. 2012. Regulation of Hyperpolarization-activated Cyclic Nucleotide-gated (HCN) Channel Activity by cCMP. *Journal of Biological Chemistry,* 287**,** 26506-26512.